An Investigation of Frequency Scanning Interferometry for the alignment of the ATLAS semiconductor tracker.

Paul Andrew Coe

St. Peter's College

University of Oxford

Thesis submitted in partial fulfilment
of the requirements for the degree of
Doctor of Philosophy

University of Oxford, Trinity Term 2001

An Investigation of Frequency Scanning Interferometry for the alignment of the ATLAS semiconductor tracker.

Paul Andrew Coe
St. Peter's College, University of Oxford

Thesis submitted in partial fulfilment of the requirements for the degree of Doctor of Philosophy

University of Oxford, Trinity Term 2001

Abstract

The relative alignment of the silicon detector modules of the ATLAS semiconductor tracker will need remote monitoring during operation, within a high radiation environment. A geodetic grid of distance measurement fibre-coupled interferometers will monitor changes in the shape of the support structure. Eight hundred fibre-coupled grid line interferometers (GLIs) will be compared simultaneously to a stable, evacuated reference interferometer using Frequency Scanning Interferometry (FSI). The GLIs, (from 70 mm to 1400 mm long, with pW level return signals) must be measured to a precision of 1 micron, to reconstruct the grid shape, in three dimensions, to a precision of 10 microns.

In this work two important limitations were overcome :

1. Inflated errors due to relative interferometer drift were significantly reduced using two lasers scanned in opposite directions.

2. The fine tuning range was effectively extended by linking the phase information in two 30 GHz fine tuning subscans, separated by a 3.5 THz coarse tuning interval.

A demonstration system was built using tunable laser diodes operating at wavelengths close to 836 nm. Several different fibre coupled GLIs were built. Each was measured against an invar reference interferometer sharing the same laboratory air.

The 400 mm GLI was measured to a (one standard deviation) precision of 120 nm and a 1195 mm GLI to a precision of 215 nm. Decreasing the GLI signal was not found to significantly degrade the measurement precision. Spurious reflections and vibrations were separately introduced to degrade the measurements. The errors were found to increase, with errors larger than 4 parts per million, observed for vibrations of 400 nm peak to peak amplitude.

Suggestions are given for reducing remaining errors. Further investigations into the effects of vibrations and spurious reflections are recommended.

Preface

As particle physics enters its second century, the focus of high energy, accelerator based research is the probing of the Standard Model at the TeV scale and the search for the long anticipated Higgs boson. This requires the production of large numbers of collisions and the search for *rare* events of interest amongst the resulting debris using detectors.

The construction of accelerator based experiments and the accompanying detectors involves tackling large numbers of diverse technological challenges simultaneously and is, therefore, a very demanding area of scientific endeavour, invoking multinational collaboration.

The technological challenge addressed here is the precise alignment of components in the tracking detector so as to guarantee particle trajectory measurement performance. The most important alignment method is track based fitting where large samples of tracking data are used to reconstruct the orientation of the detector elements. The tracks left by particles are able to connect regions of a detector, which would be inaccessible to any other alignment method. However, the precision of track fitting is limited by detector motion during the time needed to compile a sufficient volume of tracking data, for alignment. The solution is to monitor the motion of the detector independently and adjust the track based alignment accordingly.

The focus of this thesis is the development of a Frequency Scanning Interferometry technique for alignment of the Semiconductor Tracker within the ATLAS particle physics detector. The proposed interferometric alignment monitoring system, will need to make multiple simultaneous remote distance measurements within the hostile high radiation environment of the ATLAS particle detector.

Chapter 1 covers the general background for this work with concise reviews of, optical interferometry for distance measurement and alignment techniques used in tracking detectors to date. This general discussion is followed by specific descriptions of the challenges in ATLAS and the proposed FSI alignment scheme.

The next two chapters cover supporting details for the results presented in later chapters. Chapter 2 is a description of the equipment used in the FSI demonstration system, explaining the limitations of the instrumentation where relevant and the important role of timing in the data acquisition strategy. Chapter 3 is a detailed report on the data preparation and analysis methods used to extract a length measurement from the acquired interferometry data, including a description of the corrections applied for air refractivity.

Chapter 4 is a presentation of length measurements based on single fine tuning subscans, showing that the drift error which arises in the measurement from a single laser can be reduced significantly, by combining the measurements from a second laser, tuned in the opposite direction. Length measurements made by linking two subscans are presented in chapter 5, in the presence of different combinations of the following interferometer effects; large thermal drifts, vibrations, reduced interferometer signal and spurious reflections.

The errors and limitations in the use of the FSI technique are discussed in chapter 6, with a view to guiding the design of the ATLAS and other future FSI systems. The conclusions of this work are summarised in chapter 7.

To my parents and my sister.
For all your loving support and encouragement.

Non nobis, Domine, non nobis,
sed nomini tuo da gloriam
super misericordia tua et veritate tua.

Psalmus 115 (113 B) : 1

Acknowledgements

I wish to acknowledge all those who have helped to make the last $4\frac{5}{6}$ years a pleasant and memorable experience.

I must begin with my fellow ATLAS students, in particular Daniel Buira-Clark and Ankush Mitra, with whom it has been a great privilege to share an office and to cook up a warped vocabulary of humour (based loosely on Star Wars, Monthy Python and whatever else happened to be flavour of the month). Thank you both for all those discussions at the whiteboard, where we sought to find the answers to life, the Universe and all the basic physics we'd forgotten or never knew. Thanks also to Stephen Gibson and Adrian Fox-Murphy for being around at the end and the beginning of all this and for adding to their own ingredients to the humour. Thanks to Anish Grewal my immediate predecessor in the FSI lab, for performing data acquisition miracles with the clock and control card and with LabVIEW, so that any measurements were possible at all, to Antonia Lavorato for her stories and all the Italian vocabulary and Stephen Hunt for showing the way with all things computerised, to Daniel, Anish and me, (especially the Pinball game on Windows NT4).

Thanks also to the countless other office companions from LHC-b and CDF and to all my fellow students and the various members of support staff throughout the department who have made the place tick; particularly the computing support staff for all the patient provision of Gb after Gb of storage space for my data. Thanks also to the members of the physics photographic unit, who took, developed and digitised all the nice photographs of hardware which appear in this thesis and to the electronics and workshop staff with special mentions for David Smith and Bill Linford for notable contributions to the electronics and mechanical hardware respectively and to the librarians and the administration staff for all their patience.

Of course no ATLAS group would be complete without the academics, so special thanks to Richard Nickerson for withstanding considerable collaboration pressure from the rest of ATLAS worldwide, whilst everything, 'wasn't quite working yet' and Tony Weidberg for all the friendly but persistent suggestions to stop, as soon as everything was working. Thanks also to Todd and Noreen Huffman for all the thanksgiving day feasts and games of darts, to Jörn Große-Knetter for the wanton pyromania of those Feuerzangenbole evenings, to Armin Reichold for responding to all my requests for bizarre German translations without batting an eyelid and to Pedram Bargassa for all the discussions of Indo-european and other languages.

To everyone so far unmentioned who came along to the games of cricket especially Jenny Williams, Alex Nichols, Kyle Stephenson, Peter Richardson and Farrukh Azfar; 5-aside football, especially Charles Bremner, Ismail Boztosun, James Marchese, Olaf Ruske, Geoff Morton and Michelle Lefebvre, and to my ballroom/latin dancing lesson partners Amelia Luzzi and Frieda Midgley.

Thanks to all at Point Source Ltd., my sponsor company for all their financial support and for the chance to come and refresh my experience of working in the 'real world' in particular to David Pointer and Ian Alcock. My thanks to everyone in Romsey who helped me out during that time.

Just before I close I must point out my immense gratitude to Stewart Boogert, (a.k.a. Code Warrior), for porting the CERN Fortran library fitting package, MINUIT, to C. The opportunity to embed MINUIT in a LabVIEW CIN allowed me increase my data analysis rate by at least a factor of 100 and without this increase, time may well have run out before the process of linking subscans, (an important part of this research), had been properly debugged.

I reserve my most grateful thanks to my supervisor, David Howell, not just for his dedicated, (and at times overwhelming supervision - no more sailing stories *please*), but for all the hardware and electronics support (whilst wearing his engineer's hat) and most especially for hammering home the importance of tirelessly checking for logical consistency when solving problems.

Only after writing these acknowledgements do I remember how much I am indebted to you all.

Thank you.

The author gratefully acknowledges financial support for this work from PPARC and Point Source Ltd. under the auspices of the CASE studentship 9656034X.

This thesis was written using the typesetting software package LaTeX 2_ε. All graphs were generated using the Origin® graph plotting package from Microcal Inc. and the rest of the figures were generated by the author in Corel Draw 7 ™. This thesis and the research it describes, are original work carried out solely by the named author.

Published at the University of Oxford, Oxford, United Kingdom.

Contents

List of Figures

List of Tables

1. Interferometric alignment and its role in ATLAS

> In its attempts to get hints on the behaviour of matter and forces at the energy scale set by grand unified theories, modern elementary particle physics consists more and more in a search for rare events embedded in a sea of disturbing nuclear debris produced in high energy collisions.
>
> *Fabio Sauli* [Sau92]

1.1 Introduction

The 19th century development of single wavelength optical interferometry enabled sub-micron displacements to be measured for the first time. The scope of interferometry was extended by Benoit [Dit59, Coo71] using accurately known multiple wavelengths, so that length could be measured interferometrically without the need for a displacement measurement from one end to the other.

The recent widespread availability of tunable lasers with very narrow linewidths has enabled an extension of multiple wavelength interferometry, known as frequency scanning interferometry (FSI[1]) to be developed. With FSI the length of an unknown interferometer is compared with the length of a reference interferometer, by measuring the change in phase of each interferometer. This technique can be used to make simultaneous measurements of many unknown interferometers, by comparing each with the reference interferometer.

The reference interferometer based FSI length measurement has been investigated in this work for remotely monitoring the alignment of the semiconductor tracker (SCT) sub-system, used for measuring the trajectories of charged particles within the ATLAS detector. ATLAS is due to be installed as part of the Large Hadron Collider (LHC) project at CERN.

The LHC will begin operation in 2006, accelerating proton bunches in both directions around a 27 km circumference circular synchrotron until they are circulating at 11 parts in 10^9 less than the speed of light. Every 25 ns, a pair of proton bunches, travelling in opposite directions around the synchrotron, will pass through each other at the centre of ATLAS, producing up to 20 proton-proton collisions; each with a centre of mass energy of up to 14 TeV. The by-products of these collisions will expose the SCT to a very large flux of neutrons, charged hadrons and gamma rays [ATL97a].

An FSI system will be used to remotely monitor the alignment of the semiconductor tracker in this high radiation environment, by the simultaneous measurement of up to 800 fibre coupled interferometers, arranged to form the lines of a geodetic grid, with lengths ranging from 0.07 m to 1.4 m. The measurement performance of the SCT is expected to degrade by 20% if there is an unobserved relative misalignment in the three dimensional position of the detector elements of order 10 μm. This sets a baseline requirement for the geodetic alignment precision of 10 μm in three dimensions and corresponds to a 1 μm length measurement precision requirement for each grid line [ATL97a].

The basic interferometric techniques needed to measure the grid line interferometers remotely and simultaneously, (multiple lengths), to a precision of 1 μm, are investigated in this work.

[1] FSI is also known as Absolute Distance Interferometry.

1.2 Interferometric length measurement

1.2.1 Generation and detection of an interference signal

There are two important types of optical interference signal used in length measurement

- Fringe patterns, arising from coherent[2] phase differences between different interferometer beams from the same source
- Beat signals, arising from differences in frequency between different beams, from the same or different sources.

Incoherent phase differences arise continuously within a light beam, but these are lost by the averaging effect of the detection process and so do not give rise to observable fringes.

The generation of both types of signal is described below using the classical theory of electromagnetism in terms of a plane polarized electric field represented by an amplitude and phase, (based on similar discussions in [Dit59, Bor65, Coo71, Hec87]). The resultant interferometer signals described here using the classical theory of electromagnetism are in agreement with the predictions of the more advanced quantum mechanical treatment of interference, (see for example [Pfl67, Lou95]).

Interference fringe patterns

The generation of a coherent interference fringe pattern can be modelled by considering monochromatic light in the form of plane waves with an initial electric field amplitude E_0, travelling towards a beam-splitter as shown in Fig. 1.1.

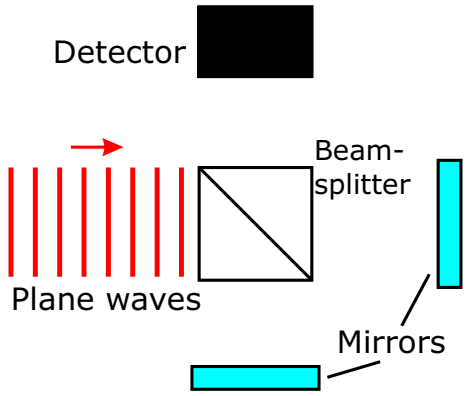

Figure 1.1: *Monochromatic plane waves in an amplitude-splitting two beam interferometer.*

The waves are separated by the beam-splitter into two beams which travel along different interferometer arms, recombine and generate an interference pattern which is recorded on a photodetector. If the optical paths of these two arms are z_1 and z_2, the electric field of the plane waves arriving on the detector from each arm of the interferometer may be written in the following form

$$E_1 = a_1 E_0 e^{i(\omega t - k z_1)} \quad (1.1a)$$

$$E_2 = a_2 E_0 e^{i(\omega t - k z_2 + \Phi_0)} \quad (1.1b)$$

where a_1 and a_2 are amplitude-coupling coefficients for each arm and Φ_0 is a general phase offset between the two beams.

If the fields in each arm have the same polarisation, the intensity of the interference pattern in a medium with electromagnetic impedance Z is given by

$$\begin{aligned} I &= \left(\frac{1}{2Z}\right)(E_1 + E_2)(E_1 + E_2)^* \\ &= \left(\frac{E_0^2}{2Z}\right)\left(a_1^2 + a_2^2 + 2a_1 a_2 \cos\Phi\right) \end{aligned} \quad (1.2)$$

[2] A phase difference is said to be *coherent* if it can be maintained for much longer than the detector response time.

where the phase term is given by

$$\begin{aligned} \Phi &= k\left(z_2 - z_1\right) + \Phi_0 \\ &= 2\pi\left(\frac{\Delta z}{\lambda}\right) + \Phi_0 \end{aligned} \tag{1.3}$$

where Δz is the optical path difference (OPD) of the interferometer and λ is the vacuum wavelength which corresponds to the wavevector k, related by

$$\lambda = \frac{2\pi}{k} \tag{1.4}$$

A more realistic model of the interferometer is required to describe the interference signal recorded by a detector sampling the interference pattern.

In a real interferometer the beams travelling in each arm cannot be infinite plane waves and the optical path difference is, in general, not a single value, but varies as a function of position across the recombined beam and therefore across the surface of a detector placed in this beam. The spatial dependence of OPD gives rise to a spatial, intensity fringe pattern.

The phase at a single point in the spatial fringe pattern changes whenever there is a change in the ratio between the relevant OPD and the vacuum wavelength of the light source. These changes are in effect temporal, intensity fringes.

The form of the detector signal may be seen using the example of a linear photodiode with responsivity R. The signal current I_{S}, generated by the sampled interference pattern intensity $I\left(\mathbf{r}, t'\right)$ is given by

$$I_S\left(t\right) = \frac{R}{\tau}\int_{t-\tau}^{t}\iint_A I\left(\mathbf{r}, t'\right) dA\; dt' \tag{1.5}$$

where $\mathbf{r}$ is the location of each element of area dA on the detector surface and τ is the effective photodiode response time.

For the purposes of the following discussion the detector signal can be represented in terms of an effective interferometer intensity, with the detector response for any given interferometer assumed to remain linear. The effective interferometer signal, therefore takes the form

$$I_{\mathrm{DET}} = I_0\left[1 + \gamma\cos\left(\Phi\right)\right] \tag{1.6}$$

with the phase term Φ taking the form of equation 1.3 for the average values of OPD and vacuum wavlength, from the integration over the detector response time and active area. The fringe contrast, or visibility, γ is maximised by

1. Sampling over as short a time period as possible.

2. Sampling over as small an area as possible.

In general, maximising the visibility imposes a direct penalty on the signal level I_0. A trade-off is therefore required to maximise the product γI_0, which is the strength of the interference signal containing the important phase information.

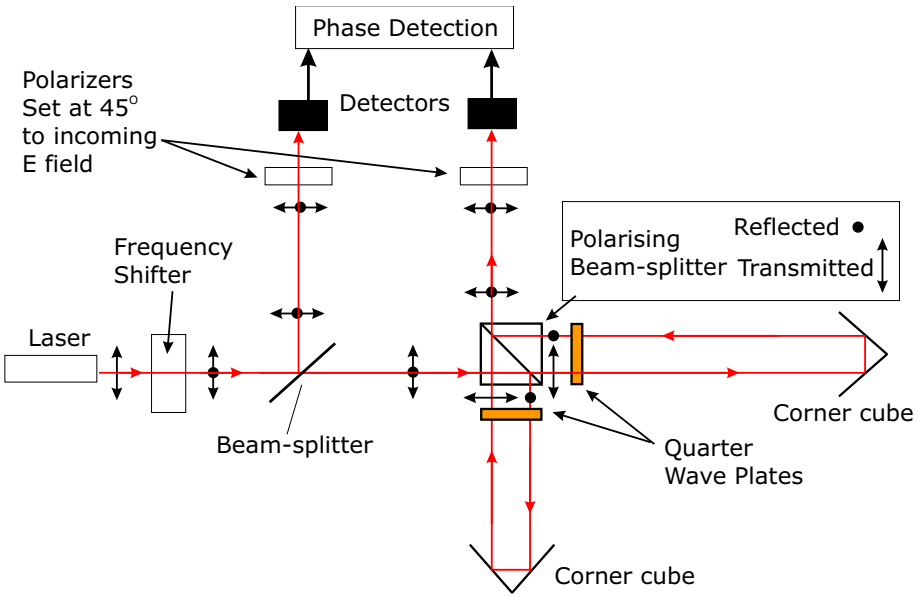

Figure 1.2: *Basic Heterodyne Interferometer(after Creath).*

Beat signals

The generation of beat signals is illustrated here by considering the widely used heterodyne interferometer. In its simplest form, this is a two beam interferometer similar to that discussed above, with modifications for the generation of a beat signal. The basic heterodyne interferometer is shown in Fig. 1.2, (after Creath [Cre93]).

The frequency shifter is often an acousto-optic modulator[3]. The two output beams are :

- An unaltered beam, which retains the original polarisation, frequency of the input beam.
- A frequency shifted beam which is polarised orthogonally with respect to the input beam.

The frequency shift is equal to the drive frequency of the acoustic transducer which generates the acoustic field within the modulator. The typical frequency shift available from a single device is of order 100 MHz. Much smaller relative shifts can be obtained using two modulators, one for each beam, with a small difference in the drive frequencies.

The first beam-splitter illuminates the first polarizer, set at 45° which lets through half the incident power at each frequency. The transmitted fractions of each beam combine at the first detector to produce a reference beat signal. At this detector, the electric field of the unshifted beam E_1 and frequency shifted beam E_2, are given by

$$E_1 = a_1 E_0 e^{i(\omega t - k z_1)} \tag{1.7a}$$
$$E_2 = a_2 E_0 e^{i((\omega+\Delta\omega)t - (k+\Delta k) z_2 + \Phi_0)} \tag{1.7b}$$

where the optical paths from frequency shifter to detector are in general different for shifted and unshifted beams. As for the monochromatic case discussed above, the intensity

[3]An acousto-optic modulator is a transparent crystal with a refractive index profile which is modified by a large amplitude acoustic field. (See for example [Xu92]).

at the left detector in Fig. 1.2 is given by equation 1.2, but the phase term, in this case, is instead given by

$$\Phi_{21} = 2\pi\left(\frac{\Delta z_{21}}{\lambda}\right) - (\Delta\omega)\,t + (\Delta k)\,z_2 + \Phi_0 \tag{1.8}$$

which corresponds to a reference beat signal at frequency f_{B}, given by

$$f_{\mathrm{B}} = \frac{\Delta\omega}{2\pi} \tag{1.9}$$

This optical method of generating the reference beat signal is preferable over an electronic alternative, (using for example the signal from the oscillator driving the frequency shifter), because any optical changes in the phase difference between the beams with shifted and unshifted optical frequencies in the system shown in Fig. 1.2, which result from changes in the path difference Δz_{21} will automatically be followed by the reference beat signal generated on the left detector. These phase changes, which have nothing to do with the interferometer being measured can therefore be cancelled from the final phase measurement, since they are also present in the light which eventually falls on the second detector on the right of Fig. 1.2.

The measurement beat signal is generated at this second detector using the beams returned by the interferometer, with the optical path difference which is to be measured. The unshifted and frequency shifted beams travel the optical paths, z_3 and z_4 respectively via the longer interferometer and shorter interferometer arms before partially transmitting through a polarizer at 45° to arrive at the second detector.

The electric fields, of the unshifted beam E_3 and of the frequency shifted beam E_4, at the second detector, are given by

$$E_3 = a_3 E_0 e^{i(\omega t - k z_3)} \tag{1.10a}$$
$$E_4 = a_4 E_0 e^{i((\omega+\Delta\omega)t - (k+\Delta k) z_4 + \Phi_0)} \tag{1.10b}$$

The intensity at the second detector is given by

$$I = \left(\frac{E_0^2}{2Z}\right)\left(a_3^2 + a_4^2 + 2a_3 a_4 \cos\Phi_{43}\right) \tag{1.11}$$

where the phase term Φ_{43} is given by

$$\Phi_{43} = 2\pi\left(\frac{\Delta z_{43}}{\lambda}\right) - (\Delta\omega)\,t + (\Delta k)\,z_4 + \Phi_0 \tag{1.12}$$

Assuming that the detectors and phase measurement electronics are able to respond at the frequency of the beat signals, the difference in detected signal phases is given by

$$\begin{aligned}\Phi &= \Phi_{43} - \Phi_{21} \\ &= 2\pi\left(\frac{\Delta z_{43} - \Delta z_{21}}{\lambda}\right) - \Delta k\,(z_4 - z_2)\end{aligned} \tag{1.13}$$

The first term on the left represents the phase contribution due to the optical path difference of the interferometer, which is the signal to be measured. The second term is a phase offset which corresponds to the difference in phase shift between light at the two optical frequencies over the difference between the optical paths (taken by the frequency

shifted beam) to the two detectors. The changes in this second order term are negligible[4] compared to the main signal under normal conditions where $z_4 - z_2$ is typically of order 1 m.

As an example, for a frequency difference of 100 MHz, $\Delta k = 2.06$ m^{-1}, so the path difference between detectors $z_4 - z_2$, would need to change by around 3.7 m, to cause a 1 μm change in the measured interferometer length, at a laser wavelength of 830 nm.

Fringe pattern phase

The phase of an interference fringe pattern is measured measured by making intensity comparisons. The intensity can be compared either at different points in the pattern, or at different moments in time or using the intensity information in two different polarisations. The aim in all cases is to establish the value of maximum and minimum intensity and determine the phase from the sinusoidal dependence of intensity.

In shape measurement and surface profiling interferometry, the interference fringe pattern is detected as an extended two dimensional pattern and in these cases the phase can be measured by comparison of the intensity from point to point in the pattern. In the length measurements discussed here, the fringe pattern is only sampled at a single spatial point, so spatial comparison of the fringe pattern is not an option.

A quadrature detection scheme for recording the interferometer signal phase was demonstrated by Pfeifer and Thiel using a quarter wave plate and a pair of woolaston prisms [Pfe93]. A schematic of this quadrature detection scheme is shown in Fig. 1.3.

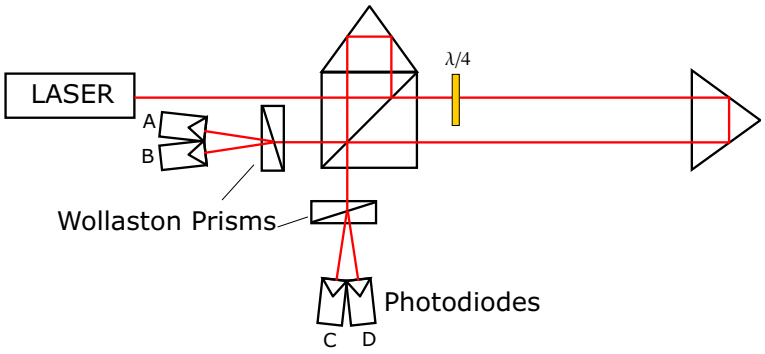

Figure 1.3: *Phase quadrature measurement scheme (after Pfeifer and Thiel).*

The four detectors record four versions of the interferometer signal with a 90° phase shift between each one. The two polarisation compoments separated by each wollaston prism are generated by the quarter wave plate, with a 90° phase difference. The beam going to one wollaston prism is 180° out of phase[5] with the beam going to the other prism. Since each beam contains light of both polarisations, there are a total of four measurements of the interferometer signal, with a 90° phase shift between each.

This quadrature technique is a simultaneous implementation of the more general phase measurement technique, known as *phase stepping*[6]. This involves deliberately introducing

[4]The error resulting from changes in this term might be important, if nanometer precision is required and if the two detectors are separated by long lengths of fibre, in a remote measurement system. If, in the design of such a system, a large path difference between detectors cannot be avoided, these errors can be reduced by keeping the frequency difference between the two arms as small as possible.

[5]This is true for any interferometer with a non-polarising beam-splitter which does not absorbs significantly. The transmitted and reflected beams are in anti-phase, so that the total power remains constant, as it must to satisfy conservation of energy.

[6]The most commonly used phase stepping techniques are described by Creath [Cre88].

fixed size phase changes or steps and recording the intensity at each phase. The phase steps are often measured one at time in sequence, rather than being available all at once. Phase stepping was used in this work, for measuring the phase of the reference interferometer, as discussed in detail in chapters 2, (for the mechanical implementation) and 3 (for the related *phase extraction* data analysis). When the phase measurements are in sequence, the phase measurement is extracted by fitting the best fit phase to the intensity data.

Another example of extracting phase information by fitting is the sinefit applied to the grid line interferometer signal, (discussed in detail in chapter 3). This relies on laser frequency scanning, (rather than phase stepping), to induce phase variations.

A less accurate method for recording the phase change in a frequency scanning system, which has the advantage of working in real time, (rather than waiting for a function to be fitted to the recorded interferometer signal), is based on counting the integer number of phase cycles using a threshold detection system [Sto99].

Beat signal phase

The phase of an interferometer beat signal is measured by comparing with a reference signal at the same frequency, generated either electronically by a local oscillator or optically as described above. Comercially available phase meters can be used to measure signals, up to around 10 MHz with a typical resolution of around $\frac{2\pi}{1000}$ [Dän88]. At lower frequency this can be improved to the level of a few percent of a degree [Bob93].

If high beat frequencies are generated beyond the range of the phase measurement electronics, the reference and interferometer signals can be shifted to within the range of a phase meter using further electronic heterodyning by electronically mixing the detector signal with a local oscillator.

The ultimate upper limit on the beat frequency in this case is the response of the detector, which needs to be traded off against the noise in the system. In general the more power available in the signal, the wider the detection electronics bandwidth can afford to be opened. Commercially available APDs[7], for example, can respond up to frequencies of order 1 GHz [Ham97].

1.2.2 Multiple wavelength interferometry

Multiple wavelength interferometry was developed to overcome the limitations of single wavelength interferometry. When an interferometer is illuminated with a single wavelength, the phase signal provides an unambiguous record of relative changes in optical path difference only over a single wavelength, corresponding to length differences of half a wavelength. The ambiguity arises because the interferometer intensity signal repeats for every change of 2π in phase. Within this limited dynamic range, the highest precision measurements (of displacement), have been demonstrated in gravitational wave detectors, which are designed to monitor changes of less than 10^{-17} m [Ju00].

In less demanding measurements, the unambiguous measurement range can be extended to cover a so-called *synthetic wavelength*, by measuring the phase using multiple wavelengths.

For two (vacuum) wavelengths λ_1 and λ_2 the synthetic wavelength is given by

$$\lambda_S = \frac{\lambda_1 \lambda_2}{|\lambda_1 - \lambda_2|} \tag{1.14}$$

[7]APD stands for Avalanche Photodiode. This and similar acronyms are given in the Glossary (Appendix A).

Two-wavelength interferometry was initially used for measuring two-dimensional surface profiles [Pol73, Fer85]. Schemes for performing two wavelength interferometry in a length measurement with a heterodyne interferometer, relied on separating the two wavelengths so they could be detected individually. This separation was achieved using dispersive or dichromatic elements, which require a significant wavelength difference to give good separation, so the dual wavelength heterodyning technique was limited to the use of longer synthetic wavelengths. This limitation was overcome in a technique introduced by Dändliker et al. [Dän88], known as superheterodyne interferometry.

Superheterodyne interferometry

Superheterodyne interferometry relies on combining two basic heterodyne interferometers into a single system. An example of superheterodyne system is shown in Fig. 1.4, (after Yokoyama et al. [Yok99]).

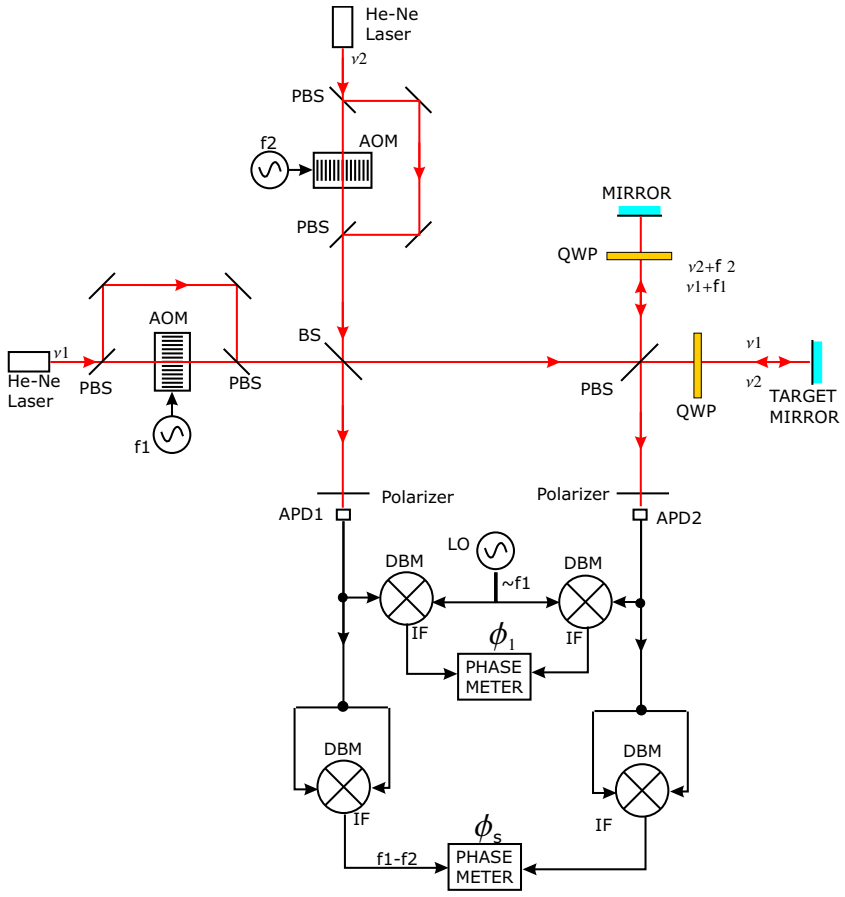

Figure 1.4: *Superheterodyne interferometer (after Yokoyama et al.). The abbreviations are : AOM - Acousto-optic modulator, APD - Avalanche Photodiode, BS - Non-polarising beam-splitter, DBM - Double balanced mixer, IF - Intermediate Frequency, LO - local oscillator, PBS - Polarising beam-splitter and QWP - Quarter wave plate.*

The first APD records reference beat signals at the two modulation frequencies f_1 and f_2 as in the basic heterodyne interferometer shown in Fig. 1.2.

The upper half of the detection electronics shown in Fig. 1.4 is used to generate a conventional heterodyne interferometer signal for measuring the phase of laser 1. The relevant beat signals are filtered out from each detector signal by mixing with a local oscillator set to

a frequency which is close to f_1 and (on the scale of f_1) far from f_2. The low pass filtered output from these mixing processes are a down-shifted copy of the reference and interferometer beat signals from laser 1. These beat signals are compared to measure the interferometer phase ϕ_1 at the laser 1 wavelength λ_1.

In the lower half of the detection electronics, each APD signal, (containing the beat signals from both lasers), is mixed with itself and low pass filtered to leave a signal at the difference frequency between the beat signal frequencies $f_1 - f_2$. The phase measured at this frequency is the phase of the synthetic wavelength, $\phi_S = \phi_2 - \phi_1$.

If the synthetic phase has been measured accurately and the distance is smaller than λ_S, ϕ_S can be used to determine the order number of the interferometer phase ϕ_1. This idea was used by Yokoyama et al. to measure distances up to half the 9.2 μm synthetic wavelength.

The key advantage of this technique is the freedom to use any two wavelengths within the detector response range to generate a wide variety of synthetic wavelengths.

Dändliker et al. extended this method further to use three different lasers at three different wavelengths operating with the superheterodyne system in pairs, to measure up to 200 mm with a reported precision of 10 μm [Dän98].

A more recent example of length measurement based on two-wavelength interferometry was reported by Zhao et al. [Zha99]. In this scheme the wavelengths of two closely spaced modes of a He-Ne laser were used to produce a synthetic wavelength of 278 mm. This relied on directly measuring the fractional phase at the two laser wavelengths to monitor a 280 mm change in a distance of approximately 25 m, with a reported accuracy of 140 μm.

The disadvantage of this two wavelength technique is that the length needs to be known initially to within a synthetic wavelength. The accuracy to which the length must be initially known can be relaxed by using multiple wavelengths and the method of excess fractions, initially developed by Benoit at the end of the 19$^{\text{th}}$ century [Dit59, Coo71].

Method of excess fractions

The method of excess fractions involves measuring the fractional part of the phase ϕ, (i.e. the phase to modulo 2π) at a set of known wavelengths and determining the length by working out the order number of each interferometer phase measurement.

The optical path difference $2nL$ can be related to the fractional phase at λ_i using

$$2nL = \left(N_i + \frac{\phi_i}{2\pi}\right)\lambda_i \tag{1.15}$$

where n is the refractive index.

For each individual measurement, there is a large range of possible integer order numbers, N_i bounded only by the relatively inaccurate initial knowledge of the measured length L. Each potential value of order number corresponds to a different potential value for the measured length. The potential lengths corresponding to phase measurements at several wavelengths can be compared and incompatible length values eliminated. If enough different wavelengths are used, the number of potential choices for measured length can be reduced to a single choice within the bounds of the initial length estimate. The greater the number of wavelengths used, the less accurate the initial length estimate needs to be.

This method has been used to make length measurements using 11 lines of a stabilised dye laser with a reported accuracy better than 10 nm over distances up to 100 mm [Ogi95] and using 6 lines of a CO_2 laser to measure 492 mm to within approximately 100 nm [Bour79]. It is limited to sources with many well determined wavelengths and requires a

phase measurement technique which works at a static phase value, such as heterodyning interferometry, phase stepping or quadrature measurements.

A variation on this method was employed by Xiaoli and Katuo with a tunable laser diode, where the phase excess fraction was measured before and after a 10 nm wavelength scan and the order number was determined by measuring different lengths in the range 0 to 4 mm, using a moving stage. Once the zero position of the length measurement had been found and the order number determined, lengths over the 4 mm range were measured with an accuracy of 3 nm [Xia98].

1.2.3 Time of flight measurements

Time of flight measurements involve the periodic modulation of some property of the light beam. The time delay due to the round trip, made by light, (along the distance being measured and back), is encoded as a change in the modulation property. Two examples are presented here to illustrate the underlying principles of each technique. The first example involves frequency modulation and the second involves intensity modulation.

Frequency Modulation

A simple example of a distance measurement system based on frequency modulation is shown in Fig. 1.5 (after Minoni et al. [Min98]). The system is based around a simple heterodyne interferometer, with the role of the frequency shifter replaced by direct frequency modulation of the laser.

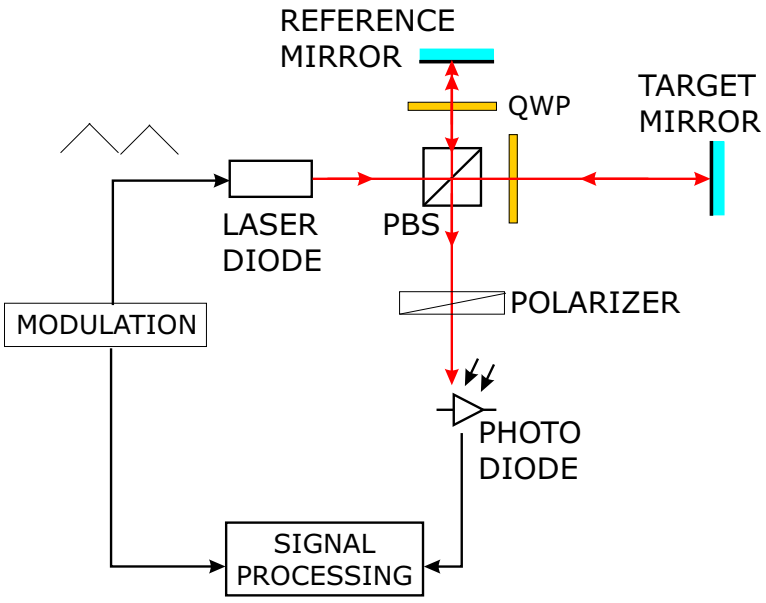

Figure 1.5: *Frequency modulated distance measurement system, (after Minoni et al.).*

The laser drive current is modulated so that the frequency follows a sawtooth time dependence as shown in Fig. 1.6. The heterodyne interferometer generates a beat frequency, at the frequency difference between the light from the short arm and the longer arm. For a constant rate of change of frequency $\dot{\nu}$, the detected signal contains the beat frequency given by

$$f_{\mathrm{B}} = \dot{\nu}\frac{2nL}{c} \tag{1.16}$$

The beat frequency is measured away from the transition regions, (shown in Fig. 1.6), where the modulation direction reverses. The length can be extracted unambiguously provided the condition

$$\frac{2nL}{c} < \frac{T_{\mathrm{MOD}}}{2} \tag{1.17}$$

is satisfied. This corresponds to a dynamic range for the length measurement given by

$$L < \frac{cT_{\mathrm{MOD}}}{4n} \tag{1.18}$$

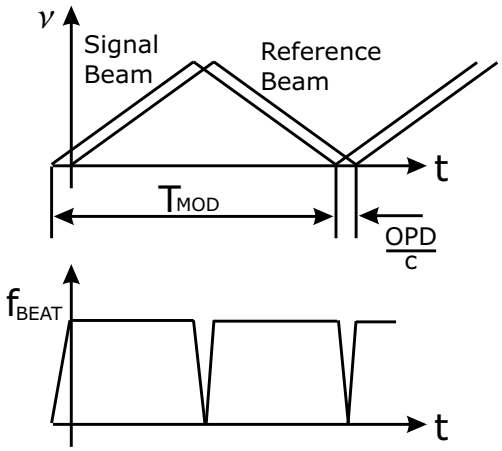

Figure 1.6: *Beat frequency produced by the detection of frequency modulation signal from two arms of the heterodyne interferometer shown in Fig. 1.5 (after Minoni et al.).*

The resolution of the length measurement is controlled by the beat frequency measurement resolution. The length resolution could, in principle, be improved by increasing the beat frequency using a faster frequency modulation rate $\dot{\nu}$. This can be achieved in one of two ways, both of which have disadvatages.

If the frequency modulation rate is increased by decreasing the period of the laser drive current modulation waveform, the unambiguous length measurement range decreases. This disadvantage is less important in cases where the length to be measured is much shorter than the ambiguity limit.

The alternative method of increasing the frequency modulation rate involves increasing the amplitude of the laser current modulation waveform. Modulating the laser drive current also modulates the laser output power. If the current modulation amplitude increases, the variation in the output power increases, making the beat frequency measurement more difficult [Min98].

Lengths at 10 mm intervals, up to 170 mm, were measured using the laser diode based system shown in Fig. 1.5 at a modulation frequency of 400 Hz. The residuals differences between the measurement results and a linear fit had a standard deviation of 350 μm which is $\approx 10^{-3}$ of the distance being measured. A static measurement at 152 mm repeated every 15 minutes over 8 hours gave a similar result.

Intensity Modulation

A distance meter was used by Fujima et al. [Fuj98] for measuring small displacements at distances up to 100 m. This system is not based on interferometry but is included in this review, because the technique is an optical technique used to tackle the same kind of distance measurement problem for which interferometric techniques have been employed. The system is shown in Fig. 1.7, with a laser diode source operating at $\lambda = 1.3$ μm.

The intensity of the laser light was modulated sinusoidally at 28 GHz using an electro-optic modulator, driven with a sinewave voltage at 14 GHz. The modulator bias voltage was set so that the output of the modulator was the second-order harmonic of the input voltage[8].

The electric field of the output of the modulator was given by

$$E = E_0 \cos(\Omega_{\mathrm{M}} t)\, e^{i(\omega t - kz)} \tag{1.19}$$

where Ω_{M} is the frequency of the oscillator driving the modulator.

[8]The operation of electro-optic modulators is discussed in [Smi95].

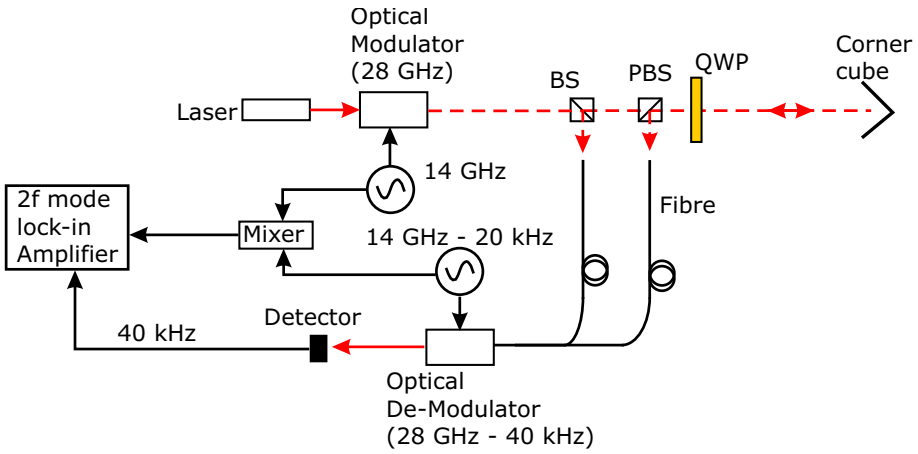

Figure 1.7: *Distance meter incorporating optical (intensity) modulators, after Fujima et al.*

This output was split using a non-polarising beam-splitter with one fraction coupled directly into a fibre with an electric field given by

$$E_1 = a_1 E_0 \cos(\Omega_M t)\, e^{i(\omega t - kz)} \tag{1.20}$$

where a_1 is an amplitude coupling coefficient. The other beam first travelled up and down the length to be measured, by reflecting from a corner cube and was then coupled into a second fibre. The electric field of this second beam in its fibre is given by

$$E_2 = a_2 E_0 \cos(\Omega_M t)\, e^{i(\omega t - kz - k\mathcal{L})} \tag{1.21}$$

where a_2 is an amplitude coefficient and $\mathcal{L}$ is the optical round trip path being measured.

The two fibres were coupled into the optical intensity demodulator, driven at a frequency $\Omega_M - \Delta\Omega$. The demodulated electric field is given by

$$E_D = \cos[(\Omega_M - \Delta\Omega)\, t]\,(E_1 + E_2) \tag{1.22}$$

The intensity of the light arriving on the detector is proportional to

$$E_D E_D^* = \cos^2[(\Omega_M - \Delta\Omega)\, t]\,(E_1 + E_2)\,(E_1^* + E_2^*) \tag{1.23a}$$

which can be re-written using the identity

$$\cos^2 A = \frac{1}{2}(1 + \cos 2A)$$

to give

$$E_D E_D^* = \frac{1 + \cos[2(\Omega_M - \Delta\Omega)\, t]}{2}\,(E_1 + E_2)\,(E_1^* + E_2^*) \tag{1.23b}$$

The last two right hand terms can be expanded, by substitution from equations 1.20 and 1.21, to give

$$\begin{aligned}(E_1 + E_2)\,(E_1^* + E_2^*) = {} & \frac{E_0^2}{2}\left[1 + \cos(\Omega_M t)\right]\left(a_1^2 + a_2^2\right) + \\ & a_1 a_2 E_0^2\left[1 + \cos(2\Omega_M t)\right]\cos(k\mathcal{L})\end{aligned} \tag{1.24}$$

The result from equation 1.24 can be substituted back into equation 1.23b using the identity

$$(1+\cos A)(1+\cos B) = 1+\cos A+\cos B+\frac{1}{2}\left[\cos(A+B)+\cos(A-B)\right]$$

to give

$$\begin{aligned} E_{\mathrm{D}}E_{\mathrm{D}}^{*} &= E_0^2\left(\frac{a_1^2+a_2^2}{4}\right)\left(1+\cos(\Omega_{\mathrm{M}}t)+\cos\left[2(\Omega_{\mathrm{M}}-\Delta\Omega)t\right]+\right. \\ &\quad \left.\frac{1}{2}\cos\left[(3\Omega_{\mathrm{M}}-2\Delta\Omega)t\right]+\frac{1}{2}\cos\left[(\Omega_{\mathrm{M}}-2\Delta\Omega)t\right]\right) \\ &+ \frac{a_1a_2}{2}E_0^2\cos(k\mathcal{L})\left(1+\cos(2\Omega_{\mathrm{M}}t)+\cos\left[2(\Omega_{\mathrm{M}}-\Delta\Omega)t\right]+\right. \\ &\quad \left.\frac{1}{2}\cos\left[(4\Omega_{\mathrm{M}}-2\Delta\Omega)t\right]+\frac{1}{2}\cos(2\Delta\Omega t)\right) \end{aligned} \tag{1.25}$$

The only frequency present in the detector signal is at $2\Delta\Omega$, (because the others are much too fast to be followed), with an amplitude proportional to $\cos(k\mathcal{L})$. The measurement of this amplitude gives an *effective interferometer phase*, equivalent to measuring the interferometer phase in the single wavelength heterodyne interferometer discussed above.

As with the heterodyne technique, the optical path difference can only be measured unambiguously over a range equal to the optical wavelength, unless the order number of phase can be determined. Fujima et al. were able to determine the order number by comparing the effective interferometer phase over a range of values of modulation difference frequency $\Delta\Omega$, using the method of excess fractions. Distances of 5 m and 100 m were measured in this way with a measurement resolution of 1 μm and 3 μm respectively.

1.2.4 Frequency Scanning Interferometry

Frequency Scanning Interferometry (FSI) length measurements are made by monitoring the change of phase of an interferometer as the laser frequency is scanned. This technique has been made significantly easier by the recent development of external cavity tunable diode lasers, which offer a wide tuning range, ultra narrow linewidth and a minimum output power of several milliwatts. More details of these lasers are given in chapter 2.

Interferometer length comparison

In most reported examples of FSI, the interferometer with the length being measured is compared with the length of a reference interferometer, by monitoring the phase change in each interferometer.

For a reference interferometer with an optical path difference $\mathcal{L}$ the phase of the detected reference[9] signal is given by

$$\Phi = \left(\frac{2\pi}{c}\right)\nu\mathcal{L}+\Phi_0 \tag{1.26}$$

[9]From this point on, the symbols Φ and $\mathcal{L}$ are used exclusively for the *reference interferometer*, because of its unique role in an FSI system.

Similarly for an unknown interferometer to be measured, with OPD $\mathcal{D}$, the phase is given by[10]

$$\Theta = \left(\frac{2\pi}{c}\right)\nu\mathcal{D} + \Theta_0 \tag{1.27}$$

Assuming that both interferometer OPDs are fixed throughout the scan, the ratio of the change in interferometer phase induced by tuning through a frequency interval $\Delta\nu$, is given by

$$q = \frac{\Delta\Phi}{\Delta\Theta} = \frac{\mathcal{L}}{\mathcal{D}} \tag{1.28}$$

The measurement of the unknown length, therefore depends on measuring the interferometer phase (change) ratio q.

The advantages of frequency scanning are :

- The measured lengths do not need to be known in advance
- The absolute order number of the interferometer is not needed, only *changes* in interferometer phase need to be measured.
- The dynamic range is very large and is limited, in principle, only by the coherence length of the light beam in the measured interferometer.

The dynamic range is limited in practice, to much less than the coherence length of the light from an external cavity laser diode[11], because the larger the optical path difference (OPD) to be measured, the greater the phase change $\Delta\Theta$ for a given change in laser frequency $\Delta\nu$, (as can be seen from equation 1.27). So, for a given rate of laser frequency scanning, a longer length interferometer requires faster phase measurements, to avoid measurement ambiguity[12]. Beyond a certain length, the phase measurement system is unable to keep track of the phase changes. This could be solved by reducing the scanning rate.

The disadvantage of this solution, is that the OPD of the interferometers drift during a scan and the longer the scan takes, the greater the drift is likely to be. A change or *drift* in the ratio of reference OPD to measured OPD, during the frequency scan, leads to an error in the interferometer length measurement which is much larger than the drift of interferometer length. This drift error is one of the main disadvantages of the simple FSI method.

Interferometer drift errors

If the optical path difference of the reference interferometer drifts by $\Delta\mathcal{L}$, whilst the frequency scans through the tuning interval $\Delta\nu$, the corresponding change in interferometer phase is

$$\Delta\Phi = \left(\frac{2\pi}{c}\right)(\mathcal{L}\Delta\nu + \nu\Delta\mathcal{L} + \Delta\nu\Delta\mathcal{L}) \tag{1.29}$$

The term $\left(\frac{2\pi}{c}\right)\mathcal{L}\Delta\nu$ represents the *intended* phase shift due to frequency scanning, with $\mathcal{L}$ given by the *scan average* reference interferometer OPD. The term $\left(\frac{2\pi}{c}\right)\nu\Delta\mathcal{L}$ represents the *unwanted* phase shift due to interferometer OPD drift, at the *scan average* laser frequency ν, such as would be generated in a displacement interferometry measurement.

[10] Similarly the symbol Θ is used exclusively for the phase of the interferometer being measured and $\mathcal{D}$ for the measured OPD.

[11] The coherence length of the beam from a narrow linewidth external cavity diode laser is typically much greater than 100 m.

[12] Faster changes in phase also lead to a decrease in interferometer signal visibility, as discussed in chapter 3.

If the tuning interval is large enough so that

$$\left|\frac{\Delta\nu}{\nu}\right| > \left|\frac{\Delta\mathcal{L}}{\mathcal{L}}\right| \tag{1.30}$$

then the terms in equation 1.29 are in descending order, so that

$$|\mathcal{L}\Delta\nu| > |\nu\Delta\mathcal{L}| > |\Delta\nu\Delta\mathcal{L}|$$

Likewise, if the OPD of the measured interferometer drifts by $\Delta\mathcal{D}$ during the same tuning interval, the corresponding change in interferometer phase is

$$\Delta\Theta = \left(\frac{2\pi}{c}\right)(\mathcal{D}\Delta\nu + \nu\Delta\mathcal{D} + \Delta\nu\Delta\mathcal{D}) \tag{1.31}$$

As above, there are terms for the *intended*, tuning phase shift and the *unwanted*, displacement phase shift, $\left(\frac{2\pi}{c}\right)\mathcal{D}\Delta\nu$ and $\left(\frac{2\pi}{c}\right)\nu\Delta\mathcal{D}$ respectively, where $\mathcal{D}$ is the *scan average* OPD of the measured interferometer.

If

$$\left|\frac{\Delta\nu}{\nu}\right| > \left|\frac{\Delta\mathcal{D}}{\mathcal{D}}\right| \tag{1.32}$$

it follows that the terms in equation 1.31 are in descending order, so that

$$|\mathcal{D}\Delta\nu| > |\nu\Delta\mathcal{D}| > |\Delta\nu\Delta\mathcal{D}|$$

For the purposes of explaining the error due to interferometer drift, the second order terms $\Delta\nu\Delta\mathcal{L}$ and $\Delta\nu\Delta\mathcal{D}$ can be neglected, if

$$\left|\frac{\Delta\nu}{\nu}\right| \ll 1 \tag{1.33}$$

which is true in most cases[13].

The measured phase ratio is therefore given by

$$\begin{aligned} q &= \frac{\Delta\Phi}{\Delta\Theta} \\ &= \frac{\left(\frac{2\pi}{c}\right)[\mathcal{L}\Delta\nu + \nu\Delta\mathcal{L}]}{\left(\frac{2\pi}{c}\right)[\mathcal{D}\Delta\nu + \nu\Delta\mathcal{D}]} \end{aligned} \tag{1.34a}$$

After cancelling the common $\left(\frac{2\pi}{c}\right)$ terms and dividing numerator and denominator by $\Delta\nu$ this becomes

$$\begin{aligned} q &= \frac{\mathcal{L} + \left(\frac{\nu}{\Delta\nu}\right)\Delta\mathcal{L}}{\mathcal{D} + \left(\frac{\nu}{\Delta\nu}\right)\Delta\mathcal{D}} \\ &= \frac{\mathcal{L}\left[1 + \left(\frac{\nu}{\Delta\nu}\right)\left(\frac{\Delta\mathcal{L}}{\mathcal{L}}\right)\right]}{\mathcal{D}\left[1 + \left(\frac{\nu}{\Delta\nu}\right)\left(\frac{\Delta\mathcal{D}}{\mathcal{D}}\right)\right]} \end{aligned} \tag{1.34b}$$

[13] If instead $\left|\frac{\Delta\nu}{\nu}\right|$ were to approach unity, the drift error would diminish (as shown below) and the presence or absence of the second order term would be irrelevant. The second order terms would only be significant if the corresponding conditions, given by equation 1.30 or equation 1.32, were not satisfied.

This can be simplified, using the approximation

$$\left(\frac{1+a}{1+b}\right) \approx 1 + a - b \text{ provided } a, b \ll 1$$

neglecting terms beyond first order, to give

$$q = \left(\frac{\mathcal{L}}{\mathcal{D}}\right)(1 + \Omega\varepsilon) \tag{1.34c}$$

where

$$\Omega = \frac{\nu}{\Delta\nu} \tag{1.35}$$

and

$$\varepsilon = \frac{\Delta\mathcal{L}}{\mathcal{L}} - \frac{\Delta\mathcal{D}}{\mathcal{D}} \tag{1.36}$$

Hence a relative interferometer drift ε leads to an error in the apparent length ratio which is magnified by the factor Ω. The size of this drift error term $\Omega\varepsilon$ is controlled by the growth rate of the accumulated tuning phase shift compared to the growth rate of the accumulated displacement phase shift. Therefore the drift error penalty which is incurred by tuning more slowly, ultimately sets the limit to the dynamic range of the length measurement technique.

The drift error is minimised by maximising the tuning speed, but this speed is limited by the phase measurement system and also by the signal to noise ratio from the interferometers which is controlled by the strength of the interferometer signal (given by γI_0 in equation 1.6). Different FSI schemes, use different methods to reduce the drift errors, where control of the environment is impractical. These control techniques involve using two lasers, as described in the following review. This review is followed by a discussion of the specific FSI technique used in this work.

A review of FSI measurements

Several groups have been using FSI to make interferometer comparison measurements in air, with different techniques for measuring the change in interferometer phase. The two interferometers were placed in the same ambient conditions, to minimise the drift errors due to air refractivity changes by ensuring that the air was common.

The system used by Stone et al. [Sto99] is shown in Fig. 1.8 with a heterodyne interferometry technique for interferometer phase measurement, similar to that described above in section 1.2.1, with a diode laser operating at 670 nm with an implied, (but never explicitly stated) tuning range of 12 nm, which corresponds to 8 THz.

The beat signals from both detectors and the drive signal for the acousto-optic modulator were electronically downshifted, (from 80 MHz to 2 MHz using double balanced mixers and a 78 MHz local oscillator), digitised and sent to fringe counters, which recorded the number of phase cycles traversed during the frequency scan, to the nearest integer.

Length measurements from 0.3 m up to 5 m with ten scans recorded in 15 s, (five up in frequency and five down in frequency, with an alternating tuning direction, to minise the effects of drift). The error on the average of forty pairs of measurements, (with one scan in each direction in each pair), was around 0.3 μm for a length of 5 m. Stone et al. observed that the errors were dominated by random effects, with the error decreasing by averaging n pairs of scans, like $n^{0.5}$, which implies an error on each pair of measurements of 1.9 μm in 5 m or 0.4 ppm.

The interferometer arms were partially shielded for some measurements to prevent air currents and the temperature variations along the 5 m measured interferometer were reduced to below 70 mK, but the reference and measured interferometers were immersed in the air of same laboratory. The dominant source of error within an *unshielded* interferometer was found to be drift errors caused by turbulence, with vibration of less importance.

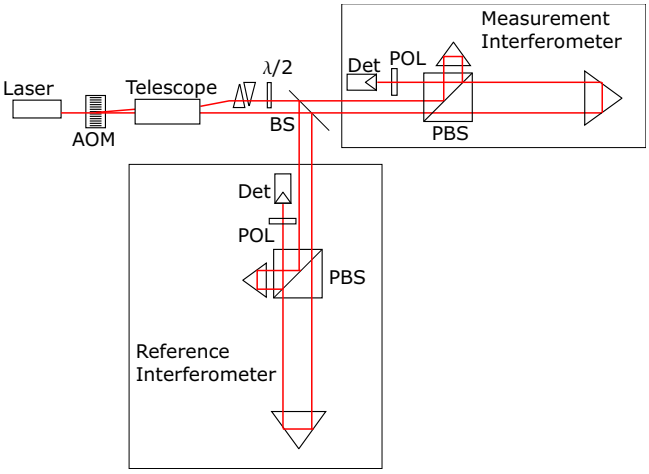

Figure 1.8: *The FSI interferometer comparison system used by Stone et al.*

In an earlier system built by Pfeifer and Thiel [Pfe93], the interferometer phase was measured using the quadrature technique discussed above and shown in Fig. 1.3. The laser diode tuned over 0.2 nm at 780 nm, ($\approx$ 100 GHz). Lengths up to 800 mm were measured with this system, with individual results at a given length lying in a range of $\approx \pm 2$ μm.

In a later version of the same system, the reference interferometer was replaced with one made from zerodur, (to reduce the thermal expansion) and a new laser diode was used which tuned over 10 nm at 1550 nm [Thi95], (a tuning range of 1.2 THz). An error of ± 40 μm was reported for measurements of 40 m, dominated by the combined effects of turbulence and mechanical vibrations.

An FSI system based on superheterodyne interferometry was used by Salewski et al [Sal96]. This system used three detectors, one to provide the reference beat signals, (as did the first detector in the superheterodyne system shown in Fig. 1.4), the other two for the reference interferometer and interferometer being measured.

The superheterodyne system reduces the errors due to drift by making the FSI phase measurements, not at the optical frequency, but instead at the beat frequency generated between the one laser frequency, fixed at ν_1 and the second laser, which is tuned from $\approx \nu_1$ to $\nu_1 + \Delta\nu$. With this technique the change of (beat) frequency is twice the scan average (beat) frequency, so the magnitude of $\Omega = \frac{\nu}{\Delta\nu}$ in this case is 0.5 and the drift error is *smaller* than the relative interferometer drift.

Two kinds of tunable laser were tested with this system, a Nd:YAG ring laser, which was temperature tuned, with a maximum uninterrupted tuning range of 19 GHz, (covered in 5 s) and a diode pumped micro-crystal Nd:YAG, which was tuned by up to 60 GHz. The measurement error for a 6 m length was found to decrease as the tuning range of the laser increased, falling below 20 μm for $\Delta\nu \approx 60$ GHz. The average of several measurements taken in quick succession was used to bring the precision below the target 10 μm.

The time taken to record multiple measurements was considered too long, so an alternative system was developed by Bechstein and Fuchs [Bec98], (half of Salewski et al.). A schematic of this later system is shown in Fig. 1.9. Isolators were used to protect the lasers from external reflections, which might otherwise disrupt the tuning continuity, (see chapter 2).

The beams from both lasers, (with mutually orthogonal polarisations), were sent through a beam-splitter and coupled into two polarisation maintaining fibres, one for each interferometer. Each interferometer was fitted with specialised front end optics, based on a Kösters

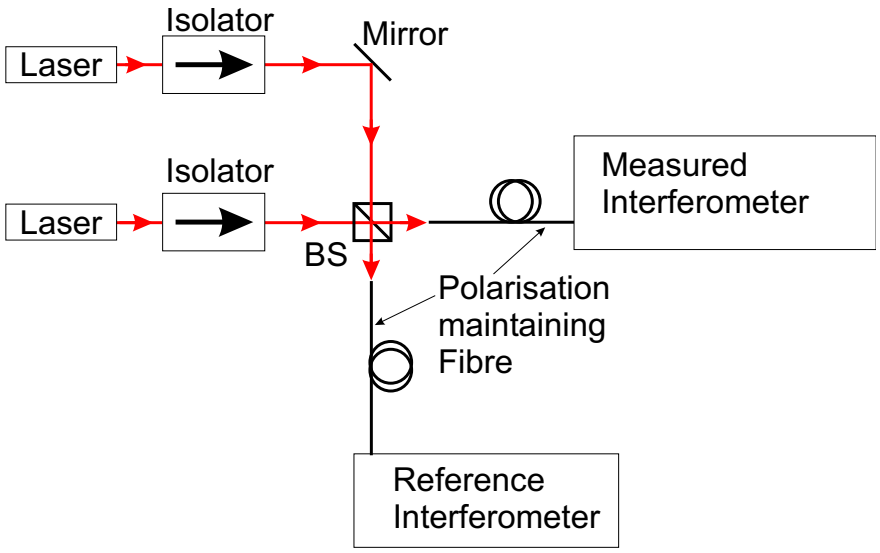

Figure 1.9: *Fibre-coupled two laser FSI system after Bechstein and Fuchs. The output beams of the isolators had mutually orthogonal polarisations.*

prism[14], to generate four phase quadrature signals, independently for each polarisation (and thereby for each laser). These quadrature signals were used to measure the interferometer phase for each laser, independently and simultaneously during laser tuning.

The lasers were tuned in opposite directions, one by 20 GHz and the other by 40 GHz with 20 scans recorded per second, to reduce the effects of interferometer drift.

Distances between 2 m and 6 m were measured 100 times in 5 s and the average of 100 length measurements compared with the interferometer length according to a commercial displacement measuring interferometer. The residual differences between the 100 measurement average and the calibrated interferometer ranged over ± 10 μm.

FSI without a reference interferometer

Under controlled vacuum conditions, Barwood et al. used a form of FSI to measure the length of a 1 m etalon to less than 1 ppb [Bar98]. The length of the etalon was stabilised by being locked to a fringe of a HeNe laser which was in turn locked to an iodine stabilised 633 nm reference laser. The stabilisation and the use of a vacuum eliminated the problems of vibration and drift.

Rather than using a reference interferometer, the optical frequency measurement was based on measuring the beat frequencies between a laser locked to one of the two Rb D lines at 780 nm and 795 nm and a laser which was scanned in frequency and locked to etalon peaks at the beginning and end of a scan[15]. The etalon measurement was made in two stages :

1. A short scan of 19 GHz, in the vicinity of 780 nm, to estimate the etalon length.

2. A single beat frequency measurement in the vicinity of 795 nm.

The beat frequency between the Rb locked laser at 780 nm and the etalon locked laser, was measured before and after, decoupling from the etalon and scanning the laser through

[14]The Kösters prism is described in [Coo71].
[15]The etalon peaks were the only features in the etalon response suitable for locking a laser.

approximately 19 GHz. This scan was chosen to cover 129 free spectral ranges, (2π phase cycles) of the etalon. This gave an initial estimate for the etalon length which was used to make an extrapolation to the location of an etalon peak in the vicinity of the second Rb line at 795 nm.

Both lasers were decoupled from the respective locking instruments, tuned to 795 nm and locked, one to the local Rb line, the other to an etalon peak. The beat frequency between these lasers allowed the final etalon peak to be located in absolute frequency. After checking to ensure that the variation with wavelength, in etalon mirror phase shift, was negligible, the absolute etalon order numbers for the peaks measured close to 780 nm and 795 nm was determined, giving final optical length measurements at each wavelength which differ by 4 parts in 10^{10}.

1.2.5 The FSI technique developed for ATLAS

The FSI technique developed for ATLAS was initially considered by D. F. Howell and R. B. Nickerson. The first experimental investigations were carried out by Fox-Murphy and continued by Grewal. These earlier developements are discussed first, followed by a description of the refinements which are presented in greater detail in the remaining chapters of this work.

The initial investigations by Fox-Murphy et al. [Fox96b], demonstrated that the design of interferometer for use inside ATLAS, (discussed below in section 1.4), was suitable for making remote interferometric measurements, with a return signal of order 10 pW. The investigation was limited by the instability of the tunable laser, which exhibited uncontrolled mode hopping [Fox96a].

Better quality tunable lasers, suitable for FSI, operate in two tuning regimes; fine and coarse tuning. In fine tuning the laser frequency is scanned in a phase continuous manner over ranges of order 10 GHz to 100 GHz, depending on the laser. Wider tuning ranges beyond 10 THz can be accessed using coarse tuning which is faster, but lacks the smooth, even progression of fine-tuning. Unambiguous interferometer phase measurements, necessary for the FSI interferometer comparison, can only be made during fine tuning. The original proposal for the ATLAS FSI system by Fox-Murphy et al. describes using two tuning regimes; fine tuning and coarse tuning, with fine tuning *subscans* separated by intervals of coarse tuning [Fox96a], to effectively extend the fine tuning range for an FSI scan.

In following work [Gre99], Grewal demonstrated that :

- With a more stable laser, single subscans could be recorded continuously over the entire fine tuning range of the laser.

- With the low return signal from the interferometer and the limitations of the data acquisition system, the time taken to record a single subscan was of order 100 s.

- The relative interferometer drift errors on this timescale would need to be controlled before subscans could be linked.

Given the time taken for each measurement, it is required that the FSI technique developed for ATLAS be capable of making measurements with sufficient precision every scan, rather than relying on averaging over multiple measurements.

In the work presented in this thesis, a two-laser technique to reduce the drift errors in a single subscan, (intra-subscan drift) is demonstrated, in the results presented in chapter 4.

Linking of subscans is then demonstrated using a further, two-laser correction for inter-subscan drift. The results of measurements made with linked subscans are presented in chapter 5.

The implementation of the two techniques is outlined here and described in more detail in chapter 3.

Dual-laser Intra-subscan drift correction

The dual-laser drift correction involves fine tuning two lasers in opposite directions as in the technique demonstrated by Bechstein and Fuchs (discussed above). In that technique, both lasers generated interferometer signals simultaneously, using polarisation to distinguish between the two lasers. The technique developed in this work, instead relies on time division multiplexing between the two lasers, avoiding the extra expense and difficultly of providing polarisation maintaining fibre for 800 remote measurements in a high radiation environment.

The interferometer signals are alternately derived from each laser, using a pair of synchronised chopper wheels to block the beam from the other laser. Each laser illuminated the interferometers for the minimum time needed to ensure a single, clean phase measurement in the reference interferometer, as discussed in chapter 2. With this technique the interferometer drift is the same in the data from either laser.

The principle behind the intra-subscan drift correction can be explained by duplicating equation 1.34c from above, for the two different lasers, referred to as laser 1 and laser 2. The individual phase ratio measurements based on the signals from a single subscan, for each laser are :

$$q_1 = \left(\frac{\mathcal{L}}{\mathcal{D}}\right)[1+\varepsilon_1\Omega_1] \tag{1.37a}$$

$$q_2 = \left(\frac{\mathcal{L}}{\mathcal{D}}\right)[1+\varepsilon_2\Omega_2] \tag{1.37b}$$

The symbol ρ will be used to represent the ratio between the drift error terms in the laser 1 and laser 2 measurement. Hence,

$$\rho = \frac{\varepsilon_2\Omega_2}{\varepsilon_1\Omega_1} \tag{1.38}$$

and equation 1.37b can be re-written as

$$q_2 = \left(\frac{\mathcal{L}}{\mathcal{D}}\right)[1+\rho\varepsilon_1\Omega_1] \tag{1.39}$$

The phase ratios measured using each laser may therefore be combined using

$$q_0 = \frac{q_2-\rho q_1}{1-\rho} \tag{1.40}$$

Hence, with the correct choice of ρ,

$$q_0 = \frac{\mathcal{L}}{\mathcal{D}}$$

If the value of the relative interferometer drift is different for each laser, there are three independent unknown quantities, q_0, ε_1 and ε_2, with only two measurements q_2 and q_1. It

is therefore essential to conduct the measurement to minimise the difference between ε_1 and ε_2 so that they can be treated as the same unknown value ε to a good approximation. In this approximation, the error contribution ratio ρ simplifies to become

$$\rho = \frac{\Omega_2}{\Omega_1} \tag{1.41}$$

which can be determined by measurement of the lasers, independently of the relative drift of unknown interferometer, ε, which is not explicitly evaluated in this measurement. The decoupling of ρ from the unknown interferometer greatly simplifies the drift correction for simultaneous measurements of multiple unknown interferometers.

When determining ρ, the measurement of ν_1 and ν_2 can be made with relatively low accuracy, using for example a wavemeter, whilst the corresponding measurements of $\Delta\nu_1$ and $\Delta\nu_2$, can be made independently using the reference interferometer, even if the length calibrations of the wavemeter and reference interferometer length differ by a scale factor, since scaling errors cancel out as common in the determination of ρ.

The inter-subscan drift correction requires more detailed explanation. This is given in chapter 3.

Linking subscans

The purpose of linking is the connection of interferometer phase information from one subscan to another. The connection of the phase relies on a reasonably accurate extrapolation from a single point in the first subscan to a single point in the target subscan. These single points are referred to below as *anchor points* and the interval between them is known as the *bridge*.

The reference interferometer phase is linked first. An extrapolation of reference phase is made using an independent measure of the laser frequency interval between anchor points. In the measurements by Barwood et al. [Bar98] discussed above, Rb lines were used to measure the frequency interval. In the work described here, the peaks of an etalon were used to measure the interval. The extrapolation in both cases, was corrected using local phase information, known beforehand only to modulo 2π. This correction is only possible to make accurately if the interval between anchor points was kept small enough to allow an extrapolation to within $\pm\pi$ of the correct phase. If this is true, the extrapolation determines the order number difference between the anchor points and the local correction determines the fractional part of the interval. After the correction therefore, the reference interferometer phase is linked from one subscan anchor point to the other. This linking correction is illustrated in Fig. 1.10.

The linking of the GLI[16] phase is similar, with an extrapolation of the unknown interferometer phase based on the change in reference phase across the bridge. The linking correction allows the measurement of the interferometer phase ratio across frequency intervals extended by coarse tuning. If further accuracy is required, the first linked measurement can form the basis for extrapolations to another subscan, over a larger frequency interval and this iteration may continue as required within the limits of the individual system. The dominant errors in the linking process are discussed in detail in chapter 6.

[16]The measured interferometers within ATLAS are referred to as grid line interferometers or GLIs.

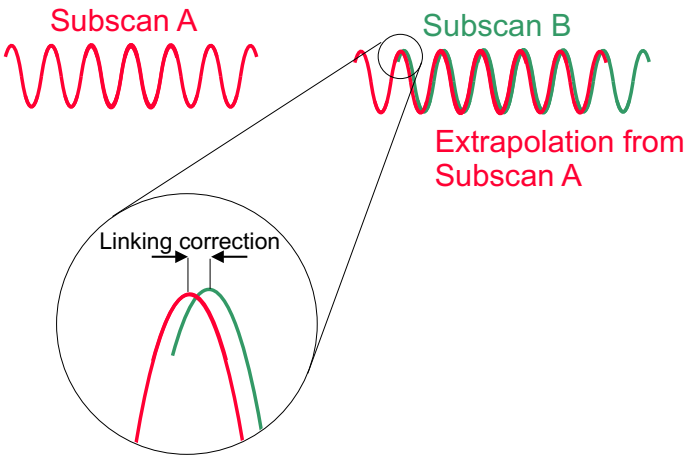

Figure 1.10: *An illustration of the linking correction.*

1.3 Alignment of Central Tracking detectors

Attention is focussed in this section on the alignment of the *central* tracker, because the dual challenges for any supplementary alignment system are the lack of space and the possibility of high levels of radiation. This rules out some of the solutions which are often employed in alignment of muon tracking systems on the outside of a particle detector, such as the RASNIK system employed in the ATLAS muon spectrometer [ATL97b].

The central tracking elements of a detector record the trajectories of high energy charged particles passing through them. The presence of a charged particle is detected by the ionisation generated within the detecting medium. Localised ionisation signals within a tracking detector are referred to as *hits*. Hits in different elements of the tracking detector are associated with the trajectories of individual particles in the process of track reconstruction. The determination of the positions of the tracking elements within a particle physics detector is referred to as alignment. Alignment is essential for correct track reconstruction.

The first step of the alignment process is the design of the mechanical support structure, which must meet two mutually contradicting requirements :

Minimum mass There must be minimum material with the tracking volume to reduce the interactions with high energy particles. Unwanted interactions deflect the trajectories of primary particles (ie those generated by the physics of interest), degrading trajectory measurements and generate showers of secondary particles, which lead to spurious hits, masking the signals of interest.

Mechanical stability On the other hand, the ideal detector would be held on an infinitely rigid support, so that the relative positions of all detector elements could be maintained throughout the lifetime of the detector. If this could be guaranteed, then track fitting could be used to provide an increasingly precise reconstruction of the detector alignment, with more reconstructed events allowing statistical errors to be steadily reduced.

An engineering compromise is reached by using relatively stiff, low mass materials, such as carbon fibre in the case of ATLAS.

Once the detector has been designed the remaining stages of alignment are :

- Initial positioning during sub-detector construction
- Position survey of the completed sub-detector
- In-situ monitoring
- Track fitting based position reconstruction

1.3.1 Initial positioning and survey

The detector element positioning is initially determined by the design of the detector and its implementation during construction. The relative positioning precision during construction is at best on the order of millimetres and therefore an initial survey is required to determine the detector element positions. In the case of the DELPHI experiment at LEP, the elements of the microvertex tracking detector were measured to an accuracy of 25 μm after a mechanical survey [Cha96].

The ATLAS semiconductor tracker (SCT) will be surveyed after construction using an x-ray tomograph [ATL97a]. The tomograph produces a collimated beam of x-rays which mimics a straight track, by generating hits along the x-ray beam. The correlation of these hits will be used to deduce the relative alignment of the assembled structure. In the SCT an accuracy of 7 μm in the azimuthal (Rϕ) co-ordinate, is the design specification. Similar alignment surveys have been performed on previous experiments using ultra-violet laser beams instead of x-rays [Kle98].

1.3.2 Track based alignment and in-situ monitoring

Once the initial survey has determined the baseline positions of the detector elements, track based alignment is used to sharpen the precision. The statistical techniques deployed for track based alignment rely on large samples of tracking data and mutually consistent solutions. This strategy is only successful if the detector does not change alignment during the accumulation of the tracking data.

A number of in-situ monitoring schemes have been developed to follow detection motion during the accumulation of tracking data, so that it can be accounted for in the tracking fitting. These schemes include :

- Capacitive sensors
- Laser spot monitoring using the tracking detector elements
- Laser beam monitoring using transparent silicon detectors
- The geodetic alignment grid proposed for the ATLAS SCT

Capacitive sensors

A capacitive displacement measurement systems were developed for use in the microvertex detector of the DELPHI experiment at LEP and the vertex detector of the Mark II detector at SLC [Bre89], based on commercially available sensors. The sensor design is shown in Fig. 1.11, after Breakstone et al.

The displacement between the sensor and a grounded target is determined by measuring the reactance of the capacitance between the central electrode and the conducting surface of the target. The central electrode is connected to an AC source with a controlled frequency,

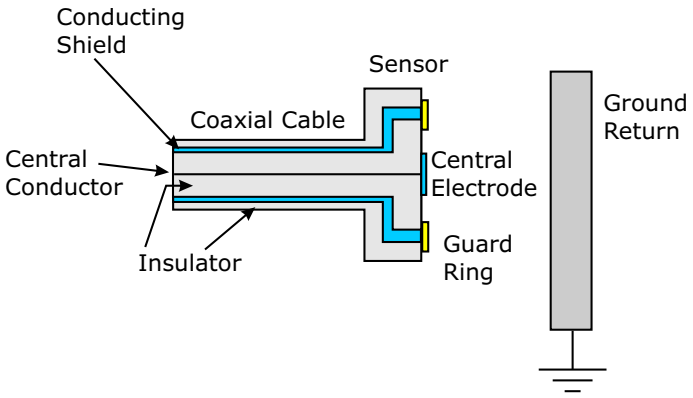

Figure 1.11: *Capacitive displacement sensor, after Breakstone et al.*

(close to 15 kHz). The capacitance of the cable, (between the central electrode and the shield) is removed from the measurement by connecting the shield to the same side of the AC source. The voltage drop across the sensor to ground capacitance is amplified with a low capacitance amplifier, rectified and readout as a voltage proportional to distance, for distances up to $\sim$ 1 mm, with a sensitivity of order 3.5 mV.μm^{-1} [Dij90, Bre89]. A guard ring connected to the shield, *reduces* the edge effects for the sensor electrode.

A capacitive displacement measurement (CDM) system deployed on the vertex detector of the Mark II detector of the SLC [Bre91] was able to monitor changes in the detector position with a short term precision of 0.5 μm. Diurnal variations of order 20 μm were observed. On the longer term drifts of the same order were detected. Other sensors were set with only a partial overlap between grounded target and sensor, so that lateral displacements could be measured. In this mode the sensitivity was reduced, with the voltage change for a 1 μm change in separation equivalent to an overlap change due a 20 μm lateral displacement.

In DELPHI, the CDM system was found to cause noise problems in some locations and some sensors needed to be switched off, while others were away from the expected positions by up to 2 cm, which is too large for the sensor to work [Cac92]. The remaining sensors were able to measure changes in the microvertex detector of up to 15 μm radially and 50 μm azimuthally (in $R\phi$).

Projected Laser spot monitoring

In the ALEPH experiment, the silicon tracking Vertex Detector was monitored by projecting laser spots, (using optical delivery fibres), onto the outer faces of the detector silicon. The laser was fired in a 6 W, 50 ns pulse, once per minute and recorded as if it were a physics event. The reconstructed spot centroid was compared with an expected position, with changes in the difference used to follow changes in the detector alignment [Sgu99].

The alignment results from the ALEPH system highlighted a change in detector shape which was later found to be correlated with humidity [Foc97]. Once the humidity had been controlled, short and medium term bowing due to differential thermal expansion was observed, with deviations ranging from 5 μm to 12 μm over periods of several hours. A longer term motion was also detected using this alignment system and confirmed using tracking data. The position changes, up to 20 μm were believed to be due to changes in the support structure, although there were other potential contributions, including, changes in delivery fibre alignment [Sgu99].

Laser beam monitoring

A Gaussian beam from a fibre-coupled laser diode, is used to provide a reference line, along which several transparent sensors are placed. Transverse motion of the structure relative to the reference beam, down to of order 1 μm can be measured using correlation in the reconstructed spot positions at each sensor.

Transparent amorphous silicon strip detectors for laser beam monitoring were developed by the Max-Planck-Institute for Physics (in Munich), originally for alignment of the ATLAS muon spectrometer [Blu96, Kro97].

A sensor, (shown in Fig. 1.12) is read out as a set of double sided silicon strip photodiodes. The ITO[17] readout strips on one side are orthogonal to those on the other. The laser spot centroid is determined in the two transverse directions, using a single sensor, by fitting the expected beam profile to the strip photocurrent signals. Two different versions of the sensor were developed, optimised for transmission at 690 nm and 790 nm, which are the operating wavelengths of commercial AlGaAs laser diodes.

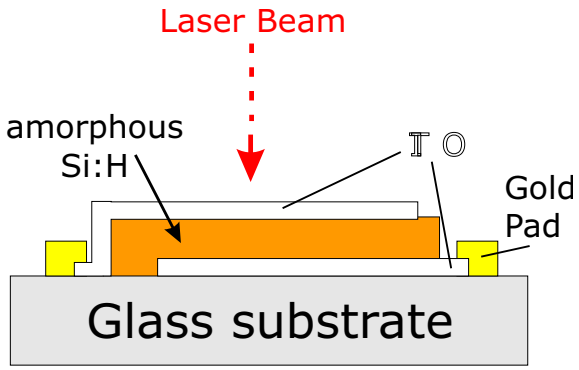

Figure 1.12: *Cross section of the amorphous silicon strip sensor after Kroha.*

The length range of the system is fundamentally limited by beam divergence, due to diffraction, given a particular sensor size. In the optimum condition, the beam behaves like a perfect TEM_{00} Gaussian mode[18] and is set with the waist (focus) halfway along the chain of sensors. If the sensors span a distance D, then a beam with a waist radius w_0, at $z = 0$ will have a radius at $\pm\frac{D}{2}$ given by

$$w\left(\frac{D}{2}\right) = w_0\sqrt{1+\left(\frac{D\lambda_n}{2\pi w_0^2}\right)^2} \tag{1.42}$$

where λ_n is the wavelength in the ambient gas along the beam. The effects of the sensors on the beam direction, scattering and diffraction need to be accounted to realise the best performance from the system.

An important drawback with this type of sensor is the Staebler-Wronski effect which leads to a decrease in detector photoconductivity and thereby in detector signal after exposure to the laser beam [Sta77].

The recently installed alignment system of the ZEUS microvertex detector [Mat01] uses transparent silicon detectors mounted along six separate, axial lines of sight, spaced at 60° intervals around the outer circumference. The operational lifetime of this system is expected to be limited to a few weeks of integrated exposure to the laser, which should be enough to last for the projected five year lifetime of the ZEUS experiment.

In the planned alignment system for the CMS experiment, a set of interlinked beam lines will connect the central tracker to the muon system, using transparent silicon detectors on each beam [Arc01].

[17]Indium tin oxide is an electrode material, widely used in optical devices because it is transparent in the visible and near infra-red.

[18]In practice, laser beams coupled from fibres best approximates the Gaussian TEM_{00} mode, if the beam is allowed to diverge straight from the bare fibre. Any additional coupling optics, to produce a collimated beam, introduces aberrations, making the beam divergence and spot size greater than would be expected from a Gaussian TEM_{00} mode, further restricting the operational length range for sensors of a given size.

Geodetic grid proposed for the ATLAS SCT

The ATLAS semiconductor tracker (SCT) will be monitored in-situ using geodetic grids, built up of one dimensional straight line length measurements.

There will be three independent geodetic grids, one for each of the three sections of the SCT[19] and the shape of the support structure of each section will be deduced from the grid line length measurements. Once the shape has been reconstructed, the positions of the individual detector elements will be guided by the initial x-ray survey and mechanical models of the support structure. The geodetic grids will be measured during the x-ray survey, to provide a comprehensive baseline measurement of the detector alignment.

1.4 ATLAS

1.4.1 Detector overview

The ATLAS detector, shown in Fig. 1.13 is designed to record the energy and momentum of the particles produced by proton-proton collisions at the LHC [ATL94]. It will be constructed in a huge underground cavern. The completed detector will be around 25 m tall and just over 40 m long.

Proton bunches will enter the detector from each direction along the evacuated beam-pipe which lies on the cylindrical axis of symmetry of the detector. The bunches will pass through each other at close to the speed of light, generating ten to twenty collisions per bunch crossing. The central region of the detector, closest to the collisions, is used for measuring the momentum of charged particles. The momentum measurement is made by recording the tracks of charged particles as they bend in an applied magnetic field. This tracking region, known as the Inner Detector, is discussed in more detail below.

The next layers in the detector, moving out from the Inner Detector, are calorimetry which is designed to bring particles to rest and measure the deposited energy. The calorimetry consists of an inner electromagnetic calorimeter designed to stop electrons and photons[20] and an outer hadron calorimeter for pions and protons, which require denser media to bring them to rest.

The outermost layers of the detector form the muon spectrometer. The muon spectrometer is used to make an accurate measurement of muon momentum, by bending the muon track in a large volume toroidal magnetic field. The superconducting coils of the toroidal magnet are shown in grey around the outside of ATLAS, taking up most of the detector volume.

1.4.2 Inner detector SCT

The following discussion covers the SCT sub-system of the Inner Detector, since this is where FSI will be used for alignment in ATLAS. The detailed roles and functions of the other sub-systems within the detector are not discussed here, but are discussed in the relevant technical design reports [ATL97a].

The Inner Detector design, shown in Fig. 1.14, is around 7 m long and just over 2 m in diameter. The following discussion is concentrated on the sub-element within the Inner Detector, known as the Semiconductor Tracker or SCT, shown in purple. The Inner Detector is discussed in more detail in [Gad01].

[19] See section 1.4, below, for a description of the SCT.

[20] High energy photons are stopped by production of electron and positron pairs [Kle98].

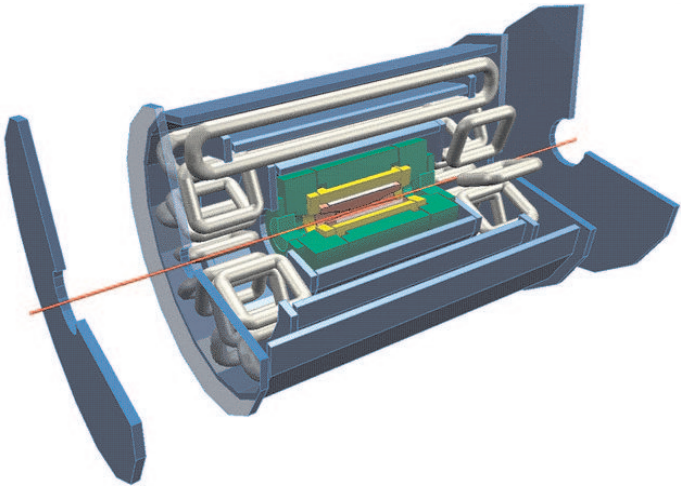

Figure 1.13: *The ATLAS detector will be around 24 m tall and over 40 m long. The colours represent: BLUE Muon Spectrometer, GREEN and YELLOW Calorimetry, RED Tracking Inner Detector, shown in more detail in Fig. 1.14. Note the beampipe running along the axis of cylindrical symmetry.*

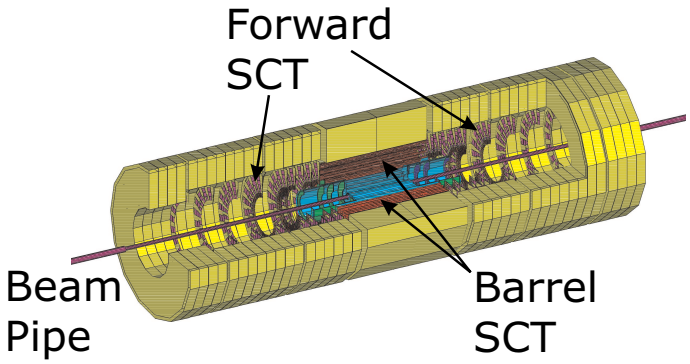

Figure 1.14: *The ATLAS Inner Detector, showing the Semiconductor Tracker (SCT). The SCT will be made from silicon detectors on a carbon fibre support structure.*

The SCT is made of back-to-back silicon strip detector modules tiled on support structures. There are four layers in the central *barrel section* each layer supported on a carbon fibre cylinder. At each end of the barrel, there is one of the *forward sections* supported on carbon fibre discs. The discs have a large central hole, to allow the innermost layers of the Inner Detector to be taken in and out without disturbing the SCT.

A solenoid magnet will be used to apply an axial magnetic field of around 2 T, which will bend the tracks of charges particles travelling out from the collision transversely to the detector axis. The curved trajectories of the charged particles passing through the SCT will be reconstructed by looking for correlated hits in different layers. It has been estimated that the measurement precision of track reconstruction would be degraded by 20% if there were a misalignment of the detector positions of 10 μm [Fox96b, ATL97a]. Further details on the SCT can be found in [Tur01].

An FSI alignment system has been devised to follow changes in the three dimensional shape of the SCT at the 10 μm level. The two forward sections and the barrel section will each contain an independent geodetic grid, made from a set of *grid line interferometers*

(GLIs). The shape of each grid will be reconstructed from the measured length of the GLIs.

The grid shape will be measured during the x-ray survey, to provide an initial connection between the detector module positions and the grid shape. Later changes in the grid shape will be used to estimate changes in the module positions.

An FSI technique, demonstrated in this work, (as described above in section 1.2.4), will be used for the measurements of the GLI lengths. Each GLI must be measured to an accuracy of around 1 μm so that the grid shape can be reconstructed in three dimensions to around 10 μm.

The SCT presents a challenging environment in which to make accurate interferometric length measurements. The main challenges are :

1. Regular proton collisions will produce a very high radiation environment within the Inner Detector. All items in the SCT must therefore be radiation hard.

2. There is very little space within the SCT volume, between detector modules, support structures and service fibres, cables and pipes, so the interferometer components must be small.

3. All items within the SCT must be low mass, to minimise the radiation length of the detector (amount of material encountered by particles).

4. The interferometers must be measured remotely, because of the high radiation levels within the ATLAS detector cavern.

5. The components on the SCT must continue to function over a 10 year period without the need for maintainence or repair.

The interferometry system designed to meet the above requirements is discussed in the final section of this chapter.

1.5 The ATLAS FSI system

The essential elements of the ATLAS FSI system are shown in Fig. 1.15. The output beams from the frequency scanning lasers will be fed along a common path to a beam-splitter. A small fraction of the power will be sent towards the reference interferometer system and the main beam will be coupled into a single-mode delivery fibre.

The fibres between the laser and the grid line interferometers and the fibres from GLIs back to the detectors *must* all be single mode, so there are only two unique optical paths from lasers, to the detectors, controlled by the two arms of the GLI[21].

The reference interferometer system will be housed in a sealed vessel at low pressure to remove the effects of gas refractivity. The different elements within the reference interferometer system will be kept at a stable temperature and will be constructed from low expansion materials. The crucial main reference interferometer against which all GLIs will be compared will be made from a low thermal expansion material, such as Zerodur.

The power from the main delivery fibre will be split in a splitter tree, to feed the $\sim$ 800 GLIs on the SCT, with a single-mode delivery fibre coupling into each interferometer.

[21]Strictly speaking there are two modes in a so-called single mode fibre, one for each polarisation of light, relative to a set of fibre axes, defined by the asymmetry of the fibre [Kam81]. Care will be needed in the detailed design and testing of the final system to ensure that polarisation dependences of the fibres do not influence the length measurement.

The interference fringe pattern of each GLI will be sampled by the input face of a single-mode return fibre, which will carry the sampled interferometer signal to a photodetector.

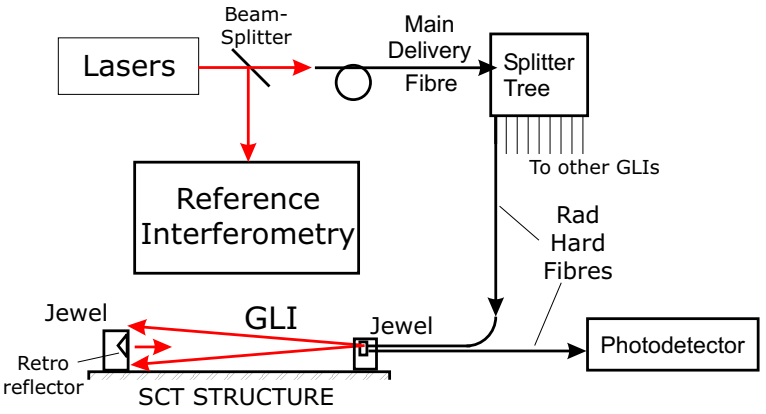

Figure 1.15: *The key elements of the proposed ATLAS FSI system.*

The photodetectors and splitter tree will be located in an equipment cavern far from the radiation environment of the detector cavern. Radiation hard fibre will be used from the splitter tree to the GLI and detector, since this route will go through the detector cavern.

The grid line interferometers, lasers and photodetectors are now discussed in more detail.

1.5.1 Grid Line Interferometer

The interferometer which has been designed for making length measurements in the SCT grid is shown in more detail in Fig. 1.16. It is a fibre-coupled common path interferometer made with radiation hard fibres, designed to satisfy the SCT conditions listed above.

The ends of the two fibres are joined together with a small beam-splitter to form a *quill*. The quill is mounted onto the SCT structure using a stable component called a *jewel*. The short arm of the interferometer is the optical path from delivery fibre to return fibre via a reflection from the front surface of the quill beam-splitter.

To form the longer arm of the interferometer, the quill is pointed at a retroreflector mounted on another jewel[22]. The retroreflector will be an external reflector made by punching an indent into metal. The longer interferometer arm is therefore the optical path via the retroreflector.

The optical path difference between the two interferometer arms will be compared with the reference OPD using FSI. The measured GLI OPD will be converted into a length measurement for the grid line using temperature and pressure measurements of the gas within the SCT to predict the refractivity.

The differences between the line of the OPD and the notional line of the grid, represent offsets which will remain essentially fixed on the micron scale.

The power in the main delivery fibre (or fibres) will be on the order of 500 mW. This will be split roughly 800 fold to feed each GLI. The beam which emerges from the delivery fibre expands due to diffraction, from a spot around 6 μm in diameter at the fibre end. The combined effect of beam expansion and small sampling area of the return fibre input face leads a very low coupling coefficient of order 10^{-8} or less (-80 dB) from the delivery fibre

[22]Dependending on the location within the grid, different jewels hold different numbers of quills and retroreflectors.

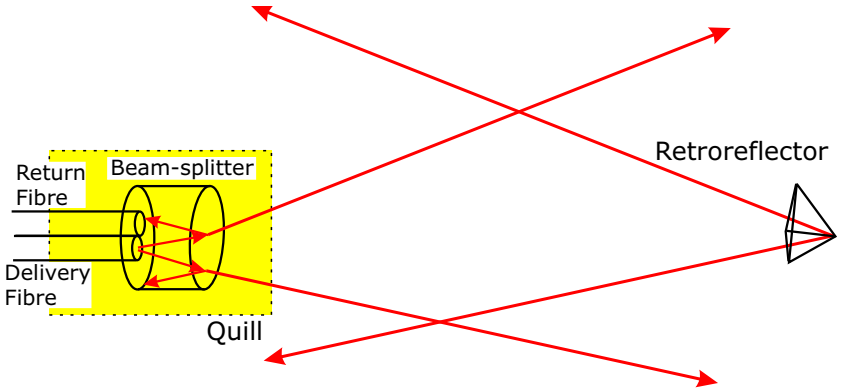

Figure 1.16: *The design of a grid line interferometer to be installed in the ATLAS SCT. N.B. The sizes of the quill and retroreflector shown here are both exaggerated.*

to the return fibre via the retroreflector. The coupling coefficent of the shorter arm will be selected to give a mean return signal on the order of 1 pW.

Tuning the GLI design

The GLI design is tuned by varying the design of the quill beam-splitter, which will be a thin piece of glass, (on the order of 1 mm thick), with cylindrical symmetry broken only by tilting the front surface through a small angle (less than 5°).

The other parameter which could have been used to tune the quill design is the separation of the end faces of the delivery and return fibres. This will be kept as constant as possible in the design of the ATLAS quills to simplify production.

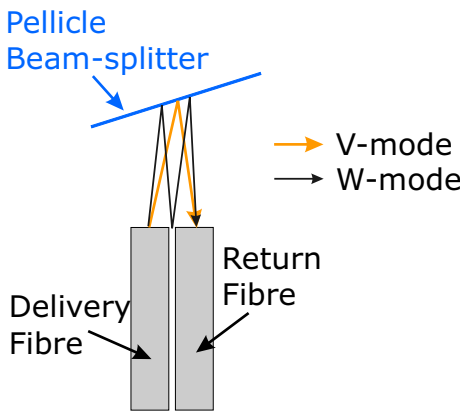

Figure 1.17: *The V and W reflection coupling modes from the beam-splitter of a GLI.*

The internal reflection of the quill couples light from delivery fibre to return fibre via the intended V mode, (named after the shape) and via the many other possible modes, via the side walls or the back surface between the fibres or some combination. The simplest unwanted alternative route is known as the W mode, (also named after the shape). The V and W modes are shown in Fig. 1.17.

The tilt angle and beam-splitter thickness are chosen to minimise the W mode coupling whilst simultaneously maintaining the V mode coupling well above the coupling coefficient from delivery to return fibre via the retroreflector, (referred to below as the R mode).

The signal to noise ratio of a photon counting limited GLI detector signal, due to the intended interference between V and R modes, can be maximised by tuning the coupling coefficient of the V mode. This is illustrated here, using the example of a photon counting detector. The same result should arise in an equivalently shot noise limited detector with a photocurrent signal.

For a mean power P_{DET} arriving at the detector, with quantum efficiency, η, integrating

(counting photons) for time τ, the corresponding photon count is given by

$$Q = \frac{\tau\eta}{h\nu} P_{\mathrm{DET}} \tag{1.43}$$

where ν is the average photon frequency, which is assumed to remain approximately constant for the time interval τ, (even in a frequency scanning interferometry system.)

The GLI signal takes the form of equation 1.6, which can be re-written in power terms as

$$P_{\mathrm{DET}} = P_0 \left[1 + \gamma \cos\left(\Theta\right)\right] \tag{1.44}$$

The mean detected power level is related to the power emerging into the GLI from the delivery fibre, P_{IN}, by

$$P_0 = C_{\mathrm{DET}} P_{\mathrm{IN}} \left(C_{\mathrm{R}} + C_{\mathrm{V}}\right) \tag{1.45}$$

where C_{DET} is the coupling coefficient from return fibre to the detector, C_{R} and C_{V} are the delivery fibre to return fibre (power) coupling coefficients of each GLI reflection mode.

The observed interferometer visibility γ is controlled by the fibre coupling coefficients and the change of GLI phase[23] during the integration time, $\Delta\Theta_\tau$, according to

$$\gamma \;=\; \mathrm{sinc}\left(\Delta\Theta_\tau\right) \left(\frac{\sqrt{2C_{\mathrm{R}}C_{\mathrm{V}}}}{C_{\mathrm{R}} + C_{\mathrm{V}}}\right) \tag{1.46}$$

The AC part of the signal due to the VR mode interference, is given by γP_0. The corresponding RMS (signal) photon count is given by

$$Q_{\mathrm{S}} \;=\; \frac{\eta\tau}{h\nu} \left(\frac{\gamma}{\sqrt{2}}\right) P_0 \tag{1.47}$$

where the factor of $2^{-0.5}$ is the RMS of a sinusoid compared to the amplitude, which represents the average for an ensemble of GLI signal measurements over all possible values of GLI phase $-\pi \leq \Theta < \pi$.

The RMS fluctuation in the photon count (governed by Poisson statistics, [Lou95]) is given by

$$Q_{\mathrm{N}} \;=\; \sqrt{\left(\frac{\eta\tau}{h\nu}\right) P_0} \tag{1.48}$$

The calculation of GLI signal to noise ratio is easier to follow if it is initially squared, hence

$$\begin{aligned} \mathrm{SNR}^2 \;&=\; \left(\frac{Q_{\mathrm{S}}}{Q_{\mathrm{N}}}\right)^2 \\ &=\; \left(\frac{\eta\tau}{h\nu}\right) P_0 \left(\frac{\gamma^2}{2}\right) \end{aligned} \tag{1.49}$$

substituting from equation 1.45 gives

$$\mathrm{SNR}^2 \;=\; \left(\frac{\eta\tau}{h\nu}\right) \left(\frac{\gamma^2}{2}\right) C_{\mathrm{DET}} P_{\mathrm{IN}} \left(C_{\mathrm{R}} + C_{\mathrm{V}}\right) \tag{1.50}$$

[23] A derivation for the sinc function dependence of visibility on the change of interferometer phase during signal integration is given in chapter 3, using the example of the reference interferometer.

and with a further substitution from equation 1.46 this becomes

$$\mathrm{SNR}^2 = P_{\mathrm{IN}} \left(\frac{\eta\tau}{h\nu}\right) \mathrm{sinc}^2\left(\Delta\Theta_\tau\right) C_{\mathrm{DET}} \left(\frac{2C_{\mathrm{R}}C_{\mathrm{V}}}{C_{\mathrm{R}}+C_{\mathrm{V}}}\right) \tag{1.51}$$

If the V-mode coupling coefficient is tuned so that

$$C_{\mathrm{V}} = \Gamma C_{\mathrm{R}} \tag{1.52}$$

then the SNR is given by

$$\mathrm{SNR} = \mathrm{sinc}\left(\Delta\Theta_\tau\right) \sqrt{2\left(\frac{\eta\tau}{h\nu}\right) C_{\mathrm{DET}} P_{\mathrm{IN}} \left(\frac{\Gamma}{1+\Gamma}\right) C_{\mathrm{R}}} \tag{1.53}$$

Hence the SNR increases with increasing Γ until $\Gamma \sim 10$ after which it levels off as shown in Fig. 1.18.

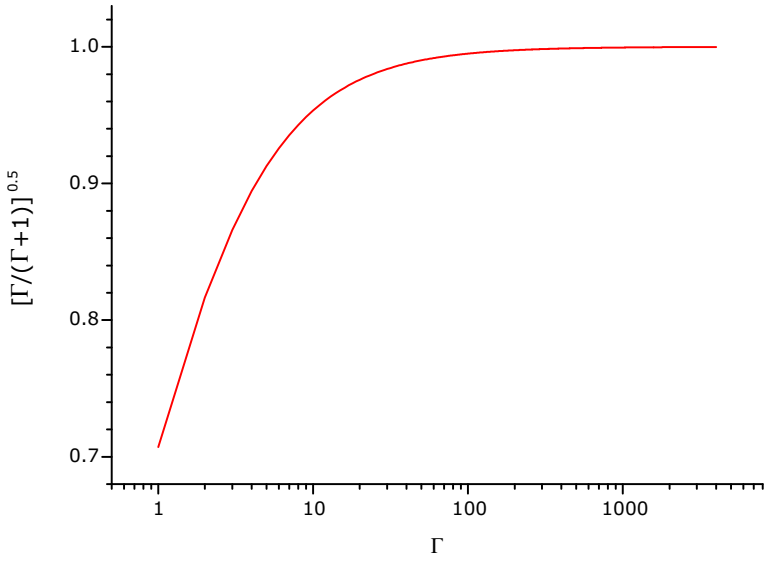

Figure 1.18: *Effect of increase in ratio of V mode to R mode coupling coefficient on GLI SNR.*

The influence of geometric details of the quill design on the relative coupling of V and W modes are not discussed here, since this work is ongoing at the time of writing[24].

1.5.2 Wavelength selection : Lasers and Photodetectors

The wavelength is influenced by the availability of :

- Narrow-linewidth tunable lasers, which can meet the power requirements of the geodetic grid.
- Sensitive photodetectors which can be used to detect pW level interferometer signals at the wavelength of the tunable laser.

[24]The work on the geometry of the quill design is being done by P. Bargassa and A. Reichold of the Oxford ATLAS group.

Laser options

Two frequency scanning sources of coherent light are required for the dual-laser drift correction discussed above. There are in principle two potential designs for satisifying the laser power requirements of the distributed GLIs :

1. A pair of high power tunable lasers deliverying 1 W or more, with the power split amongst the interferometers.

2. A small master oscillator followed by multiple amplifier stages, with each local amplifier serving a small subset of the grid.

The advantage of the high power laser system, is that commercially available Ti:Sapphire lasers appear to be able to meet the present requirements, off the shelf[25]. The disadvantages are; the potential for fibre damage, due to miscoupling of order 1 W at the input to the main delivery fibre and the vulnerability of the system to a single point failure of either main laser.

The advantage of the distributed system would be the potential improvement in power coupling efficiency (optical power delivered to the grid as a fraction of total generated optical power) and the decreased likelihood of local fibre damage due to miscoupling. The system also appears to be less vulnerable to single point failure, although the number of components which must continue to work, to provide full grid coverage increases. The key disadvantage is the lack of a developed solution of this form. The most promising idea involves a pair of tunable semiconductor laser diodes deliverying several mW of seed light, which would then be amplified in fibre, before being split and each fraction further amplified as required.

There are several unresolved issues with each option at the time of writing. The following issue are due to be addressed in the near future.

- The extent to which non-linear effects (in a high power delivery fibre), or pump light (in an oscillator-amplifier system), give rise to unwanted wavelengths in the GLI, which interfere with and thereby corrupt the length measurement signal.

- The complexity of fibre coupling system needed to ensure efficient coupling of high power light into the core of the initial delivery fibre and to prevent fibre damage.

- The levels of noise introduced by amplified spontaneous emission (ASE) in a fibre based amplifier system

Photodetectors

At the near infra-red operating range of the commercially available Ti:Sapphire lasers, there are only two types of photodetector which can be used to detect the pW level GLI signals. These are :

1. Photomultiplier Tubes (PMTs)

2. Avalanche Photodiodes (APDs)

PMTs with bi-alkali photocathodes can achieve 10% quantum efficiencies as far into the infra-red as 830 nm, although the response falls off rapidly after this. The most important disadvantage of using PMTs in a grid based system is the cost, either to buy one PMT per GLI, or to pay for a complicated power routing system which could switch power (repeatedly and reliably over ten years) between the different single mode delivery fibres of the N grid line interferometers which would all share the same PMT. The other disadvantages include :

[25]The options for tunable lasers are discussed in detail in chapter 2.

- PMTs are bulky and mechanically fragile and are not suitable for packing into a readout crate in large number
- They require specialised kV power supplies
- They are destroyed if exposed to more than 0.1 nW of light when operating

The *only* advantage of the PMT is that it can photon count arbitrarily slowly to record the interferometer signals at very low powers, but this is of little interest in ATLAS, where the FSI measurements need to be made as fast as possible, (taking a few minutes at most), to minimise the errors due to GLI drift.

In contrast, avalanche photodiodes are cheap enough to be able to use one per GLI. The other advantages of APDs are :

- APDs offer a much higher quantum efficiency ($\sim 80\%$) at 830 nm, which to first order balances the poorer noise performance compared to a PMT.
- APDs are small and rugged and can be packed in large numbers into a readout crate
- They operate at less than 200 V, which is readily available from a rectified mains supply
- They can withstand exposure to normal daylight even under full bias and are relatively cheap to replace

A detailed investigation into APD performance for the ATLAS FSI system is ongoing at the time of writing [Mit01].

2. The demonstration system

2.1 Introduction

2.1.1 Overview

In this chapter, the hardware and data acquisition software of the demonstration system are described. A functional overview of the hardware system is shown in Fig. 2.1.

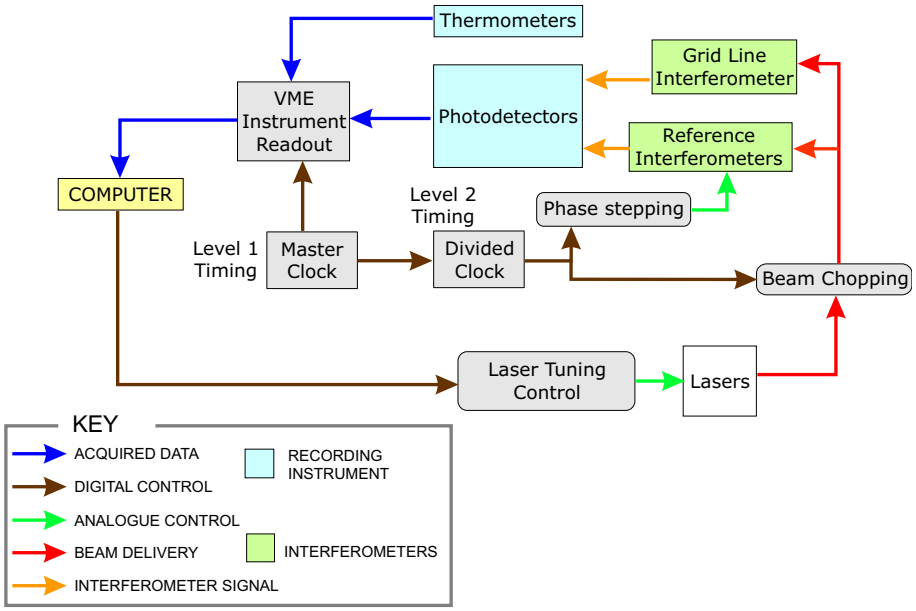

Figure 2.1: *Overview of the demonstration FSI system.*

The system was controlled by a computer, which activated and deactivated the laser tuning and read out the acquired data, in real time, via a set of VME cards. The laser tuning once active ran autonomously. The system was synchronised by a free running master clock, which controlled the timing for the data acquisition, beam chopping and long reference interferometer phase stepping. These are discussed in more detail below.

2.1.2 Setting up the demonstration system

Owing to the central role of the computer and the VME instrumentation, there existed the potential for many electrically connected loops within the system, which could have generated significant noise in the analogue readout channels. The electrical connections for all the equipment in this system were carefully distributed to minimise the possibility of mains noise and earth loops.

The optical elements of the FSI system were laid out on a steel table supported on four pneumatic legs to isolate the equipment from vibrations. A schematic of the individual elements of the optics system is shown in Fig. 2.2. The optical elements closest to the lasers, (in the region shaded yellow), were aligned to the beam from laser 1. Once these elements were in place, it was possible to align the beam from laser 2 to be colinear with laser 1. Once the two lasers had been made colinear, the reference and grid line interferometer components were aligned to the common beam path.

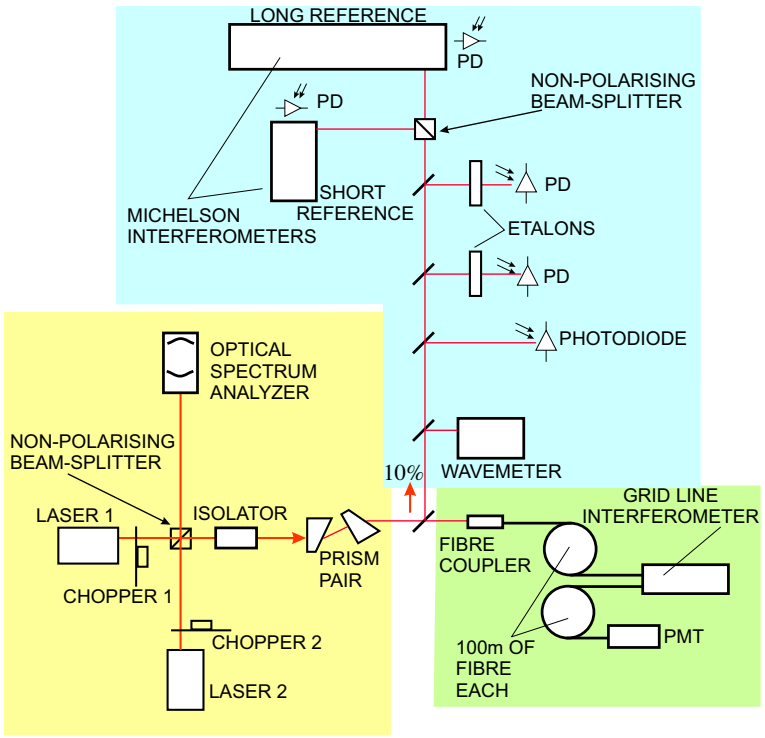

Figure 2.2: *A schematic representation of the optical system. The shaded regions are : The lasers and auxiliary beam manipulation equipment (YELLOW), The reference interferometer (BLUE) and The Grid Line Interferometer (GREEN) sections.*

The beam from laser 2 was directed using a pair of mirrors to meet the beam from laser 1 in a non-polarising anti-reflection coated beam-splitter. The combining cube had to be placed before the isolator, because both lasers needed an isolator and there was only one. To prevent reflections returning to the lasers from the combining cube and from the first polarisor cube on the isolator, all surfaces were tilted slightly away from normal to the input beams.

A CCD camera (Hitatchi 10 bit FP-100 CCD, with an active area 8.7×6.9 mm), was used to optimise the colinearity of the two beams. The path from the lasers to the camera was extended to around 7 m using mirrors to fold the beam. The colinearity was maximised by adjusting the beam of laser 2 so that the two beam spots were coincident on the CCD.

The equipment layout is shown in Fig. 2.3. Two adjustable iris apertures were used to ensure that the beams were colinear and not travelling via separate paths to coincidence on the camera. One aperture was placed just in front of the prism pair, less than 1 m from the lasers and the second a few cm before the CCD camera. To attenuate the light for use with the camera, a 10% splitter and reflecting neutral density filters were placed either side of the first aperture.

Once the colinearity of the beams had been checked, the power in each beam was recorded at different points around the system. The results of these measurements are shown in Fig. 2.4 as a fraction of the power measured directly in front of the corresponding laser.

Two beams were reflected from the last splitter shown in Fig. 2.4, which fed the reference interferometers. The weaker beam from the anti-reflection coated surface of this splitter was blocked off, to prevent it interfering with the main reflected beam. The power reading shown in Fig. 2.4 is for this main reflected beam.

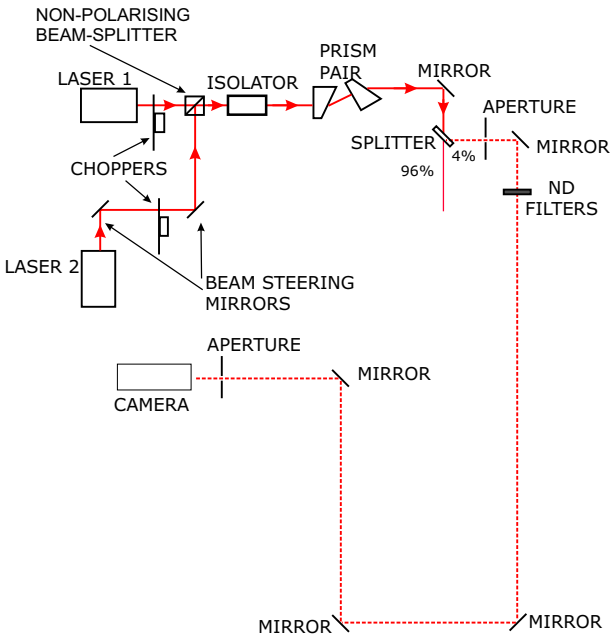

Figure 2.3: *The set-up used to maximise the beam colinearity.*

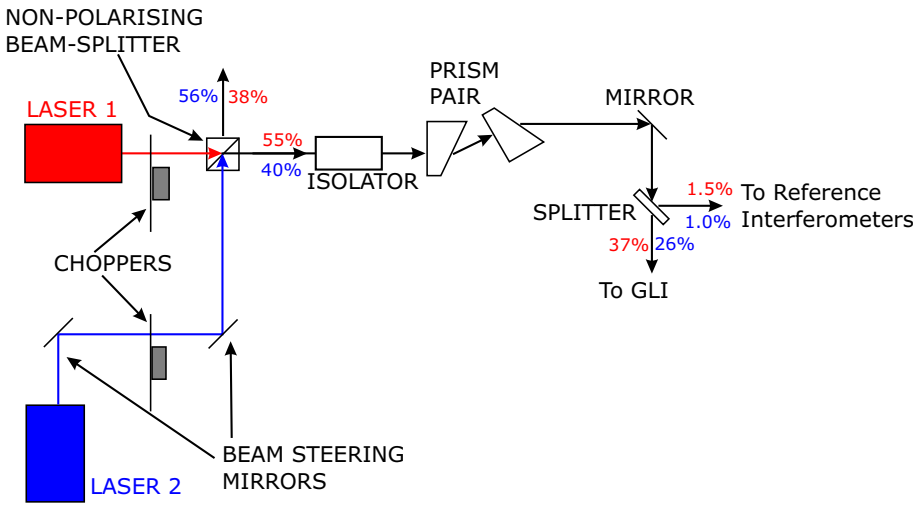

Figure 2.4: *The distribution of laser power around the source system and the input to the reference interferometers and GLI delivery fibre as a fraction of the power from each laser. Figures in RED are for laser 1 and in BLUE for laser 2.*

2.2 The Lasers and related equipment

2.2.1 The Lasers

The lasers were the most important part of the FSI sytem. Many factors were taken into account when choosing the lasers to be used for FSI. These considerations are :

- Continuous-wave operation.
- Ultra-narrow Linewidth (of order 1 MHz or less).
- Operating wavelength compatible with pW sensitive photodetectors.

- Wide coarse tunability over several percent of the optical frequency.
- Fine tunability without mode-hopping over at least tens of GHz.
- Enough power to provide each GLI with around 1 mW.

There are many forms of tunable laser available [Dua95], but this wide range of choice can be reduced to just two commercially available choices by the preceding list of requirements. These are Ti:Sapphire lasers which will be used for the 1 W level power requirements of the final ATLAS system and the semiconductor lasers used in the demonstration system, shown in Fig. 2.5. Both designs rely on external cavities to achieve the ultra-narrow linewidth required for precise interferometry.

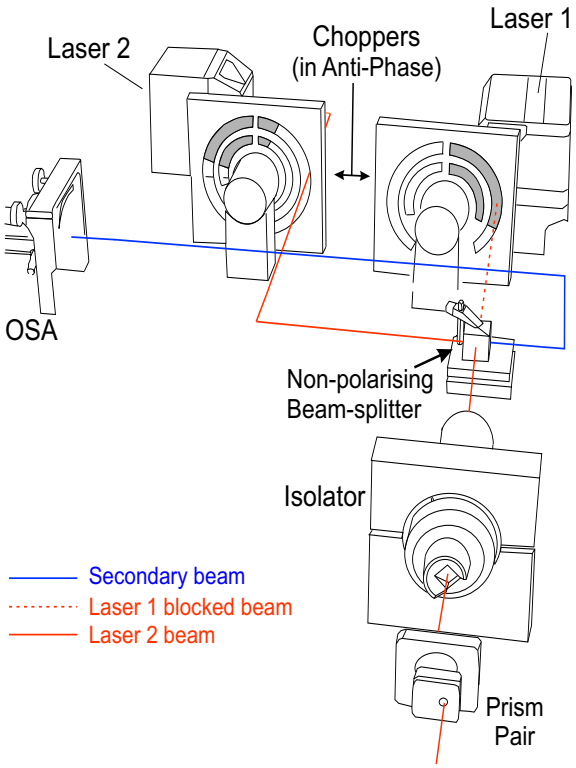

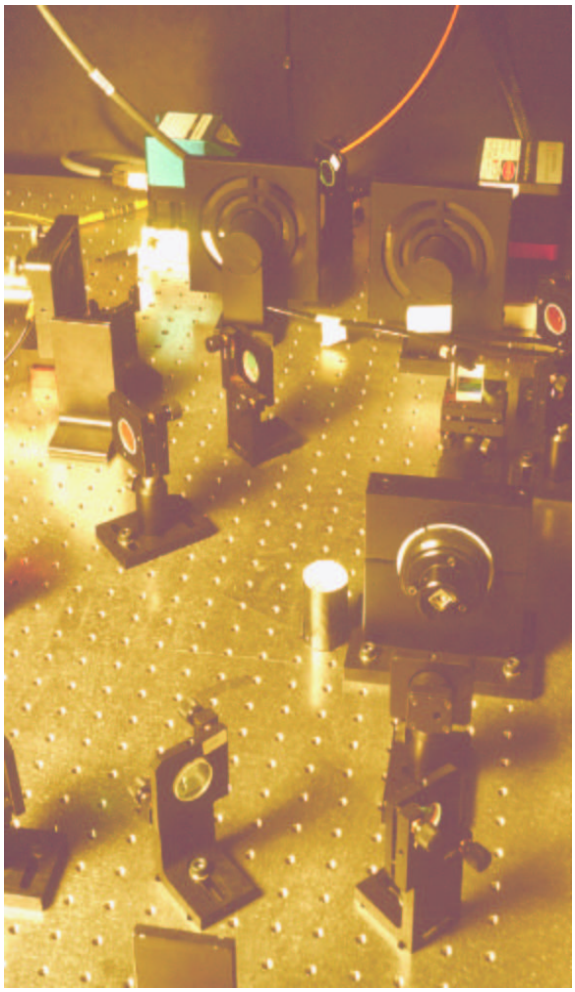

Figure 2.5: *The equipment used to combine the beams from each laser onto a single path.*

The lasers chosen for this system were external cavity laser diodes. These were the New Focus models 6226, referred to here as laser 1 and 6300 Vortex, referred to here as laser 2, which share the same basic Littman-Mettcalf design. This design is described in [Har91] and shown schematically in Fig. 2.6.

The external-cavity offers several advantages over the internal cavity laser diode. An internal cavity diode laser can be tuned by altering the temperature, current or pressure [Fle81] but the range of continuous tuning on a single mode, is limited by regions of multi-mode operation or mode-hopping. The external-cavity laser can also be tuned by changing the position of the external mirror, avoiding the need to change either the temperature or the drive current of the diode gain medium.

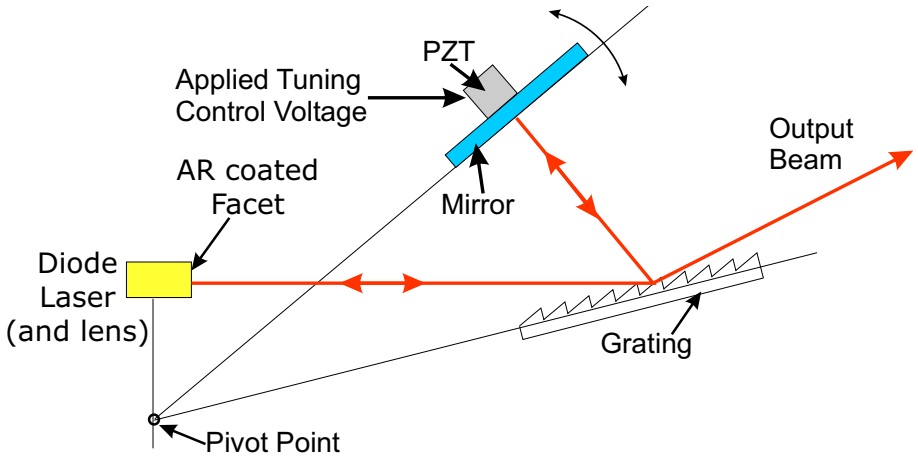

Figure 2.6: *The Littman-Mettcalf design external cavity laser. The mirror is moved about the pivot point by the Piezo-electric transducer (PZT).*

The Littman-Mettcalf design is tailored to minimising mode hops by maintaining the same external-cavity order number for as long as possible. To supress the internal cavity of the diode, the front facet is anti-reflection (AR) coated.

Residual reflection from the AR coated front facet modulates the coupling between the laser diode and the external-cavity. This was a notable problem in laser 2 of this system. At frequencies where the residual internal cavity of laser 2 was strongest, the external cavity mode was sometimes supressed by internal Fabry-Perot modes of the laser diode. The propensity for switching to internal mode lasing was small at first, but gradually increased throughout the lifetime of laser 2. The switch to multi-moded behaviour was observed to occur more often at frequencies in the vicinity of two most non-linear regions in the laser 2 tuning curves of Fig. 2.10. An example of a brief burst of multi-moded laser during fine-tuning is shown in the signal of the short reference interferometer in Fig. 2.7.

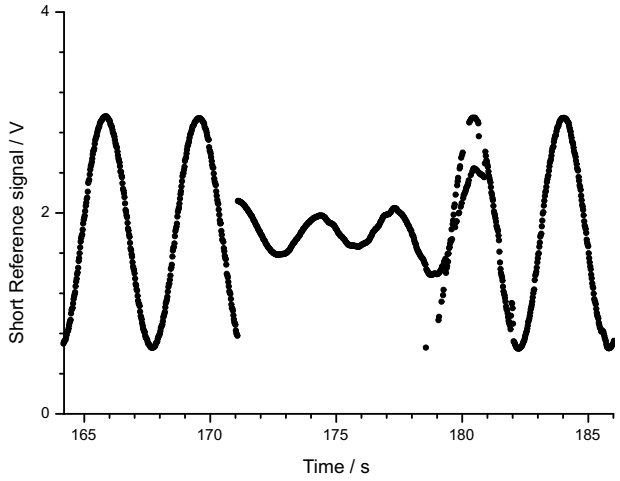

Figure 2.7: *A brief period multi-moded lasing by laser 2 shows up as a decreased visibility signal for all interferometers. The initial switch to multimoded lasing appears abruptly, but the recovery is bistable.*

Each laser consisted of a temperature stabilised laser head as shown in Fig. 2.5, powered and regulated by an external controller. Some parameters for each laser are given for

reference in Table 2.1.

Table 2.1: Parameters for the external-cavity diode lasers of the demonstration system. Those parameters which depend on coarse wavelength are marked* for laser 1. The values given here are intended as a rough guidline.

	Laser 1	Laser 2
Max. operating current /mA	68.3	97.0
Output power at max current /mW	20.7*	21.0
Threshold Current /mA	16*	30
Fine-tuning range /GHz	67	93
PZT centre voltage	47.4%	60.4 V
Coarse wavelength /nm	818 to 851	836

There were two available modes of laser operation; constant power mode and constant current mode. Constant power mode is implemented using an external photodetector to provide a power measurement which is fed back to stabilise the output power of the laser. In this mode of operation the linewidth is larger, whilst offering no advantage for FSI. Both lasers in this system were operated in constant current mode.

The linewidth of each laser was less than 5 MHz in 5 s and less than 300 kHz in 50 ms, according to the manufacturer specifications. These values are compatible with the fluctuations in long reference phase measurements shown in Fig. 2.24, given the other contributions to phase extraction error discussed in chapter 6.

The output beam from each laser had an elliptical profile, with a horizontal major axis. An anamorphic prism pair (or circularisor) was used to reduce the aspect ratio of this profile. It expanded the input beam by a factor of approximately three in the vertical axis and left the horizontal axis unaltered. Since the elliptic profile of both laser beams had the major axis lying horizontally, it was possbile to make both beams more circular using the same prism pair. The prism pair is shown at the front in Fig. 2.5.

2.2.2 Laser tuning control

Coarse tuning, necessary for linking, was only possible using laser 1. It was initiated manually via the front panel of the laser controller. The start and stop wavelengths could be selected in the range from 818 nm to 851 nm in 0.01 nm steps. The fixed coarse wavelength of laser 2 was roughly 836 nm.

Each laser was fine tuned via a voltage signal fed into the controller. This signal was added to an offset bias, (adjustable via the controller front panel), before being applied to the PZT behind the external mirror (shown in the Littman-Mettcalf cavity design in Fig. 2.6). The offset bias settings used to balance the laser tuning are given in Table 2.1.

A ramp generator was custom built to sweep the frequency of both lasers for smooth phase-continuous fine tuning. This ramp generator was activated and deactivated by the central computer. A schematic of the ramp generator is shown in Fig. 2.8.

On activation, it generated a slow ramp using a 16-bit digital counter which was incremented by a free-running clock with a programmable frequency. The frequency of this clock will be represented by f_{TUN} and referred to as the tuning rate. The 16 bits of the counter

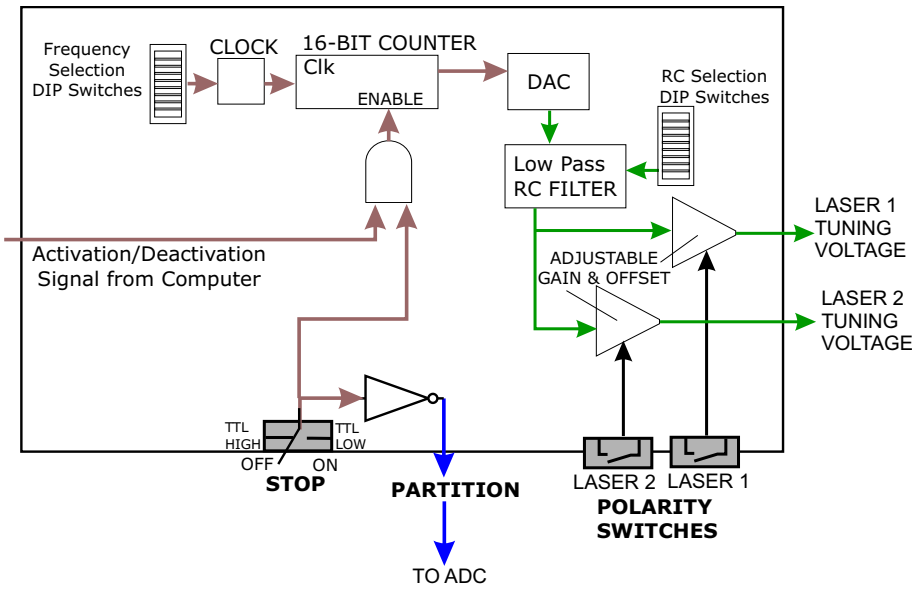

Figure 2.8: *A schematic diagram of the laser fine tuning sweep controller.*

were passed into a DAC[1]. The output of the DAC was smoothed using a low pass filter, with an RC time constant selected in proportion to the tuning rate. As an example, the RC constant was around 0.5 s for f_{TUN} of 600 Hz.

Once filtered, the signal was fed into two channels, one for each laser. Each laser channel was separately amplified and offset so that the full range of the counter could be mapped to the full tuning range of each laser. This meant that both lasers tuned simultaneously.

To make the lasers tune in opposite directions, the polarity of both switches needed to be the same, because the frequency of laser 1 tuned in the opposite direction to its control voltage and the frequency of laser 2 tuned in the same direction of its control voltage. The two polarity settings for which lasers the lasers tuned in opposite directions will be referred to here as tuning polarity *UP*, (when the tuning voltage of both lasers increased throughout a subscan) and tuning polarity *DOWN*, (when the tuning voltage of both lasers decreased throughout a subscan). For linking measurements, the full fine tuning range was split into two subscans with a period of coarse tuning in between. The fine tuning was frozen during the coarse tuning of laser 1, using the manual STOP switch of the laser tuning sweep generator. The frequency of laser 2 still shifted by a few 100 MHz during the coarse tuning of laser 1, due to mechanical inertia and discharge of the RC filter capacitor.

The STOP switch was monitored using an ADC channel which read out the PARTITION output shown in Fig. 2.8. The role of the PARTITION channel in software control is discussed below in section 2.5.4.

Typical fine-tuning curves for each laser are shown in Fig. 2.9, (change in laser frequency against time). The corresponding rate of change of laser frequency against the accumulated change of laser frequency is shown in Fig. 2.10, to emphasise the laser non-linearity.

The slowly changing curvature of each tuning curve was due to the response of the external cavity mirror PZT. The sudden slowing of laser 2 tuning at two places was believed to be caused by an interaction between the internal and external cavities [New00].

[1]Digital to Analogue Convertor.

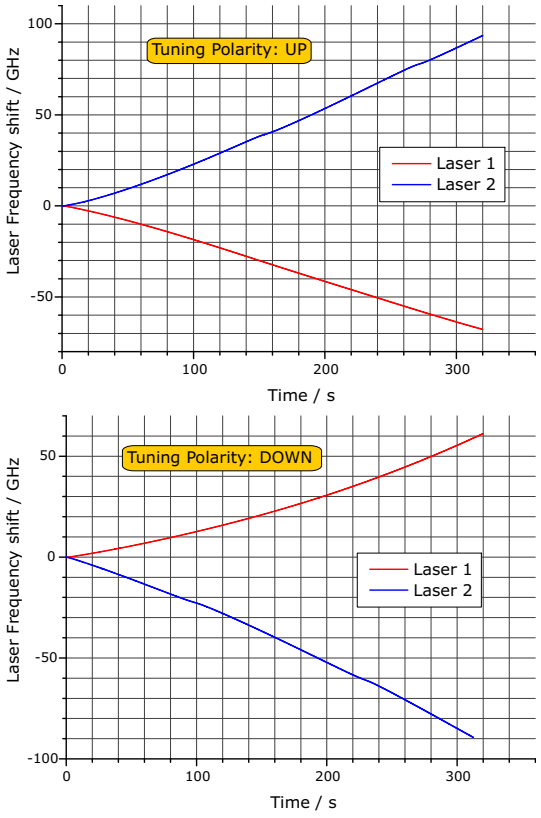

Figure 2.9: *The non-linear fine tuning curves (f_{TUN} 200 Hz). The curves were taken from measurement Set 1 presented in chapter 4.*

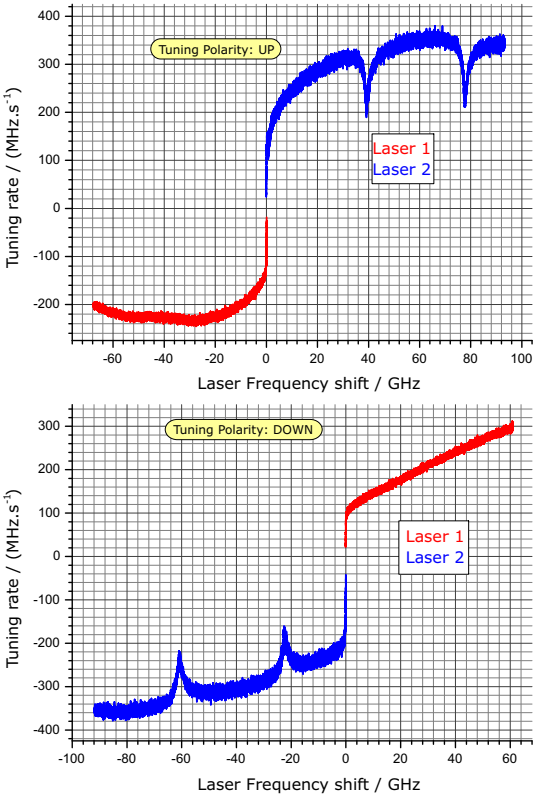

Figure 2.10: *The tuning rate is plotted against the change in laser frequency to emphasise the non-linearity. Tuning rates were calculated from the tuning curves of Fig. 2.9, using an averaging window of 470 ms.*

2.2.3 The choppers, isolator and optical spectrum analyser

The choppers

The choppers (New Focus model 3501) were used to allow only one laser beam at a time into the rest of the optical system. They were set in anti-phase so that the chopper in front of one laser was open whilst the other was closed. Each chopper was set to open for just long enough to allow a set of four succesive phase stepping measurements to be taken.

Each chopper was fitted with a two hole wheel to maximise the ratio of hole size to beam size. This minimised the proportion of time with the beam partially obscured, referred to here as chopper crossover. Measurements made during the crossover were useless, because the laser power in the beam entering the interferometers was changing rapidly and was not unambiguously from one laser. The proportion of chopper cycle spent in crossover can be seen from the power monitor signal (MAGENTA) in Fig. 2.11.

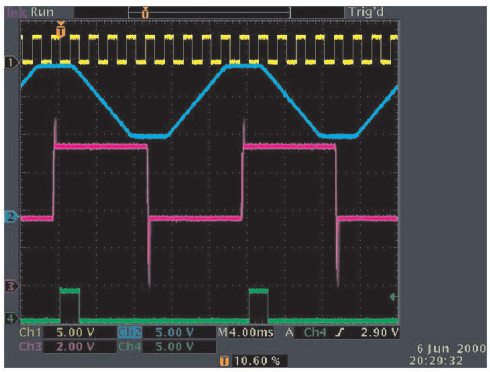

Figure 2.11: *Typical chopper cycle. The chopper behaviour was monitored using the power monitor (MAGENTA). The chopper crossover was confined to a small proportion of the cycle. Horizontal scale 4.00 ms.div^{-1}. The other signals belong to the level 2 timing system discussed below in section 2.5.4.*

The choppers were synchronised by the level 2 timing system discussed below. Jitter of the chopper phase (and thereby of the chopper crossover), with respect to the timing signals was an important problem in this system. The typical bounds of the observed jitter lay outside the manufacturers specifications, (see left half of Fig. 2.12).

To cope with increasing chopper jitter, the time interval between chopper crossovers was increased from four to five (level 1 timing) DAQ cycles. Under this modified level 2 timing scheme, the 5$^{\text{th}}$ DAQ cycle of each chopper window was used as a buffer to allow enough time for the chopper crossover to be completed outside each group of four phase stepping measurements. On rare occassions the chopper jitter exceeded even these precautions as seen in Fig. 2.13 and the right half of Fig. 2.12).

The Isolator

An isolator was used to protect the lasers from external reflections which disrupt the phase continuity of the fine-tuning. The reference interferometers were likely to reflect light back towards the lasers. Although the returning light was attenuated by beam divergence and by a series of beam-splitters in the reference interferometer section, this attenuation was

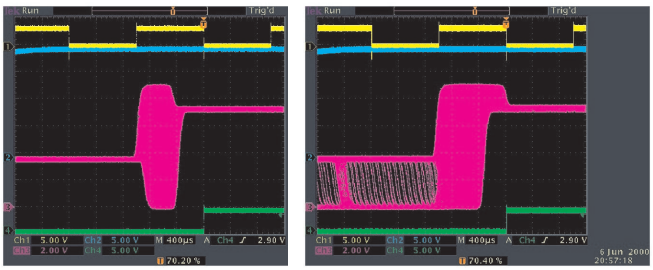

Figure 2.12: *The bounds of the chopper crossover are shown by the power monitor signal (MAGENTA) as in Fig. 2.11, here in close up (0.4 ms.div^{-1}). On the left is the typical variation. On the right is an example of the extreme jitter which led to signals like those shown in Fig. 2.13. In both cases, the photodiode signal clamps at 10 V.*

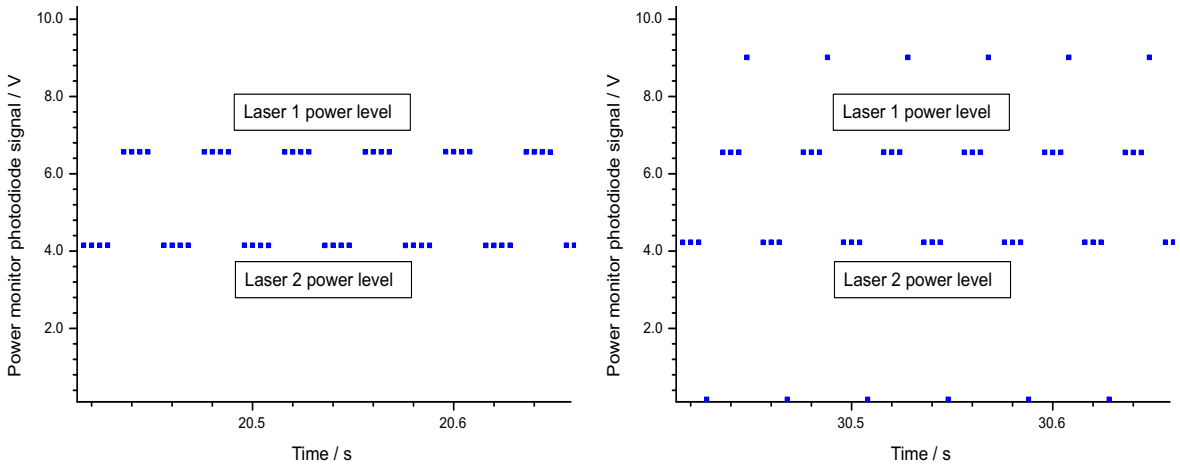

Figure 2.13: *A case of extreme chopper jitter observed using the power monitor. LEFT: Under normal conditions 4 DAQ cycles could be unambiguously attributed to each laser, with the chopper crossover confined to the* 5$^{\text{th}}$ *DAQ cycle of each chopper window. (The* 5$^{\text{th}}$ *cycle is not shown here). RIGHT: Later in the same subscan, chopper 2 started closing and opening early, adding laser 2 to the* 4$^{\text{th}}$ *DAQ cycle of laser 1 and blocking both lasers in the* 4$^{\text{th}}$ *DAQ cycle of laser 2. The corresponding long reference phase extractions were corrupted.*

expected to be insufficient. The isolator added at least an extra 30 dB to the attenuation of returned light, with the exact attenuation depending on wavelength.

The isolator consisted of a magneto-optic cylindrical rod, positioned in an axial magnetic field with a polarising beam-splitter cube at each end[2]. The surfaces of both beam-splitter cubes were anti-reflection coated. The cube on the laser side of the isolator needed to be carefully aligned to avoid reflecting light back to the lasers.

An isolator rod uses the magneto-optic Faraday effect to rotate the polarisation axis of linearly polarised light passing through it as shown in Fig. 2.14.

The size of the rotation angle depends on the wavelength dependent Verdet constant of the rod material and the axial magnetic field inside the rod [Dav96].

To optimise the isolation, the input beam-splitter cube was set to match the vertical

[2]The output polarisor can be seen set at 45° with respect to the vertical, in Fig. 2.5. (The hidden input beam-splitter cube was vertical.)

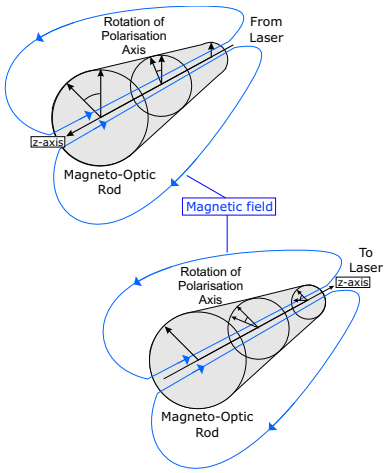

Figure 2.14: *The magneto-optic effect at work in an isolator. The upper illustration shows the vertical polarisation of light from the laser being rotated through 45° to match the pass plane of the output polarisor. The lower illustration shows the continued rotation of the polarisation of returned light so that it can be blocked by the polarisor nearest the laser. The rotation of the polarisation is continuous along the length of the rod and shown here at each half length of the rod.*

polarisation axis of the lasers. The rod was set so that the polarisation is rotated through 45°at 836 nm, (the wavelength of laser 2 and close to the centre wavelength of the laser 1 coarse-tuning range). The rotation angle was adjusted by varying the insertion depth of the rod with respect to the Samarium Cobalt magnet. The isolator in this system was the Leysop FOI 5/57 with a rod made from Terbium Gallium Garnet, (TGG) [Ley99].

The optical spectrum analyser

The optical spectrum analyser (OSA) was used to monitor the spectrum of the lasers and to check that they were tuning correctly and lasing on a single mode.

An OSA is a scanning Fabry-Perot etalon with a photodiode, which monitors the etalon transmission signal. The length of the etalon cavity is swept back and forth by driving a cavity mirror with a piezo-electric transducer (PZT). The PZT is scanned using a high voltage sawtooth waveform which scans the comb of etalon transmission peaks through a range of frequencies. The photodiode signal records a convolution of the momentary etalon transmission comb with the optical frequency spectrum of the incident light. A typical example of the OSA signal is shown in Fig. 2.15.

The OSA was a confocal cavity Tec Optics instrument with a 2 GHz free spectral range. The waveform generator was the Tec Optics SA-1-RG, which generated the sawtooth waveform driving the PZT and amplified the OSA photodiode signal.

To prevent reflections from the OSA returning to the lasers, three precautions were taken.

1. The etalon was slightly misaligned with respect to the incoming beam.

2. The etalon cap, (which has a small aperture in the centre), was placed over the input lens to attenuate the incoming and reflected light.

3. A reflecting neutral density filter (ND 2 in the visible) was placed at 45° to the beam axis in front of the OSA, to deflect most of the incoming beam into a beam dump

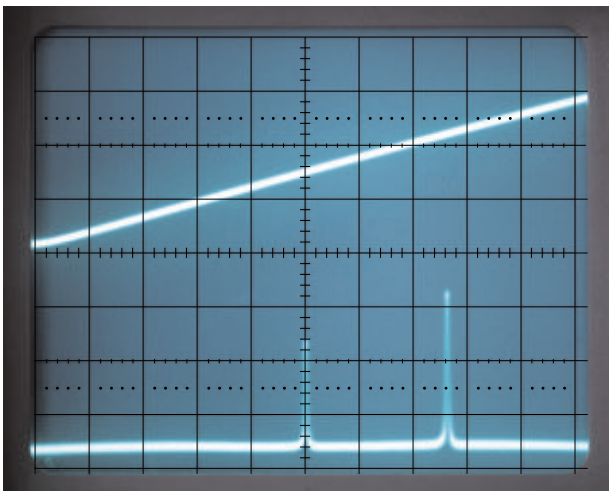

Figure 2.15: *A typical OSA trace showing the upgoing ramp of the piezo sawtooth and the two narrow spectral lines of the lasers. The frequency scale is 220 MHz.div^{-1}. The linewidth of each laser was far too small to be resolved with this instrument.*

and to further attenuate, light returning from the etalon. (The reflecting filter and the beam dump can be seen to the right of the OSA in the photograph of Fig. 2.5).

2.3 Reference Interferometers

The reference interferometer section (shown in Fig. 2.16) was used to track the frequency changes of each laser. The reference interferometers were illuminated by a 4% beam, split off from the beam which fed the GLI delivery fibre, (shown in Fig. 2.4).

The reference interferometer section had no independent temperature regulation system, because one of the aims of this work was to see if such an active temperature control system was needed to achieve the desired measurement precision. The room temperature was controlled by the heating system of the building which was active during all of the experiments reported in this thesis. The temperature was also influenced by solar input because the laboratory was on the south facing side of the building, with a significant fraction of the southern wall holding windows. A typical diurnal temperature cycle, showing the effects of solar heating is shown below in Fig. 2.30.

2.3.1 Michelson Interferometers : Length calibrations

The etalons and the wavemeter were commercially manufactured items, whereas the long and short reference Michelson interferometers were assembled in the laboratory. The lengths of the long and short reference interferometers were measured by hand. The results of these measurements are given in Table 2.2. In this work the *length* of an interferometer refers to the physical path difference between the two interferometer arms.

The length of the long reference was also measured optically by comparison with the 10 GHz etalon and wavemeter. The measurement using the 10 GHz etalon (based on linking measurements of the FSR presented in chapter 5) corresponds to a long reference interferometer length of 859.09 mm, which is compatible with the value given in Table 2.2.

The wavelength based measurement of the long reference interferometer length differed by 752 ± 35 ppm as discussed in the linearity test measurements described in section 5.3.

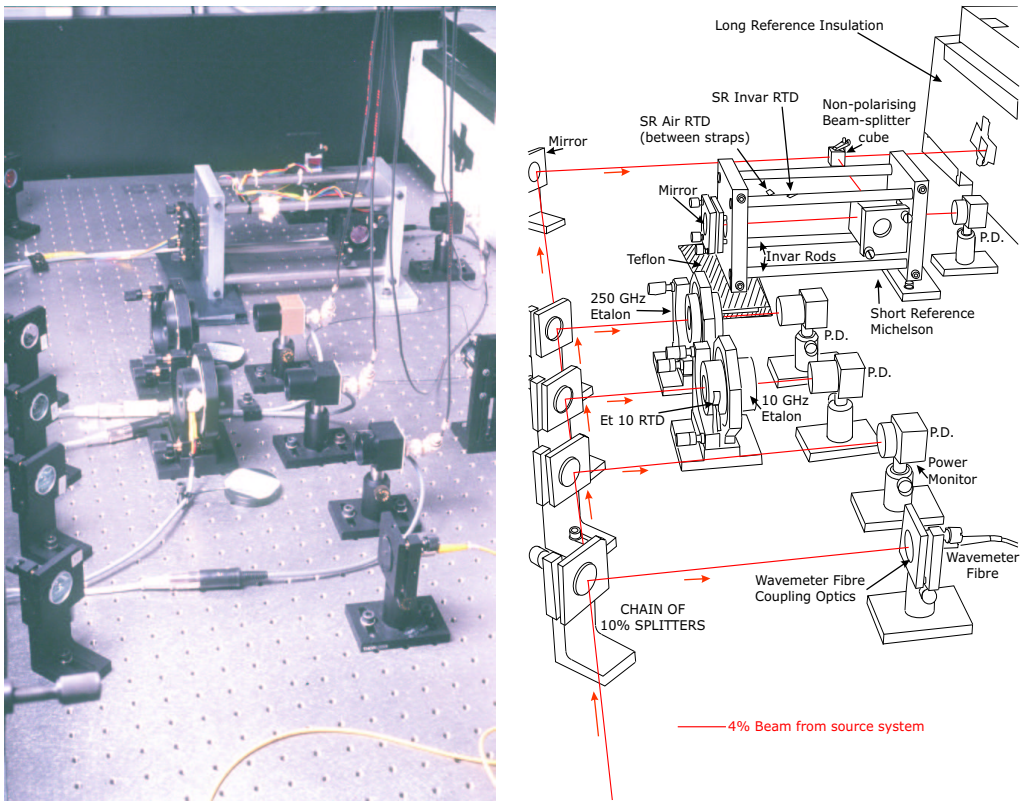

Figure 2.16: *The reference interferometers were fed from a chain of beam-splitters and - except for the wavemeter - were read out by photodiodes (labelled P.D.). The short reference is shown in more detail in Fig. 2.17.*

Table 2.2: *Estimated physical path lengths in the reference interferometers, based on measurements by hand.*

Reference Interferometer	Long	Short
Longer Arm	895.9±2.1 mm	200.9±1.9 mm
Shorter Arm	34.7±0.5 mm	30.2±0.7 mm
Arm difference	861.2±2.6 mm	170.7±2.6 mm

This difference lies outside the expected 100 ppm error tolerance of the wavemeter and is believed to be due to etalon misalignment as described below in section 2.3.5. In the absence of any calibration standard, this is as accurate as the long reference interferometer could be measured.

All the results of short reference and grid line interferometer length measurements made using FSI are quoted assuming a long reference interferometer length of 859.09 mm as explained at the beginning of chapter 3.

2.3.2 Michelson interferometers : Thermal considerations

The long and short reference were both Michelson interferometers, designed and built to be thermally stable. Both were made by clamping aluminium supporting plates onto a set of four parallel invar rods, which ran along the longer arm of each interferometer. This design

is illustrated by the short reference interferometer shown in Fig. 2.17. The beam-splitter is held in an aluminium cage connected to one of the aluminium end plates by steel rods.

These aluminium parts controlled the thermal expansion of the shorter arm in both reference interferometers. The shorter arm of each interferometer is shown in Fig. 2.18. The coefficient of thermal expansion (CTE) of aluminium is approximately 23 ppm.K^{-1} and steel approximately 11 ppm.K^{-1} [Kay89].

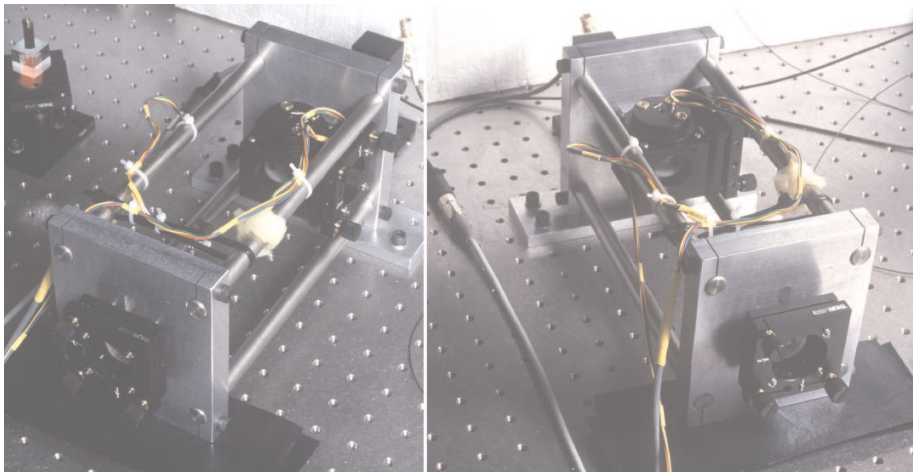

Figure 2.17: *The invar supported Michelson design of the reference interferometers. The short reference is shown without its usual insulating cover. (The basic design of the long reference interferometer is the same.)*

The CTE of the invar alloy was around 1 ppm.K^{-1} according to the supplier specifications. The invar rods were assumed to dominate the thermal expansion of the longer arm of each Michelson interferometer. To ease movement during the differential expansion of the interferometer with respect to the steel optical table, sheets of teflon were used to reduce the friction between table and the mirror end of the longer arm of each interferometer as seen for the short reference in Fig. 2.17.

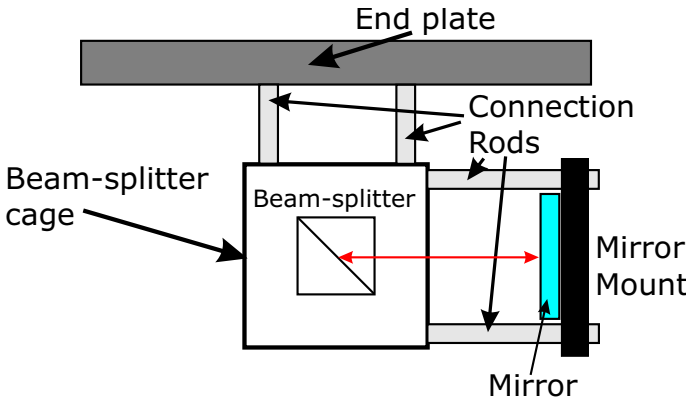

Figure 2.18: *The shorter arm of each reference interferometer was constructed using aluminium and steel. The coefficient of thermal expansion of the shorter arm (shown in red) was therefore expected to be much larger than that of invar.*

The two reference interferometers in this demonstration system were surrounded with polystyrene insulation, (shown around the long reference in Fig. 2.16), to reduce turbulent

air flow within each interferometer and slow down changes in air temperature. The thicker insulation around the long reference slowed the thermal response compared to the short reference as seen in every thermometer record, (see for example Fig. 2.30 below in section 2.5.3 or Fig. 5.1 in chapter 5).

A resistance temperature detector (RTD) was used to monitor the temperature of one of the two uppermost invar rods and the air temperature at a single point within each reference Michelson interferometer. The temperature of the aluminium cage around the beam-splitter of the long reference was also monitored by an RTD. The labelling and location of all RTDs is given below in Table 2.5.3.

2.3.3 Michelson interferometers : Optical Layout

The two reference interferometers were both set up with the same optical layout, shown in Fig. 2.19.

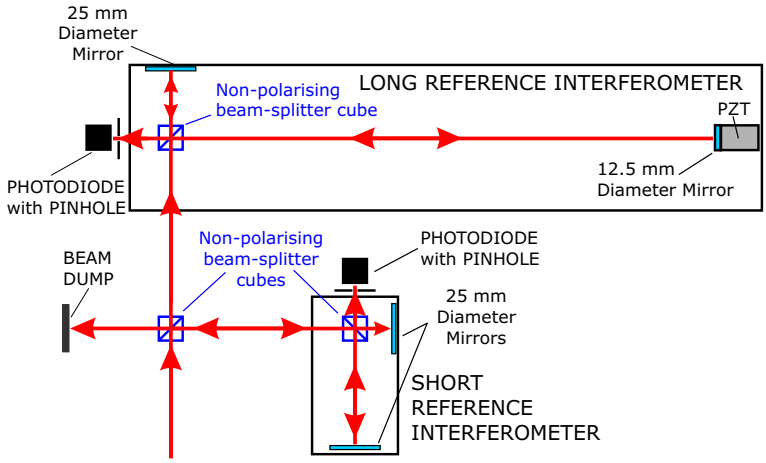

Figure 2.19: *The optical layout of the reference Michelson interferometers.*

To maintain optimum coupling to the input beam, each interferometer was fixed to the optical table at the beam-splitter end of the long arm. On entering each interferometer, the beam was split by an anti-reflection coated non-polarising 50% beam-splitter cube to feed each arm of the interferometer. After reflection from a mirror, the beam in each arm returned to the beam-splitter and recombined to form an interference pattern. A pinhole covered photodiode[3] was used to sample this interference pattern. A pinhole diameter of less than 1 mm was used to maximise the visibility of the interference signal, (see discussion of interferometer visibility in chapter 1.)

The mirrors in each interferometer were coated in high reflectivity dielectric thin films. The longer arm of the long reference interferometer was terminated in a mirror mounted on a PZT (MellesGriot 07PA5001). This mirror was small to minimise the load on the PZT. The PZT was used to step the phase of the interferometer as described in section 2.3.4.

2.3.4 Long Reference Phase stepping

The long reference PZT mounted mirror was used to cycle the optical path difference (OPD) of the long reference interferometer to implement phase stepping, (which is described in chapter 3).

[3]The photodiodes used in the reference interferometer section are described in section 2.5.2.

The PZT was driven by the amplified output of a bi-directional ramp generator. The phasestep distribution on the ramp waveform is shown in Fig. 2.20. The sawtooth drive signal was chosen after abandoning use of a staircase waveform, which excited PZT resonances giving rise to unwanted mirror oscillations.

When the PZT voltage increased, the PZT extended, shortening the longer arm of the interferometer and thereby decreasing both the OPD and the absolute phase of the interferometer signal. The order for the phase steps shown ensures that the interferometer phase increases from step A to step D. The time reversal of laser 2 phase steps, together with the fact that the lasers were always tuned in opposite directions, meant that the phase step size was increased or decreased (by a few parts per thousand) for both lasers with the tuning polarity *DOWN* or *UP* respectively.

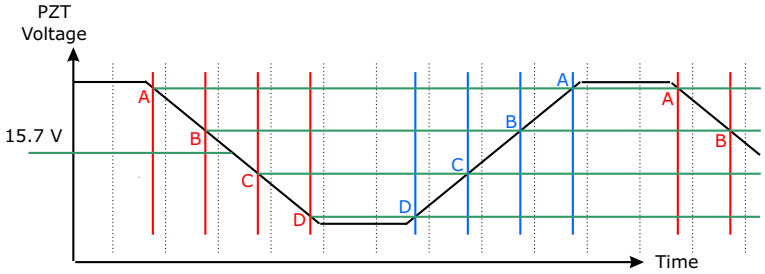

Figure 2.20: *Distribution of the phase steps on the PZT waveform. The order of phase step labelling is shown for positive phase steps. Steps for laser 1 are shown in red, steps for laser 2 in blue.*

The response of the PZT was recorded by measuring the voltage swing needed to shift the interferometer phase through 2π. The results of these measurements were converted into the PZT response which was non-linear as shown in Fig. 2.21. The PZT voltage waveform was centred on the stationary point of the fitted curve at around 15.7 V, to minimise the non-linearity of the phase steps. The dependence of phase extraction errors on PZT bias is discussed in more detail in chapter 6.

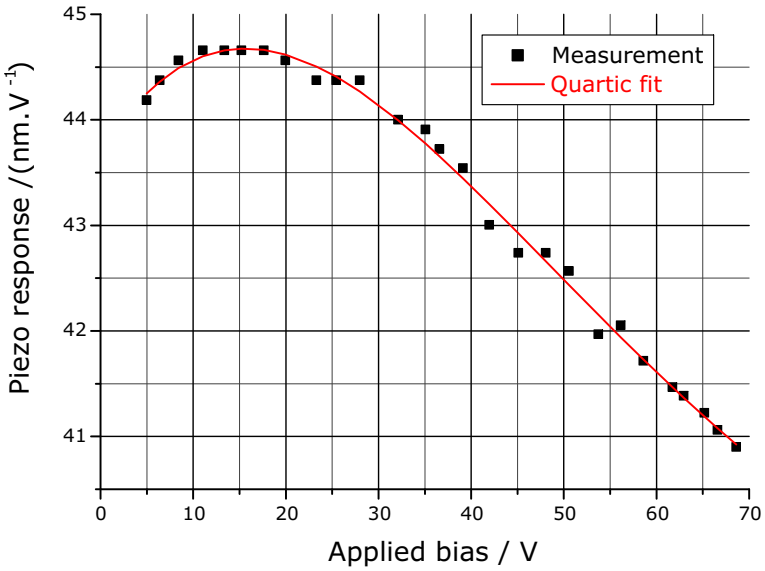

Figure 2.21: *The non-linear response of the long reference mirror PZT.*

The PZT ramp generator was synchronised to the level 2 timing system, (described below in section 2.5.4). A functional schematic of the ramp generator is shown in Fig. 2.22. The input channels monitored the level 2 timing signals used to synchronise each chopper. The signal for chopper 1 was used to initiate the decreasing voltage ramp for laser 1 and the signal for chopper 2 to initiate the increasing voltage ramp for laser 2. The falling edge of each chopper synchronisation pulse, triggered the start of the linear voltage ramp as shown in the level 2 timing diagram below (Fig. 2.34). The ramp was implemented by an integrator shown in Fig. 2.22, which was connected to a reference voltage of +10 V or −10 V, when ramping, with the slew rate controlled by the RC constant. Once a ramp had been initiated, it continued until the output of the integrator had reached the level of the opposite reference voltage. This ensured that a new ramp was not initiated until the previous ramp had been completed[4].

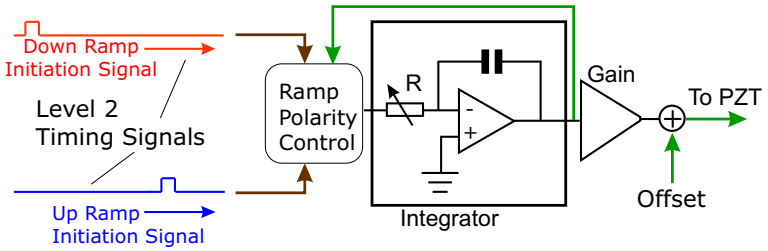

Figure 2.22: *The ramp generator for the long reference mirror PZT.*

The slew rate of the PZT ramp was set to equalise (or balance) the voltage, at corresponding phase steps for laser 1 and laser 2. This procedure will be referred to here as *PZT balancing*.

PZT balancing was optimised first with the level 2 timing set up for 4 DAQ cycles per chopper window. Once the level 2 timing was adjusted to 5 DAQ cycles per chopper window, the PZT balancing optimisation was repeated. The description below covers the latter optimisation, since all of the results presented in this thesis, excepted the first set in chapter 4 were taken with 5 DAQ cycles per chopper window.

To make a fair comparison between the up and down sweep of the PZT, during a PZT balancing measurement, the long reference interferometer was illuminated by laser 1 only, without chopping. Laser 1 was set to a coarse wavelength of 836 nm, so as to match the wavelength of laser 2. To minimise the laser frequency change during each test, the fine tuning control voltage was held fixed. Despite this the laser typically drifted over around 5 MHz in 13 s, (see Fig. 6.12).

To adjust the slew rate of the PZT ramp, the integrator RC constant was set to different values, around 13 s worth of long reference data were recorded[5] and the asymmetry between the signals from the up and down ramp was assessed for each setting.

The amplification of the PZT drive system was adjusted to set the phase step size to be around 110°, after intitial tests determined the approximate slew rate. These initial tests were necessary, because the integrator slew rate and phase step size were coupled for a given amplifier gain. Once the correct gain had been set, the asymmetry test on the long reference interferometer signal was repeated at closely spaced values of RC constant. The results of these fine adjustments are shown in Fig. 2.23.

[4]This ramp generator was designed and built by David Smith.

[5]To make this a useful comparison, the same number of data channels were acquired as in a real FSI experiment, so that the timing of the long reference measurement was the same.

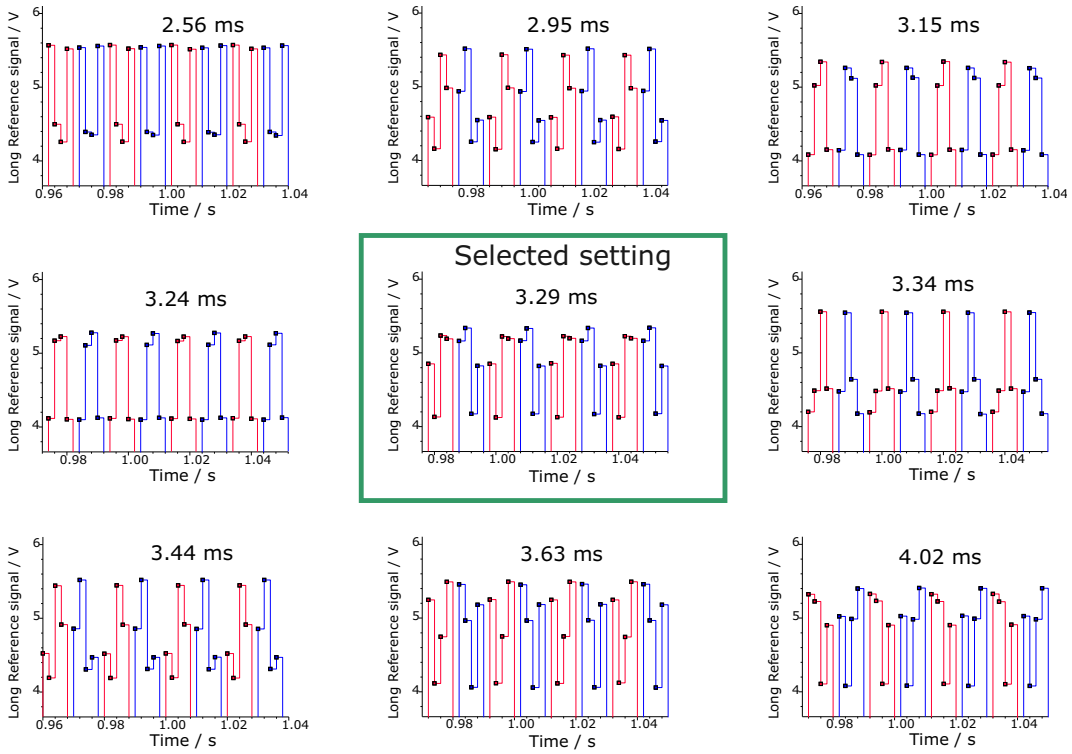

Figure 2.23: *The long reference signal asymmetry at different stages of PZT balancing. The down sweep signals are red, the up sweep signals are blue. The finally selected setting is shown in the centre.*

The corresponding tuning curves were calculated at each RC setting, from the extracted and unwrapped phase of the long reference interferometer (using the procedures described in chapter 3). The difference between the unwrapped phase for the down ramp and the following up ramp were calculated modulo 2π using the matching criteria explained in section 3.3.3, to ensure only nearest neighbour extracted phases were compared. The mean and standard deviation of the differences between points on the down ramp and up ramp tuning curves, are shown in Fig. 2.24 against RC constant and phase step voltage increment. Note that each increase of the RC constant, slowed the ramp and thereby reduced the size of the voltage increment per phase step.

The results of the balancing test at the selected PZT setting, are discussed in more detail in chapter 6, where they are used to estimate various noise contributions to the long reference phase extraction error.

2.3.5 Fabry-Perot etalons

There were two air spaced etalons in the reference interferometer section, with free spectral ranges (FSRs) of 10 GHz and 250 GHz, (TecOptics EA 202 and EA 201 respectively). Each etalon was an air spaced plane-plane cavity with fused silica spacers (CTE 0.4-0.55 ppm [Kay89]). The spacers were made to a tolerance of around 1 μm per spacer element. The 15 mm cavity of the 10 GHz etalon was manufactured using two spacers because the longest available spacer element was 10 mm [She99], thereby increasing the margin for error in the cavity length.

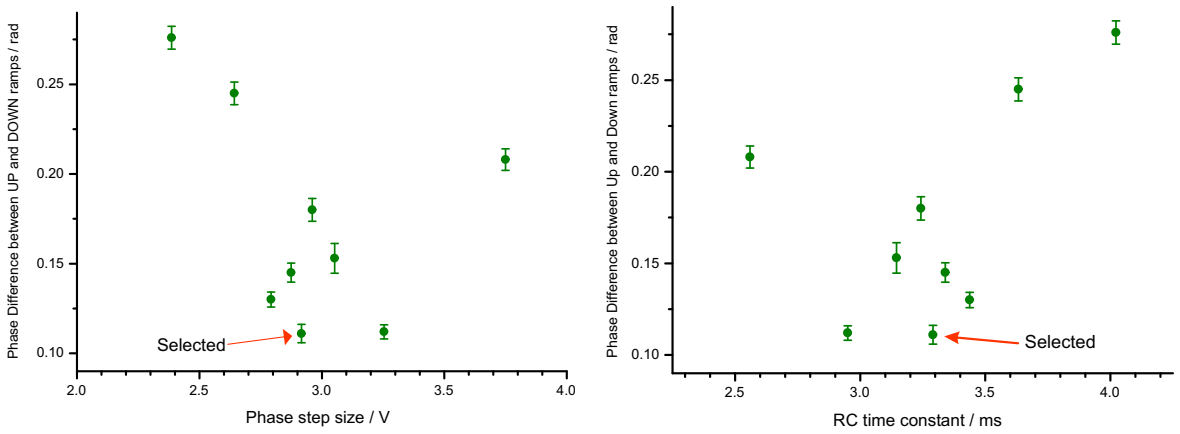

Figure 2.24: *The sample average difference between the phase extracted on neighbouring up and down sweeps of the PZT ramp as functions of the expected RC time constant and phase step voltage. The error bars show the sample standard deviation of the phase differences. NB These reults correspond to the settings shown in Fig. 2.23.*

250 GHz etalon

The 250 GHz etalon was included in the reference interferometer section as part of a descending hierarchy of frequency measurement devices from the wavemeter to the long reference. This had been intended to allow unambiguous frequency determination of every long reference order. Since this absolute frequency determination was never implemented, the 250 GHz etalon was not used and will not be discussed further in this thesis.

10 GHz etalon

The ratio of the free spectral range (FSR) of the 10 GHz etalon to one long reference fringe cycle was measured for two reasons. Firstly this ratio was used to estimate the OPD of the long reference interferometer, as a form of calibration. Secondly this ratio was used in linking, for extrapolating the long reference phase as explained in chapter 3.

Typical transmission peaks from this etalon are shown as a function of laser frequency in Fig. 2.25. For both lasers, the peak is asymmetric, with the maximum around 11 MHz (0.4 long reference radians) lower than predicted by the fit[6]. The observed peak shape is indicative of asymmetric etalon alignment, which would result in a longer cavity round trip time and smaller FSR than a symmetrically aligned cavity.

According to an indirect measurement of the etalon FSR using the wavemeter, (in the length measurement linearity tests discussed in chapter 5), the FSR was around 750 ppm less than 10 GHz.

2.3.6 The wavemeter

The Burleigh 2100 wavemeter was used to check the wavelength of each laser before a set of FSI experiments. These wavemeter readings provided the estimate of the laser frequency needed for calculation of the combined laser phase ratio estimate, for each fine tuning subscan, (as discussed in chapter 3). Any common scaling factor error in the wavelength readings would have cancelled out when calculating ρ (see equation 1.41), for the combined dual-laser

[6]The peak fitting is described in Appendix C.

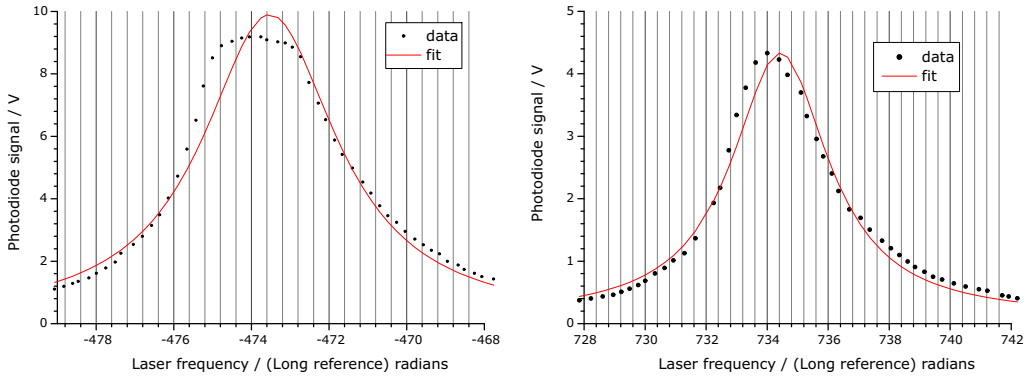

Figure 2.25: *Comparison of the asymmetric 10 GHz etalon transmission peaks with symmetric fit function. LEFT: The laser 1 signal saturated the photodiode. RIGHT: The etalon peak for laser 2*

result. The wavemeter was also used as a calibration standard for the linearity test described in chapter 5.

The wavemeter measured wavelength by generating fringes in an internal scanning Michelson. The accuracy of the wavemeter was specified to be ± 1 part in 10^4 at 1000 nm.

2.4 Grid Line Interferometer section

The grid line interferometer in the demonstration system was built to represent a single interferometer from the SCT geodetic grid to be installed in ATLAS as discussed in chapter 1.

The Grid Line Interferometer section of the apparatus consisted of the delivery and return fibres, the grid line interferometer and the photomultiplier which detected the return signal. The PMT is described in section 2.5.1.

2.4.1 Grid Line Interferometers

Several different length grid line interferometers were built on the steel optical table. These were used for testing FSI under conditions of large drift, because the CTE of steel is roughly an order of magnitude greater than that of the carbon fibre which will be used to support the SCT in ATLAS. This allowed the equivalent effects of large temperature changes in carbon to be explored over the smaller temperature range achieveable in the laboratory. As with the reference interferometers, polystyrene insulation was used to reduce turbulence and to provide thermal insulation of the interferometer environment.

In later experiments, where thermal drift was no longer of interest and needed instead to be minimised, the GLI was constructed on carbon fibre, so that the thermal drift would be much smaller. An example carbon fibre supported GLI is shown in Fig. 2.26.

In place of a quill, the fibre ends were held together in a special mount and a pellicle beam-splitter was used to provide the short arm reflection. The pellicle beam-splitter was a 5 μm thick Mylar membrane anti-reflection coated on one side to remove the unwanted second surface reflection. As with the quill beam-splitter which will be used in the ATLAS GLIs, there were V and W modes formed by the pellicle (see Fig. 1.17).

Care was needed with the adjustment of the pellicle beam-splitter to avoid setting up a so-called W-mode, where light reflects from the beam-splitter, a point between the delivery

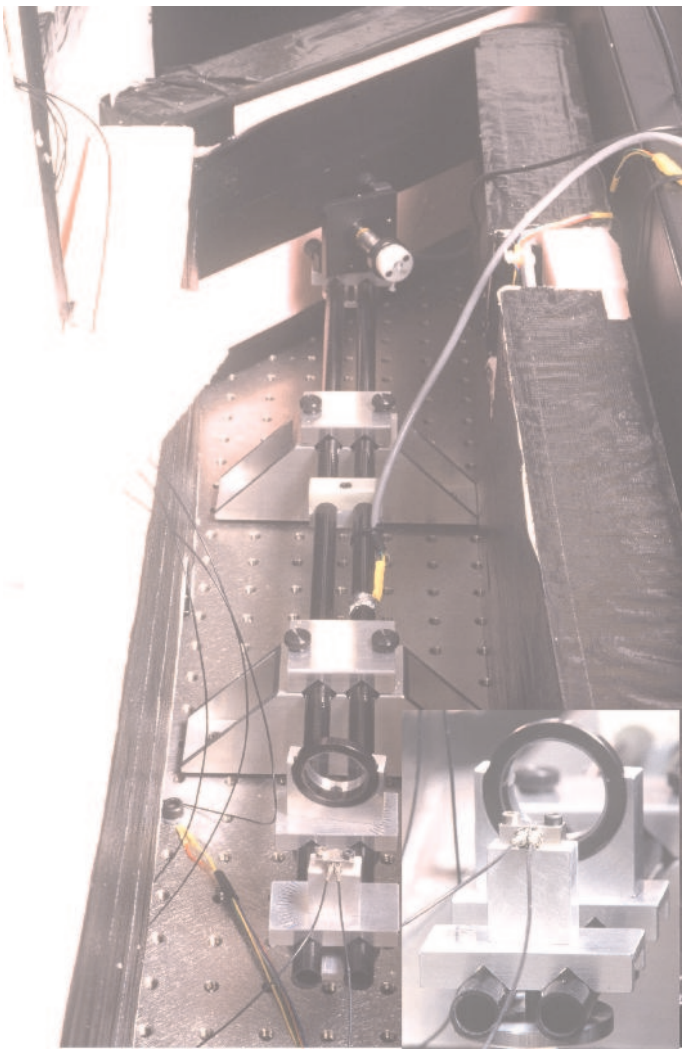

Figure 2.26: *A grid line interferometer built on two carbon fibre rods. At the nearest end, the delivery and return fibres point towards the nearby pellicle beam-splitter and the retroreflector, which was mounted on a PZT so that vibrations could be deliberately induced when required. During FSI measurements, the thermal insulation was completed by a polystyrene lid and front wall. INSET: The fibres and pellicle beam-splitter in more detail.*

and return fibres and then from the beam-splitter for a second time before coupling into the return fibre. The effects of W- and V-mode interaction with the R-mode (via the retroreflector) are discussed in chapter 6. The details of the GLI alignment procedure are given below in section 2.4.3.

The retroreflector was an internal corner-cube, with the reflecting flat faces ground from a cylindrical rod of BK7 as shown in Fig. 2.27a. The frequency dependence of the refractive index of BK7 (given by [Tec]), was fitted to the following quadratic :

$$\begin{aligned} n\,(\nu/\mathrm{GHz}) &= a_0 + a_1\nu + a_2\nu^2 \qquad (2.1)\\ a_0 &= 1.50258\\ a_1 &= 5.77\times10^{-9}\ \mathrm{GHz}^{-1}\\ a_2 &= 4.28\times10^{-14}\ \mathrm{GHz}^{-2} \end{aligned}$$

The fitted quadratic is compared with the quoted values in Fig. 2.27b.

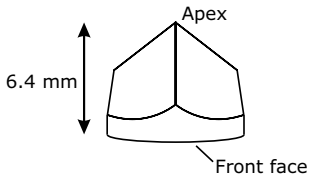

Figure 2.27a: *The GLI retroreflector.*

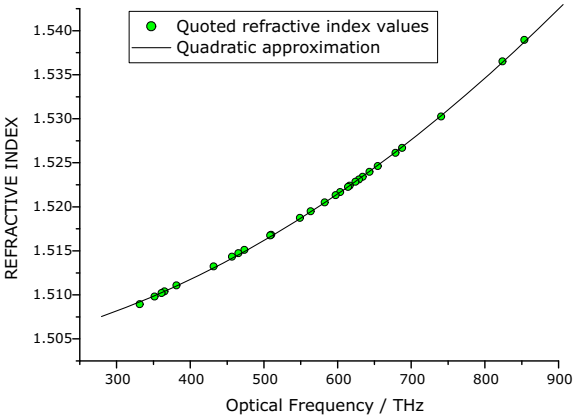

Figure 2.27b: *Frequency dependence of the Refractive index of BK7, comparing the manufacturer's data with the best fit quadratic approximation given by equation 2.1.*

The consequences of the retroreflector dispersion for measurements of the GLI OPD are discussed in chapter 6.

2.4.2 The delivery and return fibres

A 100 m length of fibre was used for each GLI fibre in this demonstration system so that the lengths of fibre would be similar to those needed in ATLAS. Unlike the fibre in ATLAS, this fibre was not radiation hard, (SM 810 fibre from FIBERCORE, NA 0.11, single mode cut-off 780 nm).

The ends of both fibres were angle-polished to prevent reflections setting up multiple optical paths. The interferometer ends of the fibres were held together in a metal block so that the coupling axes were parallel. This fibre block and the pellicle beam-splitter are shown in the inset of Fig. 2.26.

The light was coupled into the delivery fibre using a lens tube mounted in a fibre coupler (both made by Point Source). An identical lens tube at the end of the return fibre collimated the light entering the PMT. To prevent stray light leaking into the PMT, the return fibre lens tube was surrounded by a light-tight seal.

2.4.3 Setting up a Grid Line Interferometer

As a precaution against spurious reflections, the metallic surfaces, (including the retroreflector support and PZT), of the carbon fibre GLI shown in Fig. 2.26, were covered in tissue paper, when the interferometer was in use. Equivalent precautions were unnecessary for GLI built on the steel table, where the interferometer axis was more than 75 mm above the reflective surface of the table, and other components had dull black coatings.

When setting up the GLI, the retroreflector and fibres were aligned first. The retroreflector was set with the front surface at a tilt angle around 30° to the GLI axis[7], to disperse

[7]The line from the retroreflector apex to the point midway between the two fibres will be referred to here as the GLI axis.

front surface reflections and either the fibres or retroreflector were adjusted so that light from the delivery fibre travelled in the direction of the GLI axis. This adjustment was guided by monitoring the photon count received by the return fibre.

Once the axial alignment had been optimised, the retroreflector was temporarily blocked off, by a piece of dark card placed at a large tilt angle to the GLI axis ($> 45°$). To protect the PMT the delivery fibre light had to be blocked whilst introducing the pellicle beam-splitter to the interferometer. The pellicle was initially set on the GLI axis, a few cm from the fibres, at a large tilt angle to the interferometer axis. With the delivery light restored, the tilt angle was slowly reduced, whilst monitoring the photon count until the count matched the value observed at retroreflector optimisation, to within a factor of two. The retroreflector was unblocked and the GLI alignment was completed by testing the signal with a short fine tuning frequency scan.

2.5 Sensors, DAQ and timing

2.5.1 The Photomultipler tube

The PMT used in this system was the Hammamatsu R943-02. The photocathode was made from GaAs(Cs) which had extended sensitivity in the infra-red. At 830 nm the expected quantum efficiency was around 10%. The PMT was used to count photon fluxes for optical power levels from around 100 fW to 20 pW. The tube was surrounded in mu-metal to shield it from magnetic fields and was mounted well away from the strong magnetic field of the isolator.

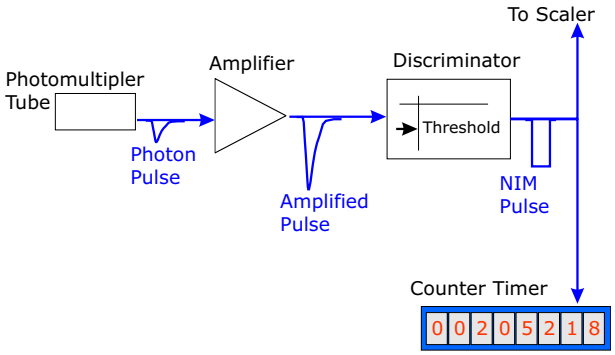

Figure 2.28: *Photon counting system.*

The chain of devices used to amplify PMT pulses and digitise them are shown in Fig. 2.28. The photon pulses generated by the PMT were fed into to an amplifier (Lecroy 612 AM) and discriminator (LeCroy model 623B 100 MHz NIM) for digitisation. A typical photon pulse is shown after amplification in Fig. 2.29. The digitised pulses were sent to the scaler (LeCroy model 1151E).

2.5.2 Photodiodes

The photodiodes (Thorlabs PDA50) were used in the reference interferometer section. One, (referred to as the power monitor), was used to monitor the variations in optical power entering the reference interferometer section.

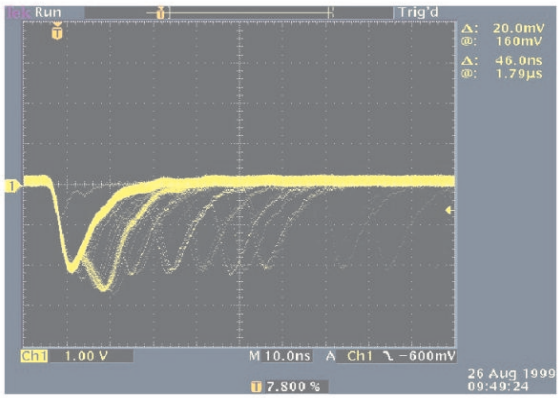

Figure 2.29: *A set of typical photomultipler pulses after amplification. N.B The discriminator threshold, (indicated by the arrow at the right), was easily crossed by the peak of a typical pulse. Vertical scale 1.0 V.div^{-1}. Horizontal scale 10 ns.div^{-1}.*

The photodiode signals were amplified and filtered by a single low pass RC stage before being readout by an ADC mounted in the VME crate. The dynamic range of the photodiodes was 0-10 V which matched the ADC conversion range. The photodiode pk-pk noise was found to be at most of order 1 mV. This was smaller than the 2.5 mV digitisation steps of the ADC operating at maximum resolution. The low pass filters were set to a cut-off frequency of approximately 5.3 kHz. This was fast compared to the chopper crossover which was the fastest timescale in the signal. The low pass cut off was also far enough above the equivalent frequency of the long reference signal. As an example; phase stepping by around 110° in 2 ms is the same rate of change of phase as a 153 Hz sinusoid.

2.5.3 Thermometer system

The thermometer system measured the temperature using type PTR 100 platinum resistance thermometers (RTDs), using a low noise custom built readout circuit[8]. The locations of the different RTDs are given in Table 2.5.3. A maximum of eight RTDs could measured at a time. In certain experiments, where either the etalon thermometer or carbon fibre thermometer were needed, the steel 2 RTD was disconnect to release this channel for the other RTD.

The readings of each RTD channel over a scan were combined to produce a single temperature value, to be used in later calculations. All temperature values presented in this work are given as scan averages. Typical examples of thermometer data are shown in Fig. 2.30. During the length measurement sets 1,2,3 and 5 presented in chapter 4, the short reference invar RTD channel was underreading, because one side of the resistor was grounded by the invar through a gap in the insulation.

Thermometer read-out circuit

Each thermometer channel was read out by the custom built circuit which converted RTD temperatures in the range 17° C to 27° C into voltage signals over the range from 0 V to 10 V. The input temperature range was chosen to cover the most likely ambient laboratory conditions and the output voltage range was selected to match the dynamic range of the

[8]This was designed and built by D. F. Howell.

Table 2.3: Thermometer locations. Names marked with (∗), replaced the Steel 2 RTD channel in some experiments. The RTDs measured by all other read out channels were always connected.

RTD name	RTD location
SR Air	In the air of the short reference interferometer
SR Invar	On an invar rod of the short reference interferometer
LR Air	In the air of the long reference interferometer
LR Invar	On an invar rod of the long reference interferometer
LR Alu	On the long reference interferometer beam-splitter cage
GLI Air	In the air of the grid line interferometer
GLI Steel	On the steel optical table near the GLI (Shown in Fig. 5.13)
Steel 2	On the steel optical table near the lasers (Shown in Fig. 5.13)
Et 10 (∗)	On the case of the 10 GHz etalon
Carbon (∗)	On the carbon support of the GLI shown in Fig. 2.26

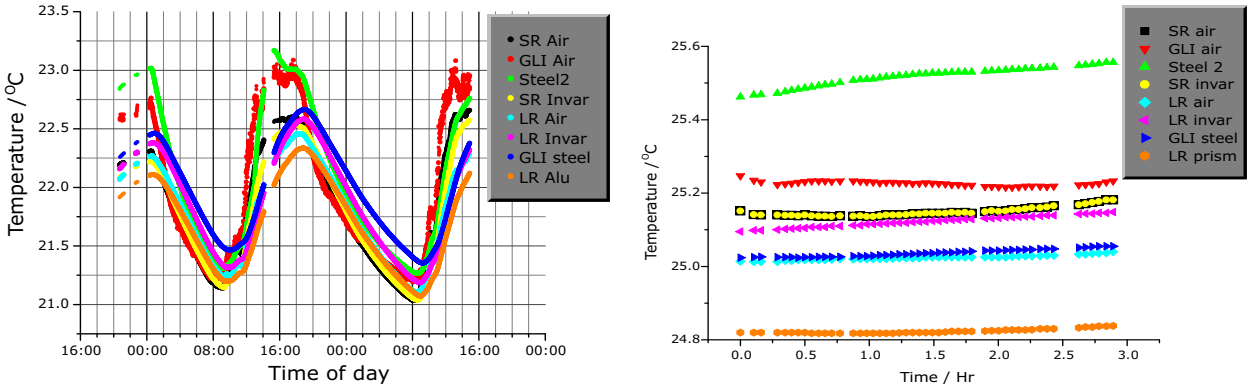

Figure 2.30: *Typical thermometer readings. The left graph shows the diurnal temperature cycle in the laboratory, with the notable effect of solar radiation. The right graph was recorded during a set of FSI scans. In both cases the building heating system was active.*

12 bit ADC. With this design specification, the least significant bit of the ADC corresponds to a temperature change of around 2.4 mK.

A schematic representation of the thermometer read-out circuit is shown in Fig. 2.31. The presence of the varying resistance RTD between the voltage references and the fixed resistors means that current drawn was not constant. As a result the voltage drop across the RTD was not a linear function of resistance. This non-linearity was small, because of the larger ratio between the fixed resistors and the RTD resistance.

Another small non-linearity in the mapping from temperature to output voltage arose from the relationship between PTR 100 resistance R and temperature ϑ °C given by[9]

$$R = R_0 \left(1 + \mathrm{A}_{90}\vartheta + \mathrm{B}_{90}\vartheta^2 + \mathrm{C}_{90}\vartheta^3 \left(\vartheta - 100\right)\right) \tag{2.2}$$

where the constants are

[9]See for example [Kay89].

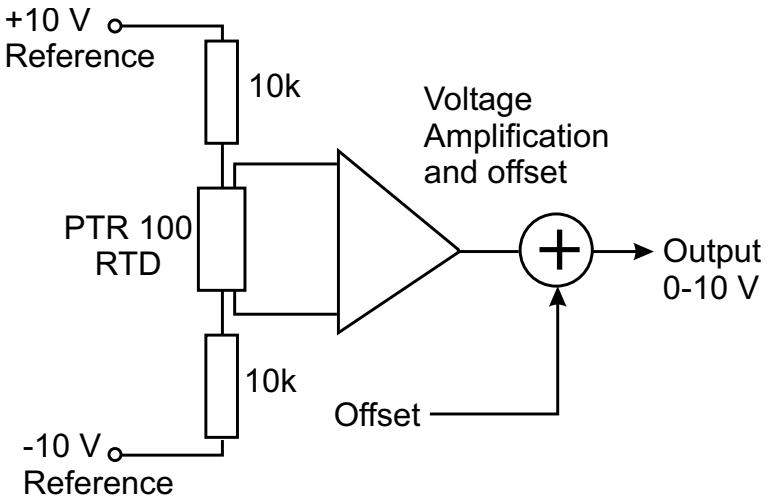

Figure 2.31: *Schematic representation of the thermometer read-out circuit. Note that the RTD resistance was measured using a four wire technique.*

$$R_0 = 100\ \Omega \qquad B_{90} = -5.775 \times 10^{-7}\ K^{-2}$$
$$A_{90} = 3.9083 \times 10^{-3}\ K^{-1} \qquad C_{90} = -4.183 \times 10^{-12}\ K^{-4}$$

The combined non-linearity varies quadratically with RTD temperature and is only small over a narrow range of temperatures.

The temperature dependence of the measurement circuit also needs to be considered. All fixed resistors in the circuit were precision resistors, (temperature coefficient 5 ppm.K^{-1} and tolerance $\pm 0.1\%$), chosen to minimise the variation in circuit gain and offset with ambient temperature. All variable resistors used for adjustment, which have a much larger temperature coefficient, were combined with fixed resistors to minimise the impact on overall circuit temperature dependence. The overall temperature dependence of the circuit was expected to correspond to a change of around 1 mV in output voltage per degree change in circuit temperature [How99].

Thermometer voltage temperature scale

Each read-out channel required individual gain and offset adjustments to optimise the mapping of the design temperature range to the design output voltage range. Once the gain and offset settings had been optimised, a linear temperature scale was defined for each channel using two calibration reference point resistors, in turn in place of an RTD, to define two fixed points on a linear voltage based temperature scale.

The calibration resistors (with a temperature coefficient of 3 ppm.K^{-1}) were measured under the same ambient conditions, within minutes of each other, using a four probe Keithley 200 multimeter to a precision of around 1 mΩ. The measured reference resistances and the corresponding fixed point temperatures are given in Table 2.4. The corresponding fixed point temperatures were taken from a linear fit to a small segment of the RTD temperature dependence of equation 2.2, with each segment $\approx$1.5°C wide, approximately centred on each reference resistance.

Table 2.4: Fixed points on the thermometer temperature scale. The errors are based on the precision of the resistor measurements.

Reference resistance	Corresponding fixed point temperature °C
106.605(1) Ω	16.942(4) °C
109.964(1) Ω	25.590(4) °C

Each channel was individually calibrated to the defined temperature scale by measuring the output voltage when each reference resistor was measured in place of an RTD. The non-linear contributions to the output voltage as a function of RTD temperature are shown in Fig. 2.32.

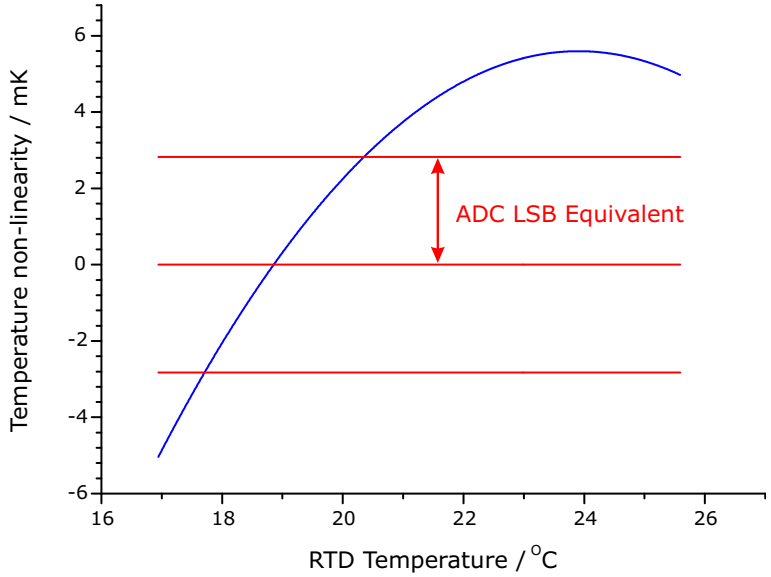

Figure 2.32: *Non-linear departure of thermometer measurement from defined linear scale based on two fixed point resistances.*

This model included non-linear effects due to :

- The non-linear PTR-100 resistance given by equation 2.2.
- The changes in RTD current in the circuit of Fig. 2.31.
- Changes in ambient circuit temperature which follow the RTD.

In this model the following assumptions were used :

- It was assumed that no current was drawn through the RTD by the rest of the circuit, so that the current through the RTD and each fixed 10k resistor was the same.
- The gain and offset were chosen so that output voltages at the fixed point temperatures were exactly 0.0 V and 10.0 V.
- To account for the fact that the circuit was in similar ambient conditions to the RTD, an extra 1 mK error was added for every 1°C increase from the midpoint temperature of 21.266°C.

The RTD power dissipation of around 0.1 mW was more or less constant as a function of RTD temperature and therefore adds a negligible contribution to the RTD non-linearity.

2.5.4 System Timing and data acquisition

A free running oscillator chip provided a master clock. The level 1 timing system, derived from the master clock and running at the same rate, controlled the timing for each data acquisition cycle. The level 1 (DAQ) clock rate was 500 Hz in all the experiments discussed in this thesis. A divided down copy of the master clock, referred to here as the level 2 timing system, governed the rate of the choppers and the long reference phase stepping.

The data acquisition was implemented by a software routine running in the central computer. The level 1 timing system synchronised the software routine using a VME backplane interrupt. This interrupt was fired by the master clock every DAQ cycle and answered in hardware by the crate controller. The driver software created a software version of each hardware interrupt signal and placed the software interrupt in a queue.

The data acquisition software acknowledged the software interrupt by calling a routine known as the interrupt handler. The interrupt handler controlled the timing of the read-out of the ADC and scaler channels, as described in full detail below.

The response time of the data acquisition software to the software interrupt, therefore had a critical effect on the synchronisation of the data acquisition. This was made more important, because of the storage of software interrupts in a queue. If the interrupts had been directly hardware driven, all interrupts would have been either answered on time or ignored, ensuring the correct phase relationship between the master clock and the data acquisition. In contrast, the software queue interrupts, if not answered immediately, were not ignored, but simply postponed. There was no control over the phase relationship between the master clock and these postponed interrupts. It was therefore of vital importance to avoid delays in interrupt handling.

The main data acquisition program was written in the LabVIEW programming environment from National Instruments. LabVIEW offers many prewritten driver software routines for handling interfacing with standard data acquisition systems such as VME. This is why it was used here. Programs written directly in the LabVIEW language, called G, are relatively slow, because the code is interpreted rather than compiled. For time critical applications, LabVIEW allows a compiled routine written in C to be embedded in the main program. These embedded C routines are known as CINs[10]. The interrupt handler in this data acquisition software was a CIN.

To ensure that the interrupt handler was called as soon as possible, all other potentially competing processes were removed. The central computer was running under the Microsoft windows NT 4 operating system and was part of a network for most of the time. Data acquisition was run under a local account rather than a network account so that the network could be physically disconnected during an experiment, without stalling the operation of the machine. This removed the interruptions from network traffic. The priority setting of the entire data acquisition software was set to the maximum of the four levels available under NT, so called Realtime mode, so that during VME interrupt handling, mouse and keyboards interrupts were ignored.

The physical RAM on board needed to be large enough to store the raw data during acquisition, without the need to use virtual memory on disk. Earlier experiments showed that a computer, with only 64 MB of RAM, suffered delays in responding to the software interrupts, every time a block of memory needed to be swapped between physical RAM and the local disk.

Only by taking the above precautions and running on a 450 MHz Pentium III computer with 128 MB of RAM was it possible to achieve stable, reliable software interrupt handling

[10]Code interface nodes.

at a DAQ rate of 500 Hz. Once the interrupt handler was initiated by an interrupt, it took priority over all other machine activity and ran at full speed to read out all six ADC channels and one scaler channel for that DAQ cycle.

The level 1 timing cycle, run by the master clock is shown in Fig. 2.33. As well as synchronising the DAQ software, this also controlled the gating of the scaler card.

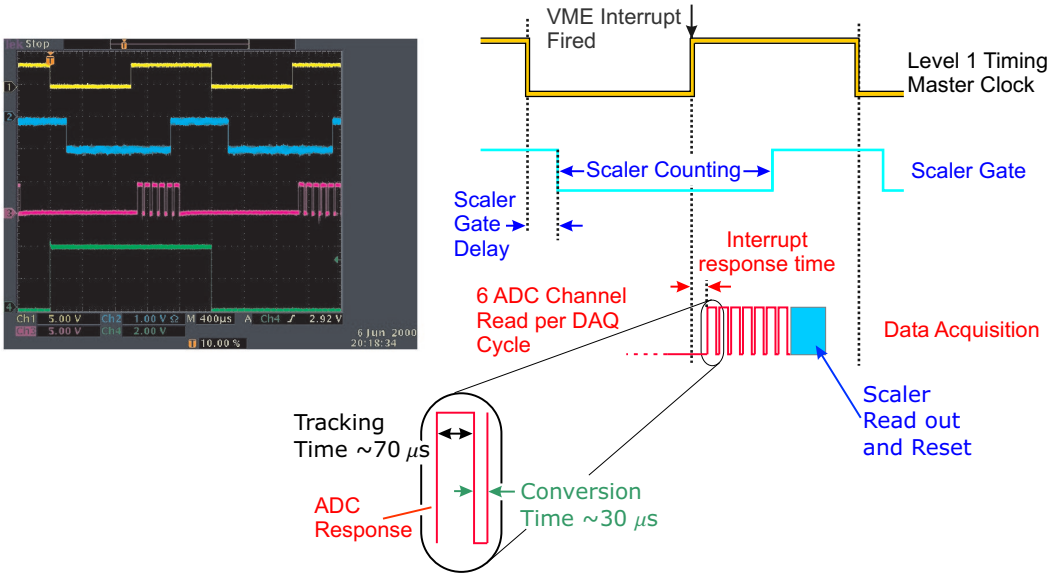

Figure 2.33: Level 1 timing cycle, a real timing trace (left) and a description based on matching colours (right). The green trace on the left, is the level 2 synchronisation signal discussed below, its only purpose here was for triggering the oscilloscope.

The scaler only counted photomultiplier pulses when the scaler gate was open. The scaler gate was driven by a copy of the master clock with variable delay and width control. The scaler gate was open, when the NIM gate voltage was switched to logical level ON, (which is more negative than the voltage representing logical OFF).

The delay to the scaler gate was set to minimise the risk of chopper crossover coinciding with the scaler gate. The width of the gate was opened for as long as was possible, whilst still ensuring it had closed before the scaler was read by the interrupt handler. The photon count was reset after every read, so it was important to ensure that counting had stopped before the scaler was read, to avoid generating leftover counts in the next reading.

The slow response of the ADC, (Burr Brown MPV 401) limited the number of ADC channels which could be read per DAQ cycle. The sixteen differential input channels of the card were fed through a multiplexer to a single convertor. The channel to be read was selected via software. For each channel to be read, the card required 70 μs to track the ADC channel voltage and 30 μs to convert as shown in the foreground in Fig. 2.33. The time taken for the interrupt handler to move from one ADC read to the next was negligible.

Fifteen of the sixteen ADC channels were used in these experiments, but only six time slots, of 100 μs each, were available per DAQ cycle, for reading the ADC. The allocation of ADC channels to the time slots was governed by an array in the DAQ software, called the Time Division Multiplexing, or TDM, table.

An example TDM table is shown in Table 2.5. This example matches the order in which the time slots were used, with the third and the sixth ADC time slots both multiplexed,

for etalon signals[11] and thermometers respectively. Only 3 thermometer channels are shown here, so that six DAQ cycles are required to return to the same read-out state and the example table is kept small. In practice all eight RTD channels and the partition channel from the laser tuning control box all used this sixth slot, leading to a TDM table 18×6.

Table 2.5: Example TDM table. The DAQ software cycled continuously round the TDM table.

KEY	
1	Power Monitor
2	Long Reference Interferometer
3	Short Reference Interferometer
4	10 GHz etalon
5	250 GHz etalon
6	Level 2 synchronisation signal
7	LR Air RTD
8	GLI Air RTD
9	GLI steel RTD

DAQ cycle $\longrightarrow$

Time Slots ↓						
	3	3	3	3	3	3
	1	1	1	1	1	1
	4	5	4	5	4	5
	6	6	6	6	6	6
	2	2	2	2	2	2
	7	8	9	7	8	9

The level 2 timing system was driven by a divided down copy of the master clock. The level 2 timing system was used to synchronise the choppers and the long reference interferometer phase stepping to the master clock. The level 2 timing cycle was intially set to match eight DAQ cycles, with the first four DAQ cycles used to acquire data for the four phase steps of laser 1 and the last four DAQ cycles used to acquire the data for the phase steps of laser 2. The chopper window was then extended to five DAQ cycles per laser, so that the chopper crossover could be contained within the fifth cycle after the phase steps had finished. The measurements made during the fifth cycle were recorded in the raw data but never used in the subsequent data analysis.

This five point level 2 timing scheme is shown in Fig. 2.34. Note that the timing of the phase steps depended upon the choice of ADC time slot for the long reference signal. The long reference interferometer signal was placed in the penultimate ADC slot, to give the mirror PZT just enough time to start moving for the first cycle in each ramp.

There was no control over the phase of the level 2 timing cycle with respect to the first DAQ cycle acquired in a scan, since the level 2 timing signals were produced by an autonomous PAL (Programmable Array Logic) unit taking the level 1 clock as a synchronising input.

A synchronisation signal, was generated by the level 2 timing system which was TTL high for the first DAQ cycle of each level 2 cycle. This was recorded using a dedicated ADC channel, allowing the phase of the level 2 timing cycle to be reconstructed, offline, after the raw data had been saved. This phase information, together with the TDM table, was used to decide which data belonged to which phase stepping cycle of which laser. Only interferometer data which could be attributed to one of the four phase stepping DAQ cycles was considered to belong to a laser.

The data was also partitioned into fine tuning subscans and coarse tuning blocks, using the PARTITION channel signal from the switch on the laser fine-tuning control box, described above in section 2.2.2.

The stored raw data, together with copies of those data points from each optical channel which had been identified with a particular laser, were held in a binary file format, specially

[11]The arrangement for the etalon channels given in this example was implemented, although ultimately the 250 GHz etalon signal was never used in the length measurements.

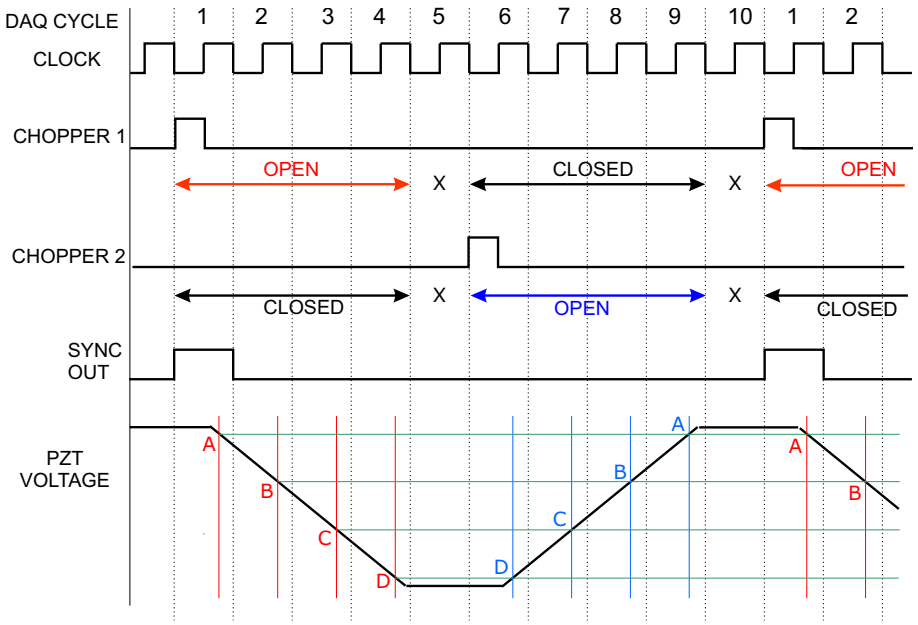

Figure 2.34: *The level 2 timing diagram. In this scheme a* 5^{th} *DAQ cycle has been allocated for chopper crossover (indicated by an X). The signals which synchronised the choppers were also used to synchronise the PZT driver, which began to sweep down (up) after the falling edge of the signal for chopper 1 (2). The approximate timing of the ADC readout slots for the long reference measurements are shown for the four phase steps, together with the corresponding PZT voltage levels, (labelled A to D) taken from Fig. 2.20 above.*

designed for ease of retrieval[12]. The interferometer data points clearly associated with each laser were then processed and analysed using the procedures discussed in chapter 3.

[12]This file format is discussed in Appendix D.

3. Data processing and analysis

3.1 Introduction

The data processing and analysis of interferometer signals using the procedures discussed in this chapter, were used to measure the reference and grid line interferometer phase[1] in each fine-tuning subscan. The phase information from different subscans was then linked to provide an interferometer phase ratio measurement, which was converted into a length ratio by applying corrections for the air refractivity, guided by air temperature measurements.

Some of the data preparation stages in the scheme presented here were not essential to the achievement of high precision length measurements, but were included as precautions during the evolution of these techniques.

The remainder of this section sets out labels and conventions which will be useful in the following discussion.

3.1.1 Interferometer Length convention

For convenience when presenting results of interferometer measurements, the *length* will be used as a label for the difference between the physical path lengths of the interferometer arms.

For the purposes of the measurements presented in this work, the length of the long reference interferometer was assumed to be a fixed value. This reference length was estimated to be 859.09 mm as discussed in chapter 2. An estimate for the length of any GLI D was based on a phase ratio estimate, q, (taken from whatever stage of the analysis), using

$$D/\mathrm{mm} = \frac{859.09}{q} \tag{3.1}$$

3.1.2 Phase notation

As introduced in chapter 1, the symbols Φ and ϕ will be used exclusively for the phase of the long reference interferometer and Θ and θ for the phase of a GLI.

For the discussion which follows it will be useful to re-write any general phase, for example a reference phase Φ, in terms of a folded phase, (represented using the lower case symbol), ϕ, and an integer order number m, such that :

$$\Phi = \phi + 2m\pi \tag{3.2}$$

where

$$-\pi \leq \phi < \pi \tag{3.3}$$

Note that ϕ is in general different from Φ modulo 2π.

The absolute value of interferometer phase cannot be determined without very accurate knowledge of the laser frequency and interferometer length. Instead the same phase value can be represented as a phase relative to an arbitrary datum phase cycle, which is given the relative order number zero. All order numbers discussed below will be relative order numbers, unless explicitly stated otherwise.

[1]When discussing GLI phase, the short reference interferometer will be counted as an honourary GLI, since it was measured like each GLI by comparison with the long reference interferometer length.

This relative phase is represented using the ordered pair notation of equation 3.2, which can be shortened to either of the following representations :

$$\phi + 2m\pi = \quad \Phi\,[m] \quad = \Big\langle \phi, m \Big\rangle$$

The shorter square bracket notation is used, when only the relative order number is of interest. The second form is a compact representation of the original equation, used in the discussion of linking.

Different datum cycles can be selected to provide different order number conventions. One and the same phase value can therefore be represented in the ordered pair notation of equation 3.2, using the respective relative order numbers, m, for one choice of datum and n for another. Hence

$$\begin{aligned} \Phi = \quad \Phi\,[m] \quad &= \Big\langle \phi, m \Big\rangle \\ = \quad \Phi\,[n] \quad &= \Big\langle \phi, n \Big\rangle \end{aligned}$$

For all choices of order number convention, the folded value ϕ is the same. A folded phase of zero corresponds to a maximum in the interferometer signal intensity fringe, because the interferometer signal as introduced in equation 1.6 is cosinusoidal.

The function which *folds* the phase Φ, so as to find ϕ, will be represented as $\mathbf{fold}\,(\Phi)$. Using the above examples

$$\phi = \quad \mathbf{fold}\,(\Phi\,[m]) \quad = \mathbf{fold}\,(\Phi\,[n])$$

A simple algorithm for folding the phase is given here.

Phase folding algorithm

For a general input phase $\Phi\,[m]$.

Initialisation : The input phase is passed to a dummy variable.

$$x_{\mathrm{OLD}} \quad = \quad \Phi\,[m]$$

Iteration : The dummy variable is iterated to bring it within the required range.

Set	$x = x_{\mathrm{OLD}}$	
If	$x \geq +\pi$	then $x_{\mathrm{OLD}} = x - 2\pi$
If	$x < -\pi$	then $x_{\mathrm{OLD}} = x + 2\pi$
If	$\lvert x_{\mathrm{OLD}} - x \rvert > \pi$	then repeatiteration
	Else	Stop iteration and go to conclusion

Conclusion : The folded phase is passed to the output.

$$\mathrm{Set} \quad \mathbf{fold}\,(\Phi\,[m]) = x_{\mathrm{OLD}}$$

Once the phase has been folded the order number m may be extracted using equation 3.4.

$$m = \frac{\Phi\,[m] - \mathbf{fold}\,(\Phi)}{2\pi} \tag{3.4}$$

This algorithm would be very slow for very large values of phase (around 10^4 or greater). An initial crude estimate for the order number m^* may be used, to speed up the folding process. In this case the input to the folding algorithm would be set to $\Phi[m] - 2\pi m^*$.

The above discussion on folded phase and relative order numbers applies equally well to general values of GLI phase, Θ, with the lower case symbol θ is used represent the folded phase.

3.2 Tracking the fine tuning of each laser

3.2.1 Phase stepping and extraction

The changes in laser frequency were monitored during a fine tuning subscan, by following changes in the phase of the long reference interferometer. This monitoring was needed, for two reasons. Firstly, because the tuning was non-linear and so the time dependence of the laser frequency, (referred to here as the tuning curve), was needed to map GLI data recorded in time, onto a laser frequency axis. Secondly, because the tuning curve was not reproducible from scan to scan.

The phase of each laser was extracted from the four data points recorded once per level 2 timing cycle using the phase stepping and extraction algorithms discussed below.

The shift in long reference interferometer phase $\Delta\Phi$, during a fine-tuning subscan, was used to follow the change in the laser frequency, based on rearranging equation 1.29, (with the assumption that the long reference interferometer length is fixed), to give

$$\Delta\nu_{\mathrm{SCAN}} = \left(\frac{c}{2\pi}\right)\left(\frac{\Delta\Phi_{\mathrm{SCAN}}}{\mathcal{L}}\right) \tag{3.5}$$

where it is assumed that the long reference interferometer optical path difference $\mathcal{L}$ was fixed during a scan.

In this section the practical technique of phase stepping and the corresponding algorithm for phase extraction are described.

The method of phase stepping is a widely used technique in interferometry for the extraction of the local phase value in an interferometer fringe pattern to modulo π or 2π [Cre88]. The method involves shifting the phase of the interferometer in discrete steps about a mean phase value and to measure the interferometer detector signal at each step. The mean phase value may be inferred from the detector signal measurements with a phase extraction algorithm, using information about the phase step size.

There are two types of phase extraction algorithm.

1. Those which use a particular size phase step.

2. Those based on the Carré formula.

Algorithms of the first type require phase steps of a particular size, (always a rational factor of π radians), for example $\frac{1}{2}\pi$. The extracted phase value produced by these alogrithms is very sensitive to small deviations in the phase step size away from the expected value [Che85]. Algorithms of the second type (first proposed by Carré [Car66]) have the advantage of smaller extraction errors over a much wider range of phase step sizes, provided the four steps used for each phase extraction are equal, (see chapter 6 for a discussion of phase extraction errors).

As discussed in section 2.3.4, phase stepping was implemented in the long reference interferometer by modulating the OPD using a PZT mounted mirror to induce displacement

phase shifts. The interferometer signal was measured once per level 1 timing cycle, with four successive signal measurements used to make one phase measurement. For this phase stepping method, the size of the phase step varies with optical frequency and therefore only Carré extraction algorithms are suitable.

Phase extraction : Original Carré formula

The Carré phase extraction formula is used to determine the mean phase of the detector signal measured at four phase values. The phase is stepped by α_S between each measurement, with the four phase values lying symmetrically about Φ_{MID}.

The interferometer signal, given by equation 1.6, may be re-written here as,

$$I_{DET} = I_{DC}\left[1 + \gamma\cos\left(\Phi\right)\right] \tag{3.6}$$

The detector signals I_1 to I_4 corresponding to the four phase steps are given by expanding equation 3.6 (to emphasise the stepping of the interferometer phase) in the form of equations 3.7a to 3.7d.

$$I_1 = I_0\left[1 + \gamma\cos\left(\Phi_{MID} - \frac{3}{2}\alpha_S\right)\right] \tag{3.7a}$$

$$I_2 = I_0\left[1 + \gamma\cos\left(\Phi_{MID} - \frac{1}{2}\alpha_S\right)\right] \tag{3.7b}$$

$$I_3 = I_0\left[1 + \gamma\cos\left(\Phi_{MID} + \frac{1}{2}\alpha_S\right)\right] \tag{3.7c}$$

$$I_4 = I_0\left[1 + \gamma\cos\left(\Phi_{MID} + \frac{3}{2}\alpha_S\right)\right] \tag{3.7d}$$

The Carré extracted phase Φ is given by

$$\Phi = \tan^{-1}\left[\frac{\sqrt{\left[3\left(I_2 - I_3\right) - \left(I_1 - I_4\right)\right]\left[\left(I_2 - I_3\right) + \left(I_1 - I_4\right)\right]}}{\left(I_2 + I_3\right) - \left(I_1 + I_4\right)}\right] \tag{3.8}$$

For some values of the interferometer phase Φ_{MID}, a correction must be applied to the extracted result Φ. The modification needed, depends on the value of the real phase and the size of the phase step α_S. For any given value of α_S, this correction is needed for half the possible range of values Φ_{MID}, due to the information loss created by taking the positive definition of the square root in the numerator.

Phase extraction : Modified Carré algorithm

A modified form of the Carré extraction algorithm was devised to avoid the need to modify the output extracted phase. This was achieved by avoiding a square root in the argument of the inverse tangent of the expression for extracted phase.

Provided the phase step lies in the range $0 < \alpha_S < \pi$, no modifications[2] are required, with the following algorithm and the phase estimate is given directly by the extracted phase Φ.

[2]If the phase steps size lies in the range $\pi \leq \alpha_S < 2\pi$, then the phase estimate is *always* given by $2\pi - \Phi$.

The first stage involves extraction of the phase step size α_S, by taking the difference between the inner symmetrical pair of equations 3.7b and 3.7c, and the outer symmetrical pair 3.7a and 3.7d. These differences give rise to equations 3.9 and 3.10 respectively.

$$I_2 - I_3 = 2I_0\gamma \sin\left(\frac{1}{2}\alpha_S\right) \sin\left(\Phi_{MID}\right) \tag{3.9}$$

$$\begin{aligned} I_1 - I_4 &= 2I_0\gamma \sin\left(\frac{3}{2}\alpha_S\right) \sin\left(\Phi_{MID}\right) \\ &= 2I_0\gamma \sin\left(\frac{1}{2}\alpha_S\right) \sin\left(\Phi_{MID}\right)\left(1 + 2\cos\alpha_S\right) \end{aligned} \tag{3.10}$$

Provided equation 3.9 is non-zero, the phase step size can be extracted using equation 3.11. This is an unambiguous determination, provided α_S lies in the range $0 < \alpha_S < \pi$.

$$\alpha_S = \cos^{-1}\left[\frac{1}{2}\left(\frac{I_1 - I_4}{I_2 - I_3} - 1\right)\right] \tag{3.11}$$

Whenever equation 3.9 is zero, the implied value of $\sin(\phi)$ is zero. In this case, α_S cannot be extracted. But because there are only two values of ϕ, which lead to this condition, Φ may be determined without determining α_S. To distinguish between the two solutions of $\phi = \sin^{-1}(0)$ the values of equations 3.7a and 3.7b may be compared, or alternatively those of equations 3.7c and 3.7d. In this algorithm both comparisons are made and cross-referenced so that if $I_2 > I_1$ and $I_3 > I_4$ then $\phi = 0$. If both inequalities are false then $\phi = \pi$. If they contradict, there has been an error in the measurement and the phase cannot be extracted. The extracted phase output Φ is set to zero and the point is labelled as a type I error, where type I represents an error during the extraction procedure. In the majority of cases, equation 3.9 is not zero and an estimate of the phase step size, α_S can be extracted.

The second stage of the algorithm uses α_S to determine the estimated phase value Φ. To this end, a useful symmetry can be highlighted by taking the difference between equations 3.7a and 3.7c to give equation 3.12 and comparing it with the difference between equations 3.7b and 3.7d, given as equation 3.13.

$$I_1 - I_3 = 2I_0\gamma \sin\left(\alpha_S\right) \sin\left(\Phi_{MID} - \frac{1}{2}\alpha_S\right) \tag{3.12}$$

$$I_2 - I_4 = 2I_0\gamma \sin\left(\alpha_S\right) \sin\left(\Phi_{MID} + \frac{1}{2}\alpha_S\right) \tag{3.13}$$

Taking the ratio of the sum and difference of these two equations leads to

$$\frac{(I_2 - I_4) + (I_1 - I_3)}{(I_2 - I_4) - (I_1 - I_3)} = \frac{\tan\left(\Phi_{MID}\right)}{\tan\left(\frac{1}{2}\alpha_S\right)} \tag{3.14}$$

which can be rearranged to extract Φ_{MID}.

So, as noted above, an inverse tangent is used in the modified Carré phase extraction algorithm, as it was in the original Carré algorithm. The extracted phase in the modified algorithm is given by

$$\Phi = \tan^{-1}\left[\frac{\tan\left(\frac{1}{2}\alpha_S\right)\left([I_2 - I_4] + [I_1 - I_3]\right)}{[I_2 - I_4] - [I_1 - I_3]}\right] \tag{3.15}$$

The inverse tangent in both forms of Carré algorithm may be calculated using the ATAN2(y,x) function which exists in FORTRAN, C and the LabVIEW programming language G. This function uses the signs of y and x and the result of $\tan^{-1}\left(\frac{y}{x}\right)$ to determine the phase value modulo 2π without phase ambiguity. Assuming the above restriction on the values of α_S holds, the value of $\tan\left(\frac{1}{2}\alpha_S\right)$ is always positive and the advantages of the ATAN2 function, lost to the original Carré algorithm, are now retained using the modified version.

The modified Carré algorithm is summarised in the flow diagram of Fig. 3.1. A short-cut step is shown between extraction of the phase step size α_S and the final extraction of Φ which has not yet been explained. This is a check to see if equations 3.12 and 3.13 were equal[3]. If they were equal, then the values of $\sin\left(\Phi_{MID} \pm \frac{1}{2}\alpha_S\right)$ were also equal, which implyies Φ_{MID} was either $\frac{1}{2}\pi$ or $\frac{3}{2}\pi$; so the phase does not need to be extracted using equation 3.15, but by choosing between the two possible values of Φ_{MID}. These are distinguished using the inequality between I_2 and I_3 as shown in the flow diagram Fig. 3.1.

The effects of the sliding interferometer phase

In the above description of phase stepping, it was assumed that the interferometer phase was constant during the detector signal measurement at each phase step. If either the OPD of the interferometer, or the optical frequency, changes linearly during an intensity measurement, the phase will shift. The effect on the phase extraction, of a phase shift with a constant rate of change can be accounted for by replacing equations 3.7a to 3.7d with 3.16a to 3.16d, where τ is the integration time of the detector system.

$$I_1 = \frac{1}{\tau}\int_{t_1-\frac{\tau}{2}}^{t_1+\frac{\tau}{2}} I_0\left[1+\gamma\cos\left(\Phi_{MID}+\dot{\Phi}\left(t-t_{MID}\right)-\frac{3}{2}\alpha_S\right)\right]dt \tag{3.16a}$$

$$I_2 = \frac{1}{\tau}\int_{t_2-\frac{\tau}{2}}^{t_2+\frac{\tau}{2}} I_0\left[1+\gamma\cos\left(\Phi_{MID}+\dot{\Phi}\left(t-t_{MID}\right)-\frac{1}{2}\alpha_S\right)\right]dt \tag{3.16b}$$

$$I_3 = \frac{1}{\tau}\int_{t_3-\frac{\tau}{2}}^{t_3+\frac{\tau}{2}} I_0\left[1+\gamma\cos\left(\Phi_{MID}+\dot{\Phi}\left(t-t_{MID}\right)+\frac{1}{2}\alpha_S\right)\right]dt \tag{3.16c}$$

$$I_4 = \frac{1}{\tau}\int_{t_4-\frac{\tau}{2}}^{t_4+\frac{\tau}{2}} I_0\left[1+\gamma\cos\left(\Phi_{MID}+\dot{\Phi}\left(t-t_{MID}\right)+\frac{3}{2}\alpha_S\right)\right]dt \tag{3.16d}$$

After the integrals are evaluated, these equations reduce to the following form

$$I_i = I_0\left[1+\gamma_{EFF}\cos\left(\Phi_{MID}+\delta_i\right)\right] \tag{3.17}$$

with an effective visibility γ_{EFF} given by

$$\gamma_{EFF} = \gamma\,\mathrm{sinc}\left(\frac{\tau}{2}\dot{\Phi}\right) \tag{3.18}$$

Assuming that times t_i are equally spaced such that, $t_{i+1}-t_i=\Delta t$ and centred about t_{MID}, the values of δ_i are given by

$$\delta_i = \left(i-\frac{5}{2}\right)\alpha_{EFF} \tag{3.19}$$

[3]Although ATAN2 checks for a zero in the denominator, this equality of equation 3.12 and equation 3.13 was used to speed up the LabVIEW code by circumventing unnecessary calls to ATAN2. The calculation of α_S was retained where possible.

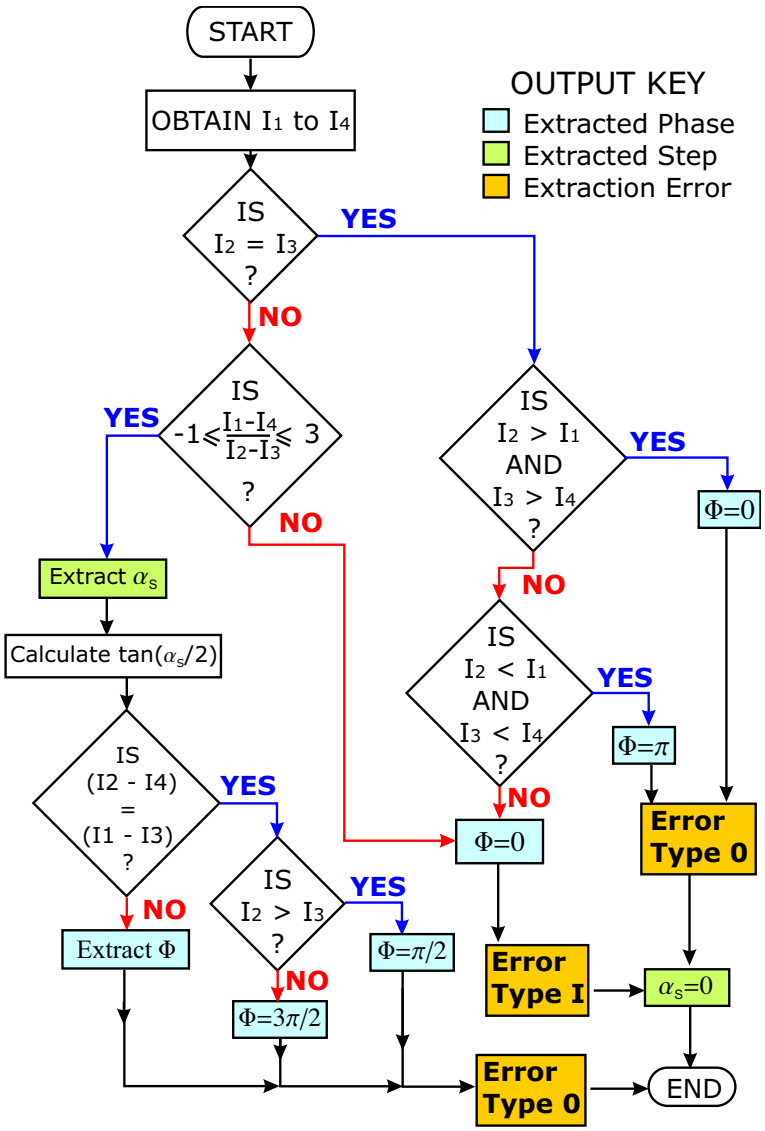

Figure 3.1: *Flow diagram of the modified Carré phase extraction algorithm. The phase step size α_S was extracted using equation 3.11 and the nominal phase value ϕ was extracted using equation 3.15.*

where the size of each phase step, is given by

$$\alpha_{EFF} = \alpha_S + \dot{\Phi}\Delta t \tag{3.20}$$

Therefore the measured detector signals for the four phase steps are of the same form as the original phase step equations 3.7a to 3.7d, and the extracted phase value is still that given by equation 3.15 and no errors are incurred as a result of the sweep in phase during the measurements. Indirectly, the changes in phase step size and visibility due to integration of the signal over a changing phase will lead to increased susceptibility to errors in phase extraction, discussed in chapter 6.

After the phase extraction had been carried out on the long reference interferometer signal from each laser for an entire subscan, the surviving extracted values, (those not already labelled as type I errors), were then folded, using the algorithm given above in section 3.1.2, in preparation for unwrapping.

3.2.2 Phase unwrapping

The unwrapping procedure started with the folded, extracted phases ϕ_i from an entire subscan. To unwrap the phases, an order number, called the unwrapping index u_i was added to each ϕ_i to create the unwrapped phase $\Phi_i[u_i]$. The unwrapping index started at zero and was incremented every time the folded phase went through a falling edge ($+\pi$ to $-\pi$) and decremented every time the folded phase went through a rising edge ($-\pi$ to $+\pi$).

The boundary between one cycle and the next was recognised by looking at the difference between neighbouring folded extracted phase values ϕ_i and ϕ_{i+1}. Whenever the difference between two points lay outside the range $-\pi$ to $+\pi$, a cycle boundary was assumed to have been crossed and the unwrapping index was altered accordingly. The unwrapping proceeded by induction, using the following algorithm :

$$
\begin{array}{lll}
 & & u_1 = 0 \\
\text{If} & (\phi_{i+1} - \phi_i) < -\pi & \text{then } u_{i+1} = u_i + 1 \\
\text{If} & (\phi_{i+1} - \phi_i) > +\pi & \text{then } u_{i+1} = u_i - 1 \\
 & \text{otherwise} & u_{i+1} = u_i
\end{array}
$$

If the boundary between one cycle and the next was not detected, because the difference between the values of ϕ_{i+1} and ϕ_i were closer together than π, (even though they belonged to different cycles), then all values of unwrapping index from u_{i+1} upwards were going to be labelled incorrectly. This created a large artificial discontinuity or *glitch* in the tuning curve, an example of which is shown in Fig. 3.2.

Once a glitch occurred in the tuning curve, the subsequent phase ratio determination of all measured interferometers was significantly affected, (see section 3.4.2, below). It was therefore essential to remove unwrapping glitches from the tuning curve. There were two principle causes of unwrapping glitches.

The most common cause was the presence of a falsely extracted value ϕ_i, on the boundary between two cycles, lying almost halfway in value between ϕ_{i-1} and ϕ_{i+1}. Although the difference between ϕ_{i+1} and ϕ_{i-1} was more than π, each point of the trio differs from the next by less than π and the boundary remained undetected. Sometimes there was more than one such false point in a cluster.

In principle the boundary detection algorithm could be extended so that the difference between pairs of points further apart were also checked but this solution is inefficient, since the number of permutations which need to be checked would have to grow disproportionately with respect to the number of avoided glitches. A more efficient solution was devised to identify the problematic false points close to cycle boundaries. This algorithm called the glitch finder is described below.

Despite several attempts, no entirely foolproof algorithm has been devised which can automatically exclude all glitches from the raw data, since every algorithm can be defeated by a large enough cluster of problematic points.

The other cause of unwrapping glitches was a cluster of absent phase values. This could occur in two cases; either due to phase extraction errors, (as shown in Fig. 3.2), or when a group of acquired data points were rejected after they could not be positively identified with the appropriate laser, (due to an error in the recorded level 2 synchronisation signal).

Potential glitches which were not dealt with at the unwrapping stage, had to be corrected by applying the appropriate change in order number to data points after the glitch. This correction was applied iteratively by hand until the tuning curve regained continuity. Around 0.6% of the subscans contained a glitch which needed removing in this way.

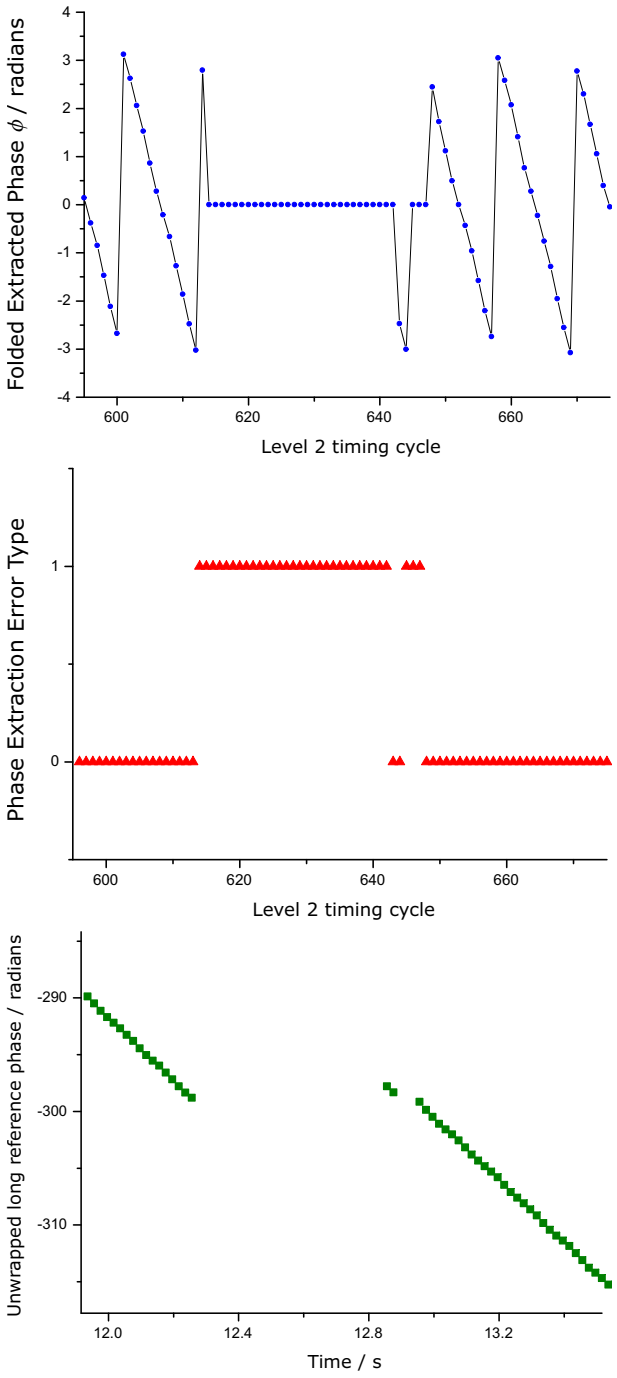

Figure 3.2: *The unwrapping glitch shown in the lowest graph, was caused by a cluster of phase extraction failures shown in the upper graph. These phase extraction cycles have been labelled as type I errors, as shown in the middle graph. N.B. Error type zero represents points which have been correctly unwrapped.*

3.2.3 Glitch finding

The extracted phase values were folded so that the boundaries between cycles occur at $\pm\pi$. To identify the problematic points (in the vicinity of cycle boundaries), the difference between the squared folded phase values was checked to see if it satisfied the following condition.

$$|\phi_i^2 - \phi_{i-1}^2| \;\leq\; \frac{1}{2}\pi^2$$

Any point ϕ_i failing this criterion was identified as a potential type II error. Caution was needed to circumvent potential failure modes. Particular care was taken to avoid premature removal of a potential type II candidate, because this it was not possible to guarantee knowing which point had caused the problem given a failure with the difference between the pair, $\left(\phi_{i-1}^2, \phi_i^2\right)$. If the problem point had survived because the *good* point of the pair was removed, the comparison with the nearest surviving neighbour would be likely to fail again, resulting in the same mislabelling and a similar rejection of the next *good* point. This failure mode could lead to the rejection of a large block of points all mislabelled type II errors, which would then guarantee the presence of the very glitch this algorithm was devised to remove.

To avoid this failure mode, a more elaborate algorithm was employed. The first step involved scanning the squared folded phase data from a single subscan over several iterations, to look for potential type II errors. When a potential type II error was identified, the search for the current iteration, was broken off at that point and resumed 10 data points away, (at $i_{\text{new}} = i_{\text{broken off}} + 10$, where the index i excludes points which had already been labelled either as type I errors - due to the phase extraction algorithm - or as potential type II errors by an earlier iteration). At the end of each iteration over the entire subscan, the list over which the index i runs was updated to account for the latest information. The iterations were halted when the total number of potential type II errors, within the subscan, settled to a constant.

The second step involved applying the same iterative search for potential type II errors, on a reverse order copy of the original array of ϕ_j^2. As for the first search, j only excluded points labelled as type I errors or as potential type II errors by earlier iterations of the reverse search. Once searches had been performed in both directions, only points identified as potential type II errors by both searches were finally confirmed as type II errors and ejected from the tuning curve data.

This more elaborate algorithm was designed to minimise the propagation of false positive identification of potential type II errors. If two genuine type II errors lay close enough to each other, this measure falsely rejected the points between the two genuine type II candidates, leaving a hole in the tuning curve which sometimes created a glitch, although such glitches were very rare.

On the rare occasions when glitches survived the glitch finder algorithm, they were corrected by hand, after unwrapping, by suitably adjusting the unwrapping order numbers of all points in the tuning curve after the glitch. Since it was impractical to manually check every tuning curve as it was generated, the surviving glitches were usually first noticed only after fitting a sinusoid to the GLI data. The effect of glitches on sinefitting are discussed below in section 3.4.2.

3.3 Subscan data preparation

3.3.1 Collection of X, Y and t data points

The set of unwrapped phases, which remained after type I and type II errors had been removed by the above algorithms, were used to generate the tuning curve for the subscan.

The unwrapped long reference phase values from the tuning curve, $\Phi[u_i]$ were used to form the frequency axis X_i for the sinusoidal fit to the GLI data, with

$$X_i = \Phi[u_i] \tag{3.21}$$

For each of the four long reference interferometer intensity measurements used to find the extracted phase for point X_i, there were four corresponding GLI intensity measurements, I_1^{GLI} to I_4^{GLI}. These were combined to produce a single data value of GLI signal intensity, Y, given by

$$Y = \sum_{j=1}^{4} I_j^{\mathrm{GLI}} \tag{3.22}$$

The value of Y corresponding to each X_i will be denoted Y_i. The first of the four level 1 timing cycles in which the data for X_i and Y_i were measured, was used to label the time of the phase measurement t_i. The subscan data for each GLI therefore consisted of a set of points with three co-ordinates (X_i,Y_i,t_i).

The frequency axis X_i plotted against time t_i will be named the *laser tuning curve*. Examples of the laser tuning curve are shown for both lasers in Fig. 3.3.

3.3.2 Cutting the tuning curve

The tuning curve of either laser was non-linear, most notably at the start where the relative rate of displacement phase shift due to thermal drift was greatest compared to the FSI phase shift, (as shown in Fig. 2.10). The first part of each subscan was cut, to minimise simultaneously the non-linearity of the tuning curve for both lasers and the relative size of the drift contribution. The size of the cuts used for each laser are given in Table 3.1.

Table 3.1: *Limits applied to unwrapped reference phase after cut applied to remove non-linearity at the start of the tuning curves.*

Tuning polarity	UP	DOWN
Laser 1	$X < -70$	$X > +70$
	1.94 GHz removed	
Laser 2	$X_i > +100$	$X_i < -100$
	2.78 GHz removed	

3.3.3 Time matching

After applying the above cuts to the two[4] tuning curves of each subscan, they were filtered in a process called time matching.

The times of surviving laser 1 subscan points (X_i, Y_i, t_i) were compared with the surviving laser 2 tuning curve points (X_j, Y_j, t_j). For each surviving laser 1 point t_i, the corresponding laser 2 point from the same level 2 timing cycle would have a time given by equation 3.23, where Δt was 4 or 5, depending on the number of level 1 timing cycles per chopper window, (see the discussion of timing in chapter 2.5.4).

[4]One tuning curve per laser.

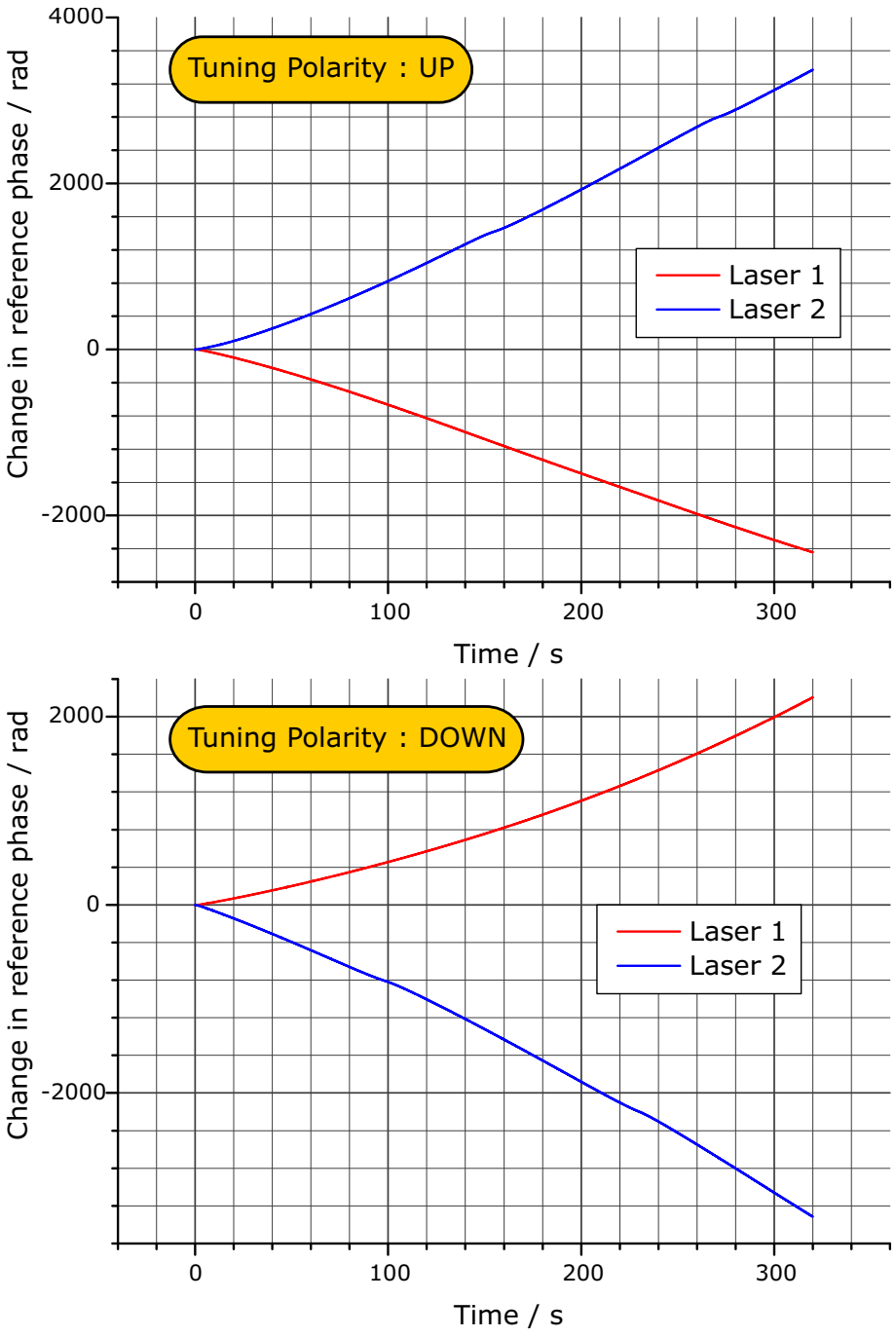

Figure 3.3: *The tuning curves of the FSI demonstration system lasers. These were obtained for the full tuning range of each lasers with a tuning clock rate of 200 Hz. This is a copy of Fig. 2.9, with relabelled vertical axes.*

$$t_j = t_i + \Delta t \tag{3.23}$$

Only those pairs of corresponding points which were recorded in the same level 2 timing cycle, were allowed to pass the time matching process. All the rest were excluded. These remaining time matched points were then used in the sinefitting process described in the next section. This ensured that the data used in the drift cancellation came from quasi-simultaneous measurements, following as closely as possible the same interferometer drift

conditions.

3.4 Sinefitting to measure the phase change in a GLI

The phase change in a GLI[5] was measured for each laser in each subscan. The measurement was made by fitting interferometer intensity Y_i to a sinusoidal function I_i, of the frequency axis X_i.

$$I_i\left(I_{\mathrm{DC}}, I_{\mathrm{AC}}, q, \alpha\right) = I_{\mathrm{DC}} + I_{\mathrm{AC}} \cos\left(\frac{X_i}{q} + \alpha\right) \tag{3.24}$$

The four fit parameters represent :

- I_{DC} The offset interferometer signal of the sinusoidal fringe pattern
- I_{AC} The amplitude of the sinusoidal fringe pattern
- q The phase ratio as introduced in equation 1.34c
- α A general phase offset

The minimisation package, MINUIT, was used to find the best fit parameters (I_{DC}, I_{AC}, q and α) from equation 3.24, for the data of each GLI, using a fit quality parameter which will be labelled χ^2, defined as

$$\chi^2 = \sum_i \left(\frac{\left[I_i\left(I_{\mathrm{DC}}, I_{\mathrm{AC}}, q, \alpha\right) - Y_i\right]}{\sigma_i}\right)^2 \tag{3.25}$$

The weighting factor, σ_i used in the denominator was taken from the standard deviation expected of Poisson statistical shot noise in the photon counting process [Lou95], in the case where dark counts are negligible, given by

$$\sigma_i = \sqrt{Y_i} \tag{3.26}$$

Even though the short reference interferometer signals were not recorded by a photomultiplier, the short reference data was also fitted using weighting factor given by equation 3.26.

It was found that, whenever this weighting factor was set instead to a constant value, (to investigate the importance of the value of σ_i), in fitting data from either the short reference or the grid line interferometer this gave rise to a negligible change in fitted phase ratio value for good quality interferometer data[6].

Examples of the sinusoidal fit to data from the short reference and GLI are given in Fig. 3.4 and Fig. 3.5 respectively.

3.4.1 Fitting strategy

The initial values of the fit parameters were carefully seeded, to avoid local minima in the χ^2 function that were close to the deepest minimum. Without these precautions the fitting software package MINUIT was prone to settle in the wrong local minimum, with the wrong fit parameters.

[5] As stated above, the short reference interferometer will be treated as if it were a GLI.

[6] The effect of this choice of weight for data degraded by interferometer vibration is discussed further in chapter 5.

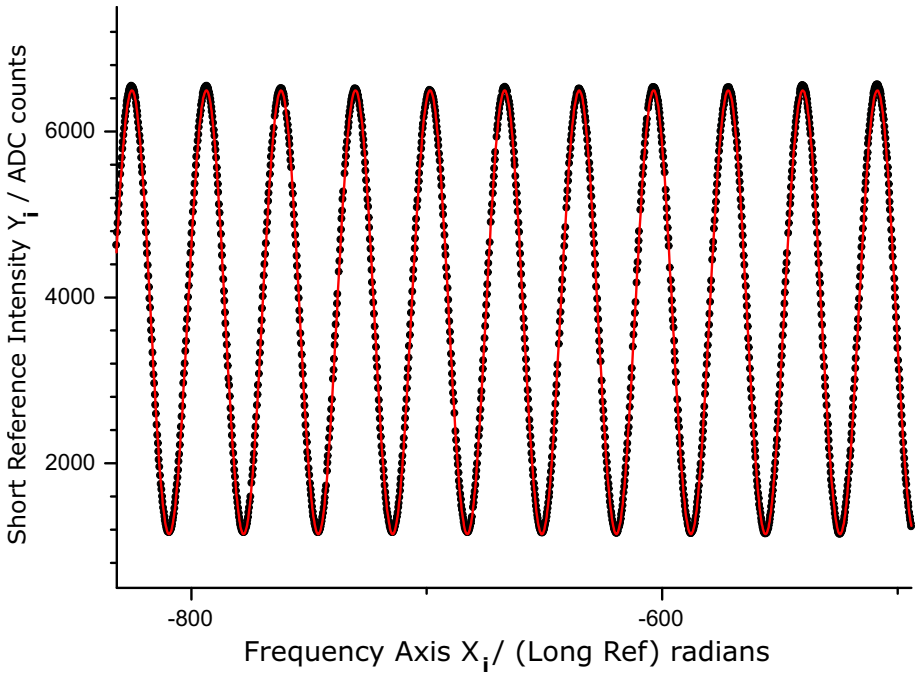

Figure 3.4: *Comparison between the short reference interferometer signal and the sinusoidal fit.*

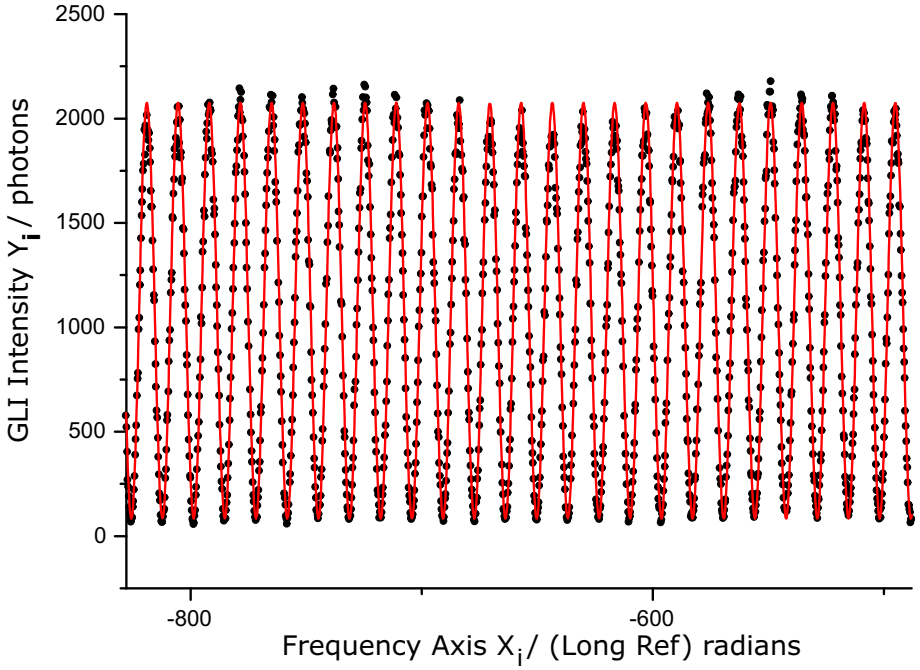

Figure 3.5: *Comparison between GLI signal and the sinusoidal fit.*

The seed values of I_{DC} and I_{AC} were taken from the mean and RMS values of the GLI intensity data I_i as in equations 3.27 and 3.28.

$$I_{\mathrm{DC}}^{\mathrm{SEED}} = \frac{1}{N}\sum_{i}^{N} I_i = \bar{I} \tag{3.27}$$

$$I_{\mathrm{AC}}^{\mathrm{SEED}} = \sqrt{\frac{1}{N}\sum_{i}^{N} I_i^2 - [I_{DC}]^2} = \sigma_I \tag{3.28}$$

The phase ratio was seeded to within a few percent of the true value, using the best estimate from ruler based measurements, or earlier FSI results. The phase offset α was always intialised at zero.

Before the full four parameter χ^2 fit was attempted, a two parameter minimisation was performed in χ^2 as a function of the phase ratio q and phase offset α, with I_{DC} and I_{AC} frozen at the seed values. This adjusted the phase offset parameter α allowing it to settle to a value compatible with the phase ratio and settled the phase ratio into the one of the local minima. A typical profile of χ^2 against phase ratio is shown in Fig. 3.6. The true minimum, was always flanked by smaller local minima, into which MINUIT occasionally settled during the intial two-parameter fit. The shape of this χ^2 profile is discussed in chapter 6.

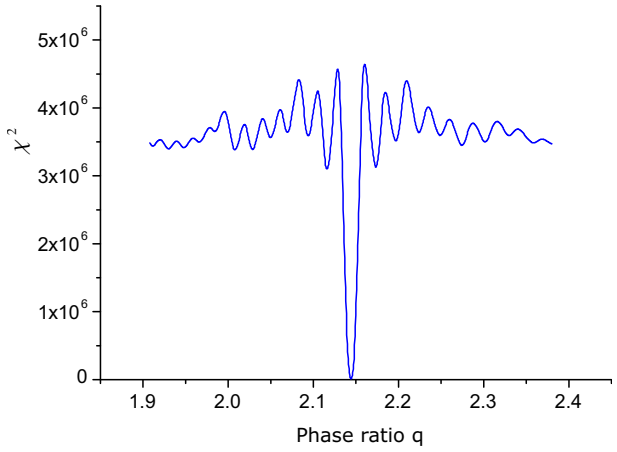

Figure 3.6: *Variation in χ^2 with phase ratio for a typical sinusoidal fit to GLI signal from a single subscan. The initial two parameter minimisation was prone to falling into the wrong local minimum.*

After this intial two parameter fit, the frozen fit parameters were released ready for the full four parameter fit.

To ensure that the final four parameter fit started in the deepest minima (with respect to phase ratio q), χ^2 was measured along a one-dimensional scan across a range of phase ratio values centred on the initial estimate. This was implemented using the internal SCAN function of MINUIT, which samples the χ^2 at up to 100 points, (90 were used). The range of the scan was set to $q^{\mathrm{SEED}} \pm w$, were the width w was a particular percentage of q^{SEED}.

On a few occasions, the value of w which had been used, needed to be changed to assist the MINUIT search in finding the deepest local minimum. No value of w was found which survived every subscan. The difficulties arose, because of the limited resolution of the SCAN function. A scan window of between $\pm 5\%$ and $\pm 10\%$ of q^{SEED}, was suitable for almost all subscans. The limited sampling granularity is a reliability issue to be addressed in future work, where the scan function could be implemented outside MINUIT with a greater number of sampling points.

After this sampling of χ^2, the fit parameters at the start of the full four parameter fit were $I_{\mathrm{DC}}^{\mathrm{SEED}}$ and $I_{\mathrm{AC}}^{\mathrm{SEED}}$, the settled value of α from the two parameter fit and the phase ratio q which gave the lowest χ^2 of those values sampled in the scan, or the outcome of the initial two parameter fit, whichever gave the lower value of χ^2.

The phase ratio and phase offset values after the final four parameter fit, were used in the subsequent stages of the data analysis.

3.4.2 Effect of unwrapping glitches

Any glitches which entered the frequency axis, showed up clearly in a plot of the intensity signal of an interferometer against the unwrapped reference phase (frequency). The glitch shows as a discontinuity in the phase of the GLI fringe pattern, which stands out, even on the scale of the entire subscan as in Fig. 3.7.

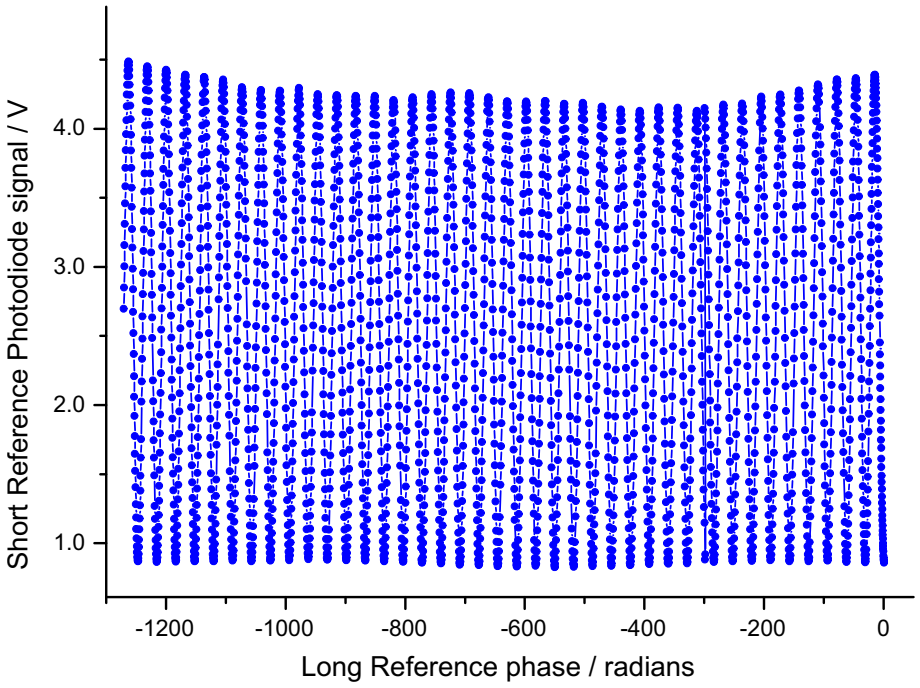

Figure 3.7: *A visible glitch, stands out in the signal from any interferometer plotted against unwrapped reference phase. (The entire subscan is shown here.) This is the glitch shown in Fig. 3.2 at around -300 radians.*

It was not efficient to inspect every subscan prior to fitting. Where a fit was attempted on data containing an unwrapping glitch, this showed itself by an anomalously high χ^2 value for the corresponding short reference and GLI fits. This was most noticeable for the short reference interferometer because the shift in χ^2 per degree of freedom of the best fit was larger on the scale of typical variations, than the corresponding change in the GLI χ^2. This χ^2 test formed the ultimate stage in glitch detection.

The difference in χ^2 as a function of the short reference phase ratio q with and without a glitch is shown in Fig. 3.8. Once the glitch was removed, there were three notable changes in the χ^2.

- The χ^2 plateau across most values of phase ratio increases.
- The profile in the vicinity of the deepest well switches from odd to even symmetry.
- The deepest minima deepens and shifts due to the change in symmetry.

These three may be useful in future work to automate glitch detection, particularly the lack of even symmetry about the global minimum.

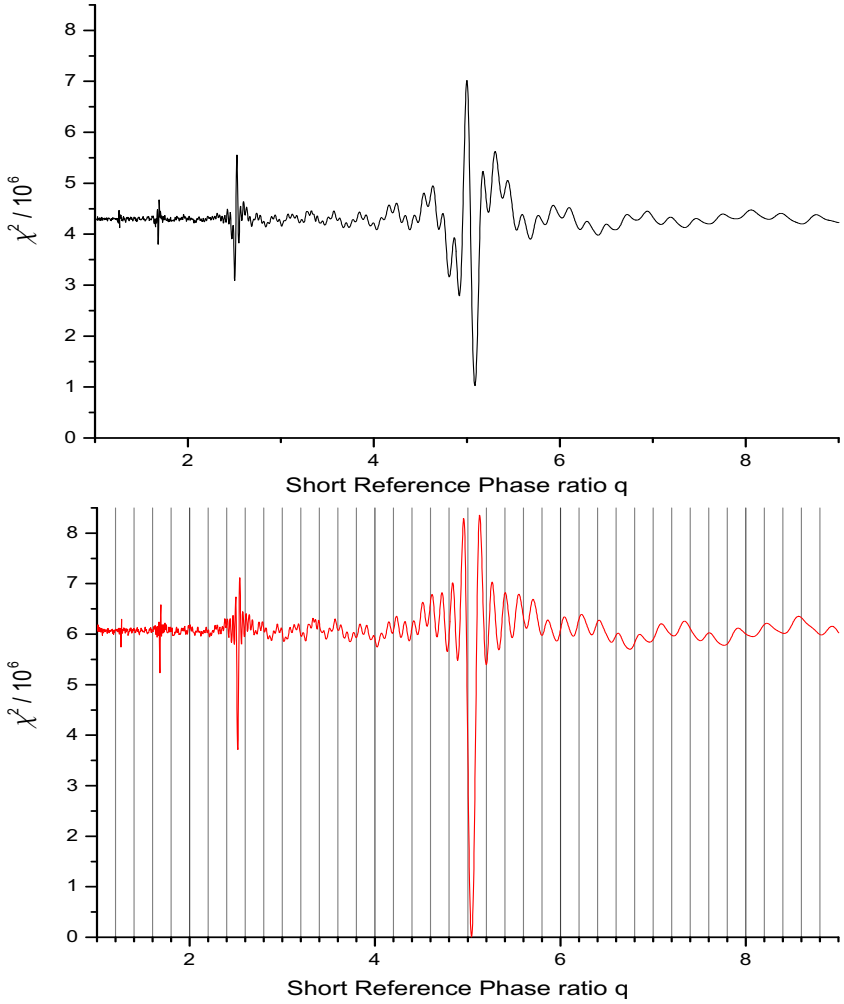

Figure 3.8: *Profile of χ^2 against short reference interferometer phase ratio before and after a glitch is removed. The structure around the phase ratio at the deepest minimum is shown here repeating at one half, one third and one quarter of that phase ratio.*

3.5 Dual-laser correction of intra-subscan drift error

The best fit phase ratios q_1 and q_2 from sine fitting the GLI data for laser 1 and laser 2 respectively, were combined using equation 1.40, to give a GLI length measurement with reduced intra-subscan drift error.

Implementation of this drift correction requires the results of the best fit single laser single subscan phase ratio estimates and the proportional frequency scanning ratio ρ. Expanding equation 1.41, gives equation 3.29, where ν_1 is the subscan average frequency of laser 1 and ν_2, likewise for laser 2.

$$\rho = \left(\frac{\nu_2}{\nu_1}\right)\left(\frac{\Delta\nu_1}{\Delta\nu_2}\right) \tag{3.29}$$

The subscan frequency interval of each laser was calculated from the difference between the start and end frequency axis points (X_1 and X_P respectively[7]), using equation 3.30 with $\mathcal{L}$ set to 1.71818 m. This is twice the long reference *length* 859.09 mm given above in section 3.1.1, ignoring a factor for the refractive index of air which cancels out as common in the calculation of ρ.

$$\Delta\nu = \left(\frac{c}{2\pi}\right)\frac{(X_P - X_1)}{\mathcal{L}} \tag{3.30}$$

The wavemeter was used to measure the vacuum wavelength of each laser, prior to the first scan in a group of measurements. The best estimate of the average frequency, was taken from the midpoint using

$$\nu_{\mathrm{MID}} = \left(\frac{c}{\lambda_{\mathrm{VAC}}}\right) - \delta\nu + \left(\frac{\Delta\nu}{2}\right) \tag{3.31}$$

where λ_{VAC} was the vacuum wavelength reading from the wavemeter.

In each subscan the transmission peaks of the 10 GHz etalon were fitted to functions of the laser frequency X_i (as described in Appendix C). The laser frequency at the centre of the first peak in the first subscan was used to track the gradual shift of the laser start frequency from one scan to the next. The correction $\delta\nu$ for the drift of the laser start frequency in scan S, (compared to the laser start frequency in the first scan), is defined in equation 3.32 where $X_{\mathrm{S}}^{\mathrm{ET}}$ is the long reference phase at centre of the first etalon peak of scan S.

$$\delta\nu = \left(\frac{c}{2\pi}\right)\left(\frac{X_{\mathrm{S}}^{\mathrm{ET}} - X_1^{\mathrm{ET}}}{\mathcal{L}}\right) \tag{3.32}$$

The errors in drift cancellation resulting from inaccuracies in the determination of laser frequency are discussed in more detail in chapter 6.

3.6 Linking subscans

3.6.1 Overview of subscan linking

The linking procedure is used to the connect the interferometer phase from two independent fine-tuning subscans. The linking of subscans was the key technique required to drastically improve the reproducibility of phase ratio measurements as introduced in section 1.2.4.

[7]Where P is the number of data points in the subscan for each laser.

The following discussion will be based around linking the first two fine-tuning subscans A and B. In the situation where many subscans were recorded, then the first two subscans would be labelled A and B and linked first using the method below. Once this first set of linking calculations had been finished, the improved estimates of interferometer phase ratio could be used to link the first to the third so on. Each iteration would be expected to improve the phase ratio estimate and allow linking over a greater range. This improvement would be achieved not just in the GLI to long reference interferometer ratio, needed for linking the GLI phase, but also in the etalon to long reference interferometer ratio needed for linking the long reference phase.

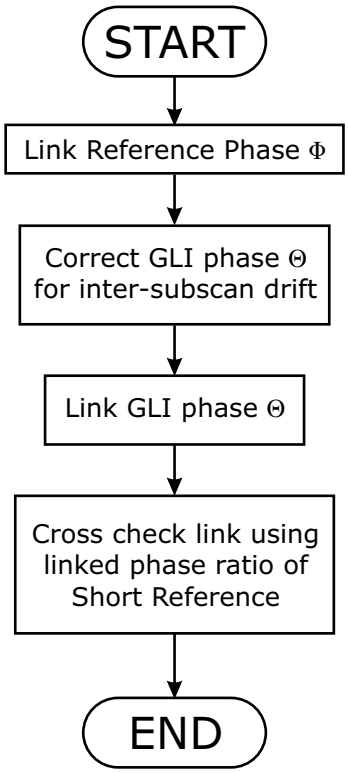

Figure 3.9: *The four stages of linking a pair of subscans. These are discussed in detail in the sections below.*

At the highest level, the linking of two subscans can be divided into 4 key steps. These are shown in the flow diagram of Fig. 3.9.

To link interferometer phase, a prediction of the phase at an anchor point in subscan B, is made by extrapolating from an equivalent anchor point in subscan A. The local measurement of the phase of the anchor point in subscan B provides a correction to the extrapolation. This correction is only valid if the prediction lies within $\pm\pi$ radians of the true phase. This linking correction is illustrated in Fig. 1.10.

Any point within either subscan may be used as the anchor: The reference interferometer phase anchors were set on the centres of etalon peaks. The GLI phase anchors were set at the middle of each subscan. The motivation for the choice of subscan midpoints for GLI phase linking comes from the expectation that the best sine fit to a subscan, will on average have minimised phase error in the middle of the subscan[8].

The phase ratio estimate obtained from linking subscans A and B, q_{AB}, is therefore given by

[8]The errors which arise in sine fitting are discussed in more detail in chapter 6.

$$q_{AB}^{\text{LINK}} = \frac{\Phi_{\text{MID(B)}} - \Phi_{\text{MID(A)}}}{\Theta_{\text{MID(B)}} - \Theta_{\text{MID(A)}}} = \frac{\Delta\Phi_{\text{AB}}}{\Delta\Theta_{\text{AB}}} \tag{3.33}$$

The method for determining the phase shift between the midpoints of each subscan for the long reference and grid line interferometers, ($\Delta\Phi_{\text{AB}}$ and $\Delta\Theta_{\text{AB}}$ respectively), is the subject of the following discussion.

3.6.2 Linking the reference interferometer phase

Since the phase of the long reference interferometer could not be tracked during the coarse tuning interval[9], the frequency span of the bridge needed to be reconstructed. This was found to be most reliably achieved by combining information from the slowly repeating etalon signal and the rapidly repeating long reference signal. In principle, any signal which varied periodically with laser frequency could have been used. The advantages of the etalon were :

1. The transmission peaks, which were :
   (a) Distinct, unambiguous with a reproducible shape.
   (b) Readily located against the background signal using an automated algorithm.
   (c) Easily fitted to a function of long reference phase to identify their centre (see Appendix C).
2. The low thermal coefficient of expansion, (relative to the long reference interferometer), which allowed the reference phase to be linked to the correct order number.
3. The well balanced value of FSR of the etalon, which was
   (a) Neither too large, so that several peaks could be guaranteed per subscan.
   (b) Nor too small, so that the number of etalon peaks between subscans became too large to be unambiguously determined.

An etalon peak was chosen from subscan A to be a datum peak, labelled peak 0. The unwrapped long reference phase at the centre of this peak was labelled $\Phi_a[m_a]$ using the order number convention of subscan A, in which m is defined to be zero for the first cycle of the subscan.

Similarly the unwrapped long reference phase $\Phi_b[n_b]$ at the centre of peak N in subscan B can be defined using the unwrapping order convention of subscan B, which places the zeroth order at the beginning of subscan B. The centre phase of this peak can be also be represented as $\Phi_b[m_b]$ using the unwrapping order number convention of subscan A.

For any anchor point Φ_b, (etalon peak centre or otherwise), in subscan B, the relationship between m_b and n_b, can be represented by equation 3.34.

$$m_b(n_b) = n_b + \psi_{ab} \;\forall\; \Phi_b \tag{3.34}$$

The value of ψ_{ab} is the same for all choices of Φ_b since the long reference interferometer is assumed to be stable[10], therefore linking the long reference phase is equivalent to finding the value of ψ_{ab}. This is illustrated in Fig. 3.10.

[9] When coarse tuning, the long reference phase shifted by 470° due to frequency scanning, during the time it took to make a 110° phase step using the PZT mounted mirror.

[10] At least for the purposes of phase ratio determination.

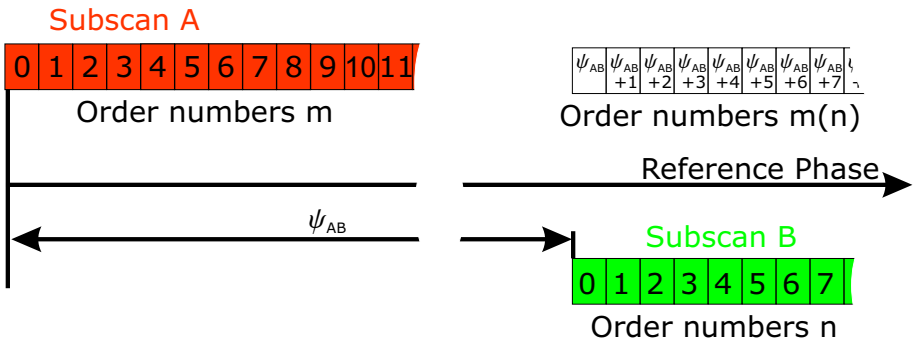

Figure 3.10: *The order numbers used to locally label subscans A and B are connected by linking the reference phase, according to equation 3.34.*

A prediction, Φ_c, for the location of peak N is based on an extrapolation from peak 0 using

$$\begin{aligned} \Phi_c &= \Phi_a + \Delta\Phi(N) \\ &= \left\langle \phi_c, m_c \right\rangle \end{aligned} \tag{3.35}$$

where the estimated long reference interferometer phase bridge is given by

$$\Delta\Phi(N) = 2\pi N q^{\mathrm{ET}} \tag{3.36}$$

where q_{ET} is the phase ratio of the etalon.

The extrapolation, depends not only on the best estimate of $\Delta\Phi_N$, but also on N, the etalon peak count. A procedure used to cross check that the correct value of N had been used is discussed below in section 3.6.4. The effect of peak miscount errors is also discussed in more detail in chapter 6.

To successfully link the long reference phase, the difference between the predicted peak location Φ_c and true peak location Φ_b, must be within $\pm\pi$. This is represented by

$$\Phi_b - \Phi_c = (\phi_b - \phi_c) + 2\pi(n_b + \psi_{ab} - m_c) \tag{3.37a}$$

$$= \Phi_{\mathrm{GAP}} + 2\pi(n_b + \psi_{ab} - m_c) \tag{3.37b}$$

$$= \left\langle \phi_{bc}, 0 \right\rangle \tag{3.37c}$$

The difference Φ_{GAP}, can be re-written as

$$\begin{aligned} \Phi_{\mathrm{GAP}} &= \mathbf{fold}(\Phi_b) - \mathbf{fold}(\Phi_c) \\ &= \phi_b - \phi_c \\ &= \left\langle \phi_{bc}, g \right\rangle \end{aligned} \tag{3.38}$$

Given the restricted range of the folded phase, (given above in equation 3.2) g must lie in the range $-1 \leq g \leq 1$.

By substituting from equation 3.38 into equation 3.37a can be rewritten as

$$\Phi_b - \Phi_c = \left\langle \phi_{bc}, (g + n_b + \psi_{ab} - m_c) \right\rangle \tag{3.39}$$

Equating the order number terms in equation 3.37c and equation 3.39, and making ψ_{ab} the subject, leads to

$$\psi_{ab} = m_c - g - n_b \tag{3.40}$$

Once ψ_{ab} has been found, the long reference phase of any point in subscan B may be expressed in the order number convention of subscan A.

The midpoint long reference interferometer phase for each subscan was calculated from the average mean of the first and last points in the corresponding frequency axis, (X_1 and X_P respectively), using

$$\Phi_{\mathrm{MID}} = \frac{X_P - X_1}{2} \tag{3.41}$$

The laser 1 reference phase shift $\Delta\Phi_{\mathrm{AB}}$ between the midpoint of each subscan is given by

$$\Delta\Phi_{\mathrm{AB}} = \left\langle \phi_{\mathrm{MID(B)}}, \left(n_{\mathrm{MID(B)}} + \psi_{ab}\right) \right\rangle - \left\langle \phi_{\mathrm{MID(A)}}, m_{\mathrm{MID(A)}} \right\rangle \tag{3.42}$$

3.6.3 Linking the GLI phase

To link the GLI phase, there must be at least one point in each subscan for which the phase of the GLI phase is known. For any point the GLI phase Θ may be estimated from the corresponding reference phase Φ using the phase term from the best fit sine function of equation 3.24. The GLI phase term is related to the best fit parameters q and α to the GLI data from the corresponding subscan and laser by

$$\Theta = \frac{\Phi}{q} + \alpha \tag{3.43}$$

The GLI phase at the midpoints of the two subscans will be represented by Θ_A and Θ_B. These were obtained by substituting the midpoint values of long reference phase, (Φ_A^{MID} and Φ_B^{MID} respectively), into equation 3.41 to give

$$\Theta_{\mathrm{A}} = \frac{\Phi_{\mathrm{MID(A)}}}{q_{\mathrm{A}}} + \alpha_{\mathrm{A}} \tag{3.44a}$$

$$\Theta_{\mathrm{B}} = \frac{\Phi_{\mathrm{MID(B)}}}{q_{\mathrm{B}}} + \alpha_{\mathrm{B}} \tag{3.44b}$$

Correcting for Inter-subscan drift

So far in the linking description, the phase of the interferometer signals due to laser 1 have been considered, since this was the laser which was coarse tuned during the bridge, thereby providing the large frequency scan needed for high resolution phase ratio measurement.

Before linking the GLI phase for laser 1, the GLI phase Θ_B needed a correction to restore it to $\Theta_{\tilde{B}}$ which is what the phase would have been, if the GLI OPD had not drifted during the time taken to tune laser 1 from one anchor point to the other. The best estimate for this displacement phase shift, $\Delta\Theta^{\mathrm{DISP}}$ was used to correct the GLI phase to give

$$\Theta_{\tilde{B}} = \Theta_B - \Delta\Theta^{\mathrm{DISP}} \tag{3.45}$$

The estimate of the GLI displacement phase shift was obtained by linking the long reference phase and GLI phase of laser 2. The long reference phase linking proceeded as for

laser 1, using the procedure given above in section 3.6.2, except that the number of etalon peaks was easily counted in the raw data, since laser 2 was never coarse tuned. The linking of the GLI phase for laser 2 was used to the measure the total laser 2 GLI phase shift $\Delta\Theta_2^{\mathrm{TOTAL}}$. The estimated GLI displacement phase shift for laser 2 is given by

$$\Delta\Theta_2^{\mathrm{DISP}} = \Delta\Theta_2^{\mathrm{TOTAL}} - \Delta\Theta_2^{\mathrm{TUN}} \tag{3.46}$$

where $\Delta\Theta_2^{\mathrm{TUN}}$ is the laser tuning phase shift for laser 2.

The contribution due to tuning laser 2 needed to be subtracted, to obtain the estimated displacement phase shift. This GLI tuning phase shift was estimated using equation 3.48 from the corresponding laser 2 long reference interferometer phase shift $\Delta\Phi_{\mathrm{AB2}}$, given by equation 3.42 and the best estimate of the GLI phase ratio q_0^{AV} given below in equation 3.50, from the average mean of the single subscan combined laser phase ratio estimates. This estimation is subject to error, due to inaccuracies in q_0^{AV}. The effect of this inaccuracy could be minimised in a future system by tuning laser 2 repeatedly over the same fine-tuning range from one subscan to the next, so that $\Delta\Phi_{\mathrm{AB2}}$ is close to zero.

$$\Delta\Theta_2^{\mathrm{TUN}} = \frac{\Delta\Phi_{\mathrm{AB2}}}{q_0^{\mathrm{AV}}} \tag{3.47}$$

This could then have been used to estimate the equivalent GLI displacement phase shift at the wavelength of laser 1, using

$$\Delta\Theta^{\mathrm{DISP}} = \Delta\Theta_2^{\mathrm{DISP}} \left(\frac{\nu_1}{\nu_2}\right) \tag{3.48}$$

where ν_k is the frequency of the k^{th} laser at the centre of its bridge, when linking subscans A and B. In practice this correction was not implemented for the results presented in chapters 5, because the difference between the laser wavelengths at the centres of the respective linking bridges, was around 836.1 ± 0.1 nm and difficult to determine to better accuracy than this, due to the potential for offsets in the wavemeter readings, taken at the start of the first scan in a group of measurements, upon which any estimate of ν_k would have been based. Therefore the best estimate for $\frac{\nu_1}{\nu_2}$ was unity for those scans where the coarse tuning interval covered wavelengths either 832.1 nm to 840.0 nm (for tuning polarity *UP*) or 839.9 nm to 832.0 nm (for tuning polarity *DOWN*). The incurred error from this assumption is shown to be small in the linking results taken with alternating tuning polarity, presented in chapter 5.

The limitations of this inter-subscan drift correction technique are discussed in chapter 6.

The final stages of GLI phase linking

The final stages of GLI phase linking are analogous to the linking of the long reference phase described above. To emphasise the analogy, the same symbols which were used in lower case for long reference linking are now used (where appropriate), in upper case for GLI linking.

From the GLI phase at the midpoint of subscan A, a prediction Θ_C was made for the GLI phase at the midpoint of subscan B using the best available estimate of the phase ratio as in equation 3.49. The relative order number convention M is set by the choice of fit parameter α returned from the sine fit to the GLI data of subscan A.

$$\Theta_C \;=\; \Theta_A + \frac{\Delta\Phi_{\mathrm{AB}}}{q_0^{\mathrm{AV}}} \tag{3.49}$$

$$\begin{aligned} &= \left\langle \theta_A, M_A \right\rangle + \frac{\Delta\Phi_{\mathrm{AB}}}{q_0^{\mathrm{AV}}} \\ &= \left\langle \theta_C, M_C \right\rangle \end{aligned}$$

This prediction is based on the linked long reference phase difference $\Delta\Phi_{AB}$ and the best available estimate of the GLI phase ratio. For the link between the first two subscans, (A and B), the best available estimate[11] is assumed to be the average mean q_0^{AV} of the intra-subscan drift corrected GLI phase ratio from each subscan. If there are only two subscans in total this takes the following form,

$$q_0^{\mathrm{AV}} = \frac{1}{2}\left[\left(q_{0(\mathrm{A})}\right) + \left(q_{0(\mathrm{B})}\right)\right] \tag{3.50}$$

If linking were to be applied to a series of successive subscans then q_0^{AV} would be calculated from the average mean of all single subscan phase ratio estimates. This single subscan average would only be used for the first link, as discussed above.

As in the case of long reference phase linking, the GLI phase link relies on the assumption that the prediction lies within $\pm\pi$ (in GLI radians) of the drift corrected target value $\Theta_{\tilde{B}}$. This assumption is expressed in equations 3.51a to 3.53, which follow by analogy from equations 3.37a to 3.37c.

$$\begin{aligned} \Theta_{\tilde{B}} - \Theta_C &= (\theta_{\tilde{B}} - \theta_C) + 2\pi\,(M_{\tilde{B}} - M_C) && \text{(3.51a)} \\ &= \Theta_{\mathrm{GAP}} + 2\pi\,(M_{\tilde{B}} - M_C) && \text{(3.51b)} \\ &= \left\langle \theta_{\tilde{B}C}, 0 \right\rangle && \text{(3.51c)} \end{aligned}$$

The difference Θ_{GAP} is defined in equation 3.52 by analogy with the long reference phase gap in equation 3.38.

$$\begin{aligned} \Theta_{\mathrm{GAP}} &= \mathbf{fold}\,(\Theta_{\tilde{B}}) - \mathbf{fold}\,(\Theta_C) \\ &= \theta_{\tilde{B}} - \theta_C \\ &= \left\langle \theta_{\tilde{B}C}, G \right\rangle \end{aligned} \tag{3.52}$$

This expression can be substituted into equation 3.51b and rearranged to give

$$M_{\tilde{B}} = M_C - G \tag{3.53}$$

The GLI phase shift $\Delta\Theta_{\mathrm{AB}}$ between the midpoint of each subscan can now be calculated using equation 3.54.

$$\Delta\Theta_{\mathrm{AB}} = \left\langle \theta_{\tilde{B}}, M_{\tilde{B}} \right\rangle - \Theta_A\,[M_A] \tag{3.54}$$

3.6.4 Linking cross check

The linked phase ratio of the short reference interferometer was used to cross check the linking of the long reference phase. The principle aim was to guarantee that the correct

[11] For the purposes of linking the short reference interferometer in this work, it was simpler to use the $q_{0(\mathrm{A})}$ instead of q_0^{AV}. This does not affect the following arguments.

number of 10 GHz etalon peaks N had been assigned to the frequency interval between the anchor points in subscan A and subscan B.

The short reference interferometer phase ratio was known to be stable within $170,421 \pm 5$ μm from single-subscan measurements given in chapter 4. This was later confirmed over the temperature range 19° C to 26° C and the short reference length found to lie within $170,421 \pm 4$ μm, (see Fig. 5.4).

To check the number of etalon peaks was correct, the short reference interferometer phase ratio was determined by linking both long and short reference interferometer phases as described above. If the linked short reference (before application of the refractive index corrections described below), was outside the normal range for the short reference, linking was repeated with an alternative integer values of N, lying close to the initial value.

This cross check was performed simultaneously on a block of FSI scans which had been recorded on the same day. An example of the short reference linked length ratio for a set of scans is given in Fig. 3.11, where the correct number of etalon peaks had been selected for most but not all scans. Viewing all of the linking results together offered two advantages, over checking one scan at a time.

1. It was easier to see which scans were in error against a backdrop of correctly linked scans.

2. It was faster to link the entire group of scans together.

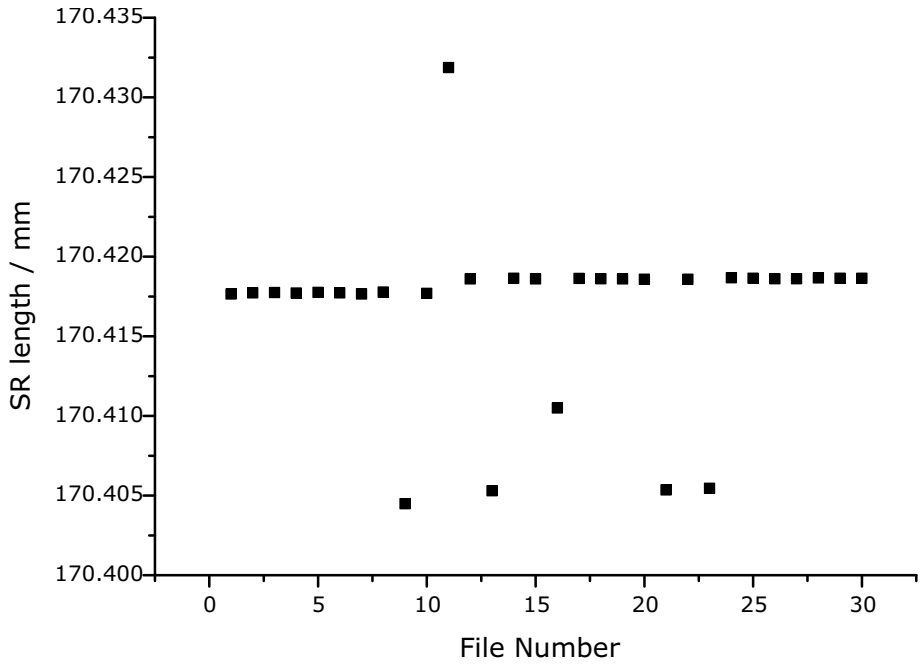

Figure 3.11: *A set of FSI scans during the process of cross checking the linking. The linked estimate of the short reference length ratio is displayed for each file, to check that it lies within* $170,421 \pm 4\mu m$. *The first 10 files were taken several hours before the others at a slightly higher temperature.*

If the correct number of etalon peaks was known to within 2 or 3, this method was sufficient to determine the current number of etalon peaks. On those rare occasions were there was greater uncertainty, other methods were needed to corroborate the correct choice,

since there was typically at least one other choice of N, within 5 or 6 etalon orders of the correct value, for which the linked short reference length estimate lay within the range $170,421 \pm 4\mu$m.

In the majority of these cases the temperature dependence of the short reference interferometer length as shown in Fig. 5.4, was enough to distinguish between the potential candidates for N.

As a last resort the number of etalon peaks in the coarse tuning bridge was counted, using an automated edge detecting algorithm. This detected and counted the number of features, (in the laser 1 coarse tuning etalon signal), which crossed a threshold value. The threshold was varied from the minimum signal level upwards in (integer) steps of ADC count. For each digitised photodiode signal threshold a feature count was taken. This feature count rolled off from a plateau as soon as the threshold was increased by 5 or so ADC counts. The plateau count was always good enough, on the rare occasions when it was needed, to bring the etalon peak count within 2 or 3 of the correct value. This was within the unambiguous range of the trial and error cross check technique described above, given the known temperature dependence of the short reference length. Recommendations for improvements which could be applied to a future system are discussed in chapter 6.

3.7 Air Refractive Index corrections

The final stage in estimating the length of the GLI was the application of a correction for the difference in the refractive index of the air in the GLI and the long reference interferometer. The refractive index of a gas is easier to model in terms of the refractivity, ϱ, given by

$$\varrho = n_{\mathrm{AIR}} - 1 \tag{3.55}$$

where n_{AIR} is the refractive index.

The refractivity of a simple molecular gas is controlled by the strength of the frequency dependent electromagnetic interactions of the molecular species which are present and the number of molecules of each species per unit volume [Ble65]. This concentration is governed by the density of the gas.

The density of air was modelled assuming ideal gas behaviour, with the density of gas within a given volume, (such as an interferometer), proportional to the pressure and inversely proportional to the temperature.

The refractivity correction which was always small, was based on the fact that the air in the GLI and the reference interferometer had pressure and composition in common and differed only in the temperature. The rate of change of air refractivity with temperature for dry air is proportional to the pressure. This is shown in Fig. 3.12 for dry air (with 400 ppm CO_2) at wavelengths 830 nm, 835 nm and 840 nm at three different values of pressure, based on formulae given in [Bir93].

The best fit straight line to the dry air refractivity data for 1000 mbar in Fig. 3.12 is given by

$$\frac{\varrho\,(\vartheta)}{10^6} = 266.62 - 0.882\,(\vartheta - 20.0) \tag{3.56}$$

for wavelengths in the range 835 ± 5 nm, where ϑ is the scan averaged[12] interferometer air temperature in °C.

This line for 1000 mbar was taken for the refractivity correction model, as 1000 mbar was a crude estimate for the mean atmospheric pressure at the 55 ± 5 m elavation above mean

[12]Calculated from RTD readings taken over the whole of an FSI scan, as described in section 2.5.3.

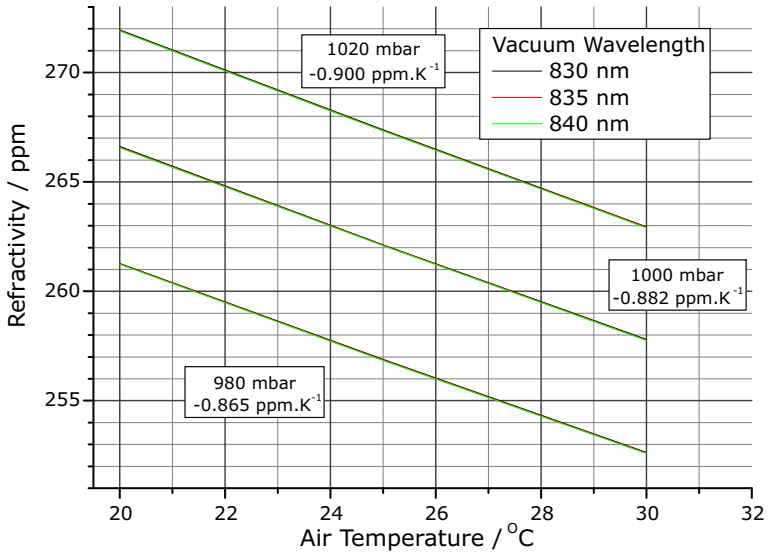

Figure 3.12: *Straight line fit to dry air refractivity at 20°C, 25°C and 30°C, at pressures of 980, 1000 and 1020 mbar. These predictions were derived using formulae given in [Bir93]. N.B. The lines for different wavelengths are almost on top of each other.*

sea level of the laboratory in which the measurements were made. Even large departures in pressure from this estimate correspond to small errors in the small refractivity correction. For example a 50 mbar error corresponds to a 5% error in the refractivity correction. Measuring the laboratory air pressure was therefore unnecessary.

An important simplification of this model is the use of the phase refractive index rather than the group refractive index for the air. As explained in chapter 6, the ratio between optical path length as measured using FSI and physical path length, is the group refractive index. In effect the corrections for differences in the group refractive index of air in each interferometer can be mapped to equivalent corrections using the phase refractive index, with a small shift in assumed air pressure, with a negligible effect on the final length measurement.

Also discussed in chapter 6 are the consequences of omitting a correction for the dispersion of the retroreflector. This omission lead to an unknown offset error, which was fixed, because the scan centre wavelength of each laser was kept within 836.0 ± 0.1 nm.

Once the scan average air temperature for each interferometer had been calculated it was converted to a refractivity at 1000 mbar using equation 3.56.

Factorising the interferometer phase ratio of equation 1.28 into terms for interferometer length and refractivity gives

$$q = \frac{L\left[1 + \varrho\left(\vartheta_{\mathrm{LR}}\right)\right]}{D\left[1 + \varrho\left(\vartheta_{\mathrm{GLI}}\right)\right]} \tag{3.57}$$

where L is the long reference interferometer length (estimated to be 859.09 mm as discussed in section 3.1.1) and D is the refractive index corrected length estimate of the GLI, given by

$$D = \left(\frac{L}{q}\right)\left[1 + \varrho\left(\vartheta_{\mathrm{LR}}\right) - \varrho\left(\vartheta_{\mathrm{GLI}}\right)\right] \tag{3.58}$$

where terms, higher than first order in ϱ, have been dropped.

The best estimate for q was the linked phase ratio estimate. For experiments on single subscans, where no linking result was available and for measurements made in the presence

of vibrations, where the measurement errors were larger than the refractivity corrections, the application of refractivity corrections was not justified.

3.8 Summary

The procedures used to prepare and analyse FSI data to extract an interferometer length measurement are summarised in the flow diagram Fig. 3.13.

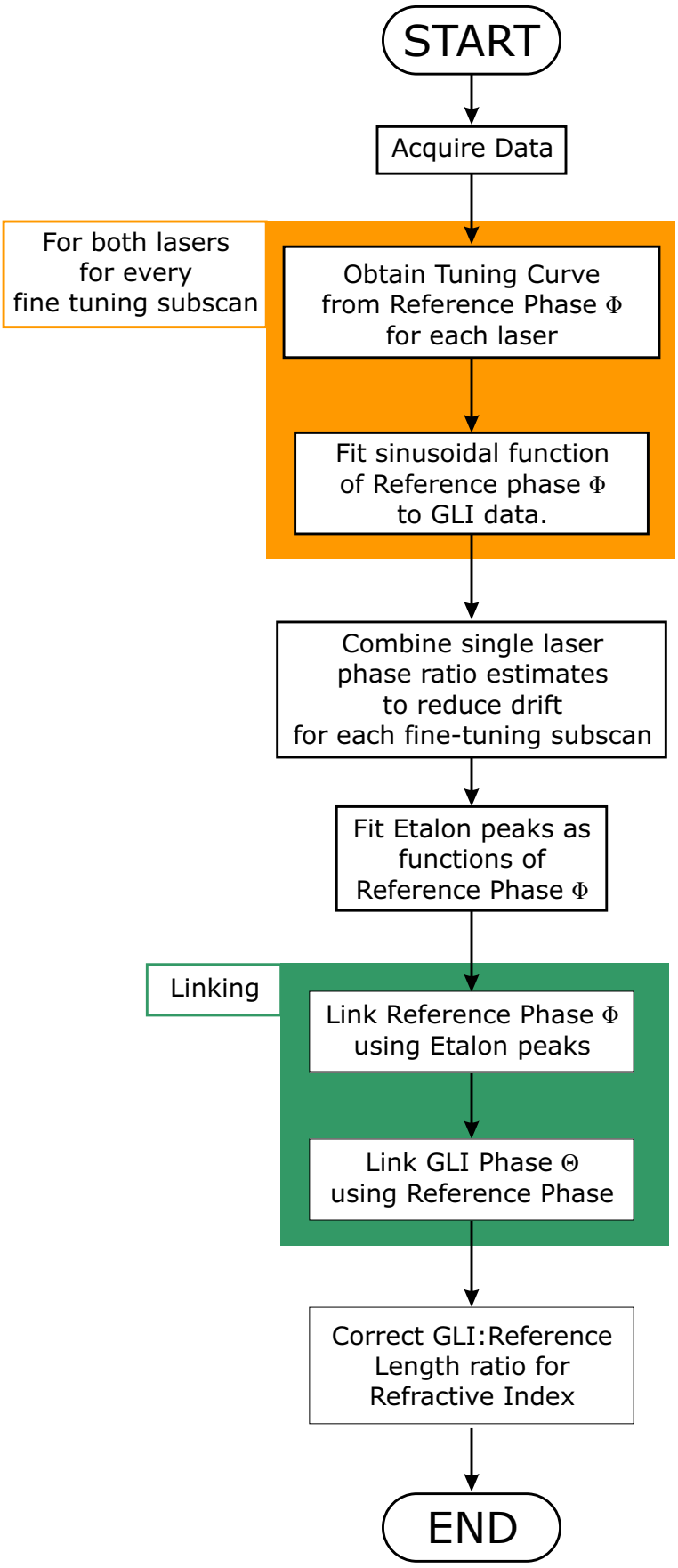

Figure 3.13: *Summary flow diagram showing the preparation and analysis of FSI data used to produce an interferometer length measurement.*

4. Length measurements with a single subscan

The measurements presented in this chapter demonstrate the dual-laser correction for intra-subscan drift errors. The importance of this correction in a multi-subscan measurement is explained in detail at the beginning of chapter 6. In short, a greater reduction of the intra-subscan drift error, allows a larger separation between subscans, so that fewer are required to span the coarse tuning range of the entire scan and the measurement time is reduced.

4.1 Experimental details

Two sets of equispaced single subscan measurements are presented in this chapter.

In Set 1 a single subscan measurement was recorded every 25 mins (apart from a short interruption) for 61 hrs to investigate the drift cancellation performance and its dependence on the laser tuning polarity (defined in section 2.2.2).

In Set 2, a single subscan measurement was recorded every 6 mins, over 24 hrs, to test the dual-laser drift reduction in the presence of as large a thermal drift as could be easily induced in the laboratory.

A GLI was built on the steel optical table, for each of the two sets of measurements. The physical path length difference of each GLI was approximately 40 cm. The setting of the pellicle beam-splitter in the GLI used for Set 1 measurements produced a significant W mode reflection. This W mode reflection was decreased for the Set 2 measurements by moving the beam-splitter and fibres further apart by a few cm and increasing the beam-splitter tilt angle, relative to the GLI axis. After these adjustements the position of the retroreflector was optimised with respect to the beam emitted by the delivery fibre. Hence the positions of all three elements in the GLI were different for Set 2 measurements and the path length difference was smaller by around 17 cm.

The layout of the GLI used in Set 2 is shown in Fig. 4.1 as measured using a ruler. The depth of the retroreflector was measured using a set of calipers. The measured GLI layout corresponds to a length of 398.6 ± 3 mm. This GLI was used without further adjustment for many of the measurements presented in chapter 5.

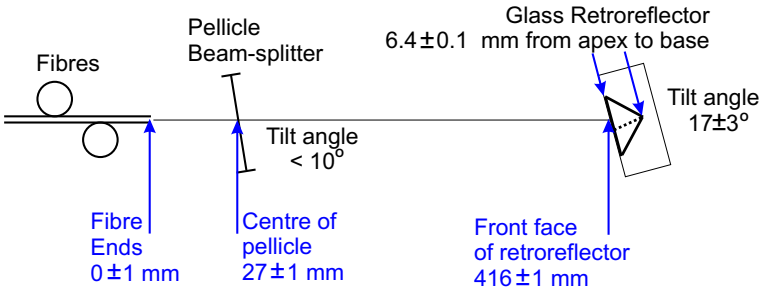

Figure 4.1: *Grid Line Interferometer layout used for Set 2 measurements, as measured with a ruler. Tilt angles are given with respect to the apparent axis from fibres to retroreflector apex. This layout corresponds to an expected interferometer length of* 398.6 ± 3 *mm.*

Each subscan in this chapter was recorded over $> 90\%$ of the fine tuning range of each laser. For the measurements in Set 1, the laser tuning polarity was *UP* for the first ten hours,

was reversed before every scan during hours 12 to 16 and was left *DOWN* for the remainder of the Set 1 scans. All the scans in Set 2 were recorded with the tuning polarity *UP*.

The vacuum wavelength of each laser was measured using the wavemeter for the first scan taken with each tuning polarity in Set 1 and for the the first scan of Set 2. These measurements and the laser tuning curves given in Fig. 2.9 were used to calculate the scan centre laser frequency ν_{MID} for each laser. These calculated values are given in Table 4.1, showing that the (sub)scan centre frequencies of each laser were closer together in each measurement of Set 1 than for the measurements in Set 2.

Table 4.1: *Scan centre laser frequencies for Sets 1 and 2.*

Measurement Set	Tuning Polarity	Scan centre frequency / THz	
		Laser 1	Laser 2
I	*UP*	358.638(36)	358.513(36)
	DOWN	358.594(36)	358.616(36)
II	*UP*	358.740(36)	358.518(36)

The timing differences between Set 1 and Set 2 measurements are summarised in Table 4.2. The level 2 timing scheme was altered from 4 DAQ cycles per chopper window for Set 1 measurements, to 5 DAQ cycles per chopper window[1]. The rate of laser tuning was also increased for subscans in Set 2.

Table 4.2: *Timing parameters for the single subscan measurements. The lasers fine tune over the same frequency interval in each set of measurements, but faster in Set 2 by a factor of 1.5 (scaling with f_{TUN}).*

	Set I	Set II
DAQ (Level 1) clock rate f_{DAQ}	500 Hz	500 Hz
Level 2 clock rate	62.5 Hz	50 Hz
Fine tuning clock rate f_{TUN}	200 Hz	300 Hz
Subscan Duration	320 s	210 - 220 s
Number of DAQ cycles per subscan	1.6×10^5	1.05×10^5 - 1.1×10^5

The laboratory temperature during Set 1 measurements was left to vary with the changes due to the heating system and the weather outside including significant input from direct sunlight, through the large windows of the laboratory in which the demonstration system was housed.

For several hours before Set 2 measurements were started, the laboratory was deliberately cooled by opening the windows to allow air from outside[2] to cool the laboratory. This influx of cold air was stopped just before Set 2 measurements started. The temperature readings in Fig. 4.4a show the the air was warming rapidly from the start, but those metal parts of

[1] Set 1 measurements were the last FSI measurements to use 4 DAQ cycles per chopper window. See section 2.5.4 for details of the level 2 timing system.

[2] Set 2 measurements were recorded in February and the air outside was significantly cooler than the air inside the laboratory.

the reference interferometer system, (which were under insulation), took several hours to respond to the change and at first continued to cool. The later smaller oscillations in air temperature, with a period of around one hour, were due to the heating system and the rapid increase in temperature near the end of Set 2 is due to solar heating in the early morning.

4.2 Results

4.2.1 Set 1 measurements

The measurements from Set 1 are shown initially in figs. 4.2a to 4.2d. The short reference interferometer and GLI length measurements are based on the values of q_1 and q_2 obtained from the sinusoidal fit to data from lasers 1 and 2 respectively and the GLI length estimate based on q_0 as defined in equation 1.40. The other figures show the measured temperatures and the calculated rate of change with time of those temperature readings. The rates of change of temperature of the short reference invar and GLI steel, were the most important because these controlled the proportional change in interferometer length during a scan. The Set 1 interferometer length measurements are shown again, separated according to laser tuning polarity in Figs. 4.3a to 4.3d.

The interferometer length results shown in figs. 4.2a to 4.2d have been separated according to tuning polarity. The results taken with the tuning polarity *UP* are given in figs. 4.3a and 4.3c and those with the tuning polarity *DOWN* are given in figs. 4.3b to 4.3d.

4.2.2 Set 2 measurements

The length measurements from Set 2, based on q_1, q_2 and q_0 are shown for the short reference interferometer in Fig. 4.4b and the GLI in Fig. 4.4d, together with corresponding temperature measurements and the calculated rate of change of temperature.

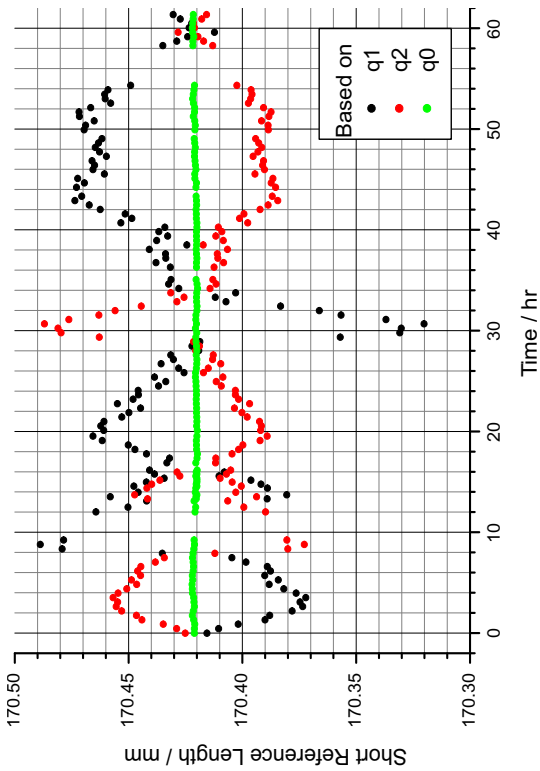

Figure 4.2b: *Set 1 SR interferometer length measurements. These are shown below separated according to tuning polarity in Fig. 4.3b and Fig. 4.3a.*

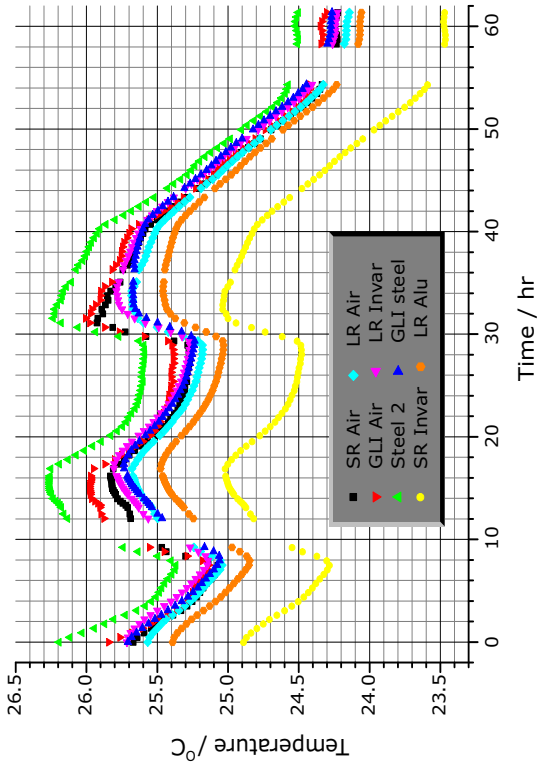

Figure 4.2a: *Set 1 Temperature measurements.*

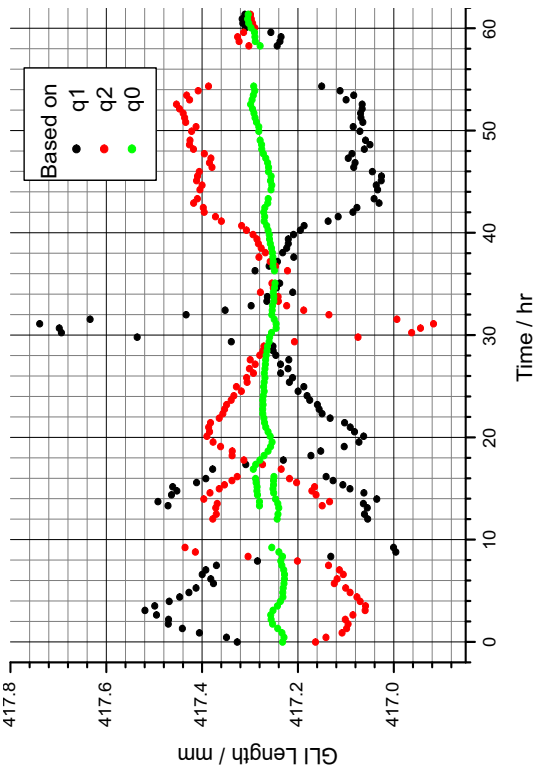

Figure 4.2d: *Set 1 GLI length measurements. These are shown below separated according to tuning polarity in Fig. 4.3d and Fig. 4.3c.*

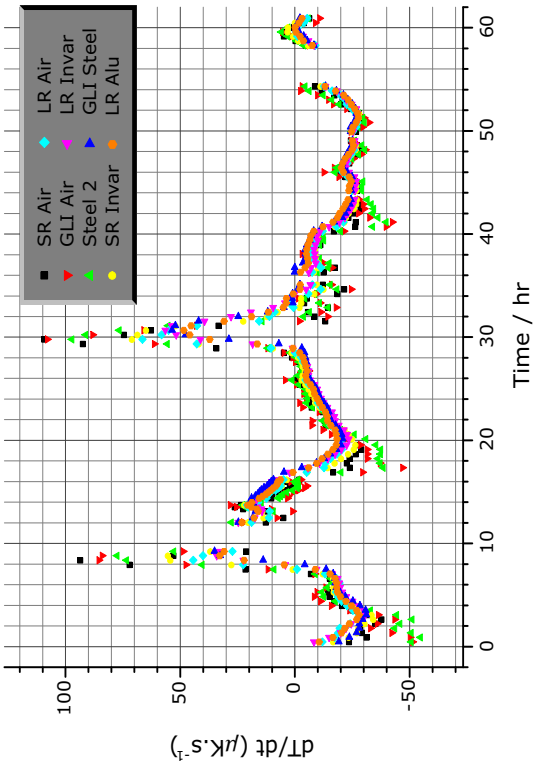

Figure 4.2c: *Set 1 Rate of change of temperature with time.*

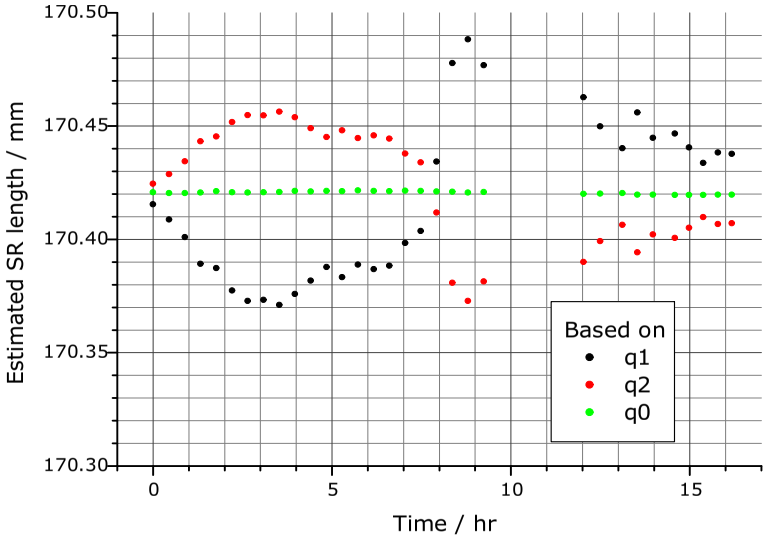

Figure 4.3a: *Set 1 (tuning polarity* UP*) SR length measurements taken from Fig. 4.2b.*

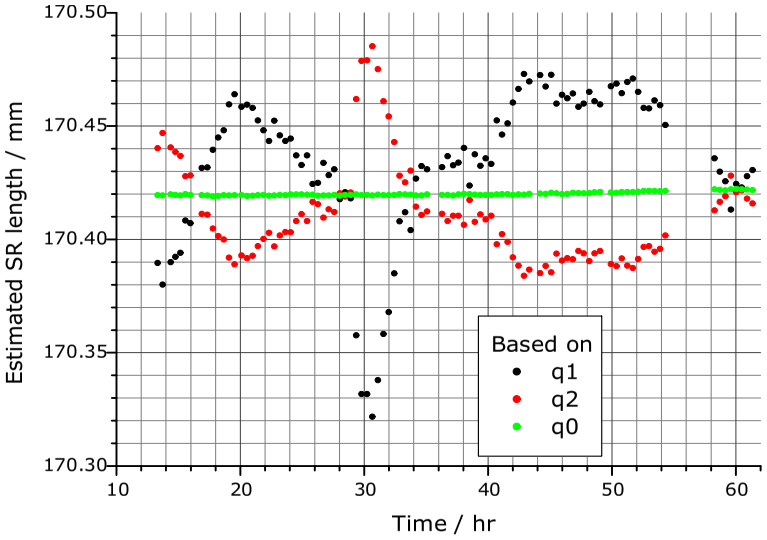

Figure 4.3b: *Set 1 (tuning polarity* DOWN*) SR interferometer length measurements taken from Fig. 4.2b.*

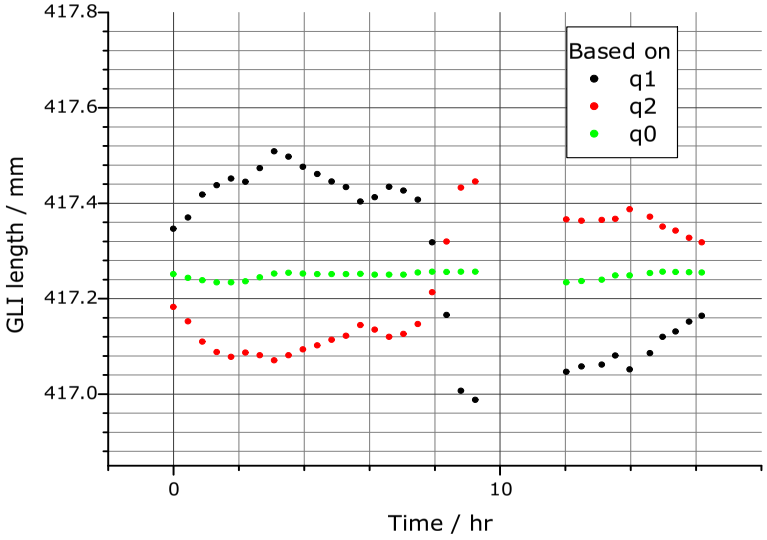

Figure 4.3c: *Set 1 (tuning polarity* UP*) GLI length measurements taken from Fig. 4.2d.*

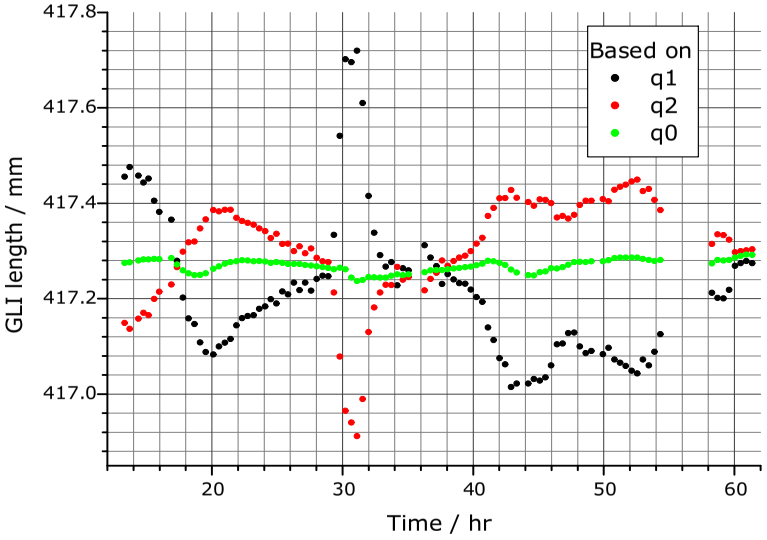

Figure 4.3d: *Set 1 (tuning polarity* DOWN*) GLI length measurements taken from Fig. 4.2d.*

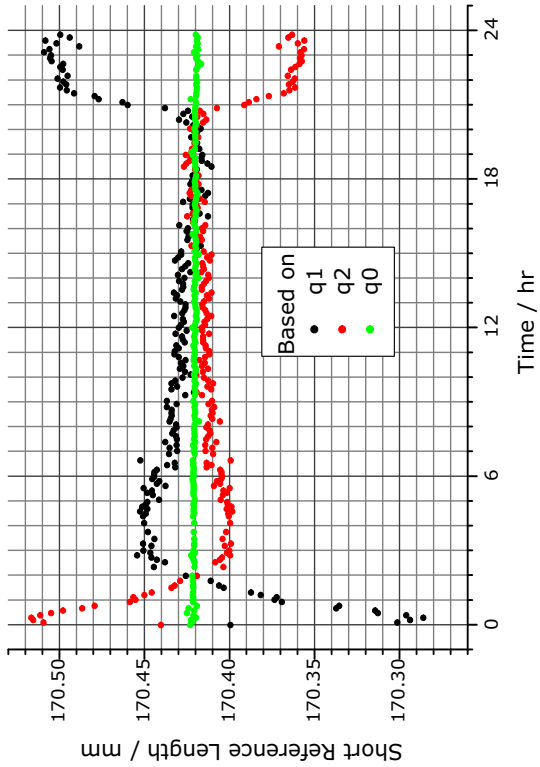

Figure 4.4b: *Set 2 SR interferometer length measurements.*

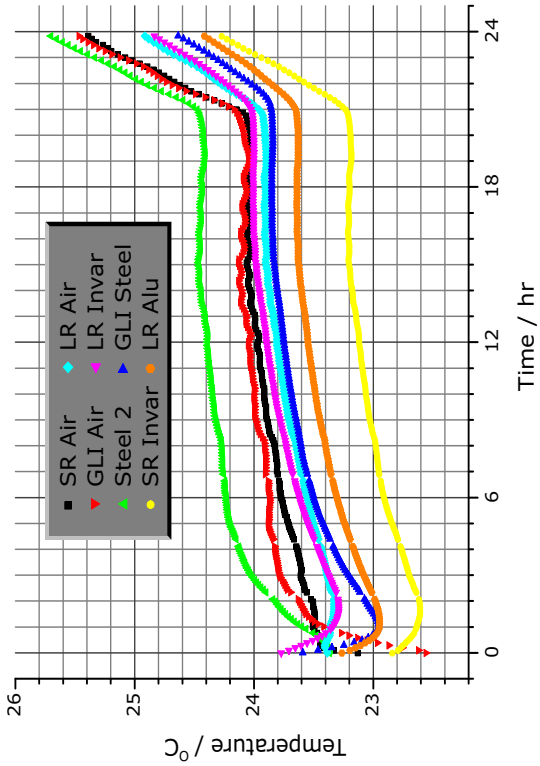

Figure 4.4a: *Set 2 Temperature measurements.*

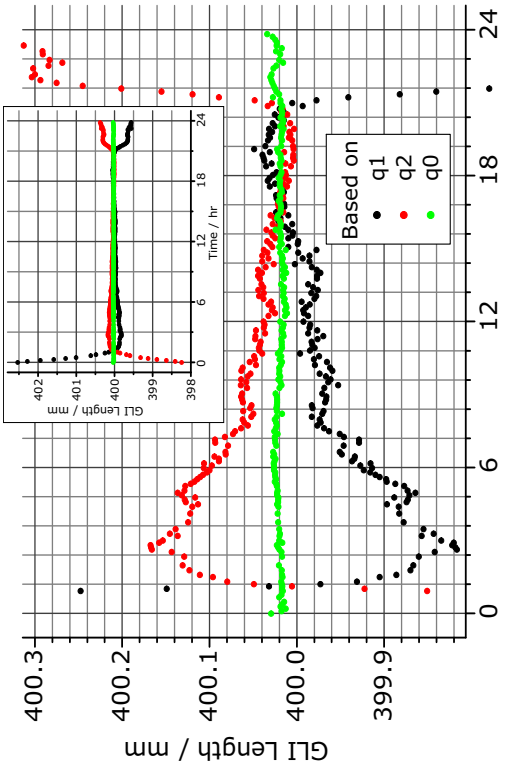

Figure 4.4d: *Set 2 GLI length measurements. (Inset) Full range of the single laser results. (Background) Larger scale version of the same graph.*

Figure 4.4c: *Set 2 rate of change of temperature with time.*

4.3 Discussion

The three parts to this discussion cover :

1. The obvious improvement in measurement precision achieved by combining the results of two lasers.

2. The most likely cause for the significant residual errors in the GLI measurements of Set 1.

3. Comparison of the thermal expansion coefficient of each interferometer obtained from the difference between the two single laser and the direct measurements of changing interferometer length in chapter 5.

4.3.1 Improvement in length measurement precision

The combined laser (q_0 based) interferometer length measurements presented in the previous section, show that the dual-laser technique reduces the error contribution due to interferometer drift.

The change in interferometer length expected from thermal expansion must be taken into account in the assessment of the single subscan measurements presented above. The model for the thermal expansion of each interferometer was based on the measurements presented in chapter 5, which show linear expansion of each interferometer with changing metal temperature.

The temperature dependence of the interferometer length is modelled as a linear expansion using

$$D = D_{20}\left(1 + \alpha_{\mathrm{T}}\left(\vartheta - 20.0\right)\right) \tag{4.1}$$

where ϑ is the interferometer metal temperature in °C and D_{20} is the interferometer length at 20.0° C and α_{T} is the coefficient of thermal expansion of the interferometer OPD with respect the long reference interferometer OPD.

Short reference interferometer measurements

The precision of the combined laser length measurements for the short reference interferometer are shown for Set 1 and Set 2 in figs. 4.5 and 4.6 respectively. In each case the variation of measured short reference length about the mean value is compared with the variation in interferometer length which would be expected given the change of invar temperature about its mean value, using the best fit coefficient of thermal expansion for the interferometer taken from the measurements over a much wider temperature range presented in chapter 5.

The standard deviation of the residual differences between the measured short reference interferometer length, (based on single laser and combined laser phase ratios) and that expected from thermal expansion is given for both sets in Table 4.3. The larger short reference residuals in Set 2 is consistent with the larger rates of change of the temperature which gave rise to larger thermal drift errors, as can be seen in the single laser measurements.

The improvement in precision from the length measurement based on q_1 to that based on q_0 is a factor of appoximately 60 for Set 1 and 40 for Set 2.

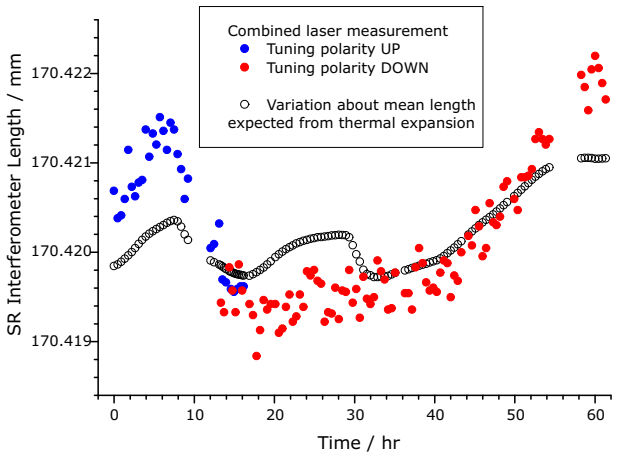

Figure 4.5: *Comparison between the change in combined laser short reference interferometer length measurements of Set 1 (solid points) and the expected thermal expansion (open circles).*

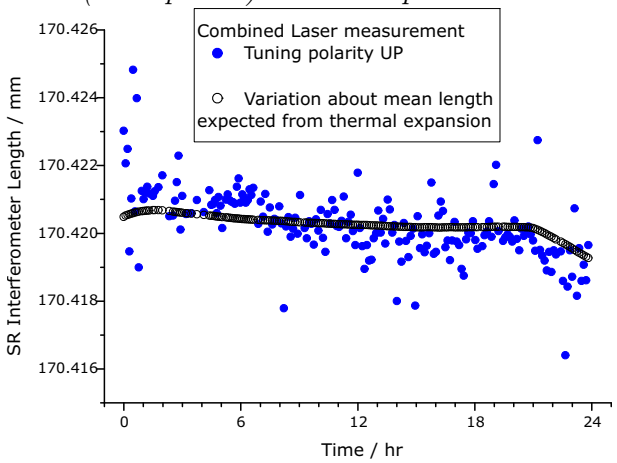

Figure 4.6: *Comparison between the change in combined laser short reference interferometer length measurements of Set 2 (solid points) and the expected thermal expansion (open circles).*

Table 4.3: *Short reference interferometer length residuals from single subscan measurements.*

Data Set	RMS residuals of measurements based on		
	q_1	q_2	q_0
Set 1	202 ppm	140 ppm	3.29 ppm
Set 2	214 ppm	156 ppm	5.11 ppm

GLI measurements

In Set 2, the laser tuning polarity was always *UP* and the dependence on tuning polarity was not investigated directly. The temperature was changing rapidly during the first hour when the precision of the combined laser result was around 10^3 better than the precision of the laser 1 results. The length measurements based on q_1 were around 2.5 mm larger than the expected interferometer length and some of the measurements based on q_0 approached within 1 μm of the expected interferometer length.

If all of the Set 2 measurements are considered, rather than focussing on the extreme

thermal drift in the first hour, the RMS residual differences between the length measurements based on q_0, q_1 and q_2 and the interferometer length expected from the variations in steel temperature were 10.3 ppm for q_0, 898 ppm for q_1 and 643 ppm for q_2.

In the Set 1 GLI length measurements, the errors due to drift were also reduced in the combined laser results, compared to the single laser measurements, but there was a significant residual error. A 30 μm residual error was observed between neighbouring measurements in Set 1 during the four hour period when the tuning polarity of the lasers was alternated after every scan, shown in close up in Fig. 4.7. There is no evidence of an equivalent

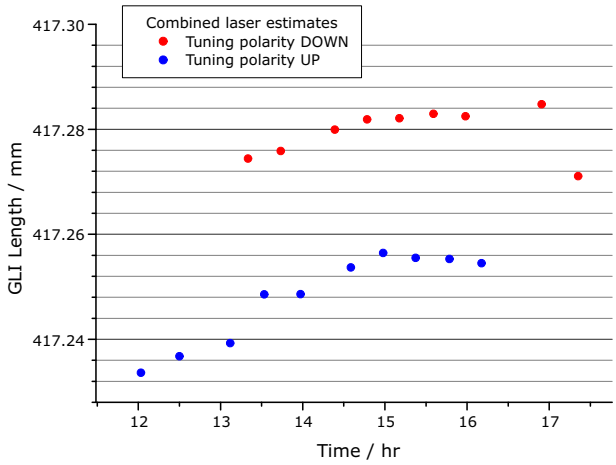

Figure 4.7: *A close-up view of the combined laser GLI measurements from Set 1 in the region where the tuning polarity was reversed between every scan. The measured length shifted by around 30 μm between each measurement, but there was no equivalent shift in the short reference interferometer measurements for the same scans as shown in Fig. 4.8.*

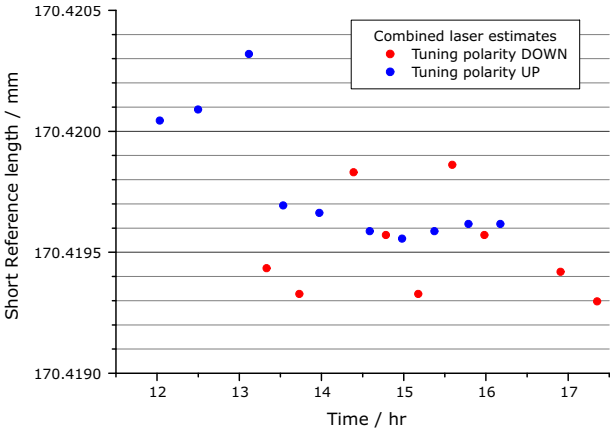

Figure 4.8: *A close-up view of the combined laser short reference interferometer measurements from Set 1 in the region where the tuning polarity was reversed between every scan. There is no apparent dependence of the measured short reference interferometer length on tuning polarity.*

variation in the short reference measurements[3], implying that the cause of this error is unique to the GLI. This rules out contributions which the interferometers have in common, such as interferometer thermal drift and the laser tuning linearity. The reproducibility of this difference also rules out random sources of error as the primary cause, so the signal to noise ratio of the GLI signal is not relevant to understanding this effect.

The three systematic factors which remain unique to the GLI are :

1. The timing of the acquired interferometer signals
2. The dispersion imbalance due to the glass retroreflector in the longer arm of the GLI.
3. The spurious reflections in the GLI

The chopper timing was changed from Set 1 to Set 2 to accommodate changes in chopper behaviour. The GLI photon count was significantly affected by chopper crossover mistiming for a group of data point in the middle of a dozen subscans in Sets 1 and 2. In each case,

[3]The short reference measurements for the same period are shown in close-up in Fig. 4.8.

the number of disrupted data points was small enough to leave the sinefitting unaffected. The fact that this small number of scans was unaffected by the most extreme examples of chopper jitter, rules out this cause as an explanation for the differences between the short reference and GLI measurements.

The changes in measured GLI length due to the frequency dependence (dispersion) of the retroreflector optical path are considered in detail in chapter 6. The change in retroreflector contribution to the GLI length was, at its largest, more than two orders of magnitude smaller than the 30 μm gap between neighbouring measurements, observed in Set 2.

Only spurious optical paths remain from the above list as a possible candidate for the cause of the large, tuning polarity dependent GLI errors.

4.3.2 Spurious optical paths

Spurious optical paths arise from unwanted reflections, which couple light back to the photodetector. Measures were taken to reduce spurious reflections in the delivery and return fibres by angle polishing all fibre ends. The significant spurious reflections arose from surfaces within the GLI, most importantly the W mode beam-splitter reflection shown in Fig. 1.17. There were no equivalent sources of significant spurious reflection in the short reference interferometer.

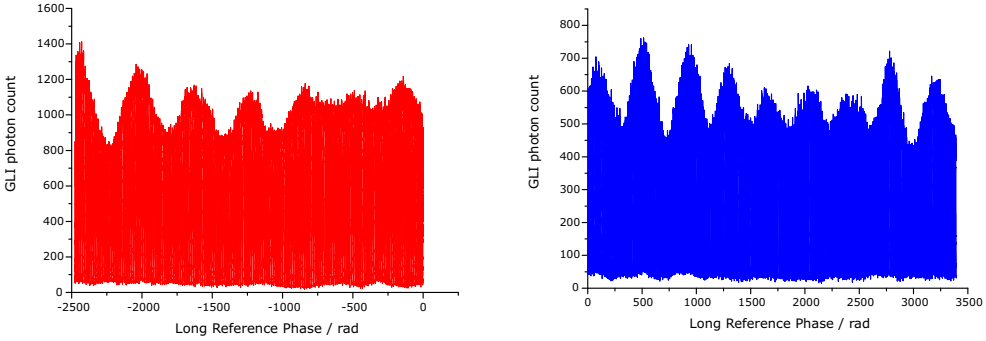

Figure 4.9a: *Oscillations in the GLI signal fringe strength due to spurious reflections, for a typical Set 1 subscan. The laser 1 GLI signal is shown on the left and the laser 2 signal on the right.*

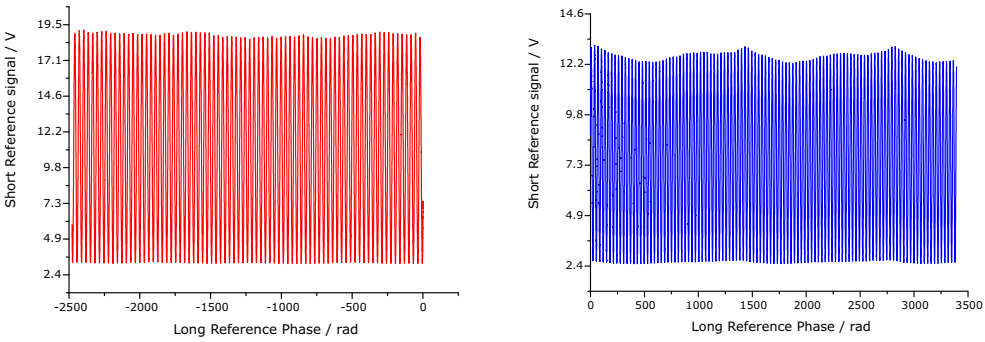

Figure 4.9b: *The short reference interferometer signal fringe amplitude shows weak modulation which follows changes in laser power. This rules out laser power as the cause of the much stronger GLI modulation. The signals shown here are for the typical same subscan, as Fig. 4.9a. The laser 1 short reference interferometer signal is shown on the left and the laser 2 signal on the right.*

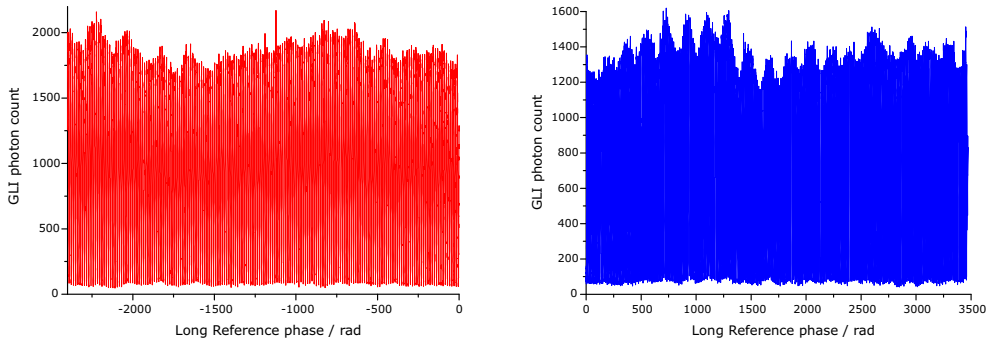

Figure 4.10: *Oscillations in the GLI signal fringe strength due to spurious reflections, for a typical Set 2 subscan. The laser 1 GLI signal is shown on the left and the laser 2 signal on the right.*

The spurious reflections modulated the maxima of V-mode retroreflector mode interference fringes in the GLI signal, as seen for Set 1 in Fig. 4.9a for either laser. The fact that this modulation depth varies with laser frequency, indicates that there was more than one spurious reflection within the GLI. The main modulation cycle period is around 400 rad in long reference phase, (11.1 GHz change in laser frequency), which corresponds to a fibre-beam-splitter separation of around 14 mm, which is on the same length scale as a V-mode W-mode interference, (VW interference).

Fringe modulations were not observed in the short reference interferometer signal of either laser, (see examples from Set 1 in Fig. 4.9b).

After the adjustments made to the GLI between Sets 1 and 2, there was still visible modulation of the GLI fringe maxima in Set 2 measurements as shown in Fig. 4.10. The new modulation cycle period was reduced to around 180 rad in long reference phase, (corresponding to the altered separation between fibre and beam-splitter of around 30 mm, which roughly matches the measured 27 ± 1 mm, shown in Fig. 4.1). The fundamental oscillation period is independent of laser, ruling out power fluctuations at the laser as a significant contribution.

A sinusoidal fit to the GLI data from Set 1 with more fit parameters, representing more reflection modes was attempted. Even with twenty fit parameters, rather than four, no fit function was found which correctly followed the modulation pattern or gave length measurements which significantly removed the tuning polarity dependence.

Further measurements in the presence of significant spurious reflections are presented in chapter 5 and the effect on the measured length is discussed in chapter 6.

4.3.3 Thermal drift correlations

The short reference and grid line interferometer lengths are proportional to the interferometer metal temperature as expressed in equation 4.1 above. The expansion coefficient of each interferometer, (relative to the long reference interferometer), is estimated here by correlating the interferometer drift in Set 1 and Set 2 measurements with the change in interferometer temperature during the subscan. Both the interferometer drift and the change in interferometer temperature were measured indirectly.

The drift in interferometer *length*[4] was estimated from the drift errors in the phase ratios

[4]The drift in interferometer length is proportional to the interferometer drift which was described in terms of the OPD when introduced in chapter 1. It was more convenient here to present the correlations in

of the single laser results; calculated from the difference of two interferometer lengths based on these phase ratios q_1 and q_2, by rearranging equation 1.34c to give

$$\Delta D = \frac{\left(\frac{L}{q_2}\right) - \left(\frac{L}{q_1}\right)}{\Omega_2 - \Omega_1} \tag{4.2}$$

The temperature change during a subscan was usually too small to be measured precisely with the RTDs. Instead the rate of change of temperature for the i^{th} scan was calculated using the scan average temperature of the i^{th} scan and the two nearest neighbour scans $(i-1)$ and $(i+1)$ using

$$\left.\frac{dT}{dt}\right)_i = \frac{1}{2}\left(\left(\frac{\vartheta_{i+1} - \vartheta_i}{t_{i+1} - t_i}\right) + \left(\frac{\vartheta_i - \vartheta_{i-1}}{t_i - t_{i-1}}\right)\right) \tag{4.3}$$

where ϑ_i is the scan average interferometer metal temperature in °C for the i^{th} scan recorded at time t_i. This rate of change of temperature was multiplied by the duration of the subscan to estimate the temperature change during the subscan.

The correlation of short reference drift with short reference invar temperature change is shown for Set 1 in Fig. 4.11 and for Set 2 in Fig. 4.12. In each case the short reference interferometer was 170.4 mm long. Similarly the correlation of GLI drift with the GLI steel temperature change is shown for Set 1 in Fig. 4.13 and for Set 2 in Fig. 4.14.

The CTE α_{T} of the short reference and grid line interferometers (relative to the long reference) was estimated from the gradient $m_\alpha = \frac{dD}{dT}$ which best fits the correlation data using

$$\alpha_{\text{T}} = \frac{m_\alpha}{D} \tag{4.4}$$

where D is the GLI length, (rather than the interferometer OPD denoted $\mathcal{D}$).

The CTE estimates from Set 1 and Set 2 drift correlations are summarised in Table 4.4. The short reference CTE estimates here are in very good agreement with each other and with the value derived from linking measurements in chapter 5 presented in Table 5.2. The two GLI CTE estimates presented here disagree, with each other and with the linking measurements result presented in Table 5.2.

Table 4.4: *Drift correlation based CTE estimates for short reference and grid line interferometers, relative to long reference interferometer. The errors quoted here, are taken from the slope errors of the straight line fit.*

	Set 1	Set 2
SR Invar CTE	-5.0 ± 0.1 ppm.K^{-1}	-4.9 ± 0.2 ppm.K^{-1}
GLI Steel CTE	11.8 ± 0.1 ppm.K^{-1}	12.6 ± 0.1 ppm.K^{-1}

terms of drifts in the interferometer length.

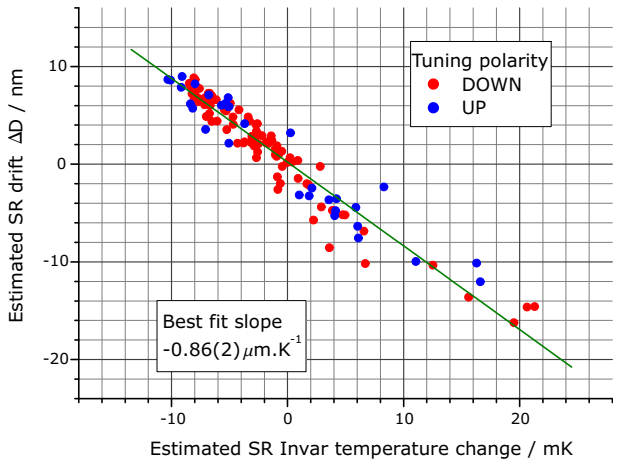

Figure 4.11: *Correlation of short reference interferometer drift with change of invar temperature in Set 1 measurements. SR Length 170.4 mm.*

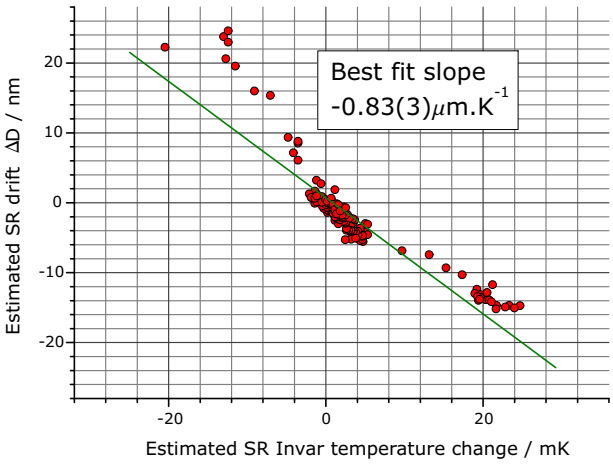

Figure 4.12: *Correlation of short reference interferometer drift with change of invar temperature in Set 2 measurements. SR Length 170.4 mm.*

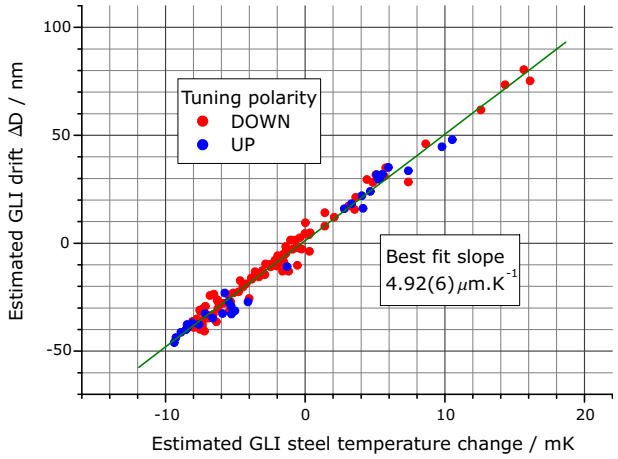

Figure 4.13: *Correlation of GLI drift estimate with change of steel temperature in Set 1 measurements. GLI Length 417 mm.*

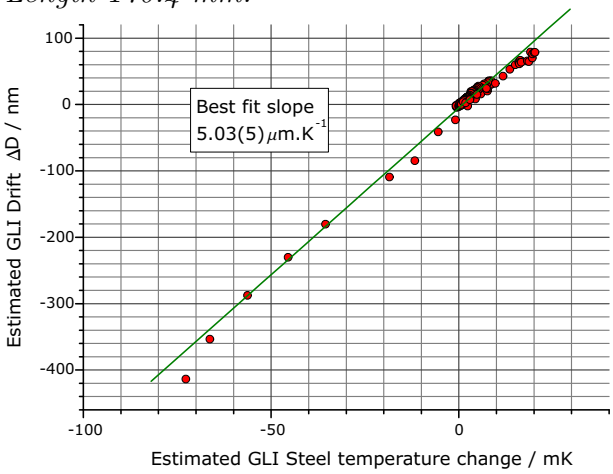

Figure 4.14: *Correlation of GLI drift with change of steel temperature in Set 2 measurements. GLI Length 400 mm.*

4.4 Summary

The length measurements of the short reference and grid line interferometers, based on frequency scanning interferometry data from a single fine tuning subscan, presented above, represent a clear demonstration of the dual-laser technique for reduction of the errors due to interferometer drift. This error reduction is necessary, if single subscans are to be linked together.

Several different reasons have been found to believe that there is a significant error contribution present in the GLI signal, which is not present in the data from the short reference interferometer. These reasons are :

- The much better agreement of the short reference interferometer CTE estimates, compared with those for the GLI.
- The much better performance of the drift reduction in the short reference interferometer.
- The significant tuning polarity dependence of the interferometer length measurements, observed only in the results for the GLI.

The extra GLI error has been attributed to multiple spurious reflections, in particular beam-splitter W mode reflections, because the majority of the possible alternative explanations rely on effects which should have been common to grid line and short reference interferometers. These are ruled out by the absence of similar errors, in the short reference results. The remaining sources of error, unique to the GLI, are too small to explain the tuning polarity dependence.

Comparison of the GLI results, for the two data sets presented in this chapter, revealed that the errors attributed to the spurious reflections decreased when the W mode contribution was reduced in Set 2. This improvement in GLI length measurement precision was achieved, despite an increase in the thermal drift in Set 2. The increase in the thermal drift error contribution, was indicated by the larger spread in short reference interferometer results in Set 2.

It is shown in the results presented in this chapter, that the intra-subscan drift error has been reduced sufficiently for linking subscans to be attempted, as demonstrated in the measurements presented in chapter 5. Control of the errors in each subscan, due to spurious reflections will be important for future measurements as discussed further in chapter 6.

5. Length measurements linking two subscans

5.1 Introduction

The length measurements presented in this chapter demonstrate the improvement in length measurement precision which can be achieved by linking together two 30 GHz subscans separated by a 3.5 THz coarse tuning interval.

The measurements can be split into three categories :

- Measurements of a GLI built on steel, with large thermal drift.
- Linearity Measurements with a much longer GLI, also built on steel.
- Measurements with a carbon fibre GLI, with a deliberately degraded interferometer signal.

The importance of correcting for inter-subscan drift in linking is demonstrated in section 5.2.2 with measurement set 4 in which large thermal drifts were deliberately induced. This set of linking measurements is examined in detail.

In further sets of linking measurements A to D, the temperature dependence of the interferometer lengths was measured over a 6°C range, allowing the coefficient of thermal expansion (CTE) of the interferometers, with respect to the long reference interferometer to be measured, as discussed in section 5.2. The best fit thermal expansion trend to the data for short reference and grid line interferometers from Sets A to D is then compared with earlier measurements in Sets 3, 4 and 5.

The range of GLI lengths for the thermal expansion measurements over the 6°C range was less than 40 μm. A longer grid line interferometer with the retroreflector end mounted on a motion stage was built to test the linearity of changes in the measured length compared with changes in the GLI length over a range of 20 mm, from 1175 mm to 1195 mm. This linearity test, discussed in section 5.3, was an extension of similar work by Grewal over a 100 μm range [Gre99].

A final set of measurements using a 456 mm carbon fibre supported GLI, were recorded with the interferometer signal degraded in one of several ways, either by reducing the interferometer signal power (increasing the relative contribution of photon counting noise), or by vibrating the GLI retroreflector, or by adding power from a spurious reflection to the GLI signal. The degradation of measurement precision is explored in each case.

5.1.1 Common timing settings for all measurements

The timing and laser tuning settings for all linking measurements presented in this chapter were the same. These settings are listed in Table 5.1. The duration of the entire scan was controlled automatically by suspending the data acquisition after a fixed number of DAQ cycles. Within this automated framework, the duration of the first fine tuning subscan was subject to variation of around ±2 s, because this subscan was brought to an end under manual control. There was greater variation of up to ±5 s in the length of the second fine tuning subscan, because this was affected by accumulated variations in the two manual operations; stopping the first fine tuning subscan and restarting fine tuning after the coarse tuning had ended. The coarse tuning was started manually but suspended automatically at the same target wavelength and always lasted for 30 s, tuning at the maximum possible rate, approximately 116 GHz.s^{-1}.

Table 5.1: *Experimental parameters for all linking measurements.*

DAQ (Level 1) clock rate f_{DAQ}	500 Hz
Level 2 clock rate	50 Hz
Fine tuning clock rate f_{TUN}	600 Hz
Subscan A duration	55 ± 2 s
Subscan B duration	55 ± 5 s
Coarse tuning duration	30 s
Bridge span	≈ 3.5 THz
Laser 1 wavelength at the start of each subscan	832 nm and 840 nm

The fine tuning rate was set to 600 Hz to minimise the impact of thermal drift during the fine tuning, because the aim of the measurements with large drift was to test the correction for *inter-subscan drift* errors. At the DAQ (level 1) clock rate of 500 Hz, the fine tuning rate of the faster laser 2, reduced the number of extracted long reference phase measurements to ten per cycle. It was assumed that the benefits of increasing the tuning rate to the next setting of 1 kHz, were outweighed by the increased risk of losing long reference interferometer phase measurements to chopper jitter.

When the tuning polarity was *UP*, (as it was for most of the scans presented here), the first fine tuning subscan had an initial laser 1 wavelength of 832 nm and the coarse tuning set the laser 1 wavelength to 840 nm. These were reversed when the tuning polarity was *DOWN*. With these laser 1 wavelengths, the scan centre wavelength, for laser 1, matched that of laser 2 at approximately 836.1 ± 0.1 nm. This simplified the inter-subscan drift correction as explained in chapter 6.

5.2 Thermal expansion measurements

5.2.1 Experimental details

The measurements presented here were made using the same interferometers as used for the measurements in Set 2 of chapter 4 after an interval of around nine weeks. The first three sets of measurements will be referred to below as sets 3, 4 and 5, each recorded on separate days. Set 4 was recorded four days after Set 3 and two days before Set 5.

To confirm that the observed changes in interferometer lengths were due to thermal expansion only, further measurements were recorded, ten days after Set 5. These measurements were made at different temperatures over the range from around 19°C to 26°C in four different sets, referred to below as Set A, Set B, Set C and Set D. These four sets were recorded within the same 24 hour period, to minimise the chances that observed length changes were due to any effects other than the variation in interferometer temperature.

Tuning polarity

A small subset of the measurements in Set D were recorded with the tuning polarity alternately *UP* then *DOWN* (as in Set 1 measurements in chapter 4), to investigate the effect

of tuning polarity on the linked result. All other linking measurements presented in this chapter were recorded with the fine tuning polarity *UP*.

Thermal considerations

For measurement Set 4, thermal drifts were deliberately increased by allowing heat to escape the laboratory through opened windows for several hours before the measurements began. The influx of colder air was stopped just before the measurements started. The heating system quickly increased the room temperature during these measurements as it had done during the Set 2 measurements, prepared in a similar manner as reported in chapter 4.

The temperature of the 10 GHz etalon was monitored using an RTD (just visible in fig. 2.16), during measurements Sets A to D. This RTD which will be referred to below as Et 10, displaced the steel 2 thermometer from the readout system, for these four sets of measurements.

The room equilibrium temperature at the start of measurement Set A was around 25°C. To reduce the temperature for Set B measurements colder air from outside was let into the laboratory. As in previous measurement sets, the influx of air was stopped before the length measurements began. To reduce the temperature further for measurements in Set C and Set D, it was necessary to open windows and doors *during* the measurements, to prevent the heating system from raising the temperature out of the range being explored. In Set D, the lowest temperature achieved was limited by the heating system, which switched on during the measurements and once operating at maximum capacity was able to exactly compensate for the heat lost through the open windows. Once this point was reached during the Set D measurements and the temperature had stopped falling, the windows were closed, to allow the temperature to rise, so that the same temperature region could be explored in reverse. The abrupt change in heat loss, with the heating system still giving maximal output, gave rise to the largest rates of change of temperature recorded in this work, shown in Fig. 5.1. Even with these extreme levels of interferometer drift, the linking results were in good agreement with the linear trend as shown for the short reference interferometer in Fig. 5.4 and the GLI in Fig. 5.5.

The RTD recording the short reference invar temperature was misreading during measurement Sets 3 to 5, due to a spurious ground connection to one side of the resistor. This fault was corrected between measurement Set 5 and Set A. Due to this fault, the temperature measurements of the short reference interferometer for measurement Sets 3 to 5 are not directly comparable with those of Sets A to D.

5.2.2 Set 4 results in detail

The measurements of Set 4 are presented in figs. 5.2a to 5.3d.

This data set has been selected for detailed presentation, specifically because of the deliberately induced rapid temperature variations, which gave rise to large interferometer drifts. This drift was induced to demonstrate the importance of the correction for inter-subscan drift error to the precision of the linked GLI phase ratio.

The results presented include :

- The scan-averaged temperature readings.
- The calculated rate of change of these temperature readings.
- Interferometer length measurements

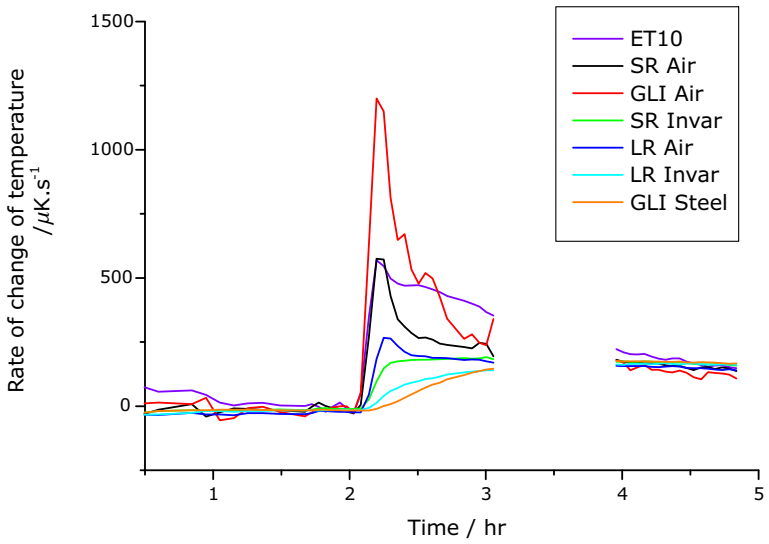

Figure 5.1: *Abrupt increase in rate of change of temperature observed in Set D measurements. Note the difference between the rapid response of the air in each interferometer, (which indicates the different levels of insulation around each one) and the much slower response of the metal, particularly the large thermal mass of the optical table (GLI steel).*

The following length measurements are shown separately for the short reference and the grid line interferometers.

- A comparison between linked length estimates, with and without a correction for inter-subscan drift, (prior to the corrections for air refractivity).
- A comparison between the final (linked and refractive index corrected) interferometer length estimate and the best length estimate available from single subscan results, based on the average of the combined laser results from fine tuning subscans A and B.
- An estimate of measurement precision by comparing the variation (in ppm) about the mean value of final linked length measurements and the variation which would be expected given the changes in interferometer metal temperature.

The last of these comparisons was identical to the estimates of precision used in chapter 4. The expected change in interferometer length about the mean measured length due to variations in temperature about the mean temperature was modelled using equation 4.1 with the best fit thermal expansion coefficient for each interferometer (relative to the long reference interferometer), given in Table 5.2.

The effects of misreading the short reference invar temperature gave rise to a scaling error but the profile of the expected thermal expansion will have retained the same shape, which is slightly different to the pattern of observed short reference measurements.

The 8^{th} single-subscan-average GLI phase ratio in Set 4 lay outside the range where the linking extrapolation error would have been within $\pm\pi$, (shown by the lines in Fig. 5.3c). This scan required an extra 2π GLI radians correction to the linking extrapolation to be put in by hand. This is the only scan where such a correction was required for this GLI. Similar corrections were needed again only with the carbon fibre GLI signals which were deliberately degraded as discussed in section 5.4. After this correction was applied, the phase ratio determined without inter-subscan drift correction, contained an error of 2π,

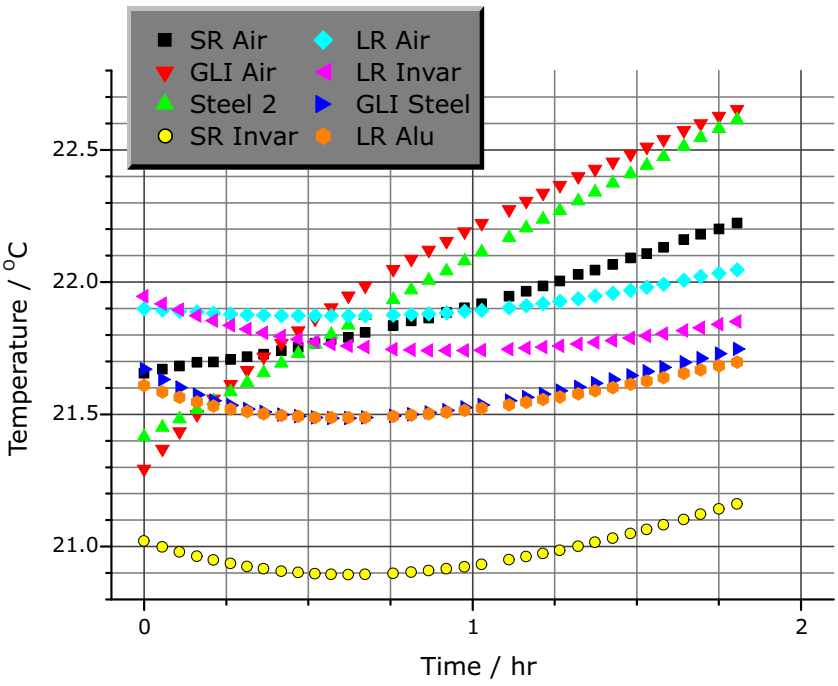

Figure 5.2a: *Set 4 Temperature measurements.*

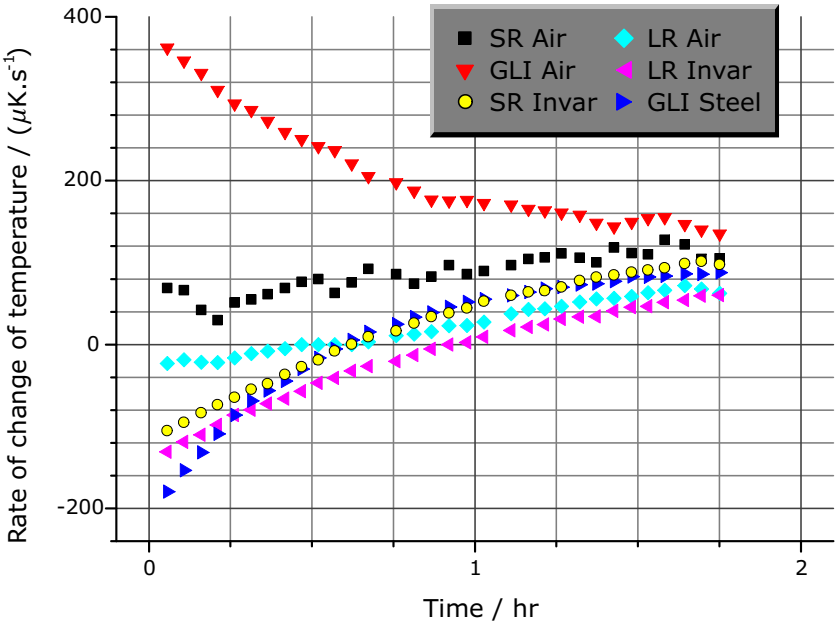

Figure 5.2b: *Set 4 Rates of change of temperature, for selected thermometer channels.*

which is why the 8$^{\text{th}}$ point for the uncorrected length measurements in Fig. 5.2d is absent. After correcting the extrapolation and applying the inter-subscan drift correction, the target anchor point lies within $\pm\pi$ of the extrapolation.

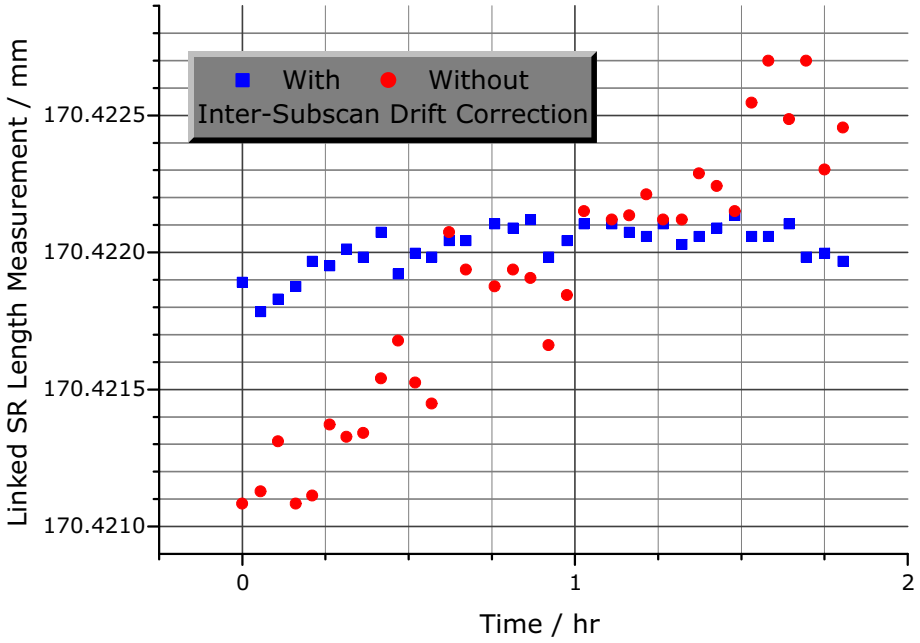

Figure 5.2c: *Set 4 The improvement to the linked SR length on correcting for inter-subscan drift. These results do not include corrections for air refractivity.*

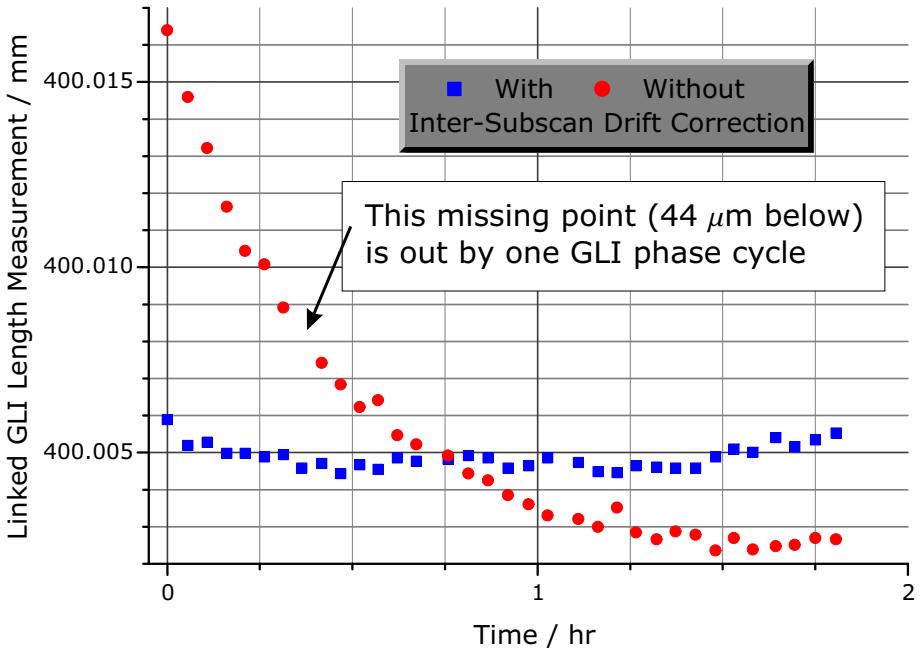

Figure 5.2d: *Set 4 The improvement to the linked GLI length on correcting for inter-subscan drift. These results do not include corrections for air refractivity.*

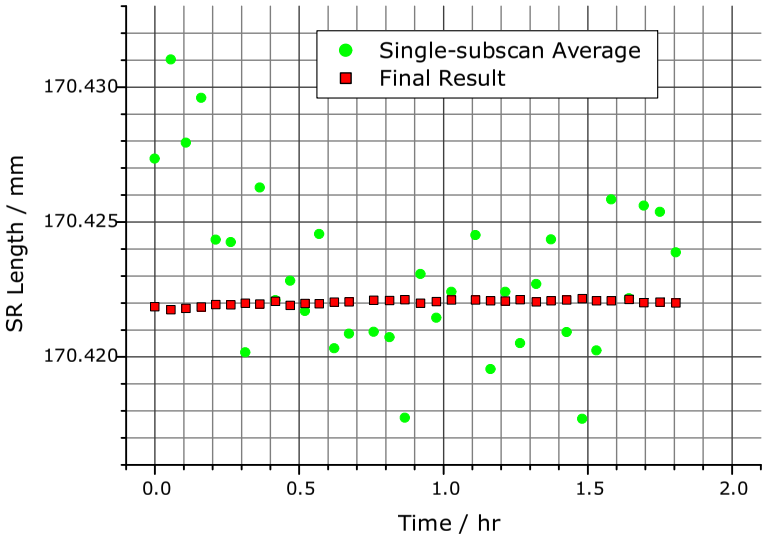

Figure 5.3a: *Set 4 Comparison between short reference interferometer length before and after linking.*

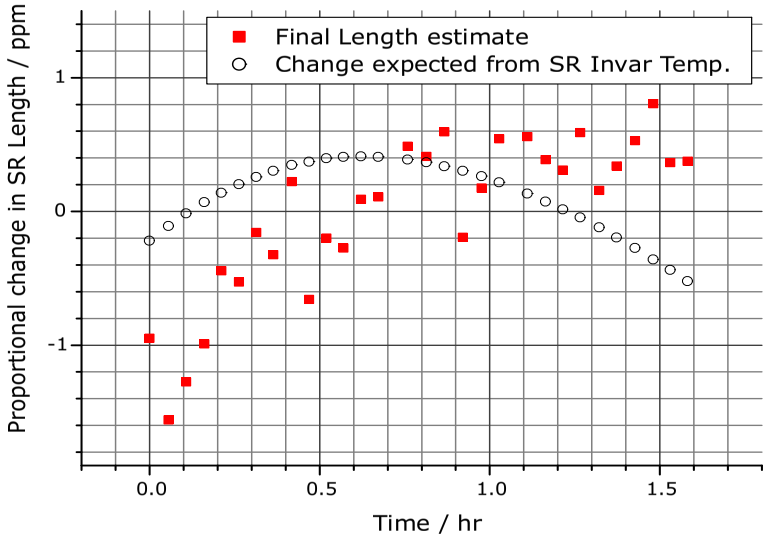

Figure 5.3b: *Set 4 Residual differences between expected and measured SR length variations.*

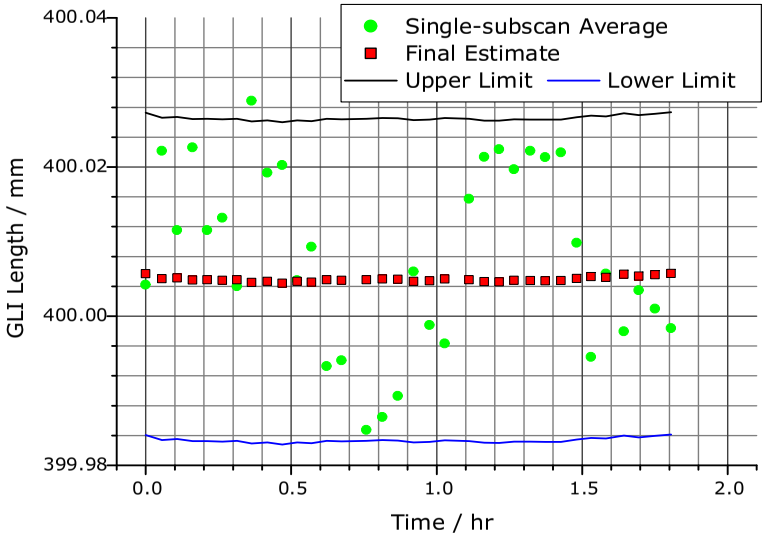

Figure 5.3c: *Set 4 GLI length before and after linking. Lines show the limits of single-subscan result for correct linking extrapolation.*

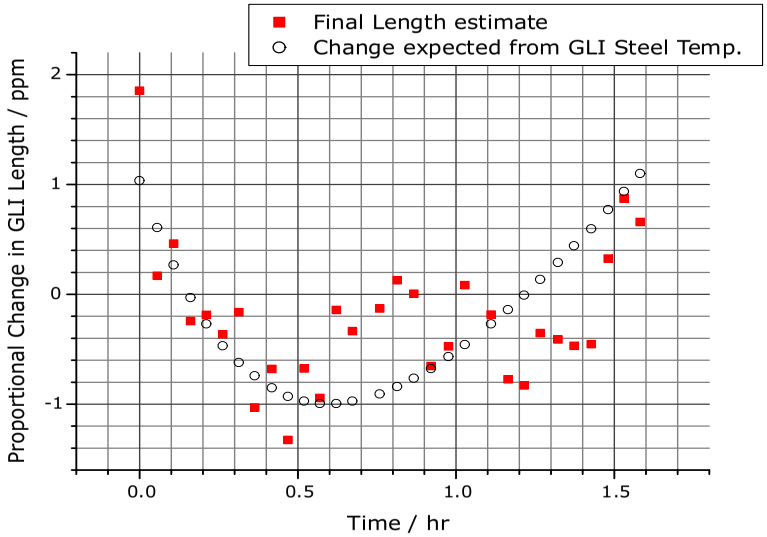

Figure 5.3d: *Set 4 Residual differences between expected and measured GLI length variations.*

5.2.3 All thermal expansion results

The changing length of the SR interferometer the GLI and the 10 GHz etalon relative to the LR interferometer as a function of the temperature of each are shown over a 6°C range. These results are taken from measurement Sets A to D and the interferometer measurements (but not the etalon measurements) have been corrected for inter-subscan drift and air refractivity differences.

The results for Set D are separated into those taken with tuning polarity *DOWN* and those taken with tuning polarity *UP*. The period within the Set D measurements, when the tuning direction was reversed after every scan, is shown below in section 5.2.4 in close-up to allow the dependence of the interferometer length measurements on tuning polarity to be assessed.

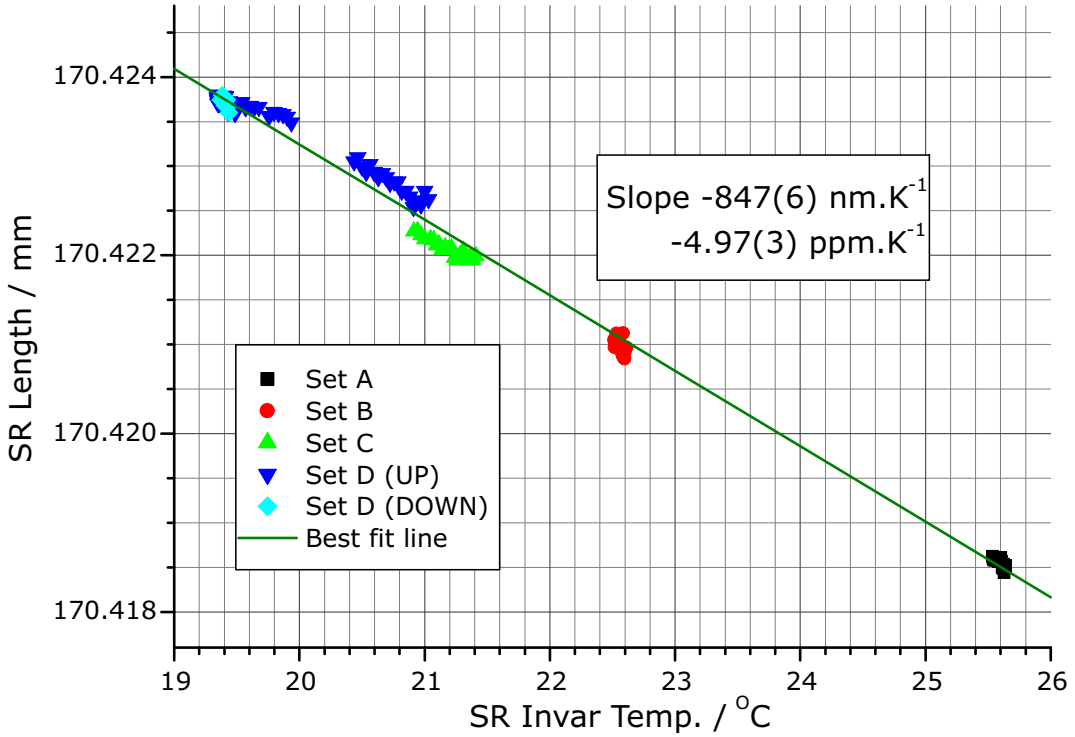

Figure 5.4: *Relative thermal expansion of the short reference interferometer against invar temperature.*

The final interferometer length measurements from the short reference and the GLI are plotted in figs. 5.4 and 5.5 respectively against the metal temperature of each interferometer.

A straight line was fitted to each plot to obtain an estimate of the relative CTE, α_T (in ppm.K^{-1}) calculated using equation 4.4. The best fit values of α_T for the short reference invar and GLI steel are given in Table 5.2, with errors taken from the fitted slope of the corresponding straight line.

The measured free spectral range of the etalon, is plotted as a function of etalon casing temperature in Fig. 5.6. Unlike the equivalent plots for the SR and GLI, the values shown in this plot are derived from the earlier stage of linking the long reference interferometer phase. The free spectral range was measured by dividing the separation in linked long reference phase between the two anchor etalon peaks by the number of free spectral ranges in the reference phase bridge. Provided the apparent etalon FSR, lay within the limits shown in Fig. 5.6, the linking extrapolation of the long reference phase was guaranteed to avoid order

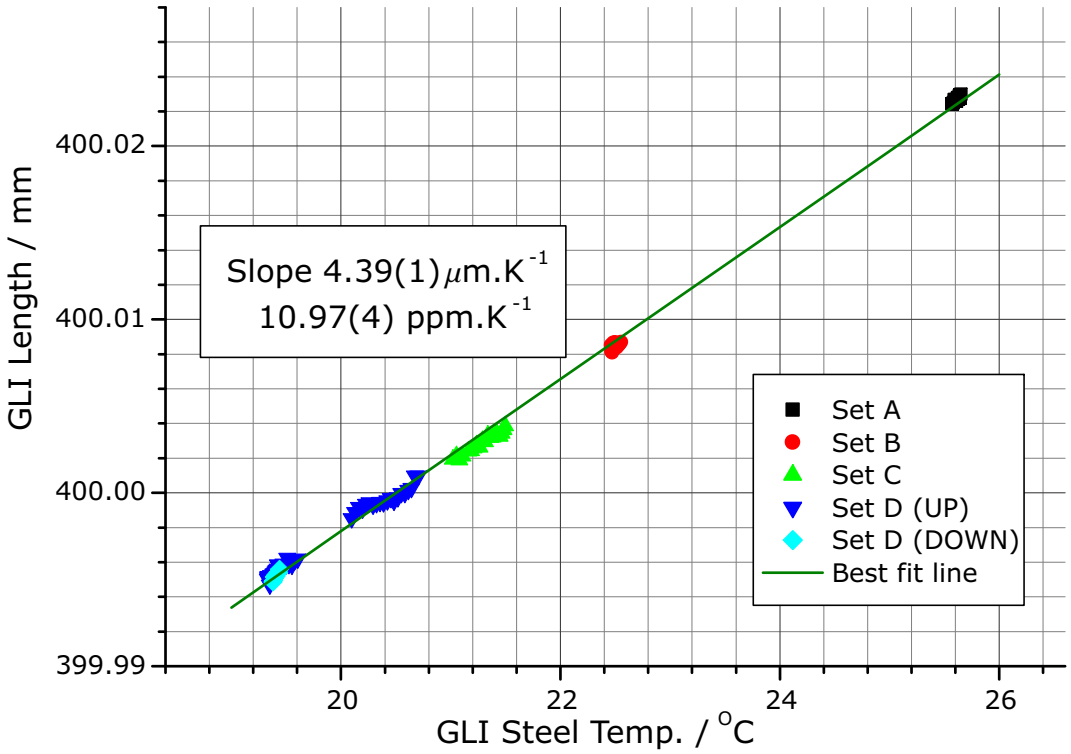

Figure 5.5: *Relative thermal expansion of the GLI against steel temperature.*

Table 5.2: *Relative interferometer CTE values derived from linking measurements presented in figs. 5.4 and 5.5.*

Interferometer (Metal)	Relative CTE
Short Reference (Invar)	-4.97 ± 0.03 ppm.K^{-1}
GLI (Steel)	10.97 ± 0.04 ppm.K^{-1}

number errors. As can be seen from Fig. 5.6, this requirement was easily fulfilled over the 6°C temperature range.

The refractive index and inter-subscan drift corrected grid line interferometer measurements from Sets 3, 4 and 5 are shown in Fig. 5.7 together with the thermal expansion characteristic fitted to the data in Fig. 5.5. These are placed in the same figure to show that the grid line interferometer measurements were consistent to within a micron, over an interval of sixteen days. The residual differences between these measurements and the fitted trend are discussed in section 5.2.4 below.

5.2.4 Thermal expansion measurements : Discussion

Drift corrections

The measurements presented in this section (above) demonstrate that it is possible to apply dual-laser drift corrections with sufficient effect, to allow two subscans, separated by 3.5 THz, to be linked together, with only 1 scan in 249 requiring an order number correction to the extrapolation prediction. If either the inter-subscan or intra-subscan drift corrections had been less effective, many more scans would have required a correction with the subscan

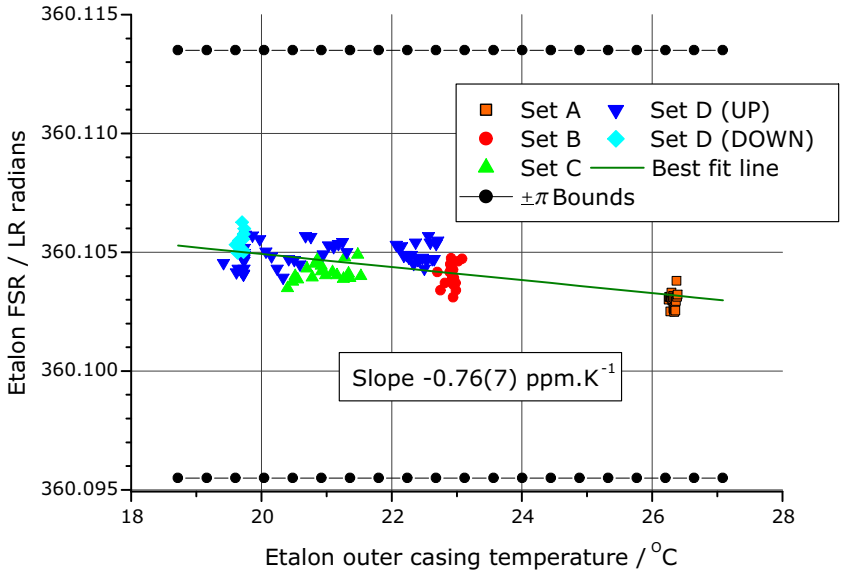

Figure 5.6: *10 GHz Etalon FSR as a function of Etalon casing Temperature, with the slope of the best fit straight line. The $\pm\pi$ bounds show how far the fitted etalon FSR would have to deviate before introducing a phase error into the linked long reference phase, for a bridge of 3.47 THz.*

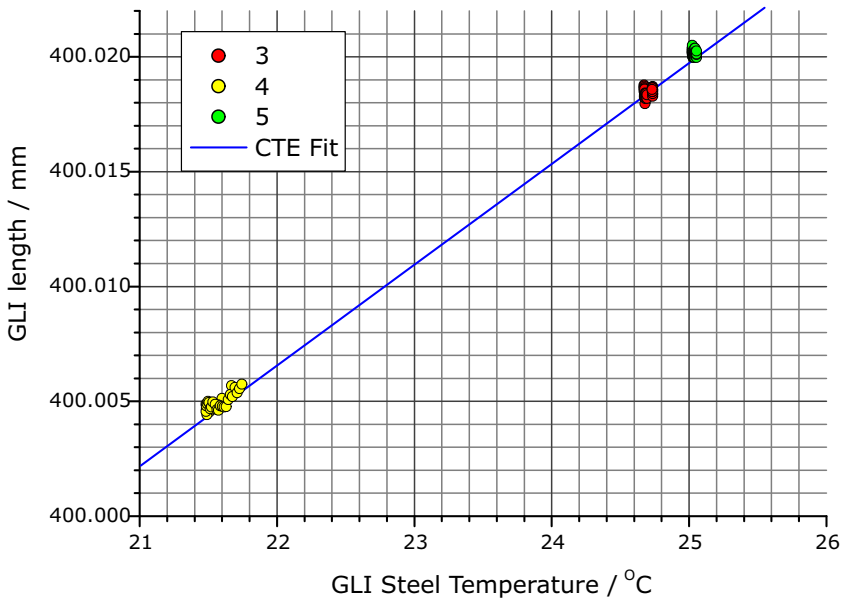

Figure 5.7: *A consistency check of GLI measurements. The thermal expansion characteristic fitted to data from Sets A to D is compared with the GLI measurements from Sets 3 to 5.*

separation of 3.5 THz. The need for good inter-subscan drift correction, to allow accurate linking was demonstrated in Set 4 measurements, especially for the 8th scan. Even without this example, the difference between length measurements with and without inter-subscan drift correction in Set 4, was up to 10 μm or 25 ppm. This difference due to the inter-subscan drift correction appears to follow the rate of change of GLI steel temperature (compare Fig. 5.2b and Fig. 5.2d), with the required inter-subscan drift correction lagging about 10 minutes behind the rate of change of steel temperature.

Etalon FSR

The relative stability of the 10 GHz etalon was crucial to the linking of the long reference interferometer phase. The etalon FSR (in units of long reference phase) was effectively measured every time the long reference phase was linked. The long reference phase interval between the two anchor etalon peaks was calculated after the linking correction had been applied and the reference phase bridge in long reference phase was determined. The etalon FSR was calculated by dividing the reference phase bridge by the number of etalon FSRs. The dominant errors in this measurement were due to the fitted centres of each anchor etalon peak. The error in the measured FSR values decreases with increasing linking bridge as the peak fitting errors are a smaller portion of the bridge. The distribution of the measured etalon FSR values from all seven sets of linking measurements presented so far, is shown in the histogram of Fig. 5.8.

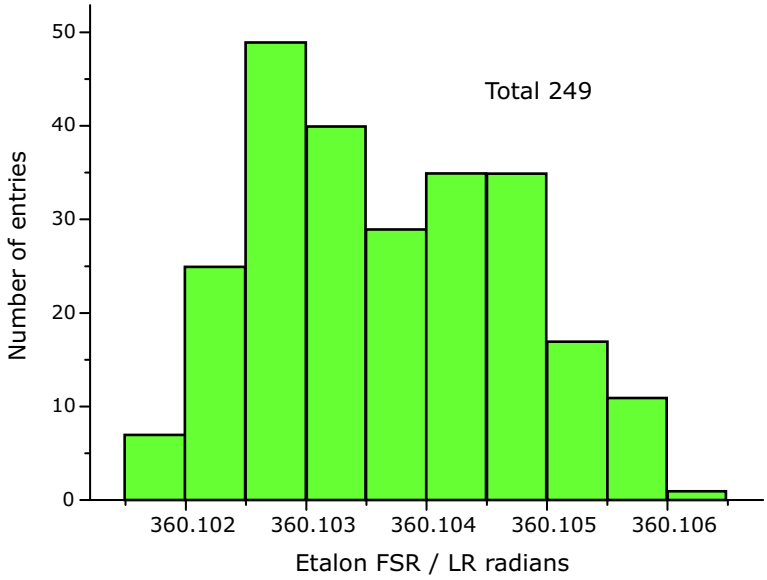

Figure 5.8: *The spread in the fitted etalon free spectral range measured when linking the long reference phase over 3.5 THz. The results are taken from all measurements in Sets 3,4,5 and A to D inclusive.*

The long reference length L was estimated from the etalon FSR in long reference radians $\Delta\Phi_{\mathrm{ET}}$ using

$$L = \left(\frac{\Delta\Phi_{\mathrm{ET}}}{2\pi}\right)\frac{c}{2\Delta\nu_{\mathrm{ET}}} \tag{5.1}$$

If the free spectral range $\Delta\nu_{\mathrm{ET}}$ is assumed to be 10.0000 GHz and air refractivity differences between the long reference interferometer and etalon are assumed to be[1] much less than 10 ppm, then long reference length which corresponds to the mean FSR (from the 249 shown in Fig. 5.8) of 360.10367(7) long reference radians, is 859.09 mm to 5 significant figures. This was the basis for the estimate of long reference length used in this thesis.

[1] A difference in air refractivity between etalon and long reference interferometer as large as 10 ppm, would require a temperature difference of more than 10 K, which is larger than the total range of temperatures observed during the linking measurements.

Short reference interferometer measurements

The observed decrease in length of the short reference interferometer with increasing temperature is believed to be due to faster expansion in the aluminium shorter arm of the short reference interferometer than in the invar longer arm, reducing the optical path difference of the interferometer when the temperature increased.

The best fit thermal expansion coefficient from measurements sets A to D shown in Fig. 5.4 is in good agreement with the expansion coefficient estimate based on intra-subscan drift errors, presented in chapter 4, despite the short reference invar thermometer underreading in the earlier measurements.

The linking measurements of thermal expansion of the short reference interferometer increased the scope of the linking cross check discussed in chapter 3, by providing a prediction of the expected short reference length to within a micron, given the invar temperature. A similar calibration of the relative thermal expansion of the auxiliary reference interferometer of a future system is recommended before it is used to cross check the number of etalon peaks. Verification of the number of etalon peaks in the reference phase linking bridge is discussed in more detail in chapter 6.

The residual differences between the best fit linear thermal expansion characteristic from Fig. 5.4 and individual measurements of the short reference interferometer in Sets A to D are shown in Fig. 5.9. The sign of the residuals is defined by

$$\text{Residual} = \text{Fit} - \text{Data}$$

The 127 residual values from Fig. 5.4 lie within a total range of 557 nm, (3.27 ppm), with a standard deviation of 131 nm (0.77 ppm). The residuals do not lie in a Gaussian distribution, which is consistent with remnant error contributions from less than perfect inter-subscan drift corrections. This is discussed further in chapter 6.

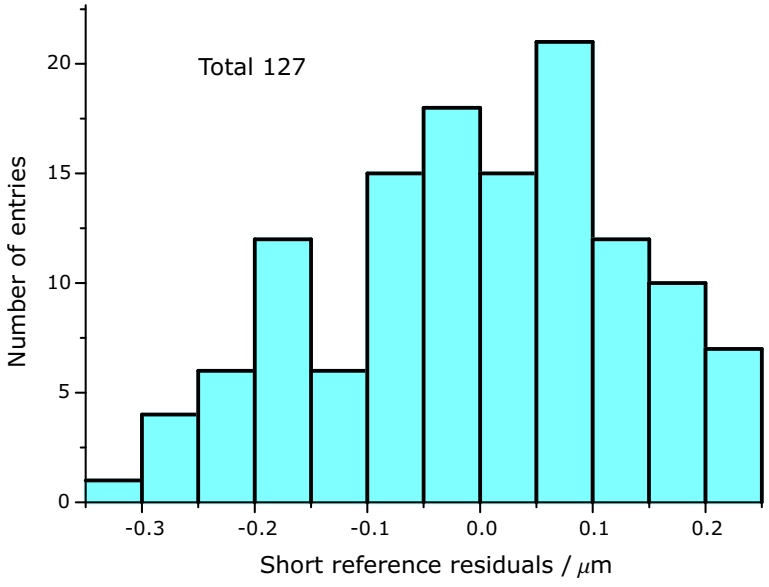

Figure 5.9: *The residual differences between short reference interferometer measurements from Sets A to D and the best fit linear thermal expansion characteristic.*

There was no discernable dependence on tuning direction, in the single subscan measurements of the short reference presented in chapter 4. This remains true for the Set D linked measurements, where the tuning polarity was alternated every scan. The Set D short

reference measurements from Fig. 5.4 are shown again in Fig. 5.10 with an expanded view of Set D, showing the independence of measurements on the tuning direction.

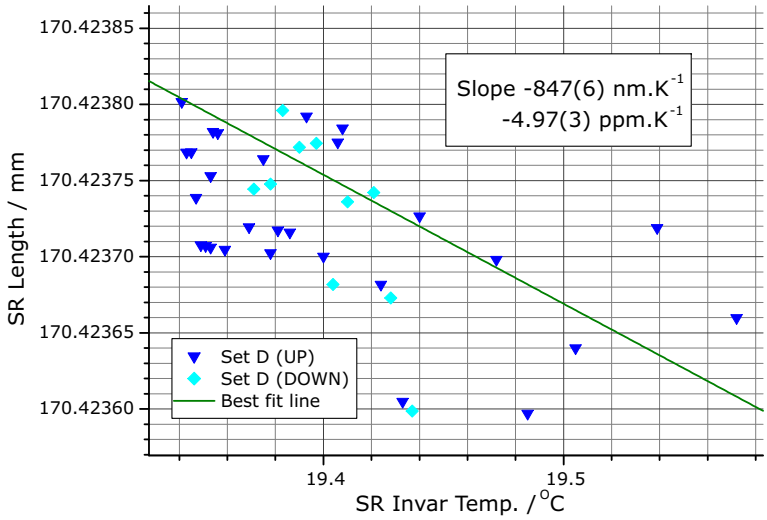

Figure 5.10: *Expanded view of Set D linked short reference measurements showing the independence of the measurements from the tuning direction.*

Grid line interferometer measurements

The residual differences between the best fit linear thermal expansion characteristic from Fig. 5.5 and individual measurements from all seven sets (3 to 5 and A to D inclusive) are shown in Fig. 5.11. The residuals are defined as they were above for the short reference interferometer results (see p. 120). The 249 GLI residuals lie within a range of 1.6 μm with a standard deviation of 300 nm (0.75 ppm). As with the short reference measurements, the GLI residuals do not lie in a Gaussian distribution, implying that the influence of thermal drifts is still present in the measured lengths. This is discussed further in chapter 6. The

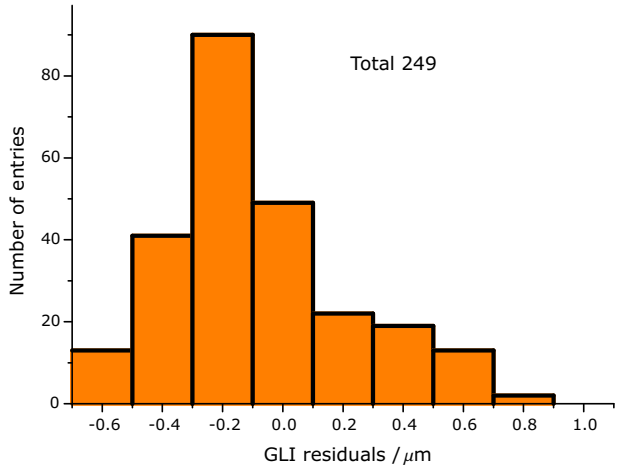

Figure 5.11: *The residual differences between the best fit linear thermal expansion characteristic fitted to Sets A to D and GLI measurements from Sets 3 to 5 and A to D.*

dependence of measured GLI length on tuning polarity was reduced to below 1 ppm by

linking, but a residual dependence was still observable as shown in Fig. 5.12, which is an expanded view of Set D from Fig. 5.5. Further measurements would be needed to check if this direction dependence is due entirely to spurious reflections in the GLI.

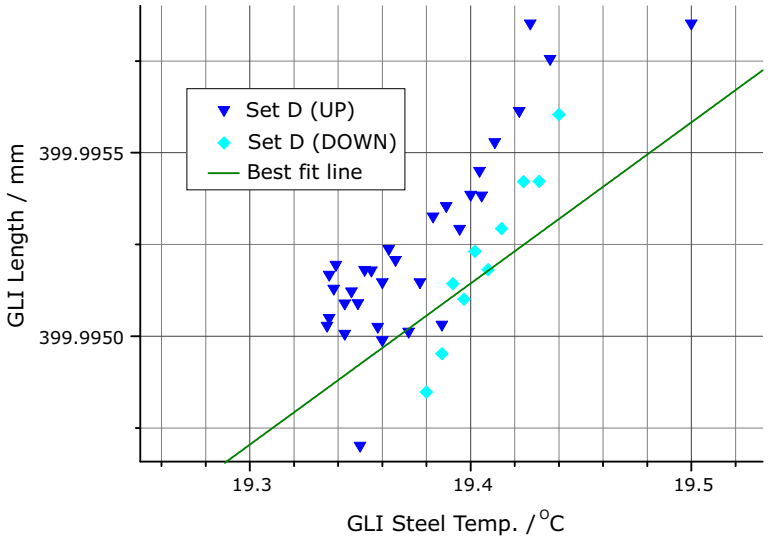

Figure 5.12: *Expanded view of Set D linked GLI measurements showing a residual dependence of the measurements on the tuning direction.*

5.3 Linearity test

The set of experiments presented in this section were designed to test the following important hypothesis:

> Any change in interferometer length leads to a directly proportional change in length measurement obtained using FSI.

5.3.1 Experimental set-up

The key to testing this hypothesis was a GLI with a variable length. For each test the initial length of the GLI was measured in a set of FSI scans. The length of the GLI was then altered by displacing the retroreflector and the change monitored by counting GLI fringes at a fixed laser frequency. A final set of FSI length measurements were made after the retroreflector displacement had been completed.

A GLI, was constructed on the steel optical table. The retroreflector was mounted on a motion stage (Physik Instrumente PI M224.50). The motion axis of the stage was aligned with the axis of the GLI, so that the two axes were parallel to better than 100 mrad. A 2 m long steel ruler was placed alongside the GLI so that the relative locations of the elements of the GLI could be roughly estimated. These locations are shown to scale in Fig. 5.13. The pellicle beam-splitter was placed 90 mm from the fibre ends, to minimise the VW fringes in the GLI signal. The retroreflector was mounted more than 1 m from the pellicle beam-splitter to investigate measurement of a long GLI.

The change in GLI length during stage motion was monitored interferometrically, because the axes of the motion of the stage and the GLI were not colinear. As the stage moved

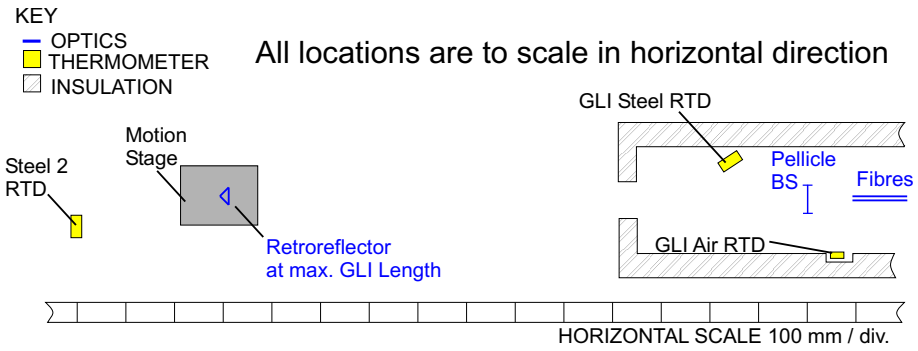

Figure 5.13: *Variable length GLI set-up for the linearity tests. N.B. The horizontal location of each element in the experiment is given by the centre of the object in the above diagram. There are 2 exceptions : The fibres, drawn to show the location of the pair of fibre ends and the retroreflector drawn to show the location of its front face.*

to extend or decrease the interferometer length, the generated displacement fringes were sampled at a DAQ rate of 500 Hz, which was just about fast enough to keep up. A typical sample of the GLI displacement fringes is shown in Fig. 5.15. Only one laser was used, to avoid breaks in the fringe signal due to chopping. Laser 1 was chosen, because more power from this laser could be coupled into the GLI than from laser 2.

The wavemeter was used to record the vacuum wavelength of laser 1, at the start of each retroreflector displacement.

5.3.2 Measurement details

There were eight linearity tests which are separated into two groups of four tests, referred to here as Group E and Group F.

In group E, all four tests involved moving the stage between the same two positions which corresponded to GLI lengths of 1175 mm and 1195 mm. For each test, a group of ten scans were recorded before and after the 20 mm stage displacement, with a 3.5 THz (8 nm) coarse tuning interval between subscans and all other settings also as given in Table 5.1 above.

The single subscan measured lengths from group E lay midway between two possible interpretations of the linked GLI measurements. The two possibilities corresponded to length measurements with a single 2π correction to the GLI phase extrapolation needed for around half the measurements for one possible length or the opposite correction needed to the remaining extrapolations for the alternative choice of length. These two possible GLI lengths were separated by 40 μm.

The first two tests in group F were used to resolve the ambiguity. These tests were recorded with the same retroreflector stage positions as used in Group E with a linking bridge of 1 nm, 2 nm, 4 nm and 8 nm for groups of 3 scans. As the bridge was increased and the precision improved, the GLI length measurements in the first half of Group F converged in each case on the majority of measurements made in Group E without extrapolation correction, confirming that this had been the correct choice.

The *a posteri* confirmation was only possible because the 40 μm ambiguity was much larger than the stage reproducibility of around 1 μm. If this had not been possible, an alternative linking method could have been used. This would involve a link from the laser 1 GLI data of the first subscan to the laser 2 data of the same subscan (a bridge of 4 nm with no inter-subscan drift correction required, because the data were recorded at the same

time), to provide an initial improvement to the phase ratio, which could then be used with greater confidence to perform the 8 nm extrapolation. This alternative analysis was not attempted since it was easier to repeat the measurements in Group F, but may be used in future measurements as discussed further in chapter 6.

After the potential ambiguities of Group E had been resolved with the first two tests of Group F, the final two tests were made with different retroreflector start and end positions, corresponding approximately to GLI lengths of 1193 mm and 1183.5 mm.

Between each test, the stage backlash was removed by asking the stage controller to move the stage 100 μm further in the direction last used and then 100 μm back, in the opposite direction which was about to be used for the large displacement in the middle of the next test.

An example of the GLI length measured before and after the backlash removal, is shown in Fig. 5.14. For each group of ten measurements, the expected change in GLI length about the group mean was modelled using equation 4.1, the effective steel temperature (discussed below in section 5.3.3) and the best fit GLI steel CTE from Table 5.2. The standard deviation of the residual differences between the GLI measurements, (corrected for inter-subscan drift and air refractivity) and the modelled temperature dependent trend is shown in the boxes in Fig. 5.14, with the larger spread of 240 nm equal to 0.2 ppm of the GLI length. The stage backlash of 1.8 μm shows up as a $> 3\sigma$ departure from each group.

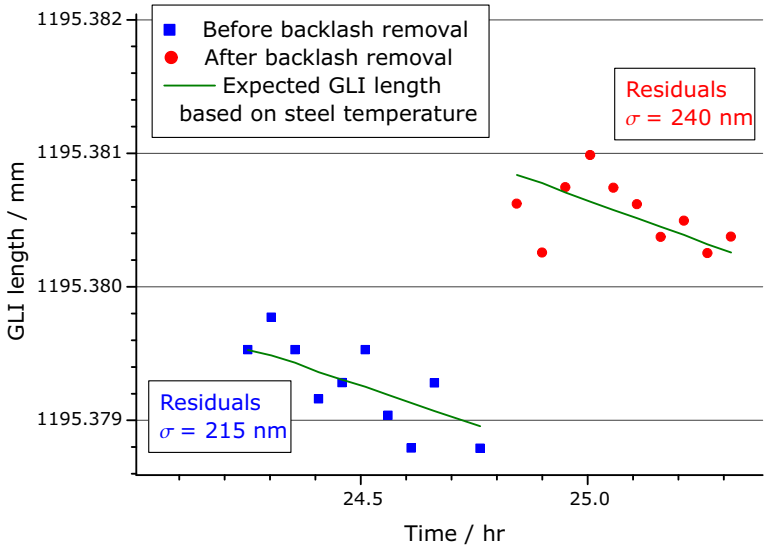

Figure 5.14: *The change in GLI length due to stage backlash, stands out against the trend of decreasing length, due to decreasing steel temperature.*

During Group E, the GLI length alternated between 1195 mm and 1175 mm starting at 1195 mm. The set of FSI measurements made either side of each displacement was a group of ten scans. Each scan was made with an 8 nm bridge using the settings given in Table 5.1, to obtain length measurements with the required reproducibility.

5.3.3 Analysis of the FSI measurements

The displacement measured by fringe counting in the GLI was taken as the baseline or benchmark, against which the FSI measurements were compared. For a fair comparison it was necessary to correct the FSI length measurement for the effects of GLI thermal expansion,

due to temperature changes from the time of the FSI scan to the time of stage displacement. The thermal expansion was estimated using the CTE for the steel bench, α_{T} taken from the length measurements presented earlier in this chapter, as given in Table 5.2.

The readings from the two RTDs at either end of the GLI, were used to model the temperature profile of the interferometer as a linear temperature gradient along the GLI axis. The expected change in GLI length due to thermal expansion, was based on the integrated thermal expansion contributions of each length element along the temperature gradient of the interferometer. The expected GLI expansion could therefore be represented by a single normalised steel temperature, which will be referred to here as the effective steel temperature.

Each of the last three FSI GLI length measurements made before a large stage displacement, were paired off in time order with the first three FSI GLI length measurements made after the stage displacement. Each pair of scans was analysed using the following algorithm, to produce a single estimate of the stage displacement.

From each pair, the GLI length measured before the stage displacement will be represented by D_1. The corresponding measurement made after the stage displacment will be represented by D_3. The corresponding scan average RTD readings for the GLI steel were used to calculate effective steel temperatures, T_1 before and T_3 after the stage displacement. The temperature readings during the stage displacement were used to calculate an effective steel temperature T_2. The GLI length just before the displacement started was predicted from the FSI and temperature measurements using

$$D_{\mathrm{B}} = D_1 \left[1 + \alpha_{\mathrm{T}} \left(T_2 - T_1\right)\right] \tag{5.2}$$

and similarly the GLI length just after the displacement was predicted using

$$D_{\mathrm{A}} = D_3 \left[1 + \alpha_{\mathrm{T}} \left(T_2 - T_3\right)\right] \tag{5.3}$$

The estimated stage displacement from each pair of scans was given by

$$\Delta D_{\mathrm{FSI}} = D_{\mathrm{A}} - D_{\mathrm{B}} \tag{5.4}$$

The three estimates of ΔD_{FSI} were combined to yield a mean value y and the RMS S_y, which was used to estimate the standard deviation of the measurements σ_y using

$$\sigma_y = \left(\frac{N}{N-1}\right)^{\frac{1}{2}} S_y \tag{5.5}$$

where N was the number of estimates taken from each test, which was 3 except for the first test of Group F, from which only two measurement results were available.

5.3.4 Analysis of the displacement fringes

The displacement fringes, generated in the GLI signal during the retroreflector displacement were counted so that the change in GLI length could be measured directly. Some of the recorded phase change of the GLI, was due to the residual tuning of the laser, which was still settling after the FSI length measurements taken a few minutes before the displacement measurement started[2]. In each case the FSI phase shift was predicted from the laser frequency change recorded by the phase stepping long reference interferometer and removed from the recorded GLI phase shift to produce the estimated GLI length[3] change ΔD_{MICH}.

[2]In the first measurement of Group E, the fine tuning was active during the first mm of retroreflector displacement.

[3]Note the distinction between GLI length D and optical path difference $\mathcal{D}$.

The fringes in the GLI were recorded typically at 4 or 5 points per fringe and varied significantly in amplitude and period, as seen in Fig. 5.15. The onset of stage motion was obvious from the sudden presence of high visibility fringes. The region of interest (ROI) containing these displacement fringes was selected from the data by eye. The fringes within the ROI were counted using an automated algorithm.

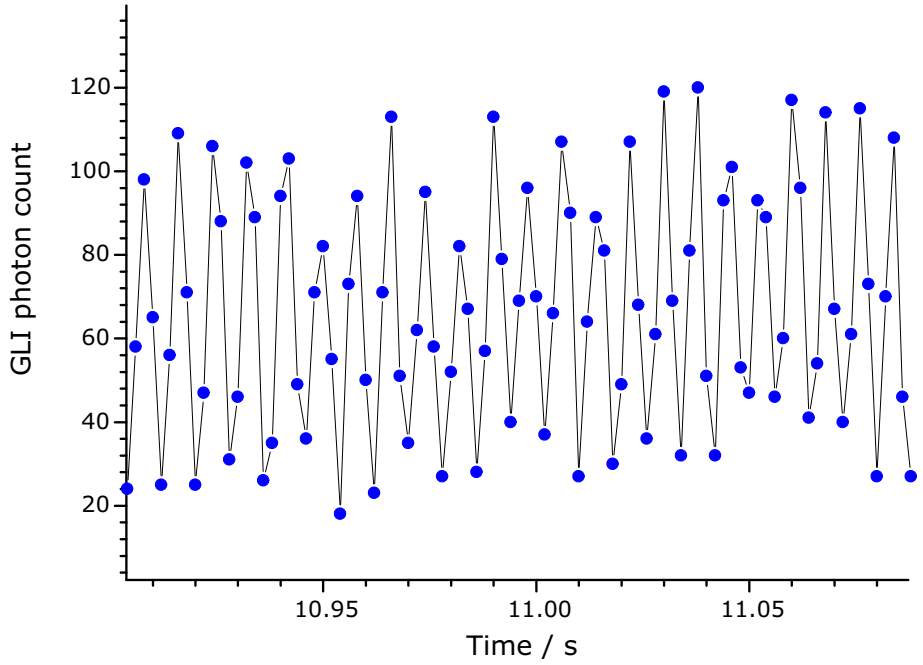

Figure 5.15: *The rapid displacement fringes generated by retroreflector displacement. The DAQ system running at 500 Hz was only just able to keep up with the fringe generation rate of the motorised stage displacement.*

The variations in the period and amplitude of the fringes ruled out any counting algorithms based, either on the interferometer signal crossing a single threshold or based on fitting a sinusoidal function to the fringe pattern. The fringes were counted instead using an algorithm which measured the sign of the difference between each GLI intensity measurement. Whenever this sign swung from positive to negative, a new fringe was counted. This technique was made more reliable for the great majority of the fringes by the low number of points per fringe. Only in the one or two fringes nearest the end, when the stage was moving more slowly and the number of points per fringe increased, was the fringe count unreliable. When selecting the ROI for the fringe pattern, great care was taken to choose start and end points such that the counting algorithm would yield a total fringe count, correct to the nearest integer N_{RAW}, by avoiding the fringes where the stage had slowed down. These remaining ten or fewer fringes at either end of the displacement, which caused difficulties for the automated algorithm, were counted by eye and added to the total. It was not necessary to measure the GLI phase shift more accurately than the nearest integer number of fringes, because the wavemeter reading, (used for converting fringe count to displacement), was only accurate to 1 part in 10^4 and the minimum number of fringes generated was over 22,000 for the shortest (9.5 mm) displacements (round trip OPD change of 19 mm).

To determine how far the laser frequency drifted during the retroreflector displacement, the time interval limits were taken from the fringe count ROI, (including the fringes counted by eye) and the unwrapped long reference phase was examined for the same time interval.

The long reference phase shift within this period, $\Delta\Phi_{\mathrm{ROI}}$, was used to infer the laser frequency shift.

The measured phase change of the GLI $\Delta\Theta_{\mathrm{ROI}}$, (given by the ROI fringe count), was calculated using

$$\begin{aligned}\Delta\Theta_{\mathrm{ROI}} &= \nu\Delta\mathcal{D} + \Delta\nu\left(\mathcal{D}+\Delta\mathcal{D}\right) \\ &= \nu\Delta\mathcal{D} + \left(\frac{\Delta\Phi_{\mathrm{ROI}}}{2\pi\mathcal{L}}\right)\left(\mathcal{D}+\Delta\mathcal{D}\right)\end{aligned} \tag{5.6}$$

where $\Delta\mathcal{D}$ is the change in the GLI OPD due to stage displacement. The second order term is retained, because the GLI length change is significant.

The raw fringe count N_{RAW}, was corrected for the effect of laser frequency drift using

$$N_{\mathrm{DISP}} = N_{\mathrm{RAW}} - \left(\frac{\Delta\Theta_{\mathrm{ROI}}}{2\pi}\right)\left(\frac{D_3+D_1}{2L}\right)\left[1+\frac{D_3-D_1}{2\left(D_3+D_1\right)}\right] \tag{5.7}$$

to give the best estimate of the number of fringes which would have been observed if the laser frequency had been fixed. This corrected number of displacement fringes gave the number of wavelengths change in the optical path difference of the GLI. This was converted to a change in interferometer length x, using

$$\begin{aligned}x &= \left(\frac{N_{\mathrm{DISP}}\lambda_0}{n}\right)\left(\frac{1}{2n}\right) \\ &= \frac{N_{\mathrm{DISP}}}{n^2}\left[\frac{\lambda_0}{2}\right]\end{aligned} \tag{5.8}$$

where λ_0 was the vacuum wavlength of the laser.

The refractive index of the GLI air n was estimated from the displacement average GLI air temperature measurement and the refractivity index model used for all refractivity corrections, discussed in chapter 3. Within the range of pressures and temperatures experienced in the laboratory environment, this was always going to be 3 parts in 10^4, which is as accurate as would be needed given that the fringe count was only to the nearest integer and that the wavemeter used to measure the laser 1 vacuum wavelength was only accurate to 1 part in 10^4.

The error on the GLI length change estimated from the displacement fringe count σ_x, was assumed to be dominated by the wavemeter, hence :

$$\sigma_x = \frac{x}{10^4}$$

5.3.5 Discussion of Results

The linearity of the FSI measurements was assessed by fitting a straight line through the results of all eight tests. The straight line fit, given by

$$F_i = mx_i + c \tag{5.9}$$

was optimised by minimising the value of χ^2 given by

$$\chi^2 = \sum_{i=1}^{8}\left[\frac{\left(F_i-y_i\right)^2}{\sigma_{yi}^2+m^2\sigma_{xi}^2}\right] \tag{5.10}$$

Table 5.3: *Characteristics of the best-fit straight line to the linearity test data.*

Slope m	0.999248(37)
Intercept c	-290 nm ± 540 nm
χ^2	5.10
χ^2 per DOF	0.85

where the index i counts over results from the eight tests.

The values of m and c needed to minimise χ^2 were found using the MINUIT software package, (also used for fitting sinusoids and etalon peak functions as discussed in chapter 3 and Appendix C respectively).

The results of the fit are given in Table 5.3. The fitted line and the data points are compared in Fig. 5.16, where the error bars indicate the size of the weight terms σ_y and σ_x.

The slope of the fitted line is smaller than unity by $(752 \pm 37) \times 10^{-6}$. The difference represents the discrepancy between the length scale of the FSI measurements given by the nominal long reference interferometer length 859.09 mm and the internal length standard of the wavemeter. This is much larger than the expected error for the wavemeter of 100 ppm. If the wavemeter had been perfectly accurate then the real interferometer length was 859.74 mm and the free spectral range of the etalon would be smaller than 10 GHz by around 750 ppm.

The three main features of the combined result from this test are :

1. The absence of any observable non-linear trend
2. A gradient which is approximately one
3. An intercept compatible with zero

All three are compatible with the hypothesis stated at the beginning of the section, that changes in the GLI length lead to proportional changes in the FSI measurement results. This hypothesis could be tested further if *accurate* length calibration standards were available.

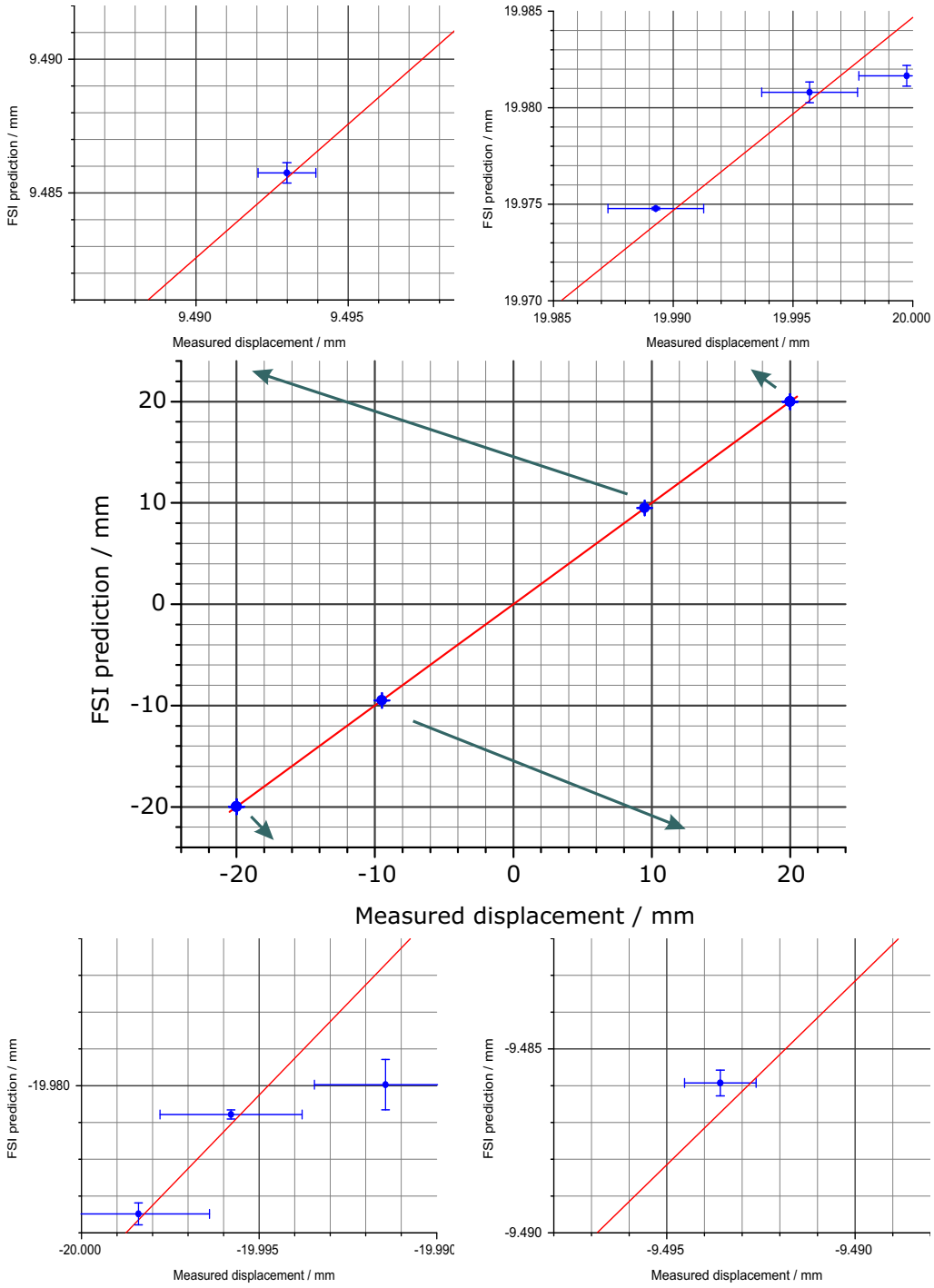

Figure 5.16: *Distribution of Linearity Test results compared to the best fit straight line shown in red, in four magnified regions of the central plot. Note the important absence of any non-linear trend.*

5.4 Measurements with degraded GLI signals

5.4.1 Carbon fibre GLI

The measurements with degraded GLI signals, were all made using the GLI supported on carbon fibre shown in Fig. 2.26. A short set of measurements were made with enhanced spurious reflections. After these measurements, the GLI was adjusted to remove the reflections and the GLI path length difference measured by ruler to be 455 ± 2 mm. The use of a carbon fibre support allowed the relative GLI drift to be much smaller than for the interferometers built on steel. This allowed the effects of signal degradation to be studied in isolation.

It was not possible to cover the same temperature range in the laboratory with the carbon fibre GLI, as had been explored in the measurements with the steel GLI, because the building heating was switched off for the summer by the time these measurements were started. As a result, there was no attempt made to determine the relative thermal expansion characteristics of the GLI OPD, neither magnitude nor direction, directly from length measurements. Attempts using the indirect techniques of chapter 4 based on correlating intra-subscan drift errors from single laser measurements, with measurements of the carbon fibre temperature proved inconclusive.

The retroreflector was mounted on a PZT, identical to that used in the long reference interferometer for phase stepping. This transducer was added to the GLI for controlled vibration of the retroreflector and during vibration and low signal tests described in this section, was biased to the same DC voltage, so that the retroreflector had the same mean position and the GLI length could be directly compared.

5.4.2 Low GLI SNR tests

The power level in the GLI was reduced by placing absorbing neutral density filters in the beam coupling into the delivery fibre. For each level of attenuation, a set of ten scans were recorded. The measurements were all recorded within a four hour period at a similar temperature.

The GLI signal from laser 2 was always weaker than that of laser 1. As a precaution against MINUIT failing to find the deepest minimum in the fit to the weaker signal, the best fit phase ratio for the laser 1 GLI data was used as a seed value for the fit to laser 2. This would have been less useful, if the GLI drift had been significant, because the difference between the best fit phase ratios would have been greater.

The variation in the GLI phase ratio q_{AV} used for the linking extrapolation was slightly greater with low SNR than observed in measurements on the 400 mm steel GLI discussed in section 5.2. On several occasions the single subscan average q_{AV} gave rise to an extrapolation error larger than $\pm\pi$, requiring correction. In all of these cases the next threshold at $\pm 3\pi$ was not exceeded. A similar problem with the extrapolation was also encountered in the measurements discussed below in the presence of vibrations, where much larger corrections were needed to the extrapolations in some cases. The number of scans in which the linking extrapolation needed to be corrected is given for the low SNR and vibration measurements in Table 5.4.

The interferometer signal quality was characterised using an *effective* signal to noise ratio, (based on equation 6.13). The effective SNR is given by

$$\mathrm{SNR}_{\mathrm{EFF}} = \frac{I_{\mathrm{AC}}}{\sqrt{2 I_{\mathrm{DC}}}} \tag{5.11}$$

where I_{AC} and I_{DC} are the best fit values from the sine fit to the GLI data, for each laser in each fine tuning subscan.

The signal level $\frac{1}{\sqrt{2}} I_{AC}$ is the RMS value of the sinusoidal contribution to the interferometer photon count. The noise level contribution assumed in equation 5.11 is the shot noise due to the DC level of the interferometer signal, averaged over an integer number of interferometer fringe cycles. Typical noise levels can be seen in Fig. 5.17 for two examples of raw data from a GLI with reduced signal, (together with the fitted sinusoid). In these examples the photon count fluctuations are consistent with the expected variation due to shot noise. The effective signal to noise ratio represents an upper limit for the GLI SNR,

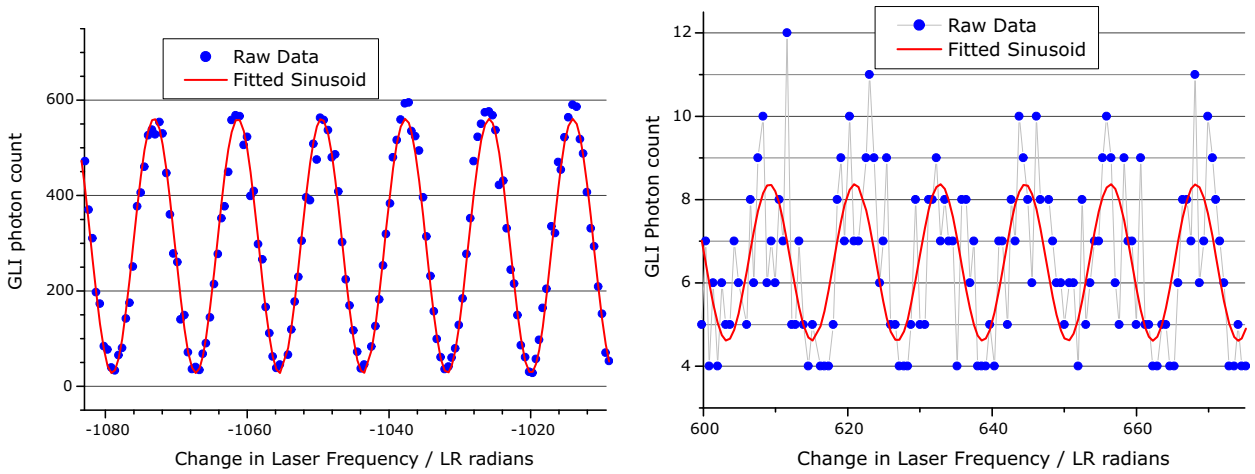

Figure 5.17: *Examples of GLI data with reduced signal and corresponding sine fit. LEFT: The signal from laser 1, with minimum attenuation (SNR* > 10*). RIGHT: The signal from laser 2, with maximum attenuation (SNR* ≈ 0.7*).*

because the shot noise is the minimum level of GLI intensity noise which could have been achieved in this system for a given signal level.

Low SNR measurement results

The GLI length measurements at different signal to noise ratios are shown in Fig. 5.18. Each data point is the mean GLI length result from a group of ten scans, with an error bar indicating $\pm 1\sigma$, where σ is the standard deviation of each group of ten length measurements, after applying the corrections for extrapolation errors. Each group of ten scans was assigned an effective signal to noise value based on the mean value of $\mathrm{SNR}_{\mathrm{EFF}}$ for laser 1 across all twenty fine tuning subscans, two per scan from a group. As the SNR decreased the χ^2 profile retained the same basic shape, but was lifted up away from zero, so that the relative depth of the deepest minimum compared to the background level, was reduced. The example χ^2 profile shown in Fig. 5.19 is from the sine fit to laser 2 in a scan with the strongest GLI signal attenuation, where $\mathrm{SNR}_{\mathrm{EFF}} \lesssim 1$.

After the effect of the reduced extrapolation precision had been corrected for, the linked measurement precision was essentially unaffected by the decrease in SNR. In future measurements, an extra subscan, closer to the first than the 3.5 THz spacing used in these measurements, could be used to remove the need for manual correction of the extrapolation phase ratio as discussed further in chapter 6. The independence of the final results on SNR shows that the anchor point phase errors did not increase significantly as the SNR decreased and that the SNR limit for linked measurements has not yet been reached.

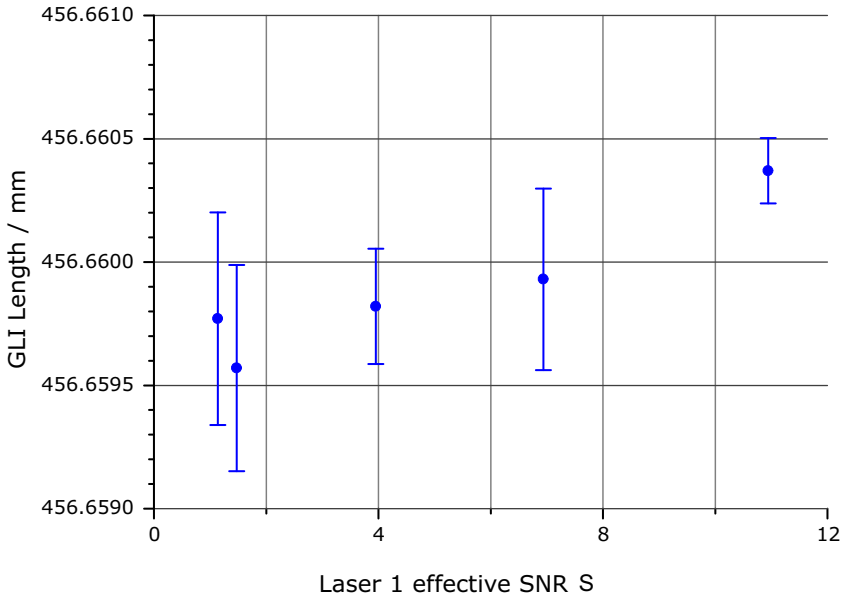

Figure 5.18: *GLI length measurements at lower SNR, all exhibit reproducibility to better than 1 ppm.*

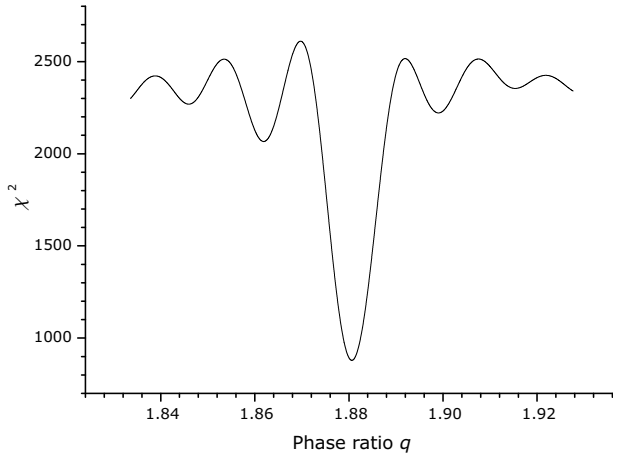

Figure 5.19: *Profile of χ^2 versus fitted phase ratio for reduced GLI signal power. This corresponds to the data shown in the right hand side of Fig. 5.17.*

5.4.3 Retroreflector vibrations

In the measurements presented here, the retroreflector was made to vibrate at frequencies from 10 Hz to 50 Hz. The range of vibration frequencies was chosen to match the most likely sources of mechanical vibration expected in the ATLAS SCT. The vibrations were generated in this GLI by driving the PZT on which the retroreflector was mounted with the amplified output of a sinusoidal oscillator.

A set of ten FSI scans were recorded for each setting of GLI vibration amplitude and frequency. The measurements were made with vibration frequencies of 10 Hz, 20 Hz, 35 Hz and 50 Hz. A further set of measurements were recorded at 35 Hz with GLI signal reduced using ND filters, as in the measurements discussed in section 5.4.2 above.

Raw GLI data in the presence of vibrations

Some examples of the GLI signal at different levels of vibration amplitude are shown in Fig. 5.20 together with the sinusoidal fit based on the technique discussed in chapter 3. As the vibration amplitude increased, the modulation of the local GLI phase of each data point was increased and the best fit sinusoidal amplitude collapsed, because the χ^2 could be lowered during the search for a minimum, by decreasing the value of I_{AC}.

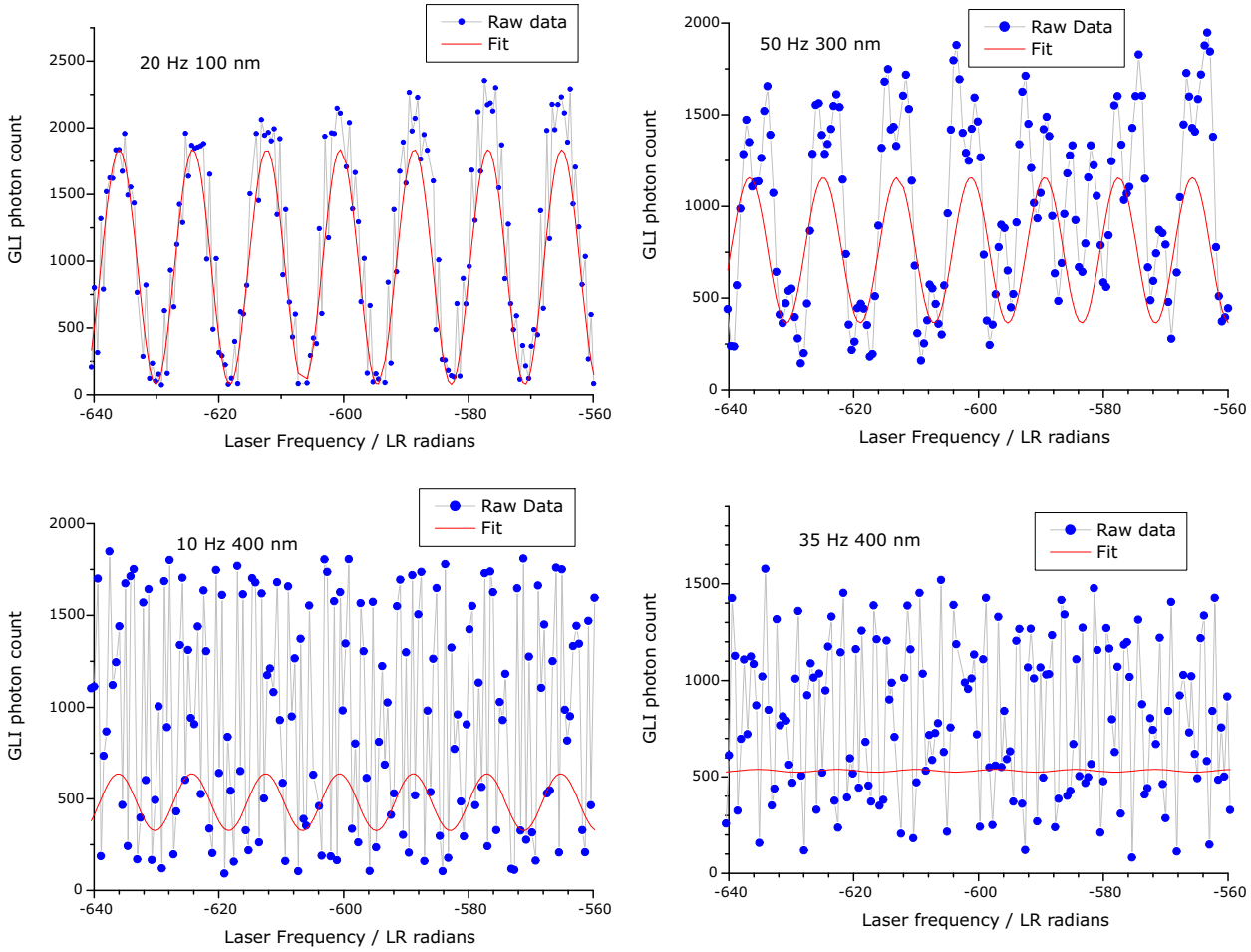

Figure 5.20: *Typical examples of GLI signal, modulated by interferometer vibration and the corresponding sinusoidal fit. In each case the peak to peak amplitude is given together with the vibration frequency.*

Alternative definitions of χ^2 for sinefitting

The change in GLI phase during a vibration cycle due to vibration alone, is related to the peak to peak vibration amplitude A_0 by

$$\begin{aligned} \Delta\Theta_{\mathrm{VIB}} &= \left(\frac{2\pi}{c}\right)\nu 2nA_0 \\ &= 4\pi\left(\frac{nA_0}{\lambda_0}\right) \end{aligned} \tag{5.12}$$

As $\Delta\Theta_{\mathrm{VIB}}$ approaches 2π it becomes more and more difficult to see the periodicity in the GLI signal due to the fringes generated by FSI, given the disruption caused by the vibration.

The fit quality parameter used to guide MINUIT was as defined in equation 3.25, reproduced here, as

$$\chi^2 = \sum_i \left(\frac{I_{\mathrm{DC}} + I_{\mathrm{AC}}\cos\left(\frac{X_i}{q}+\alpha\right) - Y_i}{\sigma_i}\right)^2 \tag{5.13a}$$

where

$$\sigma_i = Y_i \tag{5.13b}$$

In the case where significant vibration dominates the apparent structure of the raw GLI signal, the χ^2 was easily lowered significantly by decreasing the value of the fit parameter I_{AC}. This is exactly what the MINUIT search did in the examples shown above in Fig. 5.20.

Once the value of the fit parameter I_{AC} was very small compared to the real amplitude of the GLI fringes, the profile of χ^2 against fitted phase ratio q was smoother, no longer exhibiting any significant minima, with no features of any kind in the vicinity of the correct phase ratio of the GLI. This is shown in Fig. 5.21 for the 35 Hz, 400 nm example from the lower right quarter of Fig. 5.20. It can also be seen from this figure that the profile of χ^2 against GLI phase offset α, was also smooth, given the small value of I_{AC}, hardly changing when α was moved through $\pm\pi$, showing that even an inversion of the fit function was barely penalised by the local χ^2 profile.

The loss of χ^2 structure with the reduced value of I_{AC} was found to be due to the data point dependent choice of weighting factor σ_i in the definition given in equation 5.13b. If the final fit parameters from the settled fit shown in Fig. 5.21 are retained, but the weight is redefined so that

$$\sigma_i = 1 \tag{5.14}$$

(or any common constant value), the revised two-dimensional profile of χ^2 against q and α takes the form shown in Fig. 5.22, with a distinct deeper minimum at a phase ratio of $q = 1.88$ despite the low value of I_{AC}.

An alternative choice as common weight for all points in the definition of χ^2, is to use the square root of the absolute value of AC amplitude fit parameter[4], so that

$$\sigma_i = \sqrt{|I_{\mathrm{AC}}|} \tag{5.15}$$

The effect of this choice of weight, is to *penalise* reduction of the AC amplitude of the fitted sinusoid as seen in Fig. 5.22, when fitting (with the χ^2 weight according to equation 5.15)

[4]If the weight were defined to be I_{AC}, then this fit parameter would no longer represent that degree of freedom and there would only be three of the the four fit parameters tested in the fit function.

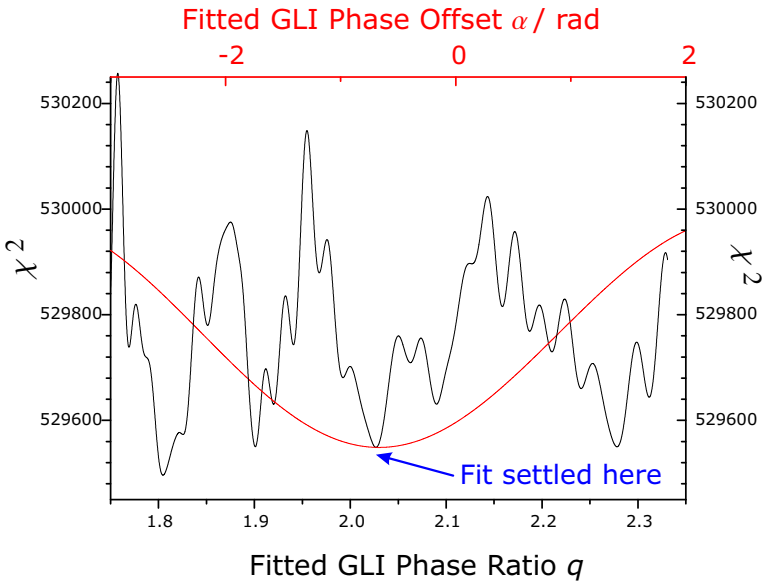

Figure 5.21: *Two dimensional profile of χ^2 (using weight defined in equation 5.13b) in vicinity of fitted minimum, for GLI signal recorded with 35 Hz, 400 nm vibration. BLACK : χ^2 against q (Note the absence of a minimum anywhere near the correct value of $q = 1.881$) RED : χ^2 against α, shows that even when the trial sinusoid is wrong by π, the χ^2 penalty is an increase of less than 800 ppm.*

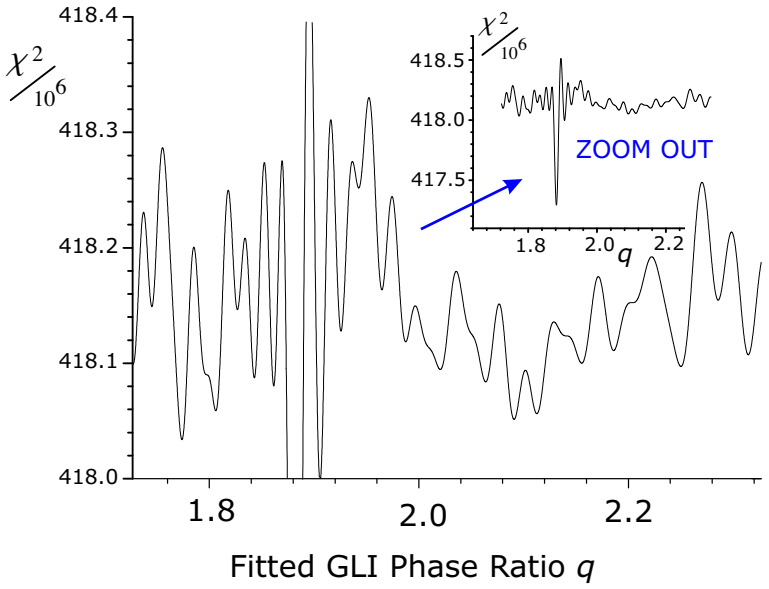

Figure 5.22: *Profile of χ^2 (using constant weight on each point) against q for the same GLI signal as was fitted in Fig. 5.21, with all other fit parameters left unaltered. With only the χ^2 weight altered, a distinct minimum appears at $q = 1.88$, corresponding to the real GLI length.*

the same data as shown in Fig. 5.21. The new fit function is compared with the same raw interferometer signal in Fig. 5.23 and the corresponding χ^2 profile against fitted phase ratio q with this choice of weight is shown in Fig. 5.24. This is very similar to the profile shown with constant weight in Fig. 5.22. Hence any χ^2 with a common weight for all data

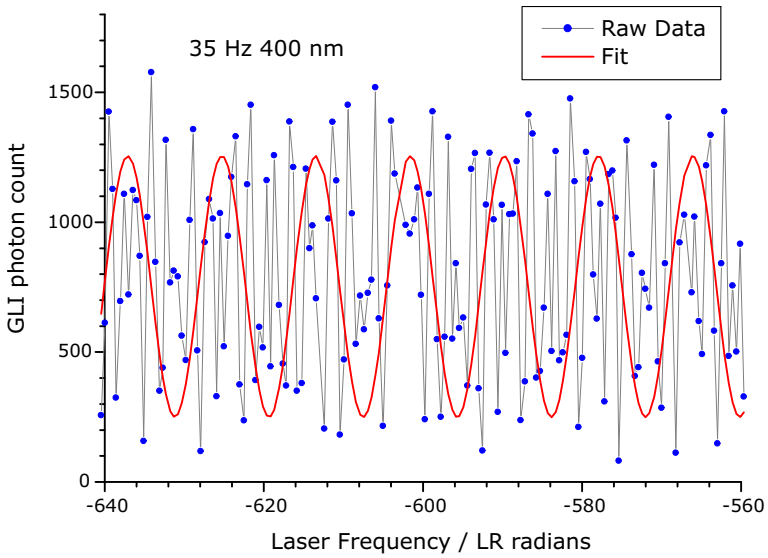

Figure 5.23: *Comparison between GLI data in the presence of (35 Hz 400 nm) vibration and corresponding sinusoidal fit based on form of χ^2 using weight defined by equation 5.15.*

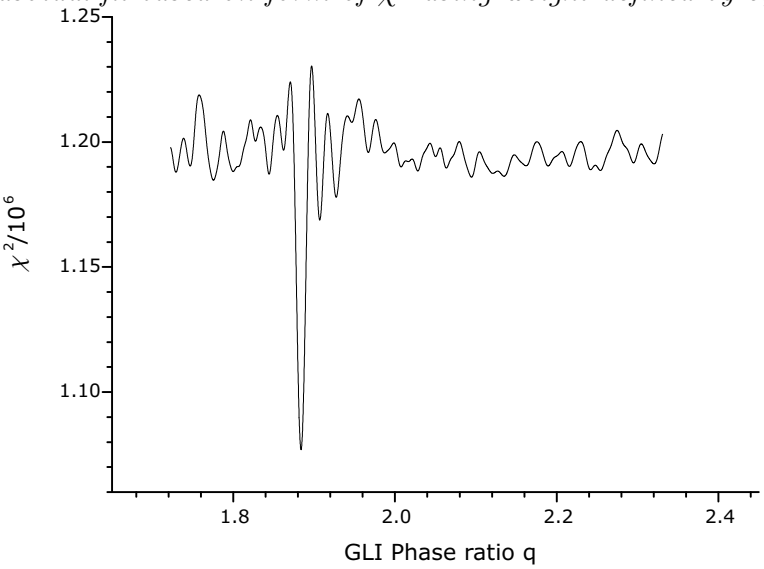

Figure 5.24: *Profile of modified χ^2 versus q for sinefit to GLI data shown in Fig. 5.23.*

points, presents a clear minimum at the GLI length ratio, even in the presence of significant GLI vibration. The extent to which the true minimum will survive even larger vibration amplitudes is an area for further investigation.

The GLI data recorded in the presence of vibrations were fitted to a sinusoidal function using χ^2 with two of the above choices of weight σ_i. The first, defined by equation 5.13b, which matches the choice of weight used for all the GLI length measurements presented above and separately, with the weight as defined by equation 5.15.

At low vibration amplitudes, there was negligible difference between the linking results based on the two different versions of χ^2, for sinefitting. At larger vibration amplitudes, the common weight fitting had the clear advantage by continuing to exhibit a clear GLI signal in the χ^2 profile, which was lost to the fitting which was weighted by the alternative, point dependent definition. The length measurement results presented below for a GLI with a vibrating retroreflector, were based on linking subscans fitted to sinusoids using the

definition of χ^2 weight given by equation 5.15.

GLI extrapolation order number corrections

As noted above for the measurements made with lower GLI signal, (presented above in section 5.4.2) the errors in the single subscan GLI extrapolations over the linking bridge of 3.5 THz were sometimes larger than $\pm\pi$, larger in some cases by several 2π cycles for larger vibration amplitudes. These extrapolation errors were corrected by hand in the results presented here, to allow the GLI phase errors and precision limits to be estimated. In principle the same linking results could have been achieved instead using more than two subscans. The number of scans for which corrections need to be applied are listed according to vibration frequency, together with the corrections for low GLI signal measurements in Table 5.4.

Table 5.4: Number of scans for which the linking extrapolation needed GLI cycle corrections for measurements presented in section 5.4.

	Measurement category					
Number of 2π cycles in correction	Low Power	GLI Vibration frequency				
		10 Hz	20 Hz	35 Hz	(Lower Power)	50 Hz
-4			1			
-3			1		1	2
-2		1	1	2	3	1
-1	8	10	12	4	16	10
0	35	29	46	41	23	28
1	6		5	2	5	9
2			2		1	1
3			1			
4				1		
7			1			
8					1	

Vibration Results

The linking based GLI length measurements after corrections to the extrapolations had been made, are shown in Fig. 5.25 and Fig. 5.26. The mean length from each group of ten scans recorded at a given vibration amplitude and frequency is shown in Fig. 5.25 and the standard deviation of each group of ten measurements is shown in Fig. 5.26. These measurememts do include the small corrections for air refractivity. These measurements may be validly compared with the refractive index corrected low SNR measurements shown above in Fig. 5.18. Both sets of measurements cluster about the same 456.660 mm GLI length, within the observed errors.

Discussion of the vibration measurements

The vibrations in the GLI degraded the accuracy of the fitted phase ratio extracted from sine fitting the data from individual lasers in each fine tuning subscan. The phase ratio used for

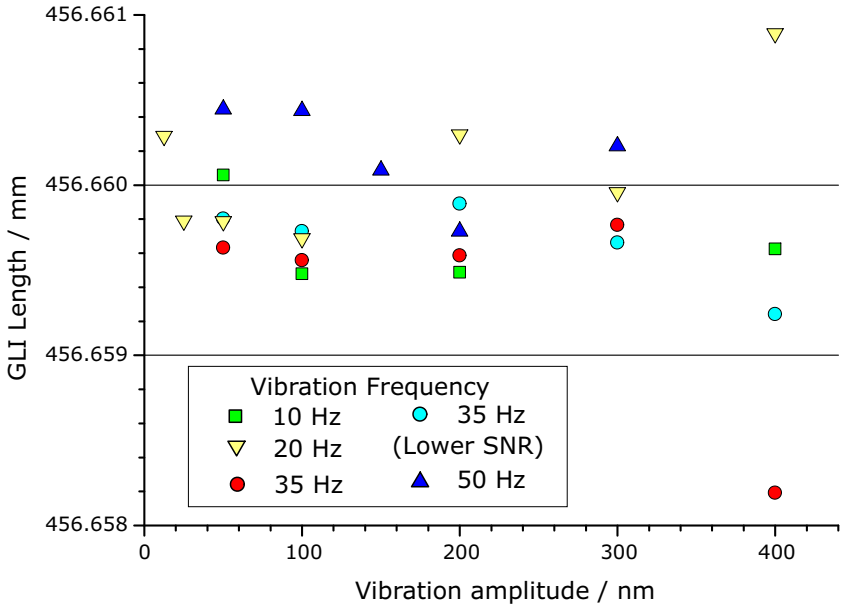

Figure 5.25: *Mean GLI length from groups of ten measurements made in presence of retroreflector vibrations with the indicated frequencies and amplitudes.*

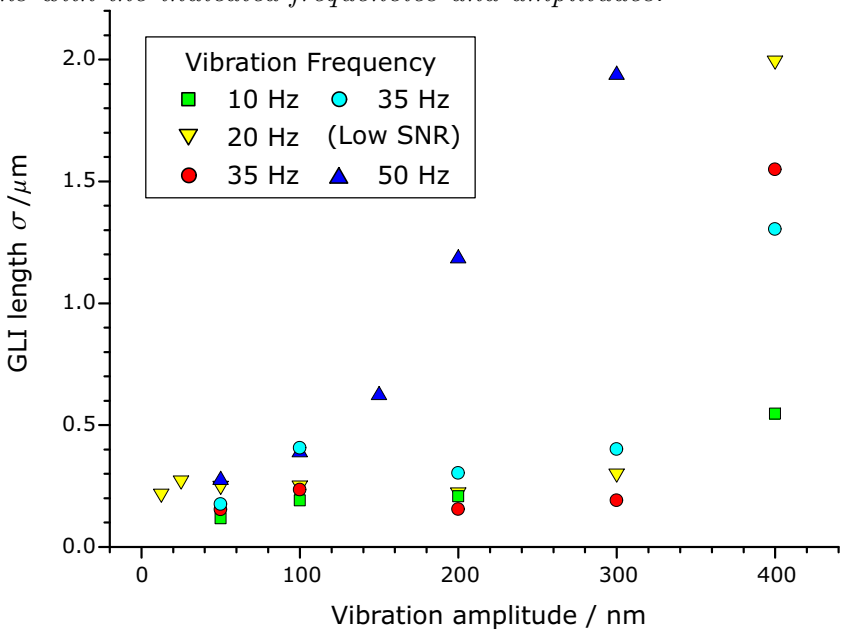

Figure 5.26: *Standard deviation from each group of ten GLI length measurements made in presence of retroreflector vibrations.*

the linking extrapolation of the GLI phase, often needed correcting, with larger corrections required more often at larger vibration amplitudes. At vibration frequencies below 50 Hz, the size of the required corrections to the phase ratio, increased significantly at a peak to peak vibration amplitude of 400 nm. At 50 Hz, (the same frequency as the level 2 timing system which governed the rate of data point acquisition for the fine tuning subscans), the error in the fitted phase ratio increased steadily with increasing vibration amplitude.

The change of χ^2 weight allowed more accurate values of GLI phase ratio to be extracted from sine fitting. Even with this improvement to the accuracy, it was still necessary to correct the extrapolations for linking two subscans separated by 3.5 THz, although the numbers of

2π cycles needed in the larger corrections were reduced.

The vibration conditions which gave rise to significant errors in the extrapolation phase ratio, corresponded to cases where the final linked results had the largest errors, showing that the anchor point phases were also affected by the vibration. These anchor point phase errors can partly be attributed to errors in the phase ratio used for the inter-subscan drift correction as discussed further in chapter 6. Possible refinements of the measurement technique which could reduce the effects of vibration are also discussed in chapter 6.

5.4.4 Spurious reflections

The relative positions of the carbon fibre GLI components were slightly altered in the interferometer measured here, which was slightly shorter, than the 456.7 mm GLI discussed in the previous two parts of this section. The tilt angle for the pellicle beam-splitter was smaller, giving rise to a significant spurious reflection, which interfered with the retroreflector and beam-splitter V reflection modes.

An example of the raw GLI data together with the fitted sinusoid, is shown in Fig. 5.27. The corresponding profile of the χ^2 (using the point dependent definition of σ_i given by equation 5.13b) against GLI phase ratio q is shown in Fig. 5.28. This has a secondary minimum at a longer length scale of around 480 mm which corresponds to an optical path difference between the beam-splitter V mode and either of the two possible directions for the optical path of the spurious mode shown in Fig. 5.29.

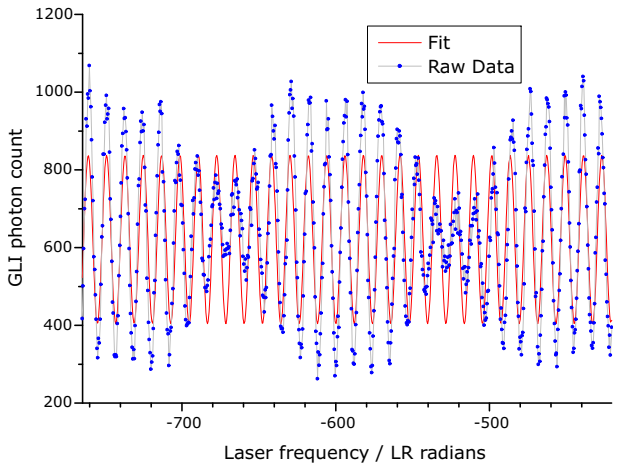

Figure 5.27: *Raw GLI data in the presence of a spurious reflection mode, together with the fitted sinusoid.*

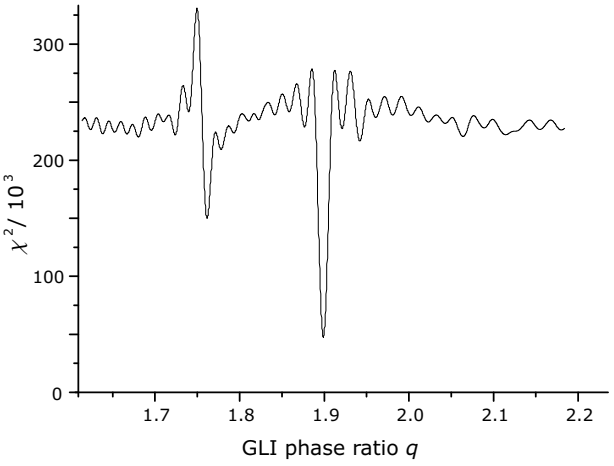

Figure 5.28: *The χ^2 profile for the GLI signal and fit shown in Fig. 5.28. The secondary minimum on the left indicates the length scale of the spurious reflecting mode.*

Measurement results

The linked results from the five scans recorded in the presence of the spurious reflections are shown in Fig. 5.30. The GLI length was approximately 4 mm shorter than length measured in the results presented above, this is consistent with the changes in the positions of the GLI components.

The linking extrapolations of the first two scans needed a correction of 2π GLI radians. The results shown in Fig. 5.30, are after these corrections to the extrapolations. The standard

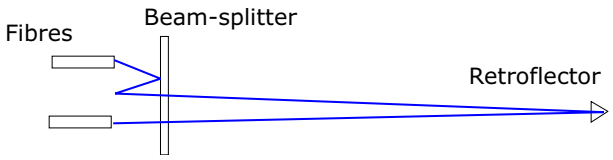

Figure 5.29: *Simplest possible reflection modes for the spurious reflection in the signal shown in Fig. 5.27. The two possible reflection modes follow the same path, differing only in direction. The precise location of the midpoint reflection is unknown.*

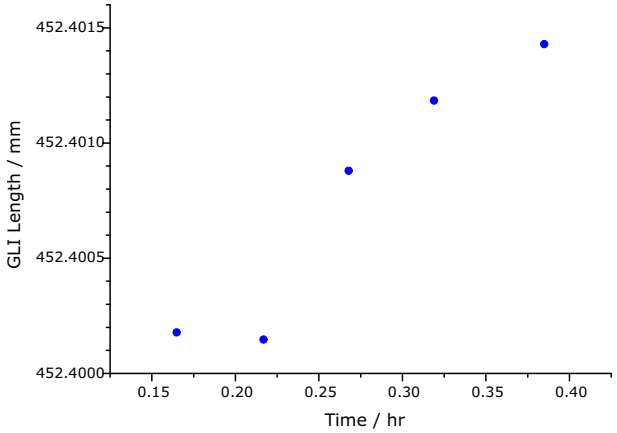

Figure 5.30: *Linked GLI length measured in the presence of spurious reflections.*

deviation of 580 nm is larger than 1 ppm, which is significantly larger than the spread of any group of results with reduced GLI SNR shown in Fig. 5.18 above.

As seen with weaker spurious reflections in the single subscan measurements of Set 1, (presented in chapter 4), spurious reflections can significantly degrade measurement precision, even when two subscans are linked together.

Further work would be needed to understand how the induced GLI phase error varies with the strength and length scale of spurious reflections. At the time of writing, potential spurious reflections in the ATLAS geodetic grid are being investigated.

5.5 Summary

Grid line interferometers with lengths of 400 mm, 457 mm, 1175 mm and 1195 mm have been measured by linking two 30 GHz subscans, separated by a $\approx$ 3.5 THz coarse tuning interval.

In many cases the 3.5 THz bridge was too large to make an extrapolation of the GLI phase without incurring an order number error which needed to be corrected by hand in the measurements presented here. In a future system, this problem would be dealt with by three or more subscans to span the same 3.5 THz range, so that each linking extrapolation could be made to within $\pm\pi$ GLI radians.

Once the order number errors were removed (by hand), the measurement results reflected the precision which would be achieved if the same 3.5 THz range had been spanned by several subscans.

The inter-subscan drift correction was tested on a 400 mm steel GLI and shown to be vital for maintaining the precision of the linked result. Improvements to this correction are

discussed in chapter 6 and an estimate of the remaining errors shows that a significant part of the remaining measurement error is due to inter-subscan drift. All measurements presented in this chapter, utilised the same inter-subscan drift correction.

The thermal expansion of the GLI was measured over a 6°C range within a 24 hr period. These measurements were shown to be consistent to within a micron, with linked subscan measurements of the same GLI made up to two weeks earlier.

A motion stage was used to extend the 1.2 m length of a GLI over a 20 mm range, to test the linearity of the FSI length measurement. The changes in measured length, (corrected to account for thermal expansion of the steel table between measurements), were directly proportional to the directly measured extensions of the GLI length. The constant of proportionality was very close to unity, with the departure from unity attributed to a scale factor discrepancy between etalon calibrated long reference interferometer and the wavemeter.

The most precise measurements in this work were recorded with a 1195 mm GLI during these tests. The standard deviation of the residual differences between a group of ten length measurements and the changes in GLI length expected from thermal expansion, was 215 nm, less than 0.18 ppm of the GLI length.

The signal from a 46 cm GLI built on carbon fibre was deliberately degraded either by decreasing the power fed to the interferometer, vibrating the retroreflector or inducing spurious reflections within the interferometer.

The effect of reducing the SNR to ≈ 1 on the final linked subscan length measurement was negligible, with the standard deviation for a group of ten measurements remaining smaller than 1 ppm and apparently independent of SNR. Further measurements with even lower SNR are required, to find the limit.

Retroreflection vibration had a much greater impact on measurement precision, with peak to peak vibration amplitudes up to approximately half a wavelength inducing errors of several ppm. It was necessary to change the form of the χ^2 used for sine fitting single subscan data, in order to prevent a collapse in the amplitude of the fitted sinusoid and corresponding loss of the χ^2 minimum at the correct phase ratio. In the presence of vibrations at 50 Hz, (which was in resonance with the data acquisition), the measurement precision degraded steadily with increasing vibration amplitude. At lower frequencies between 50 Hz and 10 Hz, the measurement precision was more or less constant below 1 ppm until the amplitude reached around half a wavelength, where it increased sharply. At 10 Hz, even in the presence of vibrations with half a wavelength peak to peak amplitude, the measurement precision remained at the 1 ppm level. Future work would be needed to investigate the relevent relationships between vibration frequency and data acquisition rates and the precision of FSI length measurements in the presence of larger vibration amplitudes.

A brief investigation of spurious reflections showed that these also have a significant impact on the length measurement precision. A quantitative understanding of the dependence of the induced errors on the strength and length scale of spurious reflection modes will require further work.

Further improvements to the measurement precision should be possible in the future by linking several subscans over a wider frequency scan. The scope for future linking measurements is discussed in more detail in chapter 6.

6. An evaluation of the length measurement technique

6.1 Introduction

The GLI length measurement technique presented in the earlier chapters is evaluated in this chapter. The important issues are highlighted in the initial discussion which includes a guide to the propagation of errors from various sources into the final measured length.

The following sections cover the main sources of error and how some of them might be reduced in future measurements, the factors which limit the measurement precision and important areas for future investigation. The conclusions of this discussion are summarised at the end of the chapter.

6.1.1 Accuracy and precision

The aim of this work has been the demonstration of a *precise* length measurement technique, with a reproducibility better than 1 part per million, rather than an *accurate* length measurement technique which would require verifyable agreeement to within a micron, with the internationally defined standard metre. This level of accuracy was not achievable with the equipment available nor was it required.

A measurement of the grid lines in the SCT, *accurate* to 1 ppm, will also be unnecessary, because :

- The initial alignment of the detector elements will be determined by the initial x-ray survey.
- The role of the FSI system is to monitor *changes* in grid shape from the initial grid shape recorded at the time of the x-ray survey.

An accurate measurement of the conceptual line between grid nodes points, would also require micron accurate knowledge of the offset difference between this conceptual line and the measured optical path. In the ATLAS SCT grid the fact that these offsets will not be known to better 100 μm is not expected to prevent precise grid shape reconstruction provided the offsets are stable to less than 1 μm. The detailed design issues relating to this stability requirement are being addressed at the time of writing.

The corrections for gas refractivity in the SCT will be based on pressure and temperature measurements recorded throughout the volume of the detector and a measurement of the gas composition, which will be predominantly nitrogen but may contain significant quantities of CO_2.

6.1.2 Overview of the issues relating to linking subscans

The effects of different sources of error on the phase ratio determined by linking subscans, manifest themselves as errors in the phase ratio used for the linking and in errors in the (folded) phase values of the anchor points. The linking of the reference phase using etalon peaks and the linking of GLI phase are illustrated in figs. 6.1a and 6.1b respectively. The phase ratio used for extrapolation to the predicted anchor point, has no upper limit to its potential inaccuracy. This is important because the extrapolation is used to determine the order number of the target anchor point. In each of the above illustrations, the potential

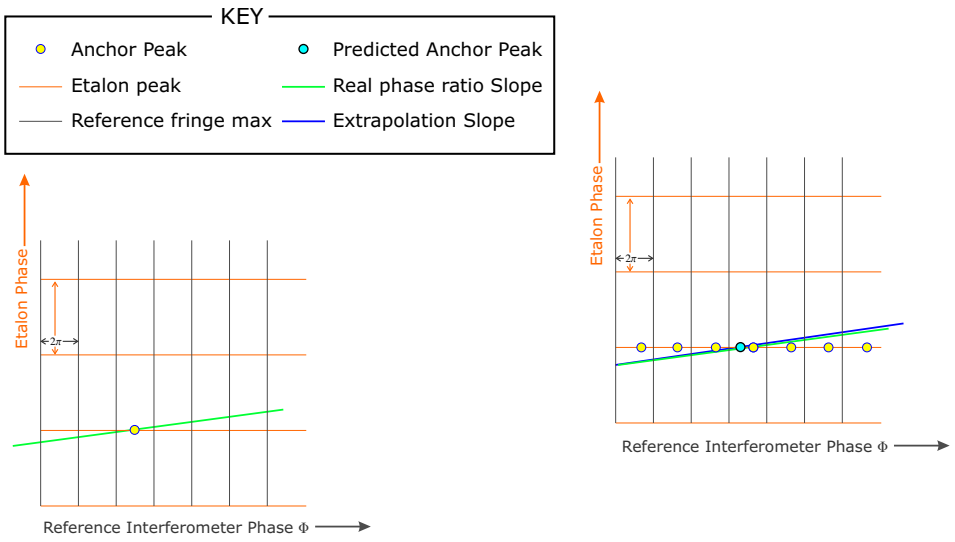

Figure 6.1a: *The linking of the reference phase represented in an interferometer phase co-ordinate system. The reference phase is shown as the independent variable, because the reference interferometer defines the length scale for the FSI system. N.B. The spacing between the subscans is not to the correct scale.*

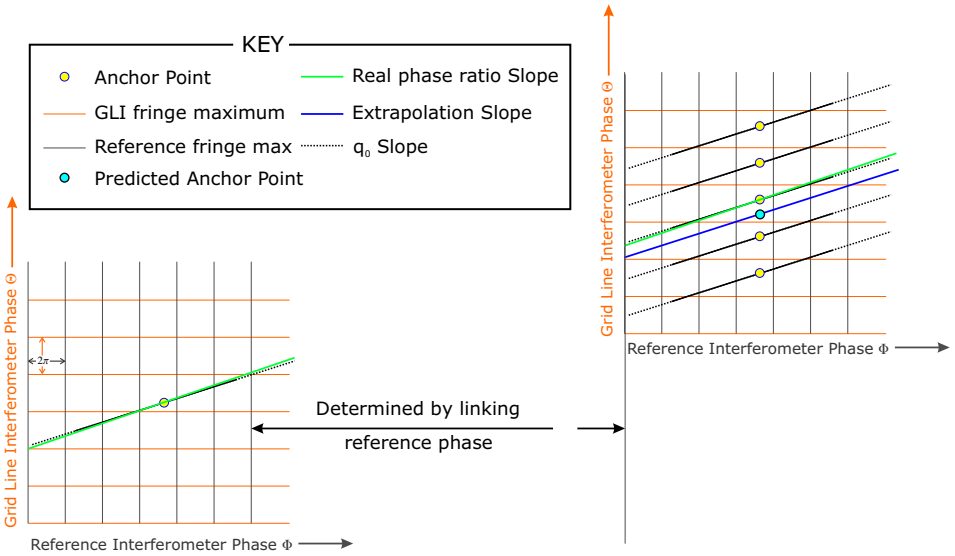

Figure 6.1b: *The linking of the GLI phase represented in an interferometer phase co-ordinate system. N.B. The values of q_0 are different for each subscan and the separation between subscans is not to scale.*

target anchor points, (after correction for inter subscan drift in the GLI case), are an infinite family of local phase values, spaced 2π radians apart. The nearest of these to the *predicted* anchor point is selected.

The accuracy of the extrapolation phase ratio sets an upper limit to the useful size of the linking bridge. An extrapolation error greater than $\pm\pi$ must be avoided. One possible strategy in the design of an FSI system, might be the imposition of a safety margin for the expected extrapolation error $\epsilon_{\Theta}^{\mathrm{HI}}$, which is slightly smaller in magnitude than π. This would reduce the range of allowed bridge sizes as shown in Fig. 6.2 and lower the probability of an order number error.

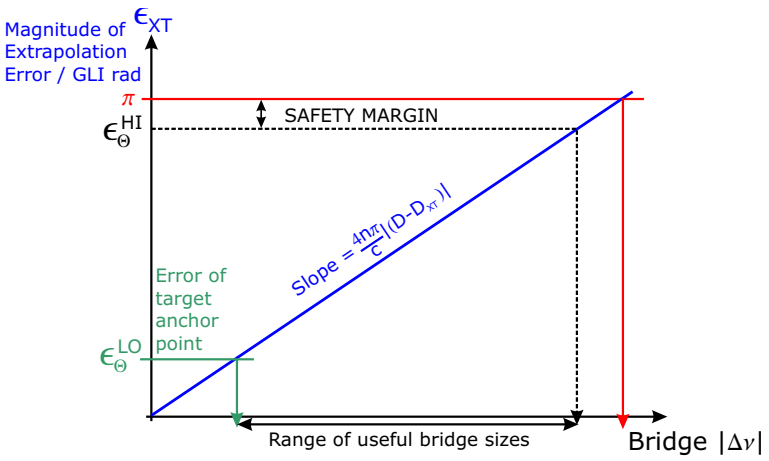

Figure 6.2: *The limitations on the range of useful bridge sizes.*

A consequence of anchor point errors is a lower limit to the useful size of the linking bridge for a phase ratio measurement. If the bridge is too small, the error on the extrapolation is smaller than the error of the target anchor point and the *linked phase ratio* is *less* accurate than the extrapolation phase ratio. Provided the correct order number is selected for the target anchor point, the error in the linked phase ratio is entirely due to the error in the relative phase difference between the two anchor points. This error can be attributed to the phase of the target anchor point. The folded phase values of the anchor points can be in error by at most $\pm\pi$, given the definition of folded phase, but an error at this level would completely rule out all linking by closing the window on useful bridge sizes.

When measuring the GLI, the main aim of linking the reference phase is not an accurate measurement of the etalon phase ratio (or FSR). The main requirement is the determination of the correct long reference order number for the target anchor point, which is unaffected by etalon peak midpoint phase errors small in magnitude[1] compared to $\pm\pi$, whereas any size anchor point phase error directly alters the measured phase ratio. This secondary role of measuring the etalon phase ratio might be used for calibrating the reference interferometers of an FSI system[2] and for partial verification of the etalon peak count as discussed below in section 6.3. Once a linking measurement of the etalon phase ratio has been obtained for a small bridge the improved accuracy can be used to extrapolate for a larger reference phase bridge and the entire process can be repeated. Such an iterative procedure could be used to calibrate a stable reference interferometer system, so that the reference phase can be linked in one step over any required tuning range without generating order number errors[3].

The phase errors on the fitted midpoints of the anchor etalon peaks in the demonstration system are discussed in more depth below in section 6.3.

[1]For the long reference linking to remain unaffected, the sum of the anchor point phase error and the extrapolation error must lie within $\pm\pi$. In principle, with negligible extrapolation errors, the determination of linked reference phase order number can tolerate errors as large as $\pm\pi$, but in practice it would be prudent to ensure that the anchor point phase errors were much smaller than $\pm\pi$, to allow for reasonable extrapolation errors.

[2]The effects of etalon peak fitting errors could be reduced in the calibration procedure by taking the average of many etalon phase ratio measurements.

[3]It is important to note that, this calibration is much more difficult if there are significant gaps in the available tuning range.

Multiple subscan links

The measured GLI phase ratio can be successively improved using multiple links within the same scan. The slope of the blue line in Fig. 6.2 represents the increase of GLI phase extrapolation error with increasing bridge size. This rate of increase is given by

$$m_{\mathrm{XT}} = \frac{4n\pi}{c}|D - D_{\mathrm{XT}}| \tag{6.1}$$

where n is the path average refractive index of the GLI (the reference interferometer is assumed to be evacuated) and D is the GLI length. The GLI phase extrapolation error, ϵ_{XT} for a given size bridge $|\Delta\nu|$ is given by

$$\epsilon_{\mathrm{XT}} = m_{\mathrm{XT}}|\Delta\nu| \tag{6.2}$$

For a given size bridge, the GLI phase extrapolation error is directly proportional to the GLI length error $|D - D_{\mathrm{XT}}|$. For example an error of $\frac{21.4}{n}$ μm leads to an extrapolation error of π for a 3.5 THz bridge irrespective of the GLI length. Therefore, the longer the GLI, the smaller the proportional error in the length D_{XT} needs to be to remain within $\pm\pi$. Equivalently, there are more GLI phase cycles within a given bridge for a longer GLI, therefore an error of $\pm\pi$ is a smaller proportion of the bridge. In a system with GLIs of different lengths, (such as the planned SCT alignment grid), the bridge sizes need to be small enough to accommodate the longest GLIs.

Each link reduces the error in the GLI length measurement from $|D-D_{\mathrm{XT}}|$ to $|D-D_{\mathrm{LINK}}|$ by reducing the GLI phase discrepancy from ϵ_{XT} to the error in the target anchor point, $\epsilon_\Theta^{\mathrm{LO}}$, as shown in Fig. 6.3. The maximum available error reduction ratio from the first link is therefore

$$\frac{|D - D_{\mathrm{XT}}|}{|D - D_{\mathrm{LINK}}|} = \frac{\epsilon_\Theta^{\mathrm{HI}}}{\epsilon_\Theta^{\mathrm{LO}}} \tag{6.3}$$

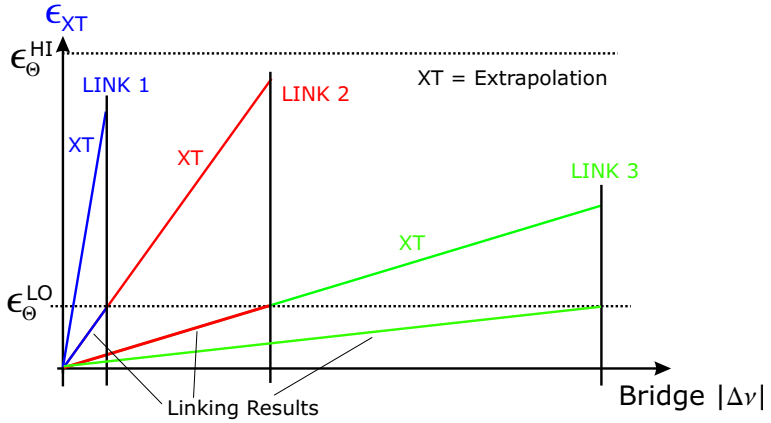

Figure 6.3: *GLI phase ratio error reduction by multiple links.*

The ultimate linking error $|D - D_{\mathrm{F}}|$ is set by the coarse tuning range of the last link, $|\Delta\nu_{\mathrm{F}}|$. The error reduction of the last link is represented geometrically in Fig. 6.3, by the slope of the final link, m_{F} given by

$$m_{\mathrm{F}} = \frac{\epsilon_\Theta^{\mathrm{LO}}}{|\Delta\nu_{\mathrm{F}}|} \tag{6.4a}$$

$$= \frac{4n\pi}{c}|D - D_{\mathrm{F}}| \tag{6.4b}$$

which can be rearranged to give the error on the phase ratio based GLI length measurement after the final link, hence

$$|D - D_{\mathrm{F}}| = \frac{c}{4n\pi} \frac{\epsilon_{\Theta}^{\mathrm{LO}}}{|\Delta\nu_{\mathrm{F}}|} \tag{6.5}$$

Therefore the final linked result is independent of the initial phase ratio error and is only controlled by the anchor point phase error of the *final* link[4] and the tuning range of the final bridge. The limitation imposed by the initial phase ratio is the minimum number of bridges required to span the final tuning range. The minimum number of bridges required to span $|\Delta\nu_{\mathrm{F}}|$ can be calculated by assuming each link is set so that the extrapolation error before each link just reaches the safety margin value $\epsilon_{\Theta}^{\mathrm{HI}}$.

The maximum allowed span of each bridge, $|\Delta\nu_i|$ is set by the slope of the initial extrapolation prior to that link m_i and the safety margin according to

$$|\Delta\nu_i| = \frac{\epsilon_{\Theta}^{\mathrm{HI}}}{m_i} \tag{6.6}$$

For all links after the first, the extrapolation error is set by the previous link, hence

$$m_i = \frac{\epsilon_{\Theta}^{\mathrm{LO}}}{|\Delta\nu_{i-1}|} \tag{6.7}$$

which can be iteratively substituted into equation 6.6 and related to the bridge of the first subscan (which is limited by the accuracy of the single subscan based initial extrapolation), to give

$$|\Delta\nu_i| = \left(\frac{\epsilon_{\Theta}^{\mathrm{HI}}}{\epsilon_{\Theta}^{\mathrm{LO}}}\right)^{i-1} |\Delta\nu_1| \tag{6.8}$$

which can be rearranged for the final number of bridges, F needed to reach $\Delta\nu_{\mathrm{F}}$,

$$\frac{|\Delta\nu_{\mathrm{F}}|}{|\Delta\nu_1|} = \left(\frac{\epsilon_{\Theta}^{\mathrm{HI}}}{\epsilon_{\Theta}^{\mathrm{LO}}}\right)^{F-1} \tag{6.9}$$

the exponent can be extracted by taking the logarithm of each side and rearranging to give

$$F = 1 + \frac{\log\left(\frac{|\Delta\nu_{\mathrm{F}}|}{|\Delta\nu_1|}\right)}{\log\left(\frac{\epsilon_{\Theta}^{\mathrm{HI}}}{\epsilon_{\Theta}^{\mathrm{LO}}}\right)} \tag{6.10}$$

Error Contributions

A simplified schematic view of the relationships between the sources which contribute to the extrapolation and anchor point phase errors, is shown in Fig. 6.4.

The different contributions are each discussed in more detail below, starting with the reference phase errors, because the reference phase frequency axis is used as the basis for all GLI and etalon signals which are used for fitting. The level of reference phase errors is shown to be around 3 mrad (in reference phase units). In the following section, the error in fitting the midpoints to each etalon peak is estimated to be 310 mrad, (in reference phase units) which is large enough to rule out the reference phase errors on the data points as the dominant contribution.

[4]Since the anchor point errors from earlier links are coupled into the error in the final extrapolation which is then rejected by the final link.

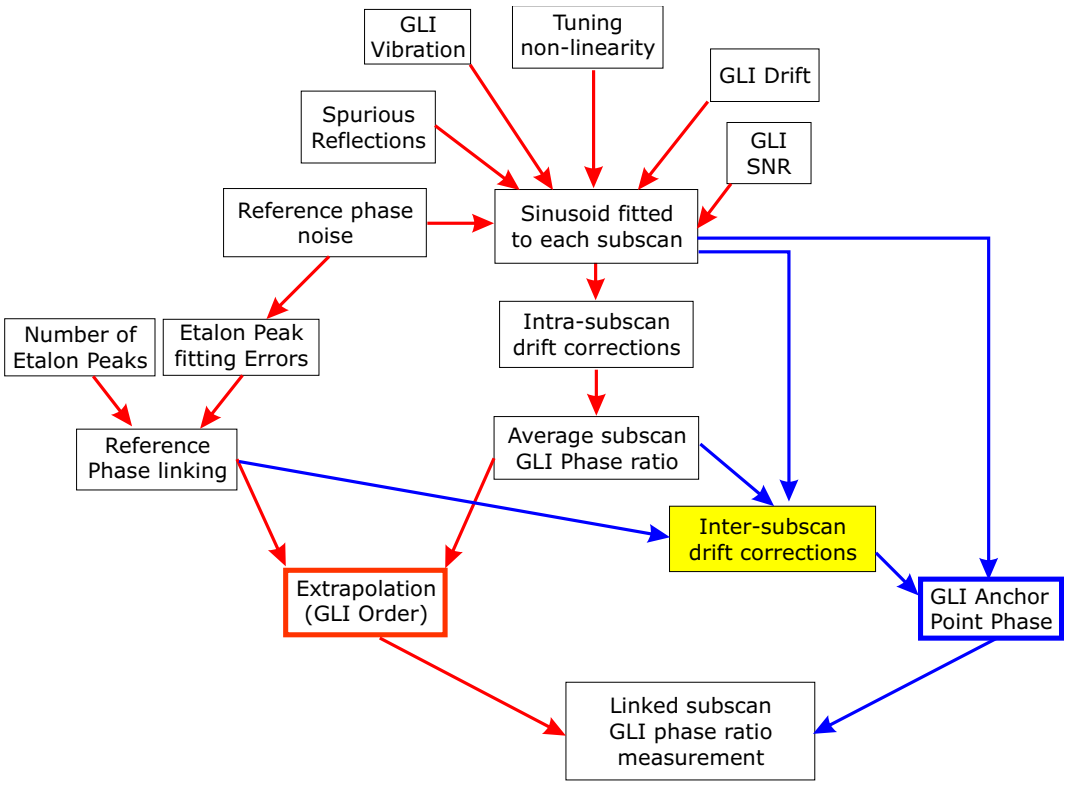

Figure 6.4: *Simplified schematic showing contributions to linking extrapolation and anchor point phase errors.*

The factors which degrade the precision of the GLI phase ratio obtained from fitting sinusoidal functions to data from single subscans are examined. The influence of the phase ratios fitted to GLI data is shown to be very important, because the single subscan phase ratio couples into the GLI anchor point phase error via the inter-subscan drift correction (highlighted in Fig. 6.4). This coupling is discussed and shown to be a significant contribution.

A modified form of inter-subscan drift correction is demonstrated using the linked phase ratio to perform a second correction for inter-subscan drift to obtain an improved linked phase ratio. The improvement is used to estimate the contribution to anchor point errors from the initial inter-subscan drift correction.

6.2 Reference phase errors within each subscan

This section is a detailed consideration of the factors which contribute errors in the extracted values of reference interferometer phase in each subscan.

The two main failure modes in extracting and unwrapping the reference phase axis of each subscan, namely :

1. Extraction failures

2. Unwrapping glitches

are discussed above in chapter 3. The extraction failures are automatically removed from the subscan data, but if several occur in a cluster, this can lead to an unwrapping glitch. At the time of writing no guaranteed method for removing all glitches has been found and this

is therefore an important subject for future work. The focus in this section is therefore on an estimation of the errors induced by phase stepping and phase extraction. As the causes of extraction errors become stronger, the probability of generating extraction failures increases.

6.2.1 Reference phase extraction errors

The potential contributions to the phase extraction errors are :

- Reference mirror PZT non-linearity.
- Interferometer signal digitisation.
- Random interferometer photodetector noise and laser power fluctuations.
- Reference mirror PZT voltage fluctuations (or equivalent acquisition timing jitter).
- Interferometer OPD fluctuations.
- Electrical hum.

The presence of electrical hum was minimised as far as practical by the layout of the demonstration system as mentioned in chapter 2. Electrical hum would have contributed signals at the 50 Hz frequency of the mains supply and integer multiple frequencies. These signals would have appeared in the tuning control voltage of each laser, leading to frequency jitter, in the PZT drive voltage leading to fluctuations and in the photodiode signal.

The frequency of the level 2 timing system was also 50 Hz to be as fast as it could be set given the timing constraints discussed in chapter 2. There was hum present on the laser tuning voltage, which seemed to be coupling from the laser power supply. This was observed in the signals of the reference interferometers. The PZT drive voltage and the photodiode signals showed no evidence of significant hum contributions. It has been possible to explain the observed long reference phase errors without the need to separate out contributions from hum, so this noise source is not considered further.

For the following discussion, the phase extraction error dependence on each of the above effects was studied in isolation using simulations. In each simulation, the extracted phase value Φ was compared with the generated interferometer phase value in the range $-\pi \leq \phi_{\mathrm{T}} < \pi$, based on the four simulated phase step intensity signals given by

$$I_i = I_{\mathrm{DC}} + I_{\mathrm{AC}} \cos\left[\phi_{\mathrm{T}} + \left(i - \frac{5}{2}\right)\alpha_{\mathrm{S}}\right] \tag{6.11}$$

In each simulation, the interferometer signal was modified by the noise source under consideration. The range of explored noise levels was wider than needed to simulate the long reference interferometer of the demonstration system, because the same results can be applied to other systems in which phase stepping might be applied the GLI signal[5].

The folded phase error of those phase extractions which did not fail[6] were calculated using

$$\epsilon_\phi = \mathbf{fold}\left(\Phi - \overline{\phi_{\mathrm{T}}}\right) \tag{6.12}$$

[5]Acousto-optic modulation might be used to induce fixed size frequency steps in the light coupled to the GLI, allowing a form of phase stepping to be implemented. Some of the noise sources considered here would be present in such a system and are simulated here to guide the design of such a system.

[6]In length measurement scans, all extraction failures were labelled as Type I errors and rejected from the data used to construct the unwrapped reference phase as explained in chapter 3. These failures were therefore also rejected from the data under consideration here, so that the extraction errors in the remaining data could be estimated.

where $\overline{\phi_T}$ is the *mean* of the interferometer phase values at each of the four phasesteps. The mean is used, to cover those cases where the interferometer phase is not constant over the four phasesteps.

For noise sources with some random element, the values of ϵ_ϕ from all successful extractions were combined to produce a root mean square extraction error, labelled below as the RMS extraction error.

For the noise sources which are reproducible, such as the PZT non-linearity, the direct extraction error was taken from a single extraction trial at each value of interferometer phase in the above range.

PZT non-linearity

The PZT bias voltage, (at the midpoint of the phase step pattern) and the phase step voltage increment both needed to be optimised. The optimum phase step size for a nearly linear phase step mechanism using the Carré type algorithms is around 110°, as reported by [Che85], for example.

The RMS extraction error was calculated for different phase step sizes in a simulation which accounted for the non-linear PZT response presented in Fig. 2.21. The simulated PZT was biased about the stationary point in the PZT response at 15.6978 V to minimise the effects of the non-linearity and the phase step size was converted into a voltage step using the rate of PZT extension in nm per volt at the stationary point, (where it is maximised). The results of this simulation for different levels of signal to noise, (using the Gaussian distributed intensity noise model discussed below in section 6.2.1), are shown in Fig. 6.5.

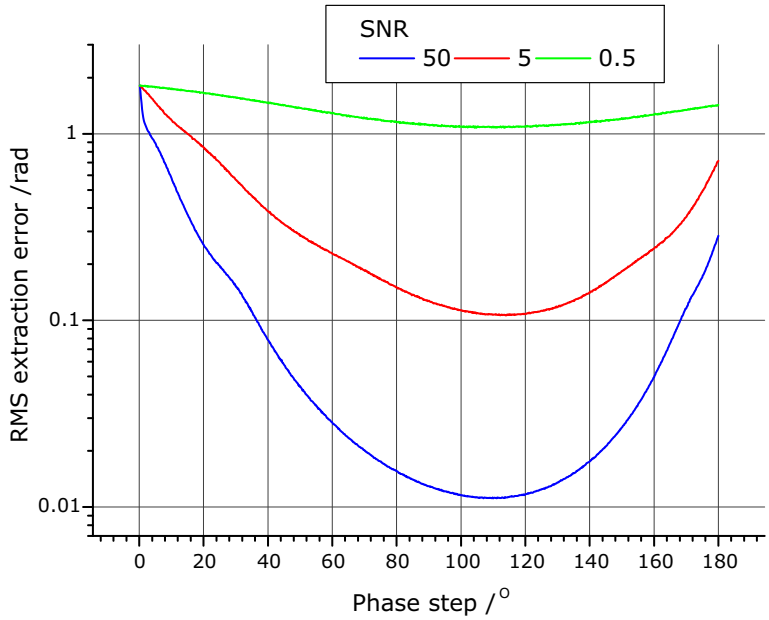

Figure 6.5: *Phase extraction error v. phase step size for the non-linear long reference mirror PZT.*

The phase step size α_S was set to ≈110° in the demonstration system. In all of the simulations presented below, a phase step size of 109.5° was used. The dependence of extraction error on PZT bias is shown in Fig. 6.6, against interferometer phase, ϕ_T. This highlights the increasing effect of PZT non-linearity for bias voltages away from the stationary point value of 15.6978 V.

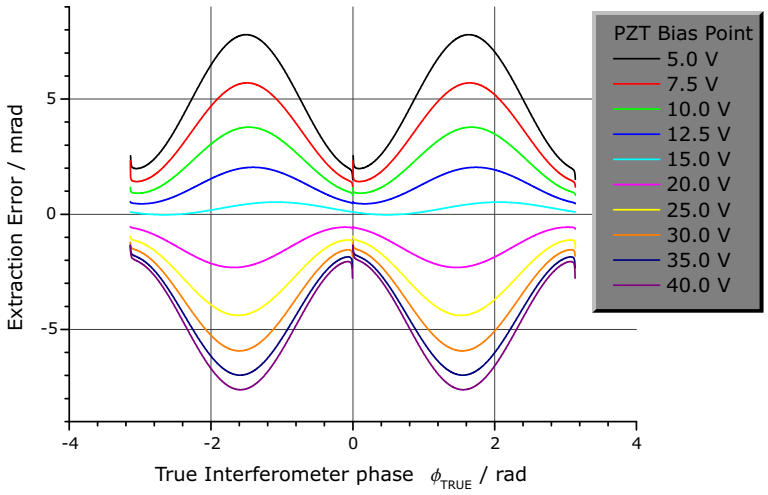

Figure 6.6: *Effect of PZT bias on phase dependence of extraction error.*

These two simulations demonstrate that the choice of PZT bias voltage and phase step voltage increment, used for phase stepping in the long reference interferometer, were close to optimum.

Reference interferometer signal digitisation

The digitisation of the reference interferometer signal by the ADC was a significant contribution to the phase extraction error. This error could be reduced in a future system, by using an ADC with more than 12 bits for digitisation. In the simulation used to explore the effects of digitisation, the value of I_{AC} was set to different values from 1000 down to 1 and the value I_i (given by equation 6.11) for each phase step was then rounded down to the nearest integer, before entering the phase extraction algorithm. The term *digitisation level* will be used to represent the ratio between the digitisation level (unity) and the value of I_{AC}. In this simulation, the digitisation levels from 10^{-3} to 1, were investigated.

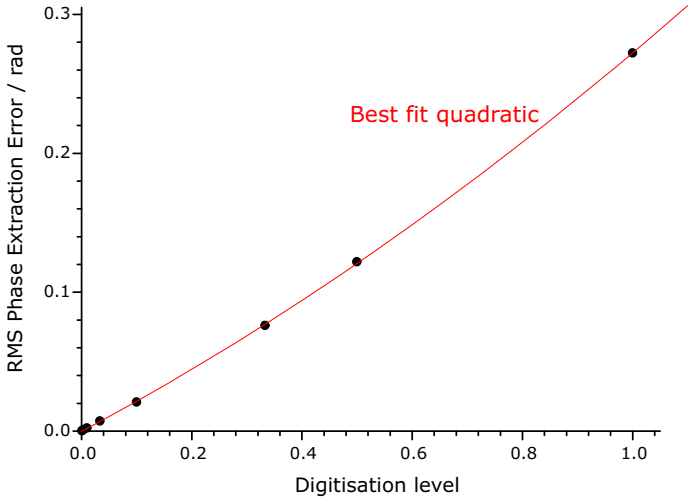

Figure 6.7: *Phase extraction error induced by interferometer signal digitisation.*

The RMS extraction error was found to scale quadratically with digitisation level as shown in Fig. 6.7.

In a GLI with a photon counting detector, the digitisation level would be set by the quantised nature of the detection process. For the GLI signal shown on the right hand side of Fig. 5.17, the digitisation level is approximately 0.5, so a phase stepping system with this level of return signal could be expected to incur a minimum extraction error of more than 100 mrad.

Reference interferometer intensity noise

Two forms of interferometer intensity noise are considered here; slower changes in laser intensity from one phase step to another and rapid, essentially random fluctuations in detected signal, either due to photodetector noise or fast fluctuations in laser power.

The slower changes in laser power were modelled using a linear ramping laser intensity across the four phase steps, with the phase step signal given by equation 6.11 multiplied by a ramp factor $1 + i\delta_{\mathrm{I}}$, where δ_{I} is a constant intensity ramp rate.

The interferometer phase dependence of the extraction error is shown for $\delta_{\mathrm{I}} = \pm 10^{-3}$ in Fig. 6.8.

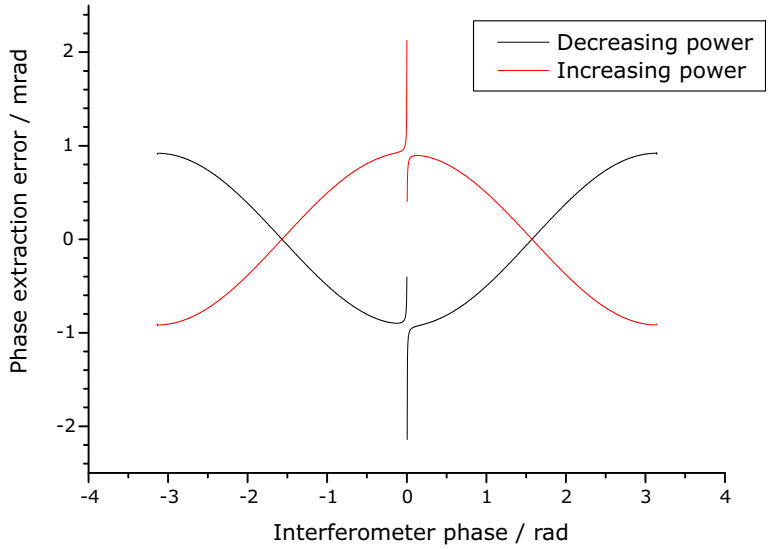

Figure 6.8: *Phase dependence of extraction errors induced by linear ramp in laser intensity.*

The shape of the phase dependence, (ignoring the discontinuities which are always present at $\phi_{\mathrm{T}} = \pm\pi$ and 0), is retained for values of δ_{I} up to 0.01 and scales with $\delta_{\mathrm{I}} \frac{I_{\mathrm{AC}}}{I_{\mathrm{DC}}}$. A change of 1% in the laser intensity between each phase step was considered an upper limit for the rate of change of laser power, so values beyond $\delta_{\mathrm{I}} = 0.01$, were not investigated.

The effect of random fluctuations was modelled by adding a randomly generated Gaussian distributed contribution to each phase step intensity given by equation 6.11. The level of noise will be described below using a signal to noise ratio, (SNR) given by

$$\mathcal{S} = \frac{1}{\sqrt{2}} \left(\frac{I_{\mathrm{AC}}}{\sigma_{\mathrm{I}}} \right) \tag{6.13}$$

where σ_{I} is the standard deviation of the Gaussian distribution of random intensity contributions. The RMS extraction error as a function of SNR is shown over several orders of magnitude in Fig. 6.9, with best fit line given by $0.56\mathcal{S}^{-1}$.

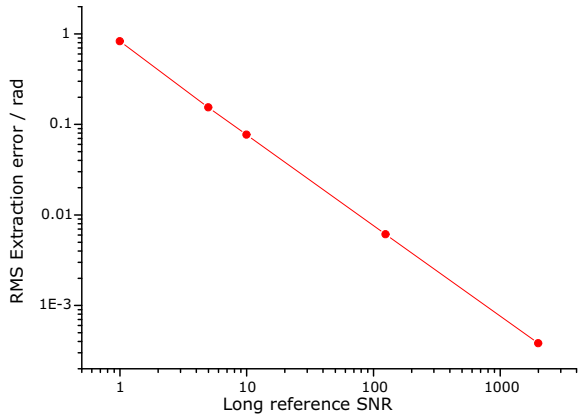

Figure 6.9: *Effects of Gaussian intensity noise on phase extraction errors.*

Linear reference phase fluctuations

Random fluctuations in the laser frequency or interferometer OPD create proportional fluctuations in value of the interferometer phase. If the reference interferometer phase fluctuates away from the deliberately induced phase steps, extraction errors result. In this case, the extraction error is defined as above, to be the folded difference between the extraction result and the mean interferometer phase, $\overline{\phi_T}$.

To assist calculation of the relative changes in laser frequency or interferometer OPD needed to induce a corresponding change in interferometer phase, the conversion table Table 6.1 is provided.

Table 6.1: Conversion between equivalent changes in long reference interferometer phase, long reference interferometer OPD and laser frequency at a laser wavelength of 836.0 nm.

Change in Long Reference interferometer phase	Equivalent changes in	
	Long Reference interferometer OPD	Laser Frequency
1.00 mrad	0.133 nm	27.8 kHz
7.52 mrad	**1.00 nm**	209 kHz
3.60 mrad	0.48 nm	**100 kHz**
2π rad	836.0 nm	174.5 MHz

The quadratic dependence of RMS extraction error on RMS interferometer phase fluctuation is shown in Fig. 6.10.

PZT voltage fluctuations

Random fluctuations in the PZT drive voltage, or equivalently, jitter in the timing of the acquired reference signal, lead to fluctuations in the interferometer OPD at each phase step. An acquisition timing jitter of around 700 ns, would lead to a PZT voltage change of 1 mV. The resulting OPD fluctuations scale non-linearly with the fluctuations in step PZT voltage, through the non-linearity of the PZT response.

The dependence of the RMS extraction error on the level of Gaussian distributed PZT voltage fluctuations is shown in Fig. 6.11. The linear dependence on voltage fluctuation

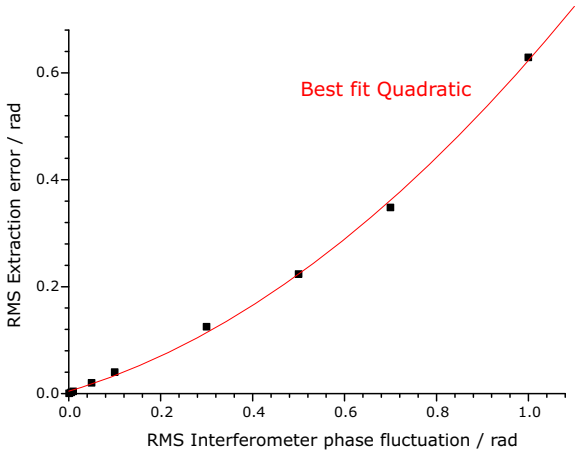

Figure 6.10: *Extraction errors induced by interferometer phase fluctuations.*

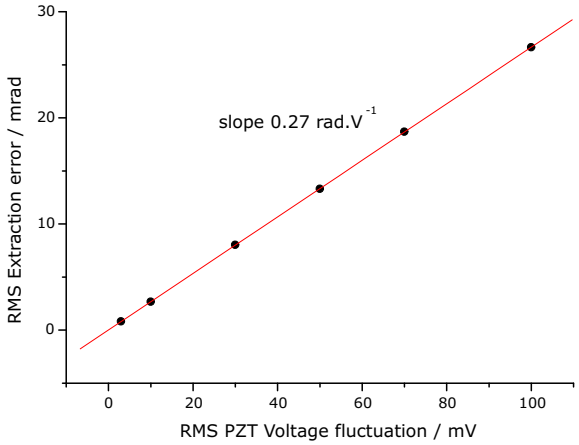

Figure 6.11: *Dependence of extraction error on small PZT voltage fluctuations about the stationary point in PZT response.*

via the non-linear PZT response, which is approximately parabolic in the vicinity of the stationary point, is consistent with the quadratic dependence on linear interferometer phase fluctuations shown in Fig. 6.10.

Combined phase extraction error simulation

The simulations discussed above, represented an interferometer in which a small subset of the potential interferometer noise sources were present. In the remainder of this section, a more realistic simulation is presented, in which all effects are present. This combined simulation was tuned to match observations from the PZT balancing test, (described in chapter 2), using additional information taken from voltage noise measurements with an RMS meter and the laser specifications.

The extracted phase values from the optimised PZT balancing test, are shown in Fig. 6.12, together with best cubic fits to each tuning curve[7].

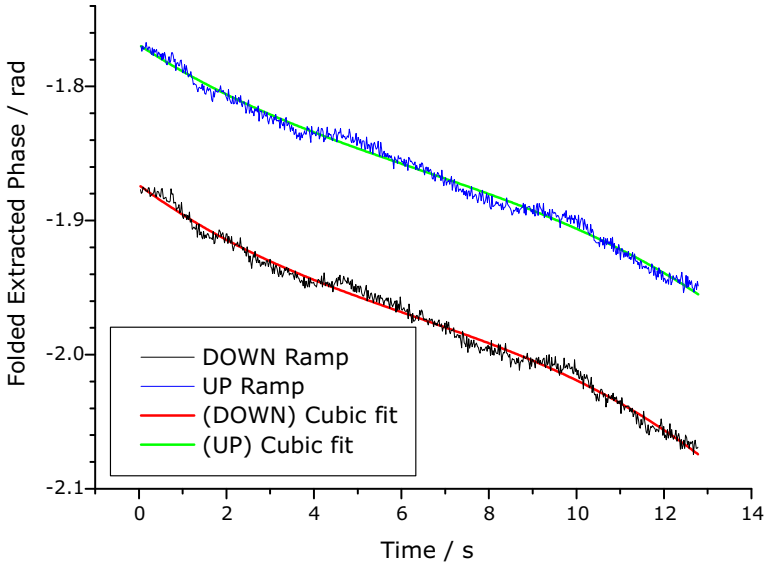

Figure 6.12: *Tuning curves from optimised PZT balancing test. N.B. The data points here have been filtered using the timing matching criteria discussed in chapter 3.*

The two tuning curves are separated by 112 ± 8 mrad which corresponds to a difference in phase step mean interferometer OPD of 7.5 ± 0.5 nm. An estimate for the phase extraction noise can be obtained in two stages. First, the difference between data and cubic fit for each tuning curve is calculated to give the phase extraction residuals shown in Fig. 6.13.

The common mode structure in these residuals, reflects the local small scale differences between the real tuning curve and a cubic best fit. The second stage in estimating the phase extraction noise, involves taking the local difference between residuals for each ramp direction, shown in Fig. 6.14.

The standard deviation of the differential residual signals is around 3.9 mrad. If each phase extraction contributed independently to the differential signal, the RMS phase extraction error is smaller by $\sqrt{2}$ at around 2.7 mrad. This RMS extraction error estimate is only valid for the interferometer phase range of the PZT balancing test, $-2.08 \leq \phi_T \leq -1.88$. The simulated interferometer phase was restricted to this range during the final stage of tuning the combined simulation.

The parameters used for the simulation are given in Table 6.2. The interferometer OPD fluctuation level was varied to see which level of RMS fluctuation would be needed to match the 2.7 mrad estimate derived above.

[7]The laser frequency shifted through around 5 MHz during the 13 s of the test.

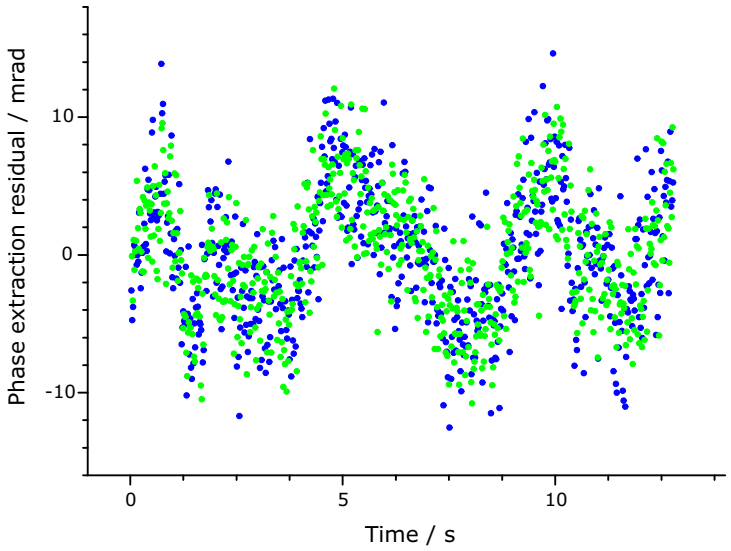

Figure 6.13: *Phase extraction residual differences between tuning curve data and best fit curves from Fig. 6.12. Residuals for the DOWN ramp are in BLUE and for the UP ramp in GREEN.*

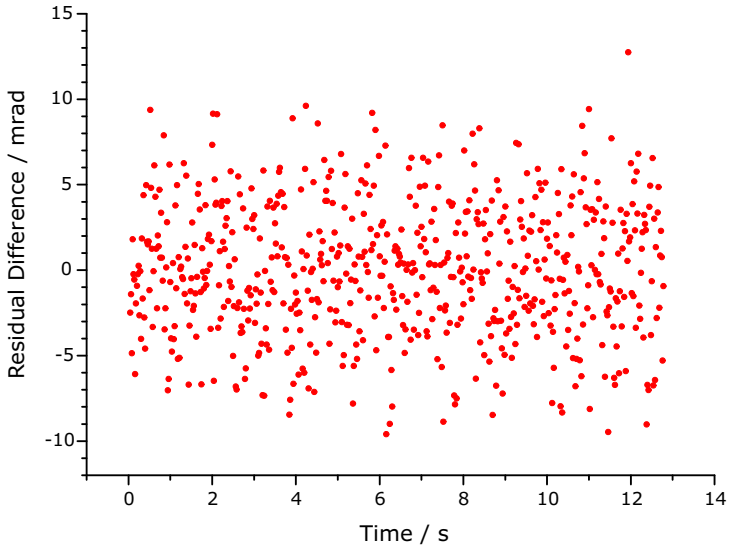

Figure 6.14: *Differential residual signals, taken from differences between each residual point for the DOWN ramp and the corresponding point for the UP ramp in Fig. 6.13.*

The PZT bias, laser wavelength and digitisation level were chosen to match the values in the PZT balancing test discussed above. The phase step size matches the value used in the above simulations, which is very close to the implemented value as seen from the extracted values of α_S taken from the PZT balancing test and shown in Fig. 6.15. The level of detector noise is the ratio between the AC amplitude of the interferometer signals and the measured photodetector noise at the input to the ADC. Similarly, the noise on the PZT drive signal was measured across the input to the PZT. The laser frequency jitter is an upper limit derived from the laser linewidth specification by the manufacturers, which claims that over 50 ms the FWHM linewidth was less than 300 kHz, which corresponds to a 120 kHz RMS frequency fluctuation.

Table 6.2: *Parameters used in combined noise source phase extraction simulation.*

Parameter	**Value**
PZT Bias voltage	15.65 V
Phase step size	109.5°
Wavelength	836.0 nm
Digitisation level	4×10^{-3}
I_{AC} : Detector noise	400 : 1
Interferometer phase ϕ_T	$-2.08 \leq \phi_T \leq -1.88$
RMS PZT drive signal	0.7 mV
RMS Laser frequency jitter	120 kHz

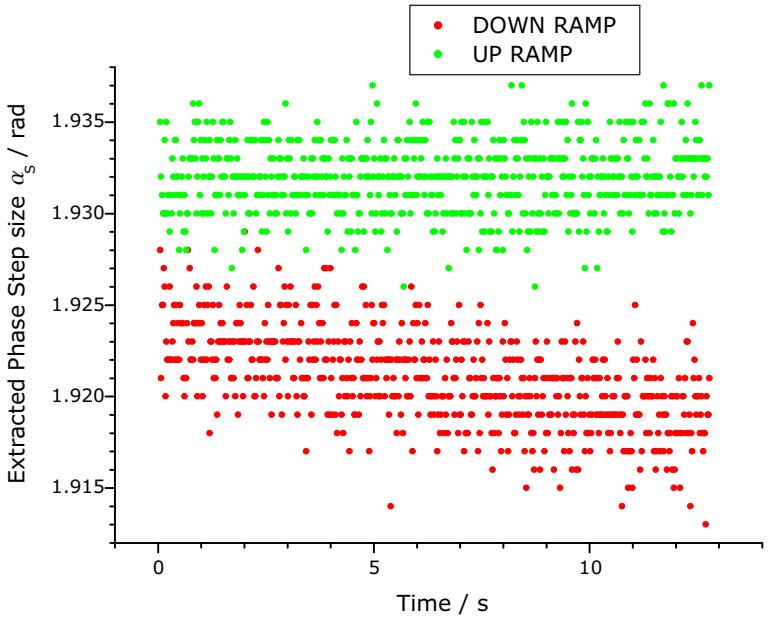

Figure 6.15: *Extracted phase step sizes from PZT balancing tests.*

The RMS phase extraction error from the combined simulation is shown against the level of interferometer OPD fluctuation in Fig. 6.16, from which it can be seen that an RMS level of 0.54 nm corresponds to a phase extraction error of 2.7 mrad.

Once the combined simulation was tuned for the narrow range of interferometer phases $-2.08 \leq \phi_T \leq -1.88$ it was used to model the RMS extraction error over the full interferometer phase range $-\pi \leq \phi_T < \pi$. The dependence of the extraction error on ϕ_T is shown in Fig. 6.17. The horizontal line marks the mean error value of 3.16 mrad.

The relative contribution of the different noise sources to the average 3.16 mrad reference phase error in the combined simulation is shown in Fig. 6.18.

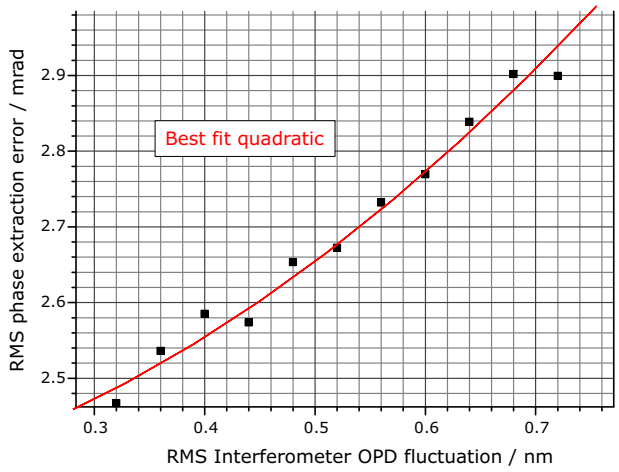

Figure 6.16: *Tuning of the combined phase extraction simulation.*

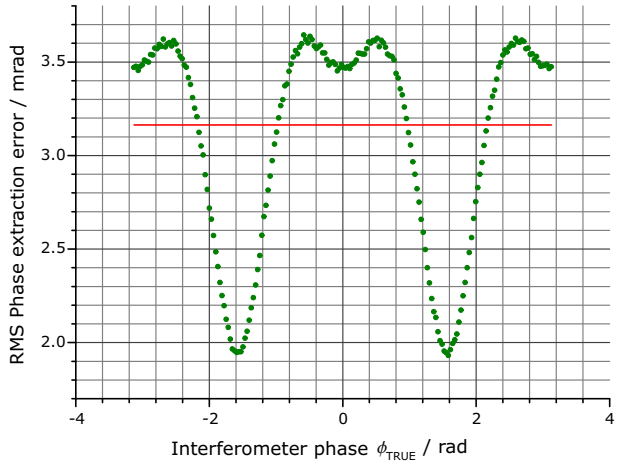

Figure 6.17: *Phase dependence of extraction errors taken from combined error simulation. The red horizontal line marks the average value 3.16 mrad.*

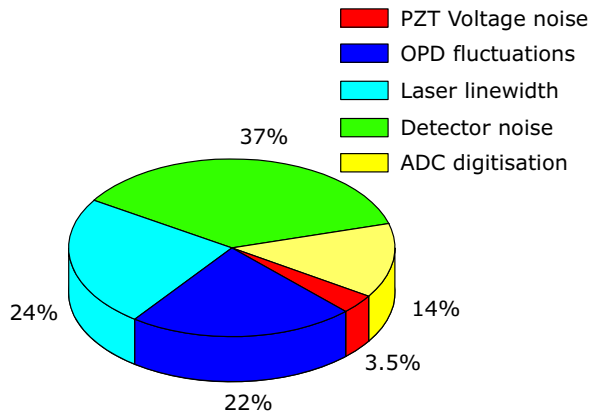

Figure 6.18: *The estimated relative contribution of each noise source to the long reference phase extraction error.*

6.3 Linking issues dependent on the etalon signal

The method of linking the reference phase using etalon peaks involves two potential types of error :

1. Reference phase errors in the midpoints of the fitted etalon peaks.

2. Miscounts of the number of etalon peaks in the linking bridge

Assuming the etalon peak count is correct, peak fitting errors which are too small to give rise to an order number error in the linked reference phase, have no effect on the order number of the GLI phase and so do not perturb the GLI phase ratio determined by linking subscans. The level of the peak fitting errors in the demonstration system is estimated in the first half of this section, showing that the peak fitting technique was always adequate for avoiding reference phase order number errors.

In the second half of this section, the effects of etalon peak miscounts are discussed and the requirements of different strategies for detecting miscounts are considered.

6.3.1 Etalon peak fitting errors

Etalon peak fitting errors, based on the measurements of the etalon FSR given in chapter 5, are presented in this section. The distribution of residual differences between individual FSR values and the fitted temperature dependence from Fig. 5.8, are shown in Fig. 6.19. Each measurement of the FSR was based on the phase difference between the reference phase anchor points separated by N free spectral ranges. The peak fitting error from each anchor point adds a contribution to the error on the reference phase interval over the N free spectral ranges. The two contributions are assumed to be independent and add in quadrature. Given these connections, the errors from fitting the individual etalon peaks can be estimated from the error on the reference phase interval of N free spectral ranges, which is in turn estimated from the FSR residual differences between the individual FSR values and the fitted temperature trend.

Each FSR residual from Fig. 5.8 was multiplied by the number of FSRs in the corresponding reference phase interval (linking bridge) to give the error on the interval. These interval errors are shown in Fig. 6.20. The standard deviation of 220 mrad was multiplied by $\sqrt{2}$ to give the estimated peak fitting error 310 mrad long reference phase[8]. This is much larger than the 3 mrad error on each long reference phase value which means that the error is dominated by the quality of the peak fitting and not by the reference phase error, on each of the ≈ 150 data points which are used in fitting each etalon peak.

The viable coarse tuning interval is limited by the errors in linking the reference phase. It is essential to avoid an order number error in the reference phase extrapolation, because the linking of every GLI depends on the reference phase. This condition is satisfied if the magnitude of the discrepancy between the predicted and target anchor points is less than π, (or to be more conservative, less than a design safety margin $\epsilon_{\Phi}^{\mathrm{HI}}$). The contributions to this discrepancy come from the error in the value of FSR used for the extrapolation and from the fitting errors of the anchor peaks, which are assumed to follow a Gaussian distribution. The largest coarse tuning interval between subscans which can be linked in a single step, is plotted in Fig. 6.21 as a function of the error in the etalon FSR used for extrapolation, for tolerance limits on the peak fitting errors of 3σ,4σ and 5σ, assuming $1\sigma = 310$ mrad as

[8]This corresponds to a frequency uncertainty of 8.6 MHz on the location of each peak centre (860 ppm of the etalon FSR).

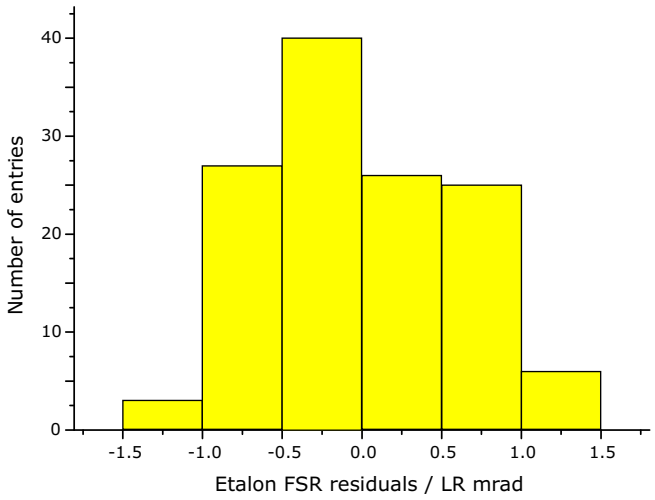

Figure 6.19: *The residual differences between etalon FSR measurements and the best fit temperature dependence of Fig. 5.8.*

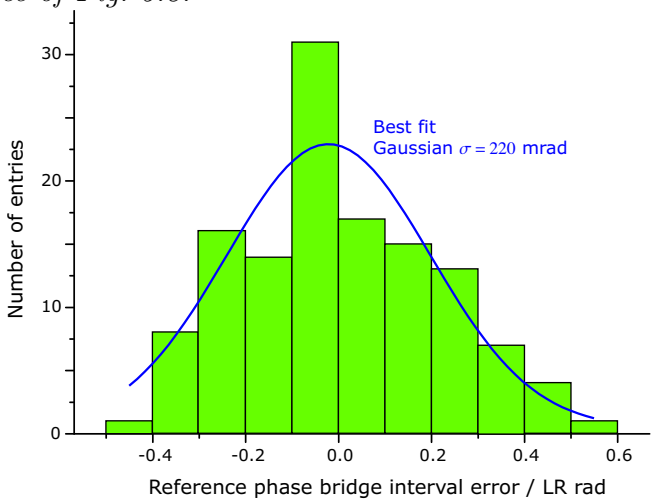

Figure 6.20: *The distribution of errors on the reference phase linking bridges estimated from the residuals of Fig. 6.19.*

estimated above. As discussed above in section 6.1, the error on the FSR can be reduced by reference interferometer calibration measurements.

The maximum (integer) number of etalon FSRs (N) in the interval which can be linked in a single bridge, is related to the error on the extrapolation FSR given by

$$\epsilon_{\mathrm{XT}} = 2\pi \left| q_{\mathrm{XT}}^{\mathrm{ET}} - q^{\mathrm{ET}} \right| \tag{6.14}$$

and the maximum allowed extrapolation discrepancy $\epsilon_{\Phi}^{\mathrm{HI}}$, by

$$\left(J\sigma + N\epsilon_{\mathrm{XT}}\right) < \epsilon_{\Phi}^{\mathrm{HI}} < \left(J\sigma + (N+1)\,\epsilon_{\mathrm{XT}}\right) \tag{6.15}$$

where J is the number of σ for the tolerance limit, ($J = 3$, 4 or 5 in the chart shown in Fig. 6.21 for which $\epsilon_{\Phi}^{\mathrm{HI}}$ was set to the maximum value π).

Etalon extrapolation limit example

If an extrapolation FSR error of 5 mrad is considered as an example from Fig. 6.21, (highlighted by the arrowed lines), with a peak fitting error standard deviation of 310 mrad, the

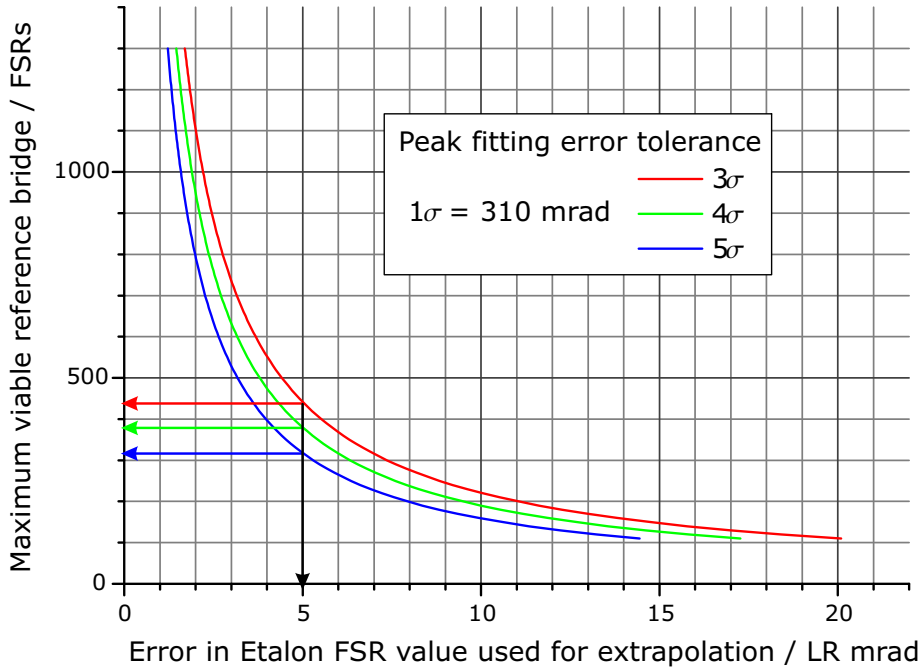

Figure 6.21: *Limits to the linking intervals imposed by the inaccuracy of the etalon FSR used for extrapolation, in the presence of peak fitting errors with $1\sigma = 310$ mrad. (The arrowed lines relate to the example discussed in the text).*

viable coarse tuning interval between subscans, is limited to 442 etalon free spectral ranges, at the 3 σ tolerance limit, 379 FSRs at 4σ and 317 FSRs at 5σ. This is independent of the size of the etalon FSR.

In the demonstration system, errors due to inter-subscan relative drift between the etalon and the long reference interferometer were much smaller than the errors in peak centre fitting because both the interferometer and the etalon had a thermally stable design. This is shown in Fig. 5.8 by the small gradient of the fitted temperature dependent FSR. The change in FSR resulting from a temperature change of several K, is smaller than the spread in FSR values, due to peak fitting errors. The errors due to etalon drift were therefore negligible.

Provided there are no order number errors in the linked long reference phase, peak fitting errors in the anchor points used in the linking of the reference phase do not affect the (subscan midpoint) anchor points used for linking the GLI phase. The only other cause of reference phase order number errors is a miscount in the number of etalon peaks.

6.3.2 Etalon peak miscount errors

The first effect of miscounting the number of free spectral ranges between initial and target etalon peaks is an error in the reference phase. This reference phase error is quantised in units of 2π reference phase radians, because the folded (reference) phase value of the infinite family of target anchor points (shown in Fig. 6.1a above), is fixed before linking by the local fit to the target etalon peak. The peak miscount redirects the extrapolation, placing the predicted anchor point in the wrong place and ensuring that the wrong reference phase target anchor is chosen. The interger order number difference between the correct reference phase anchor point and the anchor point selected in error, will be represented by the lower case symbol e. Hence the first effect of a peak miscount is an error of $2\pi e$ in the linked reference phase.

This first error in the reference phase leads to a similarly quantised error in the linked GLI phase, of $2\pi E$ GLI phase radians. As with the reference phase, the error is an integer number of phase cycles, because the folded phase of the target anchor is determined by a local (sine)fit.

Once these quantised errors have been introduced by miscounting etalon peaks, the linked phase ratio, (ignoring anchor point phase errors), is given by

$$q(e,E) \quad = \quad \frac{\Delta\Phi_{\rm AB} + 2\pi e}{\Delta\Theta_{\rm AB} + 2\pi E} \tag{6.16}$$

where $\Delta\Phi_{\rm AB}$ and $\Delta\Theta_{\rm AB}$ are, respectively, the reference interferometer and GLI phase differences between the anchor points used for linking the GLI phase. Some examples of change to the phase ratio of the short reference interferometer due to etalon peak miscounting are shown in Fig. 3.11.

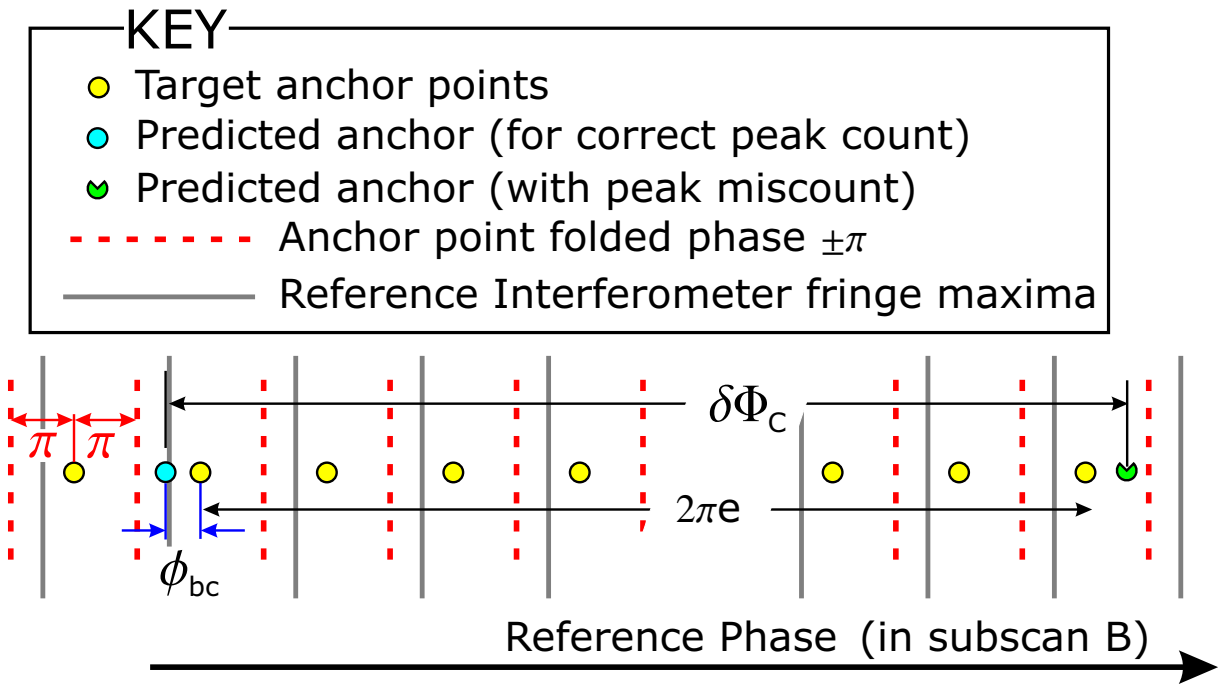

Figure 6.22: *The shift in the predicted reference phase anchor point due to a miscount in the number of etalon peaks when linking the reference phase. The red vertical lines indicate the capture range for each choice of target anchor point.*

Miscount error in the reference phase

The shift in predicted anchor point for linking the reference phase is shown in Fig. 6.22 based on the anchor points for the target subscan shown in Fig. 6.1a above. The reference phase of the shifted prediction is $\Phi_c^\star$, given by

$$\Phi_c^\star \quad = \quad \Phi_c + \delta\Phi_c \tag{6.17}$$

where $\delta\Phi_c$ is the shift in prediction due to miscounting the number of etalon peaks by δN. This shift is given by

$$\delta\Phi_c \quad = \quad 2\pi\,(\delta N)\,q_{\rm XT}^{\rm ET} \tag{6.18}$$

where $q_{\mathrm{XT}}^{\mathrm{ET}}$ is the etalon phase ratio used for the extrapolation when linking the reference interferometer phase. The phase of the unperturbed predicted anchor point, Φ_c can be expressed in terms of the correct target anchor point Φ_b by re-arranging equation 3.37c to give

$$\Phi_c = \Phi_b - \phi_{bc} \tag{6.19}$$

Substituting this into equation 6.17 gives

$$\Phi_c^{\star} = \Phi_b - \phi_{bc} + \delta\Phi_c \tag{6.20}$$

The target anchor point, nearest to the shifted predicted anchor point $\Phi_c^{\star}$ is represented by $\Phi_b^{\star}$ and is related to the correct target anchor point by

$$\Phi_b^{\star} = \Phi_b + 2\pi e \tag{6.21}$$

The gap between $\Phi_b^{\star}$ and $\Phi_c^{\star}$ is within $\pm\pi$ and so can be written as a folded phase, $\phi_{bc}^{\star\star}$, hence

$$\phi_{bc}^{\star\star} = \Phi_b^{\star} - \Phi_c^{\star} \tag{6.22}$$

The difference between the correct target anchor point and the target anchor point selected in error is given by rearranging equation 6.21 and substituting for each term from the relevant equations given above. Hence

$$\begin{aligned} 2\pi e &= \Phi_b^{\star} - \Phi_b \\ &= \phi_{bc}^{\star\star} + \Phi_c^{\star} - \Phi_b \\ &= \phi_{bc}^{\star\star} + \Phi_b - \phi_{bc} + \delta\Phi_c - \Phi_b \\ &= \phi_{bc}^{\star\star} - \phi_{bc} + \delta\Phi_c \end{aligned} \tag{6.23}$$

Subtracting $\phi_{bc}^{\star\star}$ from both sides and substituting for $\delta\Phi_c$ from equation 6.18, gives

$$2\pi e - \phi_{bc}^{\star\star} = 2\pi\,(\delta N)\,q_{\mathrm{XT}}^{\mathrm{ET}} - \phi_{bc} \tag{6.24}$$

The difference between the unperturbed predicted and target reference anchor points, ϕ_{bc} is due to the error in the etalon extrapolation, hence

$$\phi_{bc} = 2\pi N\left(q^{\mathrm{ET}} - q_{\mathrm{XT}}^{\mathrm{ET}}\right) \tag{6.25}$$

Substituting this into equation 6.24 and dividing all through by 2π gives

$$e - \frac{\phi_{bc}^{\star\star}}{2\pi} = (\delta N + N)\,q_{\mathrm{XT}}^{\mathrm{ET}} - N q^{\mathrm{ET}} \tag{6.26}$$

With $\frac{\phi_{bc}^{\star\star}}{2\pi}$ restricted to ± 0.5, the reference phase order number error e is given by rounding the right hand side to the nearest integer[9], (which will be represented by $\{\}$) hence

$$e = \{(\delta N + N)\,q_{\mathrm{XT}}^{\mathrm{ET}} - N q^{\mathrm{ET}}\} \tag{6.27}$$

[9]If q is an integer and r is a fractional term such that $-0.5 \le r < +0.5$ then $\{q + r\} = q$. If these terms are multiplied by 2π then $2\pi r$ is a folded phase and rounding to obtain q is equivalent to extracting the order number.

Propagated miscount error linking the GLI phase

The reference phase order number error propagates into the linking of the GLI phase. The error mechanism is similar to that discussed above for linking the reference phase. The order number error in the GLI phase E is analysed here by drawing a parallel with the above discussion of the reference phase miscount error. In this discussion, the target anchor point is assumed to have already been appropriately corrected for inter-subscan drift and hence denoted $\Theta_{\tilde{B}}$ following the notation of chapter 3.

The shifted predicted GLI phase anchor point $\Theta^{\star}_{C}$ is given by

$$\Theta^{\star}_{C} \;=\; \Theta_{C} + \Delta\Theta_{C} \tag{6.28}$$

where $\Delta\Theta_{C}$ is the shift in GLI phase predicted anchor point, due to the miscount error in the linked reference phase of subscan B. This shift is given by

$$\Delta\Theta_{C} \;=\; \frac{2\pi e}{q_{\mathrm{XT}}} \tag{6.29}$$

where q_{XT} is the GLI phase ratio used for extrapolation from subscan A. The phase of the unperturbed predicted anchor point Θ_{C} can be expressed in terms of the correct target anchor point Θ_{B} by re-arranging equation 3.51c to give

$$\Theta_{C} = \Theta_{\tilde{B}} - \theta_{\tilde{B}C} \tag{6.30}$$

Substituting this expression into equation 6.28 gives

$$\Theta^{\star}_{C} \;=\; \Theta_{\tilde{B}} - \theta_{\tilde{B}C} + \Delta\Theta_{C} \tag{6.31}$$

The target anchor point nearest to the shifted predicted anchor point $\Theta^{\star}_{C}$ is represented by $\Theta^{\star}_{\tilde{B}}$ and is related to the correct target anchor point by

$$\Theta^{\star}_{\tilde{B}} \;=\; \Theta_{\tilde{B}} + 2\pi E \tag{6.32}$$

The gap between $\Theta^{\star}_{\tilde{B}}$ and $\Theta^{\star}_{C}$ is within $\pm\pi$ and so can be written as a folded phase, $\Theta^{\star\star}_{\tilde{B}C}$, hence

$$\theta^{\star\star}_{\tilde{B}C} \;=\; \Theta^{\star}_{\tilde{B}} - \Theta^{\star}_{C} \tag{6.33}$$

The difference between the correct target anchor point and the target anchor point selected in error is given by rearranging equation 6.32 and substituting for each term from the relevant equations given above. Hence

$$\begin{aligned} 2\pi E &= \Theta^{\star}_{\tilde{B}} - \Theta_{\tilde{B}} \\ &= \theta^{\star\star}_{\tilde{B}C} + \Theta^{\star}_{C} - \Theta_{\tilde{B}} \\ &= \theta^{\star\star}_{\tilde{B}C} + \Theta_{\tilde{B}} - \theta_{\tilde{B}C} + \Delta\Theta_{C} - \Theta_{\tilde{B}} \\ &= \theta^{\star\star}_{\tilde{B}C} - \theta_{\tilde{B}C} + \Delta\Theta_{C} \end{aligned} \tag{6.34}$$

Subtracting $\theta^{\star\star}_{\tilde{B}C}$ from both sides and substituting for $\Delta\Theta_{C}$ from equation 6.29, gives

$$2\pi E - \theta^{\star\star}_{\tilde{B}C} \;=\; \frac{2\pi e}{q_{\mathrm{XT}}} - \theta_{\tilde{B}C} \tag{6.35}$$

The difference between the unperturbed predicted and target reference anchor points, $\theta_{\tilde{B}C}$ is due to the error in the etalon extrapolation, hence

$$\theta_{\tilde{B}C} = \frac{\Delta\Phi_{\mathrm{AB}}}{q} - \frac{\Delta\Phi_{\mathrm{AB}}}{q_{\mathrm{XT}}} \tag{6.36}$$

Substituting this into equation 6.35 and dividing all through by 2π gives

$$E - \frac{\theta^{\star\star}_{\tilde{B}C}}{2\pi} = \left(\frac{e + \frac{\Delta\Phi_{\mathrm{AB}}}{2\pi}}{q_{\mathrm{XT}}}\right) - \frac{\frac{\Delta\Phi_{\mathrm{AB}}}{2\pi}}{q} \tag{6.37}$$

With $\frac{\theta^{\star\star}_{\tilde{B}C}}{2\pi}$ restricted to ± 0.5, the GLI phase order number error E is given by rounding the right hand side to the nearest integer to give

$$E = \{\frac{e + \frac{\Delta\Phi_{\mathrm{AB}}}{2\pi}}{q_{\mathrm{XT}}} - \frac{\frac{\Delta\Phi_{\mathrm{AB}}}{2\pi}}{q}\} \tag{6.38}$$

Linked phase ratio miscount error

The expressions obtained for e and E in equations 6.27 and 6.38 respectively can be substituted into $q(e, E)$, (as given by equation 6.16), to give the phase ratio determined by linking in the presence of an etalon peak miscount error δN. Hence

$$\begin{aligned} q_{\mathrm{AB}} &= \frac{\Delta\Phi_{\mathrm{AB}} + 2\pi e}{\Delta\Theta_{\mathrm{AB}} + 2\pi E} \\ &= \frac{\Delta\Phi_{\mathrm{AB}} + 2\pi\{(\delta N + N)\, q^{\mathrm{ET}}_{\mathrm{XT}} - N q^{\mathrm{ET}}\}}{\frac{\Delta\Phi_{\mathrm{AB}}}{q} + 2\pi\{\left(\frac{e}{q_{\mathrm{XT}}}\right) + \left(\frac{\Delta\Phi_{\mathrm{AB}}}{2\pi q_{\mathrm{XT}}}\right) - \left(\frac{\Delta\Phi_{\mathrm{AB}}}{2\pi q}\right)\}} \\ &= \frac{\Delta\Phi_{\mathrm{AB}} + 2\pi\{(\delta N + N)\, q^{\mathrm{ET}}_{\mathrm{XT}} - N q^{\mathrm{ET}}\}}{\frac{\Delta\Phi_{\mathrm{AB}}}{q} + 2\pi\{\left(\frac{\{(\delta N+N) q^{\mathrm{ET}}_{\mathrm{XT}} - N q^{\mathrm{ET}}\}}{q_{\mathrm{XT}}}\right) + \left(\frac{\Delta\Phi_{\mathrm{AB}}}{2\pi q_{\mathrm{XT}}}\right) - \left(\frac{\Delta\Phi_{\mathrm{AB}}}{2\pi q}\right)\}} \end{aligned} \tag{6.39}$$

Etalon peak count verification using the short reference interferometer

The result from equation 6.39 can be used to simulate examples of etalon peak miscounts, to investigate the linking cross check technique introduced in chapter 3, where the linked short reference interferometer length is used to verify the etalon peak count.

Some example miscount errors have been calculated for different values of q_{XT}, $q^{\mathrm{ET}}_{\mathrm{XT}}$ and δN (using equation 6.39). The linked short reference lengths are shown below in Fig. 6.23 for a system similar to the demonstration system, with short reference interferometer and etalon values given by

$$\begin{aligned} q &= 5.041 \\ q^{\mathrm{ET}} &= 57.3123 \\ N &= 346 \\ \Delta\Phi_{\mathrm{AB}} &= 1.244 \times 10^5 \text{ rad} \end{aligned}$$

The extrapolation phase ratio values for the short reference interferometer and etalon were set to the largest and smallest values possible, so that the extrapolation remained just within $\pm\pi$. For non-zero δN these upper and lower limit extrapolation values gave rise to different values of e and E. When $\delta N = 0$, the extrapolations reached the correct anchor points.

There are therefore four possible values of linked short reference phase ratio, using upper and lower values for e and E. The short reference lengths based on linked phase ratios shown in Fig. 6.23 are labelled with two letters, the first letter indicates whether the higher (indicated with h) or lower (indicated with l) value of $q_{\mathrm{XT}}^{\mathrm{ET}}$ is used, respectively giving rise to upper and lower values of e. Similarly, the second (upper case) letter indicates whether the upper or lower value of q_{XT} were used, giving rise to upper or lower values of E.

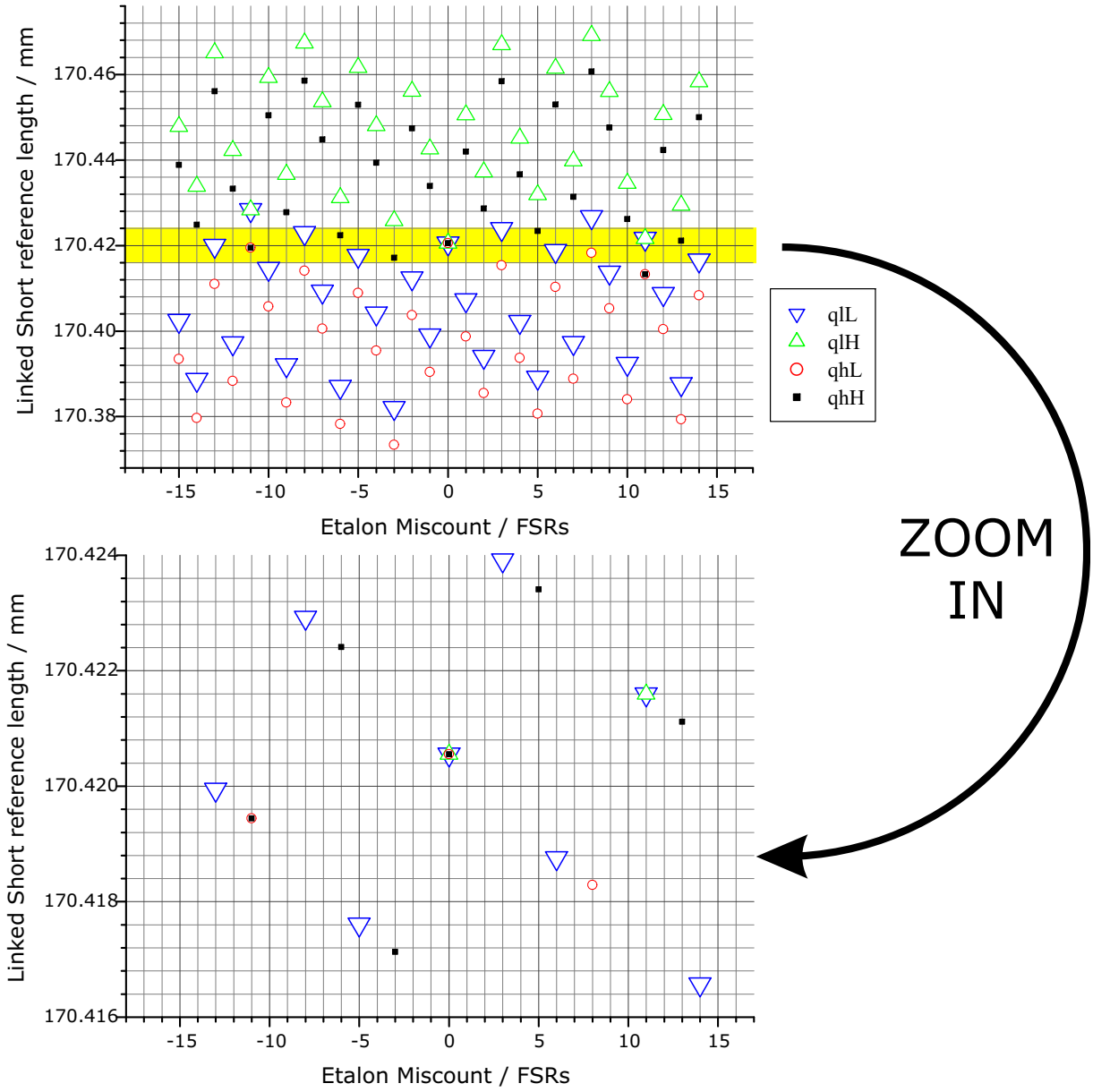

Figure 6.23: *Simulated effect of etalon peak miscount on the linked short reference phase ratio, for different values of etalon and short reference extrapolation phase ratios. The highlighted region shown in close up in the lower half of the figure, is the range of short reference lengths observed over the 7° C temperature range shown in Fig. 5.4. In this example, for a peak miscount within ±10 to be rejected using the short reference measurements, the length needs to be measured to within ±800 nm.*

As stated above, this calculation does not include the effects of anchor point phase errors, which need to be controlled for this technique to work. In the measurements presented in

chapter 5, the range of resiudal differences between linked short reference interferometer length and the fitted thermal length dependence, lay within ±400 nm.

All ambiguities in etalon peak counting were resolved using the short reference verification technique, indicating that the anchor point phase errors were small enough for this technique to be viable.

Any future system with evacuated, thermally stable reference interferometers, should have even smaller (short reference) GLI phase anchor point errors, allowing the technique to work over larger linking bridges.

Further peak count verification techniques

A similar verification technique based on the linked value of etalon FSR (rather than short reference length) has also been simulated using equation 6.27 to calculate the reference phase error e. As with the short reference simulation, anchor point phase errors, (which in this case are the errors on the fitted peak midpoints), are not included.

This test involves measuring the etalon FSR after linking the reference phase with different trial values N^* for the number of etalon FSRs in the linking bridge. As in the calculations for Fig. 6.23, in the absence of anchor point phase errors, the value of the phase ratio used for extrapolation $q_{\mathrm{XT}}^{\mathrm{ET}}$ can be set to upper and lower values which just avoid an extrapolation error. These upper and lower values are given by

$$q_{\mathrm{XT}}^{\mathrm{ET}} = q^{\mathrm{ET}} \pm \left(\frac{0.5}{N^*}\right) \tag{6.40}$$

where the ±0.5 term represents an extrapolation to a reference phase $\pm\pi$, either side of the correct target anchor point.

An example was calculated for the value of q^{ET} set at 57.3123. The calculated linked values of etalon FSR are shown in Fig. 6.24, for an etalon bridge with $N = 346$ and different values of peak miscount. The linked values of etalon FSR, using upper and lower extrapolation phase ratios only agree for the correct number of etalon peaks.

This technique was tested on data from the measurements of Set 4, (presented in chapter 5). The etalon peak fitting errors on the anchor point phase values, (present in the measured data and neglected in the above simulation), rendered the calculation of trial extrapolation phase ratio values using equation 6.40 invalid, because the effective value of q^{ET} in the presence of an anchor point phase error[10] ϵ_ϕ, is

$$q_{\mathrm{EFF}}^{\mathrm{ET}} = q^{\mathrm{ET}} + \left(\frac{\epsilon_\phi}{2N\pi}\right) \tag{6.41}$$

and it was not possible to know $q_{\mathrm{EFF}}^{\mathrm{ET}}$ in advance, without already knowing the correct value of N. The best compromise was to continue to use a best estimate for q^{ET} and to deal with the change from file to file in $q_{\mathrm{EFF}}^{\mathrm{ET}}$ by reducing the spacing between the two solutions for $q_{\mathrm{XT}}^{\mathrm{ET}}$, replacing the term ±0.5 with a smaller value and to compare the linked etalon FSR obtained using upper and lower values of trial extrapolation phase ratios. The linked etalon phase ratio for each case will be labelled here $q_{\mathrm{AB}+}^{\mathrm{ET}}$ and $q_{\mathrm{AB}-}^{\mathrm{ET}}$ respectively. The modified upper and lower trial extrapolation phase ratios, are given by generalising equation 6.40 which becomes

$$q_{\mathrm{XT}}^{\mathrm{ET}} = q^{\mathrm{ET}} \pm \left(\frac{\Delta}{N^*}\right) \tag{6.42}$$

[10] As explained in section 6.1, the independent phase error contributions from the two anchor points can be treated as if the error were entirely due to the target anchor point. This combined anchor point error is represented by ϵ_ϕ here.

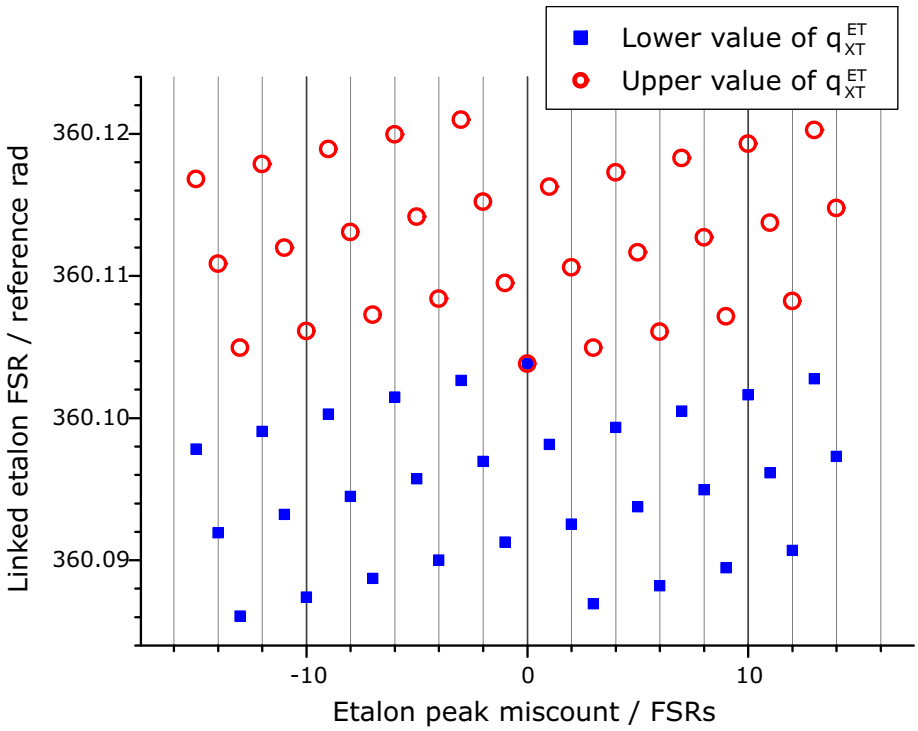

Figure 6.24: *Simulated effect of etalon peak miscount errors on linked value of etalon FSR. This simulation assumes anchor peak phase errors are zero.*

When the spacing Δ is too small,

$$q_{\mathrm{AB}+}^{\mathrm{ET}} = q_{\mathrm{AB}-}^{\mathrm{ET}} \tag{6.43}$$

is satisfied by almost every value of trial count in the range

$$N - 15 \leq N^* \leq N + 15$$

and the correct value does not stand out.

When the spacing Δ is too large,

$$q_{\mathrm{AB}+}^{\mathrm{ET}} \neq q_{\mathrm{AB}-}^{\mathrm{ET}}$$

even for the correct count.

In most scans from Set 4, with an (apparent optimum) value of

$$\Delta = \frac{2.75}{2\pi}$$

and assuming

$$q^{\mathrm{ET}} = \frac{360.1039}{2\pi}$$

the two reference phase links using the correct etalon peak count, (using each of the trial extrapolation phase ratios given by equation 6.42), both satisifed equation 6.43. In most cases, there was at least one other trial value of peak count N^*, which also met this condition. The trail values of peak count which passed the test, for some of the scans in Set 4 are listed in Table 6.3. There was no setting for q^{ET} and Δ, which would uniquely indicate the correct count in all scans. This was because of the larger variation in $q_{\mathrm{EFF}}^{\mathrm{ET}}$ due to the high level of etalon peak fitting errors.

Table 6.3: *Trial values of etalon peak count satisfying the verification test based on linked FSR measurement for the first ten scans from Set 4. All tests on the scans not shown here, passed the correct value and anything from zero up to two other trial counts. N.B. The counts are negative because laser 1 was tuning down in frequency.*

Scan number	Correct peak count	Trial counts which pass
1	-347	-347
2	-347	None passed
3	-346	-343, -346, -349
4	-347	-347, -350
5	-346	-346, -349
6	-347	-347
7	-347	-344, -347
8	-346	-346, -349
9	-346	-346, -349
10	-346	-343, -346, -349
30	-347	None passed
31	-346	None passed
32	-347	-344 ONLY
33	-346	-343, -346, -349
34	-347	-347, -350

A similar FSR based test might be reliable in a future system, if the peak fitting errors are reduced significantly from the levels observed with the demonstration system, (estimated to be around $1\sigma \approx 310$ mrad earlier in this section). If these errors were reduced, this could be a powerful peak count verification tests, which would complement the test based on the linking the short reference interferometer, described in chapter 3 and above.

Vernier etalons

The reference interferometer section of a future system could include two etalons acting as a vernier pair, with a distinct periodic pattern for the spacing between peaks of the first etalon and the nearest corresponding peak of the second etalon. In the smallest repeating unit there are P FSRs for the first etalon and Q FSRs for the second etalon, where P and Q are integers.

The magnitude of the spacing in reference phase between the $N_{\mathrm{ABS}}{}^{\mathrm{th}}$ peak[11] of the first etalon and the nearest peak from the second etalon, is given by

$$|\delta\Phi\left(N_{\mathrm{ABS}}, P\right)| = 2\pi q_1^{\mathrm{ET}} \left| \frac{N_{\mathrm{ABS}} \bmod P}{Q} \right| \tag{6.44}$$

where q_1^{ET} is the phase ratio of the first etalon. When

$$N_{\mathrm{ABS}} \bmod P = 0$$

[11]Here N_{ABS} is the absolute order number of the peak. The absolute order number convention starts from a hypothetical peak, labelled zero at zero optical frequency.

the peaks from each vernier etalon coincide. This case must be measurably distinct from the neighbouring case, with

$$N_{\mathrm{ABS}} \bmod P = 1$$

where the separation between the nearest peaks of each etalon is given by

$$\delta\Phi = \frac{\Delta\Phi_1^{\mathrm{ET}}}{Q} = \frac{\Delta\Phi_2^{\mathrm{ET}}}{P} \tag{6.45}$$

and $\Delta\Phi_1^{\mathrm{ET}}$ and $\Delta\Phi_2^{\mathrm{ET}}$ are the FSRs in reference phase, of the first and second vernier etalons, respectively. The change in vernier peak spacing is the same from any peak of the first etalon to the next, so to resolve the different positions in the vernier cycle, the largest peak fitting error must be smaller than half the value of $\delta\Phi$ given by equation 6.45, taking the conservative (or worst case) limit where the peak fitting errors from both etalons act in concert.

If the peak fitting errors of the first etalon, are to be tolerated within a reference phase range $\pm J\sigma_1$, the vernier spacing resolution limit requires that

$$\sigma_1 < \left(\frac{\pi}{J}\right)\left(\frac{q_1^{\mathrm{ET}}}{Q}\right) \tag{6.46}$$

If the first etalon is to be used for linking the reference phase, it must also satisfy the condition given above in equation 6.15, which can be re-written as

$$\sigma_1 < \frac{\epsilon_\Phi^{\mathrm{HI}} - N\epsilon_{\mathrm{XT}}}{J} \tag{6.47}$$

To ensure that the reference phase linking condition is more demanding than the vernier spacing requirement, Q must satisfy,

$$Q \leq \frac{\pi q_1^{\mathrm{ET}}}{\epsilon_\Phi^{\mathrm{HI}} - N\epsilon_{\mathrm{XT}}} \tag{6.48}$$

and similarly for the second etalon

$$P \leq \frac{\pi q_2^{\mathrm{ET}}}{\epsilon_\Phi^{\mathrm{HI}} - \{\frac{NQ}{P}\}\epsilon_{\mathrm{XT}}} \tag{6.49}$$

As an example, based on parameter values similar to those of the demonstration system, with

$$\begin{aligned} q_1^{\mathrm{ET}} &= 57.3123 \\ \epsilon_\Phi^{\mathrm{HI}} &= 3 \text{ rad} \\ N &= 346 \\ \epsilon_{\mathrm{XT}} &= 5 \times 10^{-3} \text{ rad} \\ Q &\leq 141 \end{aligned}$$

If $\sigma_1 \approx 310$ mrad, then $Q \leq 141$ satisfies equation 6.46, for $J \leq 4$. It should therefore be possible to use a pair of vernier etalons, even with the high level of peak fitting errors observed in the demonstration system.

A practical vernier scale can be have $10 \leq Q \leq 20$ and $P = Q - 1$, which would quantise the etalon peak miscount in integer multiples of $\pm Q$. A wavemeter can be used to distinguish[12] between laser frequencies to a precision of $\pm Q$, so with the correct design of vernier, the etalon peak count will always be correct.

[12] If $Q = 20$ for an etalon with a 5 GHz FSR, $\pm Q$ FSRs is a shift of 100 GHz equivalent to a shift in wavelength of ± 0.23 nm at 836 nm or 3 parts in 10^4, easily measureable with a wavemeter.

6.4 Fitted sinusoids to GLI data from single subscans

The inital estimate of GLI phase ratio was based on the combined laser results from individual subscans, calculated using the procedures discussed in chapter 3. This initial GLI phase ratio estimate was used for the linking extrapolation between the first two subscans and for the inter-subscan drift correction. Errors in the inter-subscan drift correction contributed to the GLI phase error of the target anchor point used for linking.

The factors which influence the phase ratio q and phase offset α fitted to each subscan are discussed here. The effect of errors in the phase ratio on the inter-subscan drift correction are considered in section 6.5.2 below.

6.4.1 The χ^2 profile used for sinefitting

It is important to bear in mind that the fitting of a sinusoidal function to the GLI data was guided by the dependence of χ^2 on the values of the fit parameters. This dependence can be represented as a multi-dimensional surface where the height of the surface represents χ^2 and every other dimension represents one of fit parameters. The search routine MINUIT, which was used to fit GLI data, works by finding a local minimum on this surface.

To ease visualisation, a lower dimensional slice through this surface can be taken by fixing the values of a subset of the fit parameters. Many examples of these slices showing the dependence of the χ^2 or χ^2 per degree of freedom are given in earlier chapters and later in this chapter. These slices are referred to as χ^2 profiles.

An important effect arises when fitting a periodic function such as the sinusoids used to model the GLI signal. The density of local minima in the profile of χ^2 versus phase ratio, varies significantly if the reference phase (x-values) assigned to the data are shifted by an offset. This is very important, because the x-values of unwrapped reference phase in the data from a subscan which were passed to MINUIT for sine fitting, were labelled using an arbitrary choice of unwrapping order number. This profile dependence on the x values of the data for a sinusoid is contrasted below with equivalent profiles for a straight line fit, which always have a single minimum.

Simulated noise free examples

Seven example data sets have been simulated, each of the seven examples are derived from the same parent functions; a straight line and a sine wave. The seven samples of the straight line are paired off with the seven samples of the sine wave, with each member of the pair sharing common values of x data. The only difference between examples is the choice of x values at which the parent function is sampled.

The range and number of x data points is given for each pair in Table 6.4. The y data for the straight line is equivalent to the phase of the sinusoid, which is labelled Θ as if it were the phase of a GLI.

The first three examples are different length subscans, 4000, 400 and 40000 pts long, respectively, all with the same data point density in x. The fourth and fifth examples have 4000 pts and cover the same range in x as the third and second examples respectively. This is achieved by changing the spacing between neighbouring points, so that it is either an order of magnitude larger or smaller than in the first example. The penultimate example is the same as the first except for a global shift in the value of the x co-ordinates. In these first six examples the data points are in one continuous block, simulating a single subscan. The final example set of x data consists of two continuous blocks of equal size separated by an

interval, large compared to the length of each block, representing two fine tuning subscans separated by a coarse tuning interval.

Table 6.4: *Seven examples of reference phase data used in χ^2 profile simulations comparing equivalent straight line and sinusoidal fit functions.*

CASE	Number of data points N	Width of data block(s) / rad Δx	Midpoint location(s) / rad $\overline{x}$
A	4000	1081.2	541.054
B	400	108.12	54.514
C	40000	10812	5406.454
D	4000	10812	5406.454
E	4000	108.12	54.514
F	4000	1081.2	5041.054
G	4000	540.6 each	270.754 and 10811.354

Each simulated sinusoid $Y_i(x_i)$ is defined by

$$Y_i(x_i) = A + B\cos\left(\frac{x_i}{q} + \alpha\right) \tag{6.50}$$

where $q = 2.56$ and $\alpha = -0.789$. The sinusoid is compared with a fit function given by

$$I_i(x_i) = A + B\cos\left(\frac{x_i}{qf} + \alpha\right) \tag{6.51}$$

where f is a normalised phase ratio, which always equals unity at the correct phase ratio.

In each example, the three fit parameters, A,B and α are set to the values of the function used to generate the simulated data and the χ^2 (defined below) is calculated as a function of f.

The corresponding straight line function, (which represents the linear dependence of the GLI phase on reference phase, in the hypothetical case where there is no relative interferometer drift), is defined by

$$Y_i(x_i) = \frac{x_i}{q} + \alpha \tag{6.52}$$

with the values of q and α given above. This line is compared with a fit given by

$$I_i(x_i) = \frac{x_i}{qf} + \alpha \tag{6.53}$$

For both the linear fit and the sine fit, the profile of χ^2 per degree of freedom, as a function of f, is calculated over the range

$$0.93 \leq f < 1.07$$

using

$$\chi^2/\mathrm{DOF} \approx \frac{1}{N}\sum_{i=1}^{N}\left(\frac{I_i(x_i) - Y_i(x_i)}{\sigma_i}\right)^2 \tag{6.54}$$

where $\sigma_i = 1.0$ for the linefit and $\sigma_i = \sqrt{Y_i(x_i)}$ for the sinefit[13].

[13]In these noise free simulation examples, the use of either weight for the sinefit gives the same *shape* profile, with the scale of the vertical axis as the only difference. The choice of weight does not affect the location, density and relative depth of local minima.

The simulated examples of straight line fits, A to E are shown in figs. 6.25a to 6.25c. The corresponding χ^2 per degree of freedom profiles, (shown in figs. 6.25d to 6.25f), exhibit a quasi-parabolic[14] profile with a single minimum as a function of normalised phase ratio.

The shape of the profile, for these simulated noise free examples, can be calculated by approximating the χ^2 per degree of freedom, (as given by the summation in equation 6.54), to an integral in the limit of an infinite number of equispaced data points.

For a general function $F(X)$ which is sampled at equispaced points x_i, the average μ is given by

$$\begin{aligned} \mu &\approx \lim_{N\to\infty} \frac{1}{N} \sum_{i=1}^{N} F(X_i) \\ &= \frac{1}{\Delta X} \int_{\overline{X}-\Delta X/2}^{\overline{X}+\Delta X/2} F(X)\, dX \end{aligned} \tag{6.55}$$

If the sampled function, in equation 6.55 takes the form

$$F(X_i) = \left(\frac{Y_i - I_i}{\sigma_i} \right)^2 \tag{6.56}$$

then μ approximates the χ^2 per degree of freedom in the limit of an infinite number of data points. Given the above definitions of Y_i in equation 6.52 and I_i in equation 6.53, the integral for μ in the case of a linear fit over data distributed continuously within

$$\left(\overline{x} - \frac{\Delta x}{2} \right) \leq x \leq \left(\overline{x} + \frac{\Delta x}{2} \right)$$

is given by

$$\begin{aligned} \mu(f) &= \frac{1}{q^2 \Delta x} \int_{\overline{x}-\Delta x/2}^{\overline{x}+\Delta x/2} \left(\frac{1}{f} - 1 \right)^2 x^2 dx \\ &= \frac{1}{q^2} \left(\overline{x}^2 + \frac{\Delta x^2}{12} \right) \left(\frac{1}{f} - 1 \right)^2 \end{aligned} \tag{6.57}$$

So the χ^2 per degree of freedom profile for a straight line fit, is a parabola in $\frac{1}{f}$, centred on a minimum at $f = 1$. The vertical scale of this parabola increases with the square of the slope ($\frac{1}{q}$) and is also affected by a dual lever arm action. The first lever arm term ($\overline{x}^2$) represents the distance from the centre of gravity of the data block to the y axis where the fixed intercept pins the fit function to a fixed pivot. The second term represents the internal lever arm of the data about its own centre. The first lever effect dominates, unless

$$\Delta x \gtrsim \sqrt{12}\, \overline{x}$$

For a single block of *continuous* data the artefact of the first lever arm effect is governed by the arbitrary choice of $x = 0$. It can be eliminated by redefining the x data using

$$x'_i = x_i - \overline{x} \tag{6.58}$$

while still leaving only the second, internal lever arm.

[14]The profile is exactly parabolic in $\frac{1}{f} - 1$ and therefore close to parabolic in f, close to $f = 1$, as shown in equation 6.57.

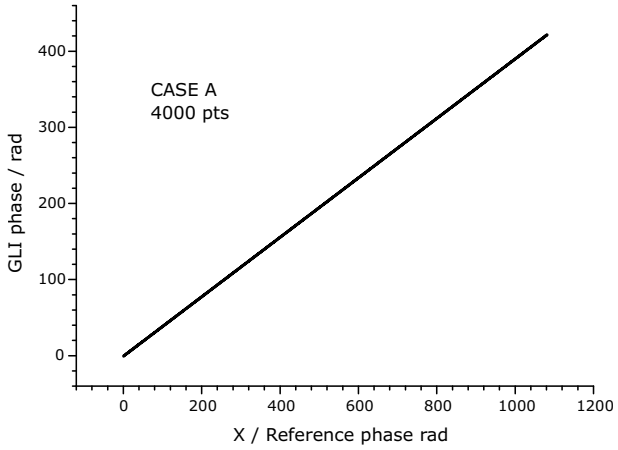

Figure 6.25a: *The simulated straight line data for example A of Table 6.4.*

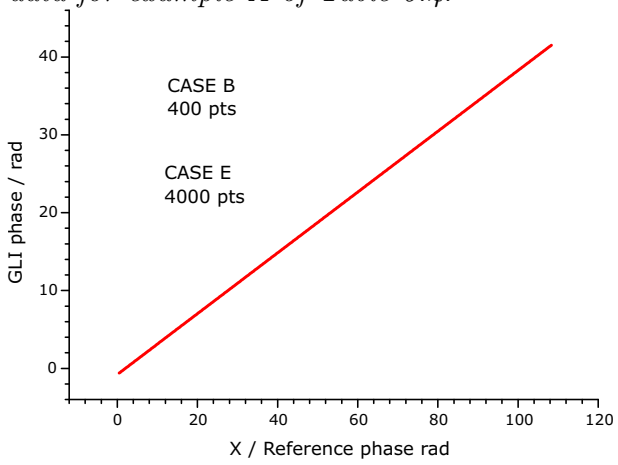

Figure 6.25b: *The simulated straight line data for example B of Table 6.4. The data in example E covers the same range, with a tenfold increase in point density.*

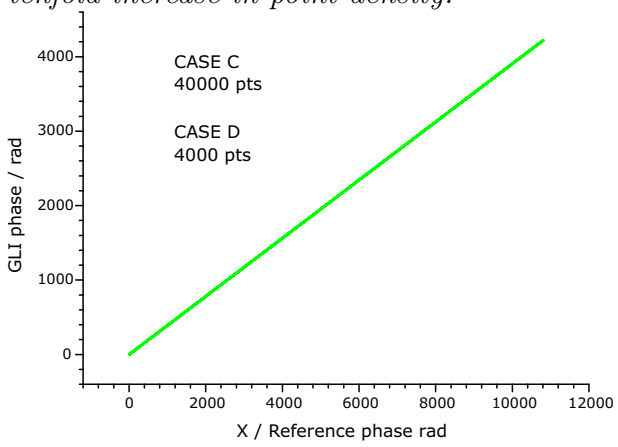

Figure 6.25c: *The simulated straight line data from example C of Table 6.4. The data in example D covers the same range, with a tenfold increase in point density.*

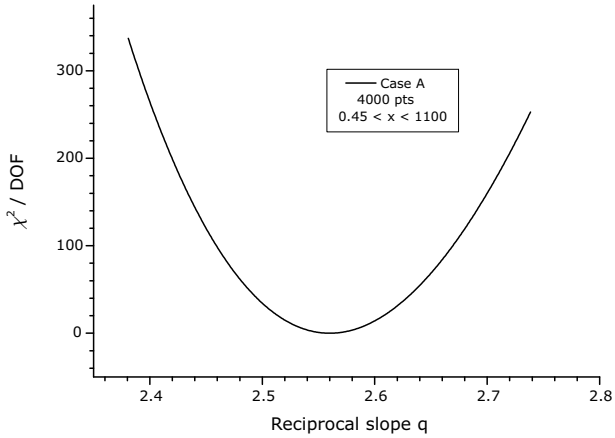

Figure 6.25d: *Parabolic χ^2 /DOF profile of fit to straight line from example A of Table 6.4.*

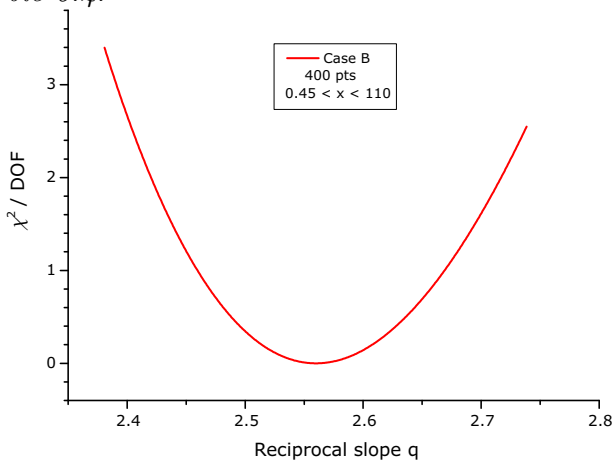

Figure 6.25e: *Parabolic χ^2 /DOF profile of fit to straight line from example B of Table 6.4. This is identical to the profile for the fit to example E data.*

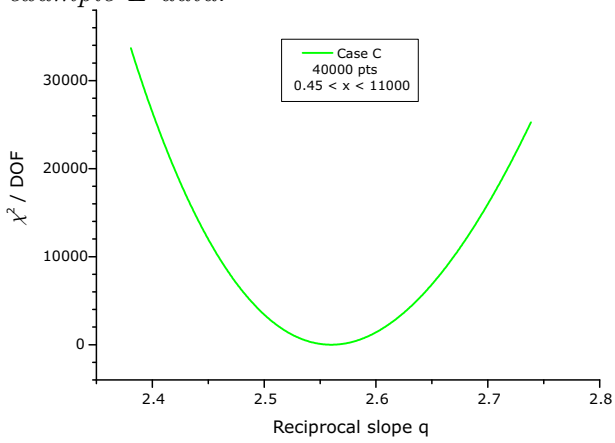

Figure 6.25f: *Parabolic χ^2 /DOF profile of fit to straight line from example C of Table 6.4. This is identical to the profile for the fit to example D data.*

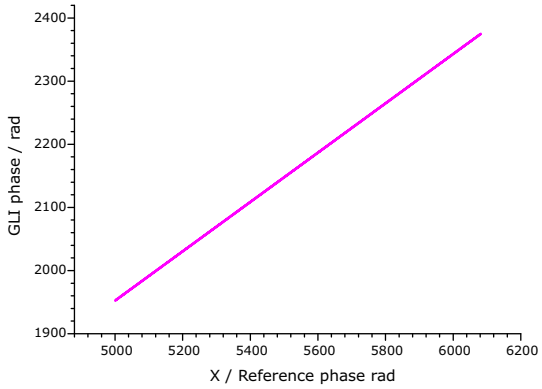

Figure 6.26: *The simulated straight line data for example F of Table 6.4.*

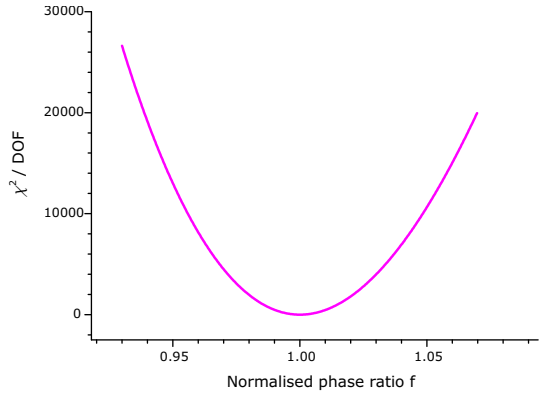

Figure 6.27: *Parabolic χ^2 /DOF profile of fit to straight line from example F of Table 6.4.*

The straight line data for case F is shown in Fig. 6.26. This has the same length and number of data points as the line from case A, but is shifted in x and y. The corresponding χ^2 per degree of freedom profile, shown in Fig. 6.27, is around two orders of magnitude larger than the profile for case A, due to the first lever arm effect.

After removing the first lever arm effect by substituting the values of x'_i (as defined in equation 6.58) in place of x_i and recalculating each y_i using x'_i, the simulated straight line data for case F, lie either side of the small offset from origin given by the intercept ($\alpha = 0.45$). The corresponding χ^2 per degree of freedom profile changes to that shown in Fig. 6.28, which is one quarter the height of the profile from case A, as predicted by equation 6.57.

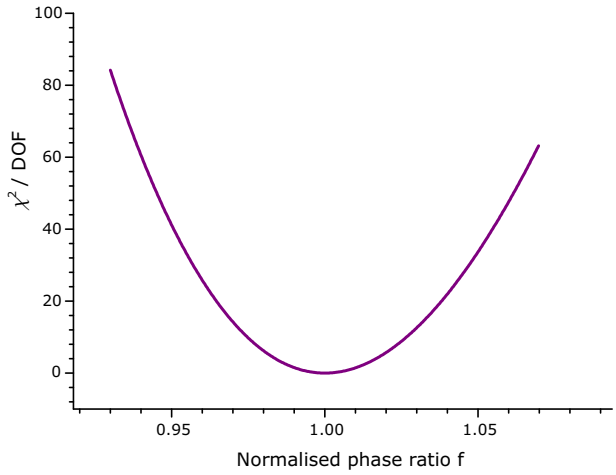

Figure 6.28: *Parabolic χ^2 / DOF profile of fit to straight line from example F of Table 6.4, after shifting x values so that the line is balanced either side of the y axis. This is one quarter the height of profile from case A.*

For the final example, case G, the simulated straight line data lies in two separate blocks, as shown in Fig. 6.29. The corresponding χ^2 per degree of freedom profile is shown in Fig. 6.30. This profile can be calculated by taking the average of the result from equation 6.57 calculated seperately for each block. This average has equal contributions from each block because the number of points is the same in each block. In general the combination of results for block 1 with N_1 data points and a χ^2 per degree of freedom, μ_1 calculated from

equation 6.57 and μ_2 for block 2 with N_2 data points, leads to a χ^2 per degree of freedom given by

$$\begin{aligned} \mu &= \left(\frac{\chi_1^2 + \chi_2^2}{N_1 + N_2}\right) \\ &= \frac{\mu_1 N_1 + \mu_2 N_2}{N_1 + N_2} \\ &= \mu_1 \left(\frac{N_1}{N_1 + N_2}\right) + \mu_2 \left(\frac{N_2}{N_1 + N_2}\right) \end{aligned} \tag{6.59}$$

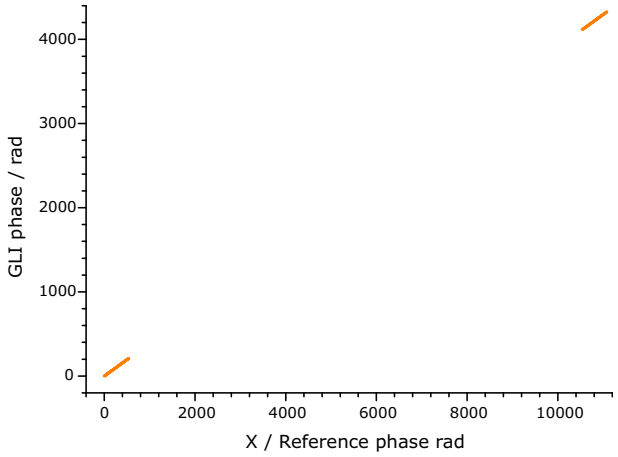

Figure 6.29: *The simulated straight line data for example G of Table 6.4.*

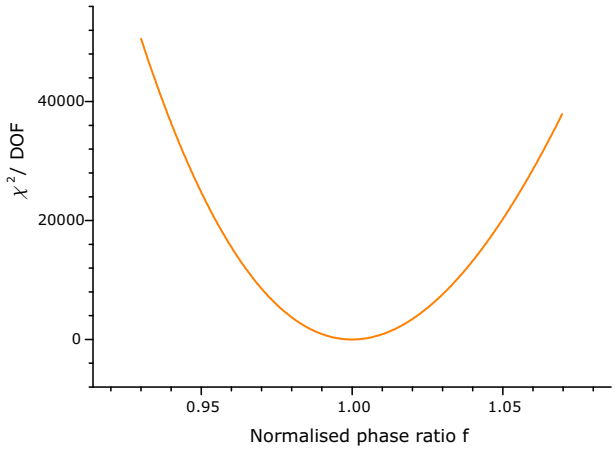

Figure 6.30: *Parabolic χ^2 /DOF profile of fit to straight line from example G of Table 6.4.*

The χ^2 per degree of freedom profile for example G, is steeper than all the previous profiles, showing the increased lever arm. The effect of the differences in distribution of the straight line data on the corresponding χ^2 per degree of freedom is contrasted in the following discussion with the very different effects which arise in the corresponding cases with sinusoidal data, using the same x axis distributions.

The first five sinusoidal data examples from Table 6.4 are shown in figs. 6.31a to 6.31c, with the corresponding χ^2 per degree of freedom profiles shown in figs. 6.32a to 6.32c. As in the straight line examples, the data from cases B and E cover the same distribution, and give rise to the same χ^2 per degree of freedom profile. Similarly for cases C and D.

As shown above for the straight line fitting case, the changes in shape of the χ^2 per degree of freedom for a sine fit can also be described using equation 6.55 and equation 6.56, with appropriate substitutions from equation 6.50 and equation 6.51. After these substitutions, equation 6.55 can be written as

$$\mu(f) = \frac{B^2}{\Delta x}\int_{\overline{x}-\Delta x/2}^{\overline{x}+\Delta x/2}\left[\cos\left(\frac{x}{q}+\alpha\right)-\cos\left(\frac{x}{qf}+\alpha\right)\right]^2 dx \tag{6.60}$$

after expanding the integrand and evaluating the integral, the expression for μ becomes

$$\begin{aligned}\mu(f) = B^2\Bigg(\ & 1+\frac{1}{2}\mathrm{sinc}\left(\frac{\Delta x}{q}\right)\cos\left[2\left(\frac{\overline{x}}{q}+\alpha\right)\right] \\ & +\frac{1}{2}\mathrm{sinc}\left(\frac{\Delta x}{qf}\right)\cos\left[2\left(\frac{\overline{x}}{qf}+\alpha\right)\right] \\ & -\mathrm{sinc}\left[\left(1+\frac{1}{f}\right)\left(\frac{\Delta x}{2q}\right)\right]\cos\left[\left(1+\frac{1}{f}\right)\left(\frac{\overline{x}}{q}\right)+2\alpha\right] \\ & -\mathrm{sinc}\left[\left(1-\frac{1}{f}\right)\left(\frac{\Delta x}{2q}\right)\right]\cos\left[\left(1-\frac{1}{f}\right)\left(\frac{\overline{x}}{q}\right)\right]\Bigg)\end{aligned} \tag{6.61}$$

If the data in each block covers many cycles, so that $\frac{\Delta x}{q} \gg 2\pi$, the last term dominates[15], so that

$$\mu \approx B^2\left(1-\mathrm{sinc}\left[\left(1-\frac{1}{f}\right)\left(\frac{\Delta x}{2q}\right)\right]\cos\left[\left(1-\frac{1}{f}\right)\left(\frac{\overline{x}}{q}\right)\right]\right) \tag{6.62}$$

The χ^2 per degree of freedom has a background plateau at values of fitted phase ratio, far from the correct value at $f = 1$, which scales with the square of the sinusoidal signal amplitude B^2.

In each of the seven examples from Table 6.4, the amplitude of the sinusoid is the same, so the plateau in each corresponding χ^2 per degree of freedom profile is ten[16].

[15]The five terms inside the main pair of brackets of equation 6.61, can be thought of (in order) as : The background, A term for the interval $\Delta\Theta$ ($= \frac{\Delta x}{q}$) covered by the data, a term for the equivalent interval in Θ covered by the fit function, a term for the sum of these two intervals and a term for their difference. The background term is always present. Of the other four terms, the difference term dominates because the argument of this sinc is much smaller for the difference term, (in the vicinity of $f \approx 1$ where the fit and data are similar), than the argument of the other sinc terms.

[16]This is much smaller than the value predicted from equation 6.62 (since $B^2 = 10^4$). However, equation 6.62 is based on a χ^2 calculated with the weight σ_i set to unity, whereas the χ^2 per degree of freedom profiles for sine fitting have been simulated using a weight given by $\sigma_i = \sqrt{Y_i}$ and the simulated GLI signal is on average equal to the DC value so the weight is on average $\sqrt{1000}$. The χ^2 per degree of freedom profiles are therefore smaller than predicted by the ratio of σ_i^2 which is 1000.

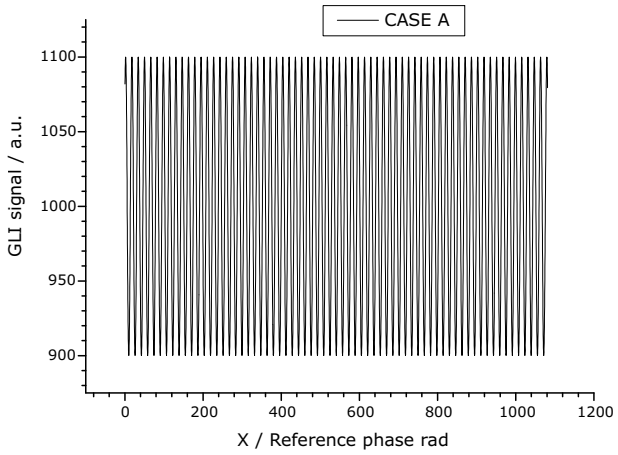

Figure 6.31a: *The sinusoidal data simulated for example A of Table 6.4.*

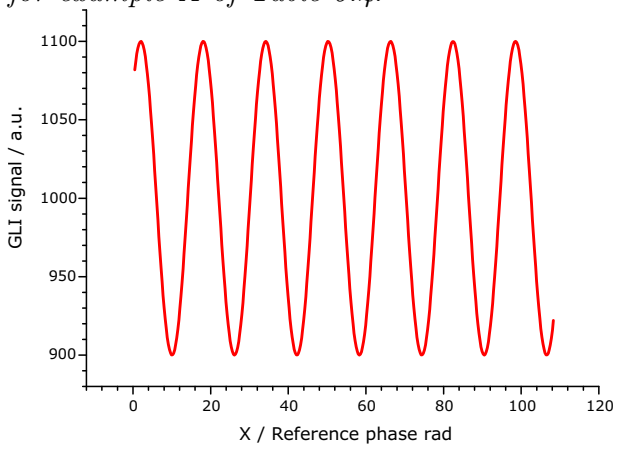

Figure 6.31b: *The sinusoidal data simulated for example B of Table 6.4. The data in example E covers the same range, with a tenfold increase in point density.*

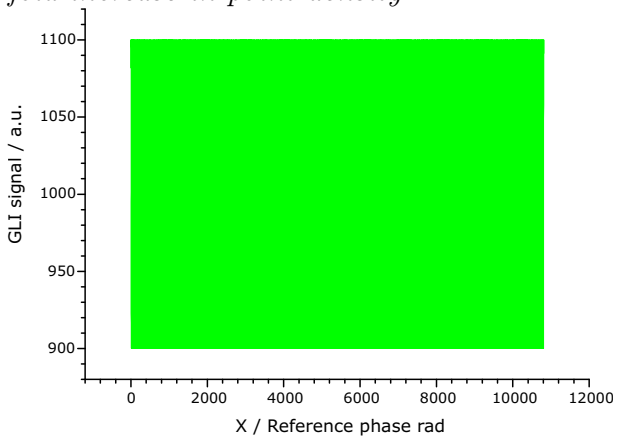

Figure 6.31c: *The sinusoidal data simulated for example C of Table 6.4. The data in example D covers the same range, with a tenfold increase in point density.*

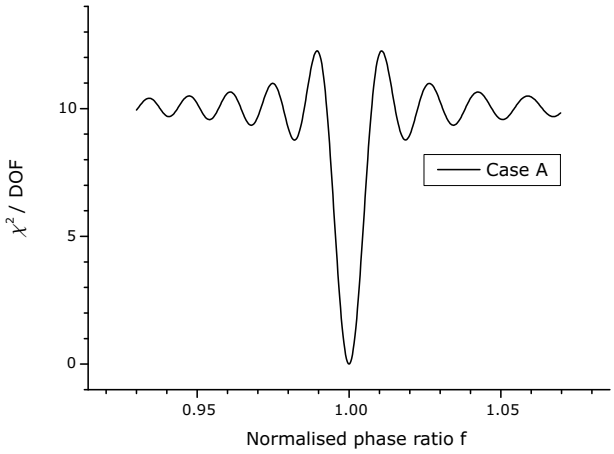

Figure 6.32a: *Inverted sinc χ^2 /DOF profile of fit to sinusoid from example A of Table 6.4.*

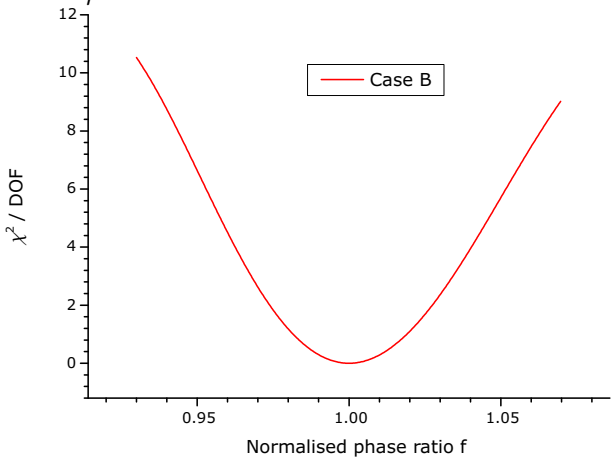

Figure 6.32b: *Inverted sinc χ^2 /DOF profile of fit to sinusoid from example B of Table 6.4. This is identical to the profile for the fit to example E data.*

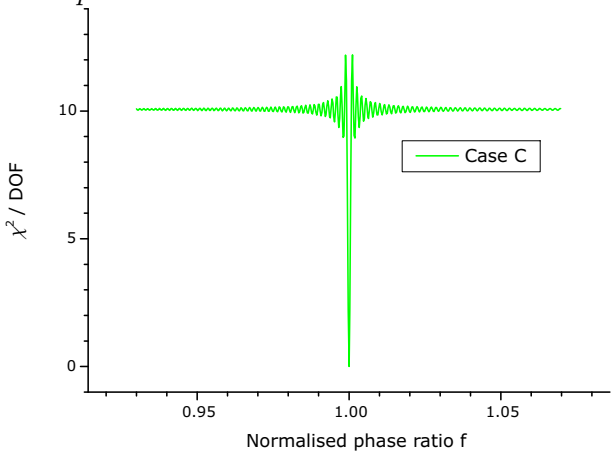

Figure 6.32c: *Inverted sinc χ^2 /DOF profile of fit to sinusoid from example C of Table 6.4. This is identical to the profile for the fit to example D data.*

In general the global χ^2 per degree of freedom is smaller for weaker return signals. It is not possible to normalise the χ^2 used for guiding the four parameter sine fit by dividing by $I_{\rm AC}^2$, (or in the notation of this discussion B^2) because this decouples the AC amplitude and leaves the χ^2 independent of $I_{\rm AC}$ as a three parameter fit. It could be considered for normalising the final result once the settled fit parameter values have been found, allowing the χ^2 per degree of freedom for different fits to the same interferometer, made at different times with different strength signals, to be compared.

In the χ^2 per degree of freedom profiles, for the first five examples, an increase in the span of the data Δx, (which corresponds to an increase in second type of lever arm when fitting a straight line), results in narrower sinc function, with a sharper central minimum. An increase in the midpoint of each block of data, (corresponding to an lever arm of the first type when fitting a straight line) results in an increase in the frequency of the cosinusoid. For the first five examples, the modulation of the cosinusoidal term is not immediately apparent, because the result retains the shape of an inverted sinc function. Once the frequency of sinc and cosinusoid in the χ^2 per degree of freedom profile become very different, as with the sinusoidal data from example F of Table 6.4, shown in Fig. 6.33, the cosinusoidal modulation is readily apparent as seen in Fig. 6.34.

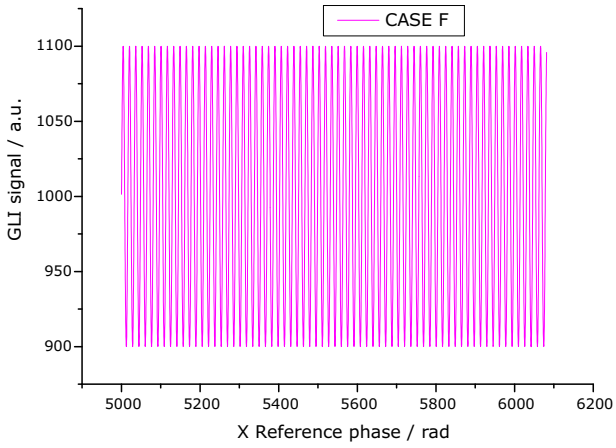

Figure 6.33: *The sinusoidal data simulated for example F of Table 6.4.*

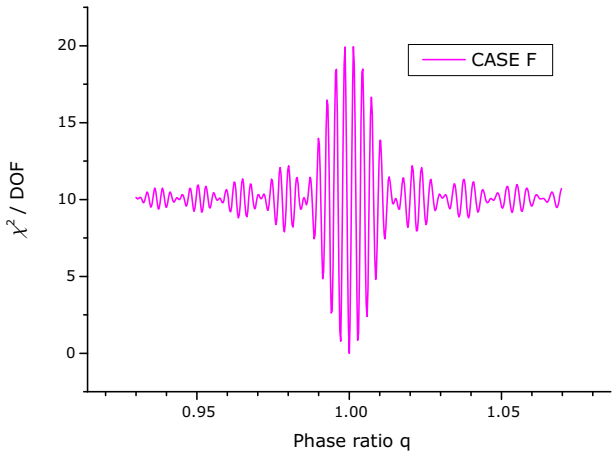

Figure 6.34: *Profile of χ^2 per degree of freedom for sine fitting example F of Table 6.4. The rapid cosinusoidal modulation is a result of the lever arm of the centre of the sinusoidal GLI data being fitted.*

The data set from example F spans the same range Δx as the data in example A and so the basic sinc envelope of the χ^2 per degree of freedom profile is the same in both cases. This similarity is *not* apparent on comparing the profile for example A shown in Fig. 6.32a and Fig. 6.34, because both inverted sinc envelopes are modulated by a cosinusoid.

The midpoint lever arm effect can be reduced for the sinefitting example F, by redefining the x axis values using equation 6.58 above. The simulated sinusoidal signal was recalculated for the new values of x_i' and the corresponding χ^2 per degree of freedom profile changes to that shown in Fig. 6.35, in which the frequency of the cosinusoidal modulation is reduced significantly, leaving a smooth function, with a more distinct global minimum, which is much easier to find for a fitting algorithm. The sinusoidal data for example G of Table 6.4 is shown in Fig. 6.36. The corresponding χ^2 per degree of freedom profile is shown at the same scale as all the other profiles in Fig. 6.37a and in close up around the region where $f = 1$ in Fig. 6.37b to show the distinct, steep-sided, multiple local minima.

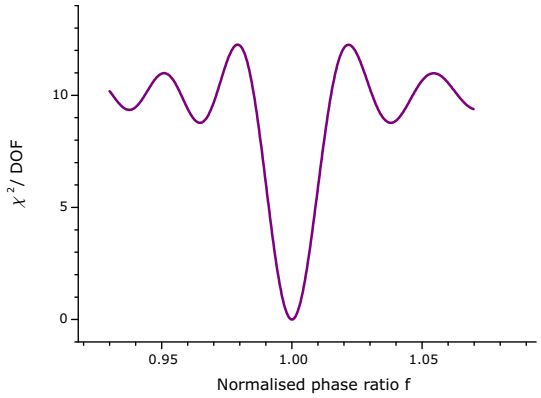

Figure 6.35: *The χ^2 per degree of freedom profile for the sine fitting example F of Table 6.4, after redefining the x values to make the sinusoidal data straddle the y axis.*

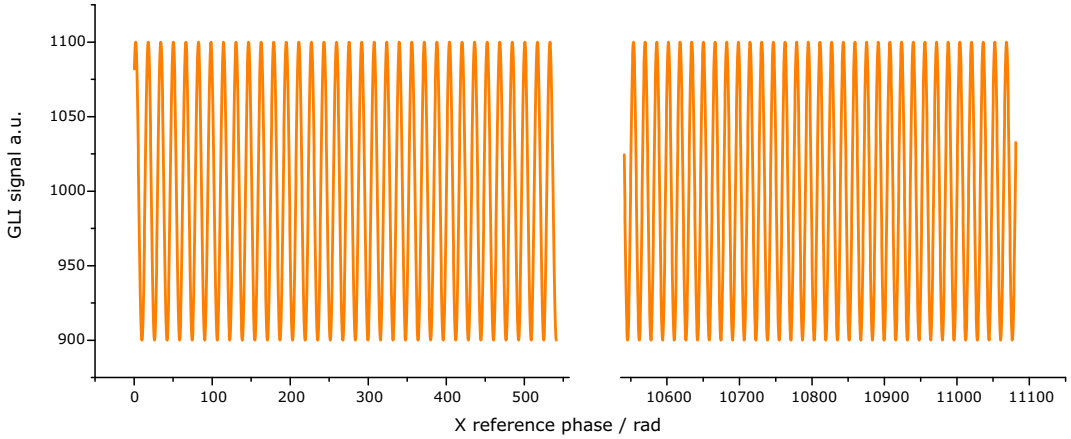

Figure 6.36: *The sinusoidal data simulated for example G of Table 6.4.*

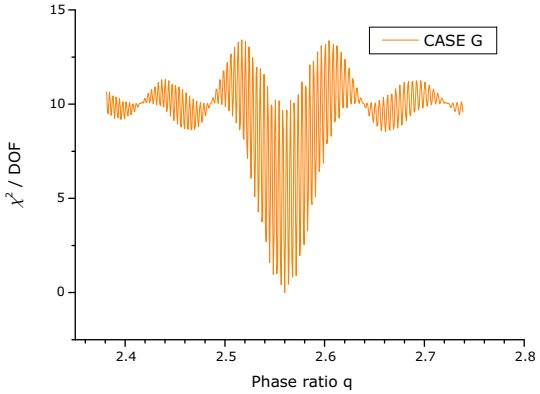

Figure 6.37a: *The χ^2 per degree of freedom profile for the sine fit applied to the simulated data for example G of Table 6.4.*

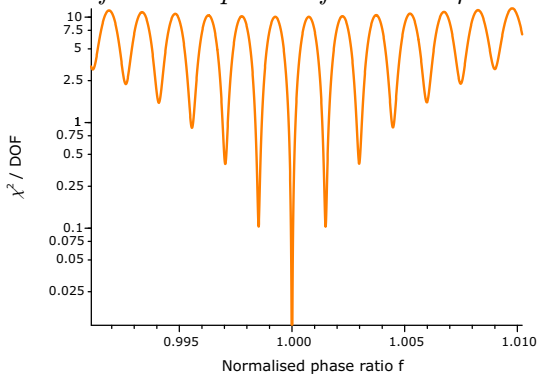

Figure 6.37b: *The χ^2 per degree of freedom profile for the sine fit applied to the simulated data for example G of Table 6.4, shown in close up around $f = 1$ to allow the distinct local minima to be seen. The log scale for the vertical axis allows the depths to be compared.*

The relative depth of these local minima can be changed by small errors in the initial value phase offset fit parameter. The effect of a 150 mrad error in the phase offset is demonstrated for the sine fitting example G of Table 6.4, in Fig. 6.38, where it can be seen that the deepest minimum is closer to $f \approx 1.0015$ than $f = 1.0000$. If MINUIT were initially set with a phase offset in error by at least 150 mrad, it would find on scanning the χ^2 profile in fitted phase ratio, that the local minimum at $f \approx 1.0000$ was not the deepest and would instead converge on a different minimum adjusting the four fit parameters to reach the bottom of this steep sided local minima in the χ^2. This would result in a phase ratio error larger than 1000 ppm.

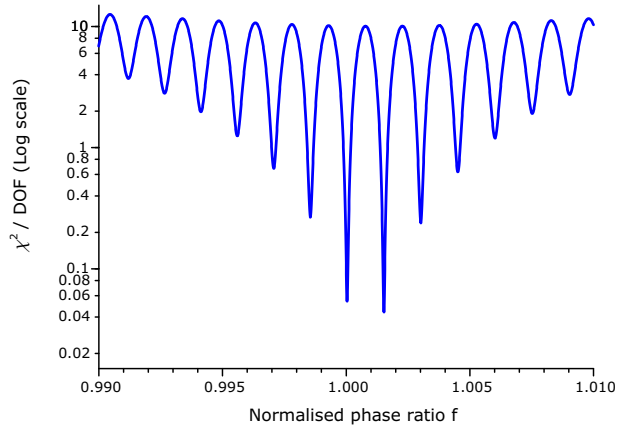

Figure 6.38: *The change in relative depth of the local minima in the χ^2 per degree of freedom profile induced by an error of 150 mrad in the phase offset fit parameter for sine fitting example G of Table 6.4. Compare these minima with those for zero phase offset error shown in Fig. 6.37b.*

The high frequency cosinusoidal modulation can only be removed for each individual block of data independently by redefining the x data for each block so that it straddles the y axis. This removes the inter-block lever arm. If this were removed for two subscans, by adjusting the x data of both, rather than being linked together they would be fitted individually, wasting the potential lever arm, which linked subscans benefit from.

If the modulation were allowed to remained and a χ^2 based method for linking subscans were attempted, the modulation features would be distorted by interferometer drift, vibrations and spurious reflections, making it very difficult to find the correct minimum.

The linked subscan data presented in chapter 5 can be taken as an example. A 400 mm GLI was measured using two subscans of around 35 GHz, separated by a coarse tuning interval of approximately 3.5 THz. The separation between subscans, was 100 times the subscan length which is ten times larger than the relative separation in the sine fitting example G. Even in the absence of noise, drift, vibration or spurious reflections, there would therefore be approximately ten times the density of local minima within the main minimum of the inverted sinc envelope, than shown for the example G in Fig. 6.37a, which has a similar phase ratio to the 400 mm GLI ($q \approx 2.14$), making it very difficult to find the correct minimum.

6.4.2 Sine fitting errors due to reference phase noise

The simulation discussed in section 6.4.1 was modified to add random errors with a Gaussian probability distribution, to the reference phase x data, for subscans otherwise identical to the sine fitting example A from Table 6.4. The simulated GLI signal had the same phase

ratio ($q = 2.56$) and the same offset phase ($\alpha = -0.789$) and the same amplitudes as the signal shown in Fig. 6.31a.

For each level of Gaussian reference phase noise, (given by the standard deviation of the Gaussian distribution in reference phase units), forty subscans were simulated and the standard deviation of the errors in phase ratio and subscan midpoint phase were calculated.

The error on the fitted phase ratio, ϵ_q was calculated in ppm using

$$\epsilon_q = 10^6 \left(\frac{q_{\mathrm{FIT}} - q}{q} \right) \tag{6.63}$$

where q was the true phase ratio for the simulated GLI.

The error on the fitted subscan midpoint phase, $\epsilon_{\overline{\Theta}}$ (GLI) radians, was defined to be

$$\epsilon_{\overline{\Theta}} = \overline{\Theta} - \overline{\Theta_{\mathrm{FIT}}} \tag{6.64}$$

where the fitted midpoint phase was calculated using

$$\overline{\Theta_{\mathrm{FIT}}} = \left(\frac{x_N + x_1}{2q_{\mathrm{FIT}}} \right) + \alpha_{\mathrm{FIT}} \tag{6.65}$$

where x_1 and x_N are, respectively, the first and last subscan values of simulated *measured* reference phase, including the reference phase noise.

The benchmark GLI midpoint phase was calculated using

$$\overline{\Theta} = \left(\frac{\Phi_N + \Phi_1}{2q} \right) + \alpha \tag{6.66}$$

where Φ_1 and Φ_N are the simulated *true* reference phase values at the start and end of the subscan, respectively.

The simulated phase ratio and midpoint phase errors are shown in Fig. 6.39 plotted against reference phase noise level for the range 1 to 10 mrad, covering the order of magnitude in which the reference phase errors of the demonstration system were estimated to lie, (as discussed above in section 6.2).

Some of these simulations were repeated with the x data shifted by $-86 \times 2\pi$ reference radians, so that the subscan data straddled the y axis. No significant differences from the errors in fitted phase ratio and subscan midpoint GLI phase shown in Fig. 6.39 were found after redefining the x values to straddle the y axis.

6.4.3 Sine fitting errors due to GLI intensity noise

The simulation discussed in section 6.4.2 was modified to generate Gaussian distributed random intensity noise on the GLI signal with noise free reference phase values. This intensity noise simulation was used to study the effects of decreasing GLI signal to noise ratio (SNR) on the fitted phase ratio and subscan midpoint phase. In these simulations, the signal to noise ratio was lowered by increasing the noise level, while keeping the signal fixed. Given that the signal level was simulated in arbitrary units, increasing the simulated noise was equivalent to a simulation of fixed Gaussian noise with decreasing signal power.

The effect of lowering the SNR on χ^2 profile for a sine fit, is to leave the basic inverted sinc function shape unaltered but raised up as shown in the profile for measured data with reduced GLI signal of Fig. 5.19.

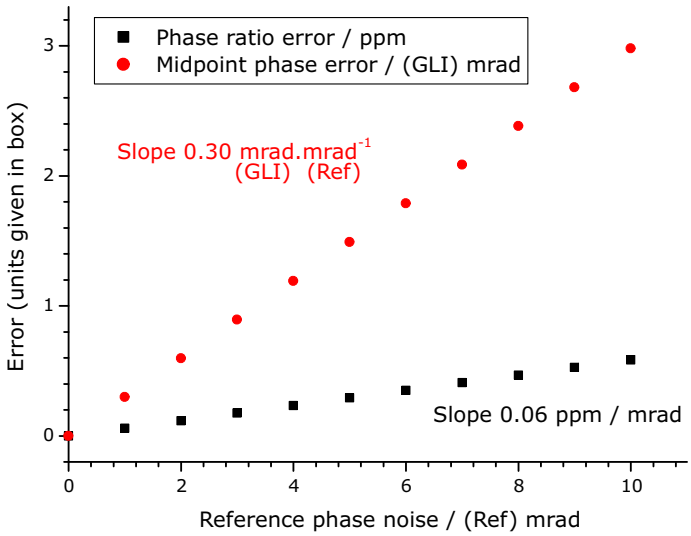

Figure 6.39: *Linear dependence of the errors in fitted phase ratio an subscan midpoint GLI phase with increasing reference phase noise, for sine fitting to a single subscan.*

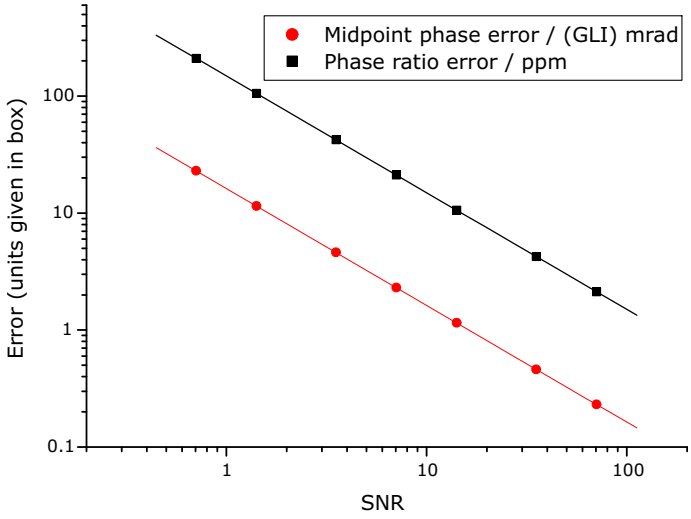

Figure 6.40: *The SNR dependence of errors in phase ratio and subscan midpoint phase fitted to data from a single subscan.*

The results of the low SNR simulation are shown in Fig. 6.40 for a range of SNRs. The SNR in each case was calculated using equation 6.13. These results show that phase ratio errors and errors in the midpoint phase are both inversely proportional to the SNR.

The errors in the linked phase ratio which would result from *subscan midpoint phase* errors at the level predicted by this simulation can be compared with the results of the linked subscan measurements recorded with low SNR presented in chapter 5. The phase shift of the 456.66 mm GLI between anchor points, ≈ 3.47 THz apart, was $\approx 6.64 \times 10^4$ rad. An error of 10 mrad in the phase of each GLI anchor point, (taken from Fig. 6.40 for a SNR of ≈ 1.5), is equivalent to a 14 mrad error in the target anchor point, assuming the error contribution from each anchor point is independent, which corresponds to an error in the linked phase ratio of 0.21 ppm. The corresponding error in the GLI length would be ≈ 100 nm, which is significantly smaller than the spread in the measured lengths, showing

that other contributions to the measurement error were significant.

The large *phase ratio* errors predicted by the simulation at low SNR would give rise to large variations in the value of GLI phase used for the linking extrapolations for linking the GLI phase and for the inter-subscan drift correction. Some of the extrapolations of GLI phase in the scans recorded at low SNR, needed corrections for $\pm 2\pi$ errors in the predicted anchor phase (see Table 5.4), but the corresponding errors in the inter-subscan drift corrections were not removed. The propagation of phase ratio errors into the inter-subscan drift correction is discussed below in section 6.5.2.

6.4.4 Combined effect of tuning-non linearity and intra-subscan drift

The combined effect of linear GLI intra-subscan drift and non-linear tuning on the fitted values of phase ratio and the GLI phase of linking anchor points was analysed using simulations[17]. These simulations show that the error contributions from this effect are always small.

The simulated drift was large and linear with time. This is a good model for drift of the steel table on which some of the demonstration GLIs were built, because the table had a large thermal mass which smoothed out the rate of change of temperature.[18]

Any combination of non-linear tuning and small non-linear drift is assumed to be equivalent to some other combination of linear drift and (slightly modified) non-linear tuning. In this work, only combinations of simplistic quadratic non-linearities in laser tuning together with linear drift have been simulated.

Simulated tuning non-linearities

The simulated tuning curve was made non-linear by adding a parabola to a linear function. The normalised non-linearity is given by the ratio of the maximum deviation (in reference phase) from the linear tuning curve, represented by b_X, to the total shift in reference phase along the linear tuning curve, represented by ΔX. Some example tuning curves for different values of normalised non-linearity (b_X/Δ_X) are shown in Fig. 6.41.

Subscan midpoint phase errors

The error on the anchor point phase, depends upon on the choice of definition for subscan midpoint phase. In analysing data for the measurements presented in the earlier chapters, the GLI midpoint phase was always calculated from the midpoint reference phase using equation 3.43.

There are at least three possibile definitions for the subscan midpoint reference phase :

1. The mean of the reference phase values at the subscan end points as defined in equation 3.41.

2. The reference phase interpolated at the moment of time midway through the duration of the subscan.

[17]These simulations were independent of those discussed above in the earlier parts of this section.

[18]The alternative carbon fibre supports for the GLIs had a much smaller coefficient of thermal expansion and so the drift was much smaller. Therefore the non-linear drift terms were small for GLIs supported by either structure, but because the simulation needed a large drift to make the resulting errors more obvious, it is a closer model to a metal support structure with large thermal mass.

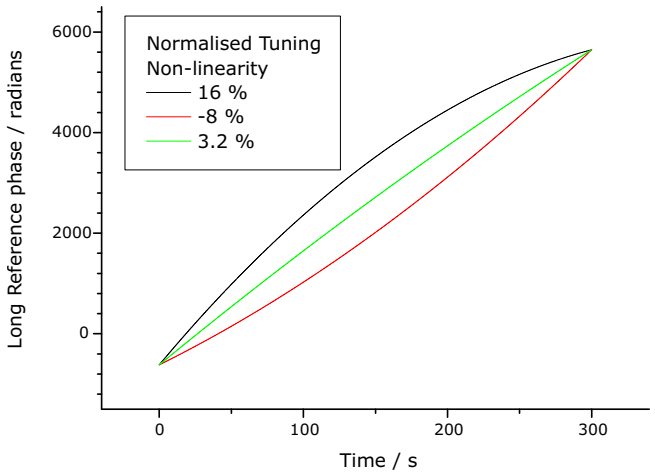

Figure 6.41: *Examples of simulated non-linear tuning curves.*

3. The mean of all unwrapped reference phase data from the subscan.

The first definition was used in the analysis software, because it was the simplest. The second definition would be difficult to implement and has no obvious advantages over the simpler first choice. The third is analogous to the centre of gravity of the subscan. This choice has the advantage that the phase offset fit parameter in the sine fit appears to be selected to minimise the difference between the fit function and the data at this point.

In these (non-linear tuning plus intra-subscan drift) simulations, the difference between the GLI phase at the true subscan centre of gravity and the fitted centre of gravity GLI phase was always smaller than 1 mrad, even in cases with large drift. In future, it would seem to be better to use this definition of subscan midpoint for the GLI phase anchor points in the analysis software, rather than the first definition of the above list.

The difference between the true centre of gravity of the GLI phase and the fitted midpoint value, (based on the first definition of subscan midpoint reference phase), was recorded in these simulations at different levels of tuning linearity. This difference ϵ_Θ was found to follow

$$\epsilon_\Theta = \mathbf{fold}\left(4\left(\frac{\Delta\mathcal{D}}{\lambda}\right)\left(\frac{b_X}{\Delta X}\right)\right) \tag{6.67}$$

to within $\pm 3\%$, where $\Delta\mathcal{D}$ is the change in GLI OPD due to interferometer drift during the subscan being fitted. This is proportional to the difference which would be expected between the first and third definitions of midpoint phase.

Phase ratio errors

The effect of increasing the magnitude of the tuning non-linearity on the phase ratio fitted to the subscan data for a single laser, is shown in Fig. 6.42, for a simulated 400 mm GLI. The simulation used a laser wavelength of around 859 nm with zero random noise in the reference phase or in the GLI intensity signal. The intra-subscan drift was deliberately exaggerated so that changes in the induced drift error would be easier to follow.

The induced change in GLI OPD in this simulation was $\Delta\mathcal{D} = 1.5$ μm with the tuning curve, following the basic form shown in Fig. 6.41 for different levels of non-linearity. In this case, the expected drift error according to equation 1.34c would be -3757 ppm of the GLI phase ratio. The fitted phase ratio is smaller than the true value, because Ω is positive and ε is negative for positive GLI drift, (an expanding GLI).

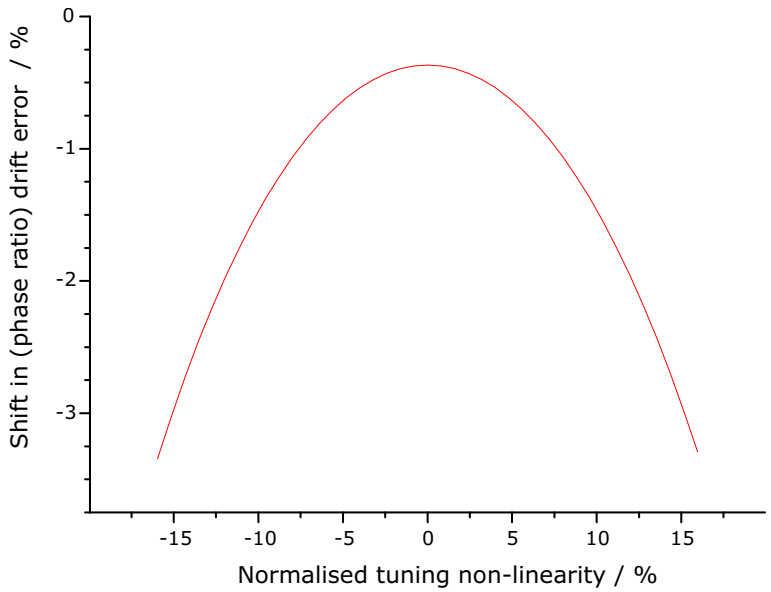

Figure 6.42: *Shift in phase ratio intra-subscan drift error from the expected value of error (in percent of the expected value) as a function of tuning non-linearity, for a sine fit to single subscan data from a single laser, with very large drift of* 1.5 μm *change in OPD. Note that even with linear tuning the error in the fitted phase ratio was not identical to the error predicted by equation 1.34c, due to higher order drift contributions.*

The magnitude of the drift error in the simulation results, was always smaller than that of the drift error predicted by equation 1.34c, even in the case of linear tuning ($b_X = 0$), $|q_{\mathrm{FIT}} - q|$ it was smaller than predicted by 17 ppm. This small difference was due to second order drift terms, which were dropped from the derivation of equation 1.34c.

In cases of large thermal drift, the contribution of higher order drift terms to the phase ratio error from single laser data may have been several ppm, but this would have been on the background of the main drift error of several thousand parts per million. These contributions may explain some of the error in the combined laser results, but only in cases of very large drift. Given that the errors in the combined laser result were always at the same level, regardless of the drift conditions, higher order drift contributions were never an important source of error in GLI length measurements.

6.4.5 Effect of GLI vibrations and turbulence

The effect on the GLI length measurement, of cyclic variations in GLI OPD due to vibration, turbulence and acoustic noise, depends on the amplitude and frequency of the oscillation relative to the natural length and timescales of the FSI system.

The natural length scale for an FSI measurement was the optical wavelength. The change in GLI phase as the length oscillates, scales with the ratio between the vibration peak to peak amplitude A_0 and the optical wavelength in the gas, $\frac{\lambda}{n}$. The GLI phase change over the half cycle between the two extremes in the OPD, is given by

$$\Delta\Theta_{\mathrm{VIB}} = 4n\pi\frac{A_0}{\lambda} \tag{6.68}$$

An important transition can be expected as $\Delta\Theta_{\mathrm{VIB}}$ approaches 2π, when the peak to peak vibration amplitude is around half a wavelength. This was observed for vibration frequencies

lower than the 50 Hz rate of long reference phase measurement.

The vibration frequency needs to be compared with several timescales which are relevent to an FSI scan. These are summarised in Fig. 6.43. Vibrations with a period similar to or longer than a subscan are caused by thermal and mechanical drift and the resulting influence on the single subscan results is already mitigated by the dual-laser technique discussed above. Acoustic noise and turbulence mimic rapid mechanical vibrations and once these are faster than the DAQ cycle time, the phase changes they induce tend to be averaged out in the subscan data.

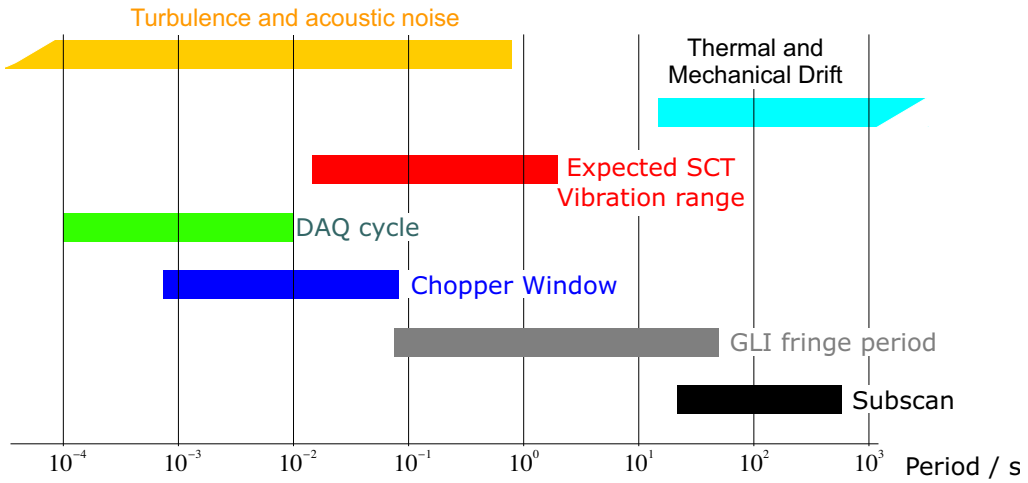

Figure 6.43: *Comparison between FSI system timescales and changes in GLI OPD.*

The linking measurements made in the presence of retroreflector vibration represent a crude first glance at the degradation of measurement precision, which will need to be followed up if the limitations imposed by vibration are to be better understood.

The importance of redefining the χ^2 used for guiding the sine fit in the presence of vibrations has been demonstrated as discussed in chapter 5. Given that the performance of the sine fit appears to be similar with good quality signals and better with degraded signals, the definition of χ^2 with a weight given by equation 5.15, appears to be the best choice found so far and is therefore recommended for use in future FSI measurements.

The following issues should be addressed in future studies of FSI in the presence of vibration :

- The effectiveness of changes to the measurement and analysis techniques which can be used to decrease the induced errors.

The key issue regarding the linked subscan technique for GLIs with significant vibration, is the potential for improvement. The use of more subscans and a wider total frequency range for the scan are expected to reduce the errors, but this needs to be demonstrated. For example, the 2.0 μm spread in GLI length measurements made in the presence of vibrations with a peak to peak amplitude of 400 nm and at 20 Hz, should decrease to 1.0 μm, if the total tuning range of laser 1 were widened to 16 nm ($\approx$ 7 THz), but this has not yet been demonstrated, because the demonstration system described in chapter 2 was not suitable for generating scans with more than two subscans.

Several changes to the data analysis are also possible. Apart from the change to the definition of χ^2 used to guide the fitting of sinusoids to GLI data, which has already been

used in the analysis of vibration measurements, changes to the inter-subscan drift correction are proposed below.

- The relationship between vibration and DAQ frequencies.

To design the ATLAS FSI system to cope with the range of possible vibration frequencies which may appear in the SCT, it will be necessary to understand how the errors induced by vibration depend on the ratio between vibration and data acquisition frequencies. In the measurements presented in chapter 5, the error on the GLI length at all vibration amplitudes, increased significantly when the vibration frequency and the rate of subscan data point acquisition were equal. It would be interesting to repeat the measurements at a higher DAQ frequency, with faster vibrations, to see if the induced errors always increase when the frequencies are equal and to investigate what happens when the vibrations are faster than the data acquisition.

- The effect of vibration amplitudes larger than half a wavelength.

It would interesting to know how the measurement error depends on the vibration amplitude, for larger amplitudes.

6.4.6 Spurious reflections

Spurious reflections were found to increase measurement errors in a brief set of linked subscan measurements presented in chapter 5 and have been selected as the most likely cause of the large tuning polarity dependent errors in the Set 1 single subscan measurements of chapter 4. A much smaller tuning polarity dependence was observed in the GLI measurements of Set D, but there was no large spurious reflection present in the measurements of Set D. The presence of very small spurious reflections cannot be ruled out, even if when there is no direct evidence in the raw interferometer signal or in the χ^2 profile.

Further work would be needed to show how significant a problem spurious reflection could be in the ATLAS system and what difference, if any could be made by improving the analysis, for example by fitting sinusoids using a χ^2 defined with a common weight on each data point as used in chapter 5 to improve the fitting of data taken in the presence of vibrations.

Even weak spurious reflections have the potential to cause problems, because the quills in the FSI system will be designed to create large interference signals by combining the weak retroreflector signal with large beam-splitter V mode signals as discussed in chapter 1. The same enhancement will apply to unwanted weak reflection modes, those from within the GLI or from within the fibres.

6.5 Corrections for relative interferometer drift

The main sources of error for the two types of drift correction are discussed in this section. The phase ratio used for the first linking extrapolation and the first inter-subscan drift correction was based on the average of intra-subscan drift corrected phase ratio values from each subscan and so errors in the intra-subscan drift contributed to errors in the inter-subscan drift. The corrections for intra-subscan drift are therefore considered first.

6.5.1 Dual laser intra-subscan drift correction

The drift corrected phase ratio, q_0 was calculated using equation 1.40, which combines the best fit phase ratios for data from each laser q_1 and q_2 using a weighting ratio ρ used to combine them.

The best estimate for the correct value of ρ was based on the measured values for Ω_1 and Ω_2 and equation 1.41. The measured values, with errors, will be represented as $\Omega_1^\star$ and $\Omega_2^\star$ respectively. From these an estimated value, $\rho^\star$ is given by

$$\rho^\star = \frac{\Omega_2^\star}{\Omega_1^\star} \tag{6.69}$$

As pointed out in equation 1.38, the appropriate value of ρ, for calculating q_0 is the ratio of the differences between the single laser fitted GLI phase ratios and the true GLI phase ratio, even if those differences contain contributions other than those predicted to arise from intra-subscan drift. Therefore the only discrepancy in $\rho^\star$ which matters, is the difference between the value of $\rho^\star$, used for all grid line interferometers and the GLI specific (and subscan specific) value ρ_{GLI} given by

$$\rho_{\mathrm{GLI}} = \frac{q_2 - q_{\mathrm{GLI}}}{q_1 - q_{\mathrm{GLI}}} \tag{6.70}$$

which would exactly cancel out errors in the combined laser result, so that $q_0 = q$.

A mismatch between $\rho^\star$ and the GLI specific ρ_{GLI}, leads to a remnant of the original error in q_1, (or equivalently[19] in q_2), appearing in the combined laser phase ratio q_0. The size of this residual error, $q_0 - q_{\mathrm{GLI}}$ as a percentage of the original error in $q_1 - q_{\mathrm{GLI}}$ (usually dominated by the contribution from intra-subscan drift) is shown in Fig. 6.44 as a function of the ratio between $\rho^\star$ and ρ_{GLI}, over a range of $\pm 10\%$ in ρ_{GLI} for different values of ρ_{GLI}.

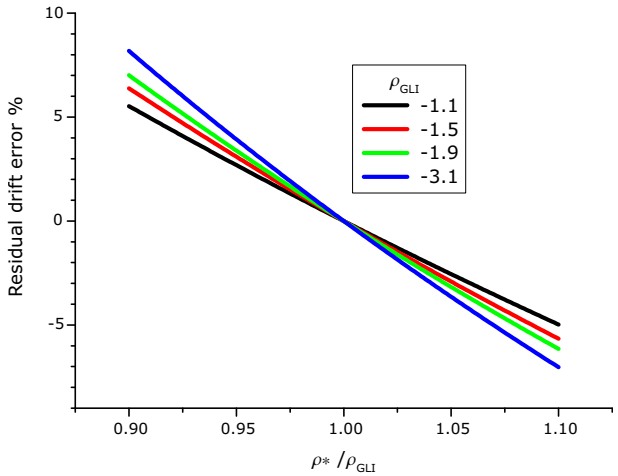

Figure 6.44: *The dependence of the residual intra-subscan drift error in q_0 on the mismatch of the estiamted value of ρ.*

Because the two lasers tune in opposite directions, ρ is always negative. Common optics in any FSI system ensures that the laser frequencies are the same to within $\pm 10\%$ and the fine tuning range of laser 1 can be expected to be at least one third of the laser 2 fine tuning

[19]The expressions which follow, refer to the error in q_1. The result from laser 1 has no special status and an equivalent set of equations could just as easily be based on q_2 instead.

range, so $|\rho| \leq 3$. When considering a lower bound for the magnitude of ρ, if the laser which tunes over the larger proportional frequency range is labelled laser 2 for the purposes of calculating q_0, then $|\rho| \geq 1$. In that case, the intra-subscan drift error of laser 1 will be the larger.

As shown in Fig. 6.44, the largest residual intra-subscan drift dominated error in q_0 is within $\pm 10\%$ of the error in q_1, for errors in the estimate of ρ up to $\pm 10\%$ and the closer the magnitude of ρ to unity, the smaller the residual error in q_0.

6.5.2 Inter-subscan drift correction

The inter-subscan drift correction was used to adjust the GLI phase of the linking target anchor point from its measured value Θ_B to the value it would have had $\Theta_{\tilde{B}}$ if there had been no inter-subscan drift.

The required correction was made by linking the laser 2 GLI data in each fine tuning subscan. The inter-subscan drift correction was taken to be the difference between the laser 2 predicted anchor point Θ_{C2} and the nearest choice of laser 2 target anchor point Θ_{B2}. Hence the inter-subscan drift correction is calculated using

$$\begin{aligned} \Theta_{\tilde{B}} &= \Theta_B - (\Theta_{C2} - \Theta_{B2}) \\ &= \Theta_B - \left(\Theta_{A2} + \frac{\Phi_{\mathrm{AB2}}}{q_{\mathrm{AV}}} - \Theta_{B2} \right) \end{aligned} \tag{6.71}$$

The size of the correction term $(\Theta_{C2} - \Theta_{B2})$, always lies within $\pm\pi$ GLI radians, because Θ_{B2} is always the *nearest* choice of anchor point to Θ_{C2}.

There are three important potential sources of error[20] using the inter-subscan drift correction in its present form :

1. Differential phase errors in anchor points Θ_{A2} and Θ_{B2}.

2. Errors in the phase ratio q_{AV} used to predict Θ_{C2}.

3. A significant departure from the (implicit) assumption that the bridge centre optical frequencies of the two lasers are identical.

The first error is inherent in the sine fitting results from the single subscan data for laser 2. The reduction of this error would require an improvement in the sine fitting. One improvement was demonstrated in chapter 5, with a common weight per data point in the definition of χ^2, although this was not assessed for improvements in the precision of the fitted phase ratio rather than anchor point phase. Assessment of the improvement in the precision of the fitted anchor point phase would have been much more difficult, because indirect means would have been required. Another way of reducing the anchor point phase errors is to use anchor points at the centre of gravity of each subscan, rather than at the midpoint between the two ends. This change should help to reduce errors due to the combined effect of intra-subscan drift and tuning non-linearity as discussed above in section 6.4.

The effect of errors in the phase ratio used for extrapolation q_{AV} can be minimised in the future by reducing the lever arm between the two subscans of laser 2, $\Delta\Phi_{\mathrm{AB2}}$. If the frequency of laser 2 is reset to the frequency at which laser 2 subscan A started, while laser 1

[20]Errors due to miscounting the number of laser 2 etalon peaks for reference phase linking were very unlikely, because this laser was only fine tuned in the same direction throughout a scan so the small number of etalon peaks were easily counted from the raw data without ambiguity.

is coarse tuning, subscan A and B for laser 2 would cover the same frequency interval. The frequency difference between the two anchor points, and therefore errors in the inter-subscan drift correction from using the wrong phase ratio, should be reduced in this way by at least two orders of magnitude.

The contribution of the second error to the phase error of the target anchor point used for linking was estimated for Set 4 linked subscan measurements, introduced in chapter 5, by a second correction for inter-subscan drift, using the initially drift corrected linked phase ratio to recalculate the laser 2 linking extrapolation in place of q_{AV} in equation 6.71.

The variation of the GLI lengths in Set 4 were predicted using the GLI steel temperature and these predictions were compared with the measurements corrected for refractive index and inter-subscan drift in Fig. 5.3d. After applying a second correction for inter-subscan drift using the first value of linked phase ratio, (as described above), the residual differences between the length measurements and the thermal trend (predicted from the steel temperature) decrease as shown in Fig. 6.45.

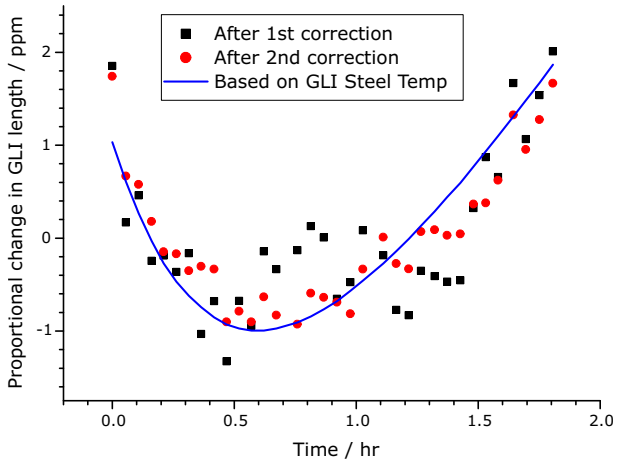

Figure 6.45: *Set 4 Comparison of expected GLI length variations and measured variations after 1st and 2nd corrections for inter subscan drift correction. The 2nd correction decreases the residual differences between the predicted trend and the measurements.*

The decrease in the residual differences between measured and predicted GLI length, after the application of the first drift correction, ϵ_1, compared to the residual differences after the second correction ϵ_2. The standard deviation of residual differences after the first and second drift corrections, were $\sigma_{\epsilon 1} = 0.54$ ppm and $\sigma_{\epsilon 2} = 0.33$ ppm, a decrease of approximately one third.

The decrease in the residuals after the second correction is evidence that the phase ratio error in the initial correction was a significant contribution to the phase error of the target anchor point and thereby to the linked subscan GLI length measurement. Iterations beyond the second correction are very unlikely to produce further significant improvements, given that the linked phase ratio after the first inter-subscan drift correction, (which is used for the second correction), is already within one ppm of the expected length.

To address the third potential source of error in the above list, it would be necessary to calculate the optical frequency at each anchor point for each laser. These frequencies ν_{A1} and ν_{B1} for laser 1 in subscans A and B respectively and ν_{A2} and ν_{B2} similarly for laser 2, would be used to calculate the correction ratio for scaling the phase shift of the inter-subscan drift correction measured using laser 2 so that the appropriate phase correction is applied

to laser 1. The drift correction of equation 6.71 should therefore be modified to incorporate this rescaling for the difference laser frequencies.

The phase change induced in the GLI, due to a change in OPD, (inter-subscan drift), of $\Delta\mathcal{D}$ is given by subtracting the change in phase due to frequency scanning, from the total change in interferometer phase given by equation 1.31 and dropping the second order term, hence

$$\Delta\Theta_1^{\mathrm{DISP}} = \left(\frac{2\pi}{c}\right)\nu_1\Delta\mathcal{D} \tag{6.72}$$

for laser 1 and similarly for laser 2

$$\Delta\Theta_2^{\mathrm{DISP}} = \left(\frac{2\pi}{c}\right)\nu_2\Delta\mathcal{D} \tag{6.73}$$

The phase change for laser 1 is estimated from the change measured in laser 2 data using

$$\Delta\Theta_1 = \frac{\nu_1}{\nu_2}\Delta\Theta_2 \tag{6.74}$$

Therefore the corrected target anchor point for laser 1, accounting for differences in laser frequency, is given by

$$\Theta_{\tilde{B}} = \Theta_B - \left(\frac{\nu_{A1}+\nu_{B1}}{\nu_{A2}+\nu_{B2}}\right)\left(\Theta_{A2} + \left(\frac{\Phi_{\mathrm{AB2}}}{q_{\mathrm{AV}}}\right) - \Theta_{B2}\right) \tag{6.75}$$

As discussed in chapter 3, the scan centre wavelengths of the two lasers remained within 836.1 ± 0.1. The ratio $\left(\frac{\nu_{A1}+\nu_{B1}}{\nu_{A2}+\nu_{B2}}\right)$ was therefore always within $1 \pm 2.5 \times 10^{-4}$ so the most significant remaining error contribution in the phase of the target anchor point used for linking the GLI phase of laser 1, was a combination of phase errors in the anchor points of laser 2, used to produce the inter-subscan drift correction and equivalent GLI phase errors in the target anchor point for laser 1, which would be supplemented by the remaining errors in the inter-subscan drift correction, when it was applied.

FSI with three lasers

In a future FSI system, it might be possible to make FSI measurements using three lasers simultaneously rather than two, if only two subscans are needed to achieve the required measurement precision[21]. The chopping between lasers, would have to be altered so that two lasers were blocked, while one was illuminating the interferometers.

The aim with three lasers would be to use laser 1 and laser 2 to generate subscan A as in the usual two laser measurement. At the same time, laser 3 would be fine-tuned over the frequency range usually covered later by laser 1 in subscan B. The data from laser 3 would be used as if it were subscan B laser 1 data and the data from laser 2 could be used to cancel intra-subscan drift with laser 1 and laser 3, since the only requirement is that lasers 1 and 3 tune in the opposite direction from laser 2. This method would remove inter-subscan drift and halve the time taken for a scan at the cost of increased complexity in multiplexing.

[21] If more N subscans were required, a system using N lasers could be considered, but would rapidly become more complicated as N increased.

6.6 Refractivity corrections

Once the interferometer phase ratio had been determined, the refractivity corrections were applied to convert the phase ratio to a length ratio and thereby make the length measurement. This ratio between the measured optical path and the physical path is given by the *group* refractive index as explained in the first part of the following discussion.

6.6.1 Dispersion and the group refractive index

The dispersion of interferometer components such as beam-splitters and retroreflectors and even the air within the interferometers meant that the optical path difference of each interferometer was a function of wavelength.

It is shown in this section, that provided the frequency scan covered a region in which the refractivity changes linearly, the scan average optical path of each medium is given by the physical path of the beam through the medium multiplied by the group refractive index, n_g given by

$$n_g = n - \lambda \left(\frac{dn}{d\lambda}\right) = n + \nu \left(\frac{dn}{d\nu}\right) \tag{6.76}$$

where n is the (phase) refractive index of the medium under consideration.

The contributions to the frequency dependent optical path difference of a GLI $\mathcal{D}$, at a fixed laser frequency can be represented by

$$\mathcal{D} = 2\left(\sum_{i}^{\text{Long Arm}} n_i D_i - \sum_{j}^{\text{Short Arm}} n_j D_j\right) \tag{6.77}$$

with the factor of two accounting for the round trip, through each element of each interferometer arm.

Therefore the GLI phase at a particular laser frequency ν is given by

$$\Theta = \left(\frac{4\pi}{c}\right)\left(\sum_{i}^{\text{Long Arm}} n_i D_i - \sum_{j}^{\text{Short Arm}} n_j D_j\right)\nu \tag{6.78}$$

The following discussion has been made easier to follow, by considering the case where there is no interferometer drift. The absence or presence of interferometer drift does not alter the conclusion that group refractive index rather than phase refractive index is the relevant factor for converting phase ratio measurements into lengths.

The change of GLI phase due to scanning the laser frequency is given by

$$\Delta\Theta = \left(\frac{4\pi}{c}\right)\left[\overline{\mathcal{D}}\Delta\nu + \overline{\nu}\left(\sum_{i}^{\text{Long Arm}} D_i \Delta n_i - \sum_{j}^{\text{Short Arm}} D_j \Delta n_j\right)\right] \tag{6.79}$$

where $\overline{\mathcal{D}}$ is the scan average value of OPD and $\overline{\nu}$ is the scan average laser frequency.

The change in refractive index of each medium within the GLI during the frequency scan can be re-written as

$$\Delta n = \Delta\nu \left(\frac{dn}{d\nu}\right) \tag{6.80}$$

Substituting this back into equation 6.79 gives

$$\Delta\Theta = \left(\frac{4\pi}{c}\right)\Delta\nu\left[\sum_{i}^{\text{Long Arm}} D_i\left(\overline{n}_i + \overline{\nu}\left(\frac{dn_i}{d\nu}\right)\right) - \sum_{j}^{\text{Short Arm}} D_j\left(\overline{n}_j + \overline{\nu}\left(\frac{dn_j}{d\nu}\right)\right)\right] \tag{6.81}$$

which can be simplified by substituting group refractive index terms from equation 6.76 to give

$$\Delta\Theta = \left(\frac{4\pi}{c}\right)\Delta\nu\left[\sum_{i}^{\text{Long Arm}} D_i\overline{n}_{gi} - \sum_{j}^{\text{Short Arm}} D_j\overline{n}_{gj}\right] \tag{6.82}$$

Hence the measured GLI length is related to the measured OPD by the scan averaged beam path average group refractive index, $\overline{n}_g$, which is a function of the frequency interval used for the scan. In the GLI measurements presented in this thesis, the scan range for laser 1 was always from around 832.0 nm to around 840.0 nm so that the mean scan wavelength was always 836.1 ± 0.1 nm. This was the same for laser 2 to within ± 0.1 nm.

The effect on GLI length of a difference in scan centre wavelength of order 0.1 nm is negligible for air. The common path design of the grid line interferometer eliminated the effects of fibre dispersion on the measured length. The dominant differential dispersive contribution was due to the retroreflector, which was made out of BK7 as discussed in chapter 2. The group refractive index of BK7, is given by substituting equation 2.1 into equation 6.76 to give

$$n_g\left(\nu/\text{GHz}\right) = a_0 + 2a_1\nu + 3a_2\nu^2 \tag{6.83}$$

where the coefficients are

$$\begin{aligned} a_0 &= 1.50258 \\ a_1 &= 5.77 \times 10^{-9}\ \text{GHz}^{-1} \\ a_2 &= 4.28 \times 10^{-14}\ \text{GHz}^{-2} \end{aligned}$$

as given in chapter 2. The rate of change of BK7 group refractive index with frequency at a laser wavelength of 836 nm, ($\nu = 358.6$ THz) is approximately 1.0×10^{-7} per GHz.

The optical path in the retroreflector was treated as a constant offset in the length measurement of the GLI, approximately equal to the 6.4 mm depth of the retroreflector glass[22], multiplied by the scan average group refractive index. The change in group refractive index of the retroreflector with changes in scan centre laser frequency, leads to a rate of change in offset of around 0.7 nm.GHz^{-1}. If the scan average wavelength was maintained within ± 0.1 nm, the retroreflector offset was stable to around ± 30 nm.

6.6.2 Corrections for Air Refractivity

The simplified model used to calculate a correction for the refractivity difference between the air in the long reference and grid line interferometers is discussed in section 3.7 above. In that simplified model, the correction for air refractivity was based on differences in dry air refractivity due temperature, with pressure and gas composition assumed to be common.

In this section the difference between using refractive index and group refractive index for dry air is shown to be equivalent to a small change in air pressure. This is followed by an indication that the refractivity contributions due to water vapour, although not accurately measured in the near-infra red can be assumed to be negligible for the small corrections applied to the GLI length measurements.

The group refractive index of dry air

As stated above, the refractivity of a gas, ϱ, may be separated into a factor which represents the frequency dependent electromagnetic interaction, $\alpha\left(\nu\right)$ and a factor for the gas density,

[22]The exact value depends on the exact beam path through the glass retroreflector.

$\beta(p,\vartheta)$, which depends on the pressure, p and temperature ϑ. Therefore the refractive index may be written as

$$n = 1 + \varrho = 1 + \alpha(\nu)\,\beta(p,\vartheta) \tag{6.84}$$

where $\alpha\beta \ll 1$. This expression may be substituted into equation 6.76 to give the group refractive index

$$n_g = 1 + \beta\left[\alpha + \nu\left(\frac{d\alpha}{d\nu}\right)\right] \tag{6.85}$$

The applied air refractivity correction, expressed in equation 3.58 can be re-written as

$$D = \left(\frac{L}{q}\right)\left[1 + \alpha\left(\beta(\vartheta_{\mathrm{LR}}) - \beta(\vartheta_{\mathrm{GLI}})\right)\right] \tag{6.86}$$

where the common pressure was assumed to be around 1000 mbar and therefore from the 1000 mbar line of Fig. 3.12

$$\alpha\frac{\partial\beta}{\partial\vartheta} = -0.882 \times 10^{-6}\ \mathrm{K}^{-1}$$

at laser wavelengths in the range 830 nm to 840 nm, for dry air with 400 ppm of CO_2.

If the phase refractivity term α is replaced by the group refractivity term $\alpha + \nu\left(\frac{d\alpha}{d\nu}\right)$, this gives the air group refractivity corrected length,

$$D = \left(\frac{L}{q}\right)\left[1 + \left(\alpha + \nu\frac{d\alpha}{d\nu}\right)\left(\beta(p,\vartheta_{\mathrm{LR}}) - \beta(p,\vartheta_{\mathrm{GLI}})\right)\right] \tag{6.87}$$

The ratio between group refractivity and phase refractivity was calculated using expressions for phase and group refractivity of dry air taken from [Cid96] again assuming 400 ppm of CO_2. The ratio is shown as a function of vacuum wavelength in Fig. 6.46.

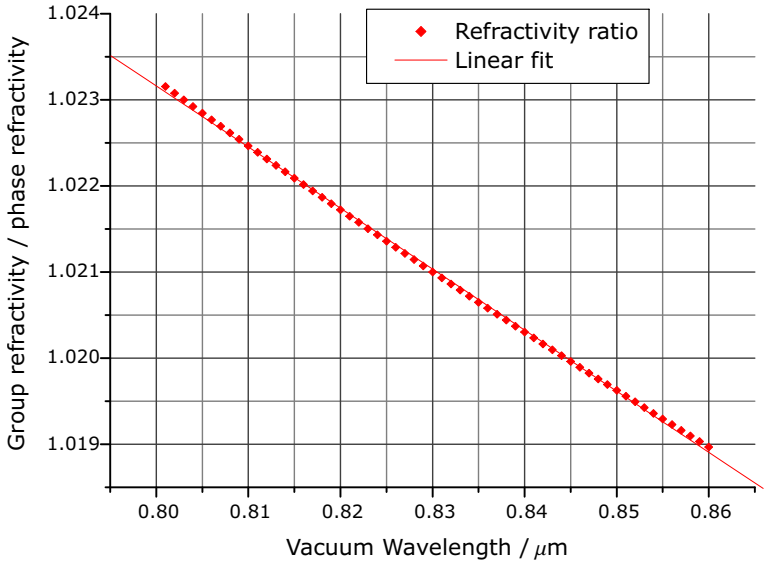

Figure 6.46: *Ratio between group and phase refractivity of dry air.*

The ratio is around 1.021 for wavelengths in the range 832 nm to 840 nm. So the applied correction which was based on phase refractivity of dry air at 1000 mbar is equivalent to a correction based on the group refractivity of dry air at around 980 mbar. The errors in the applied refractivity correction due to a departure in atmospheric pressure from 980 mbar, were around 1% of the correction per 10 mbar. The range of applied refractivity corrections

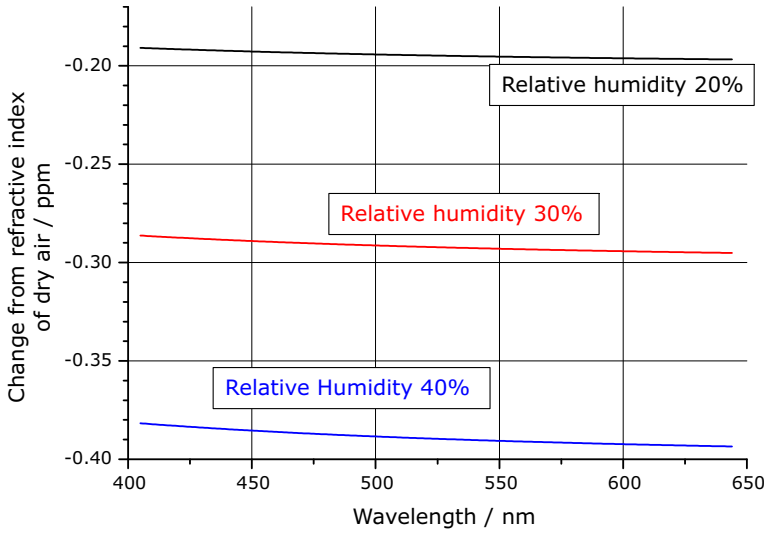

Figure 6.47: *Difference in refractive index between dry air and air at different humidity levels at 20°C and 1000 mbar, for visible wavelengths up to 650 nm.*

ranged from +0.6 ppm to −1.2 ppm, therefore an error of a few per cent in these corrections has very little effect on the determined length.

The pressure was not measured routinely, but can be safely assumed to have remained well within the range 900 mbar $\leq p \leq$ 1100 mbar, so that the maximum error on the refractivity correction would have been less than 0.1 ppm of the GLI length.

Refractivity of water vapour

The effects of water vapour on the refractivity of air were smaller than the errors due to uncertainty in the air pressure. As the air was common to all interferometers in the demonstration system, the effects of water vapour refractivity cancel to first order.

The refractivity of water vapour is lower than that of air, so that as the humidity of air increases, its refractive index decreases. There is limited data available for the water vapour in the near infra-red [Cid96]. The original Edlén equation given in [Kay89], covers the visible wavelength range from 350 nm to 650 nm. This equation has been used to calculate the difference in refractive index between dry air and moist air at 20° C and 1000 mbar, shown in Fig. 6.47 for the range of relative humidity levels from 20% to 40%. This was the relative humidity range in the demonstration system, with the air kept drier than ambient by continuous pumping of dry air into the room.

At the time of writing there appear to be no accurate measurements, available on the refractivity of water vapour in the near infra-red [Cid96, Bar00, Gre00].

If it is assumed that the magnitude of the difference in group refractivity between dry air and 40% relative humidity is at most 10^{-6} in the near infra-red, this is a decrease by less than 0.5% of the total air refractivity, equivalent to a change in pressure of 5 mbar and therefore negligible.

6.7 Summary

The FSI measurement technique presented in earlier chapters has been considered in detail with a view to understanding the dominant sources of error and recommending future improvements. As demonstrated, this subscan linking FSI technique can be used to measure more than one interferometer simultaneously, to a precision of better than 1 ppm, for lengths up to 1.2 m. This will be required for ATLAS SCT alignment.

Sinefitting was shown to be inappropriate as an alternative analysis technique for linking subscans. The reason for this is the presence of multiple densely packed minima in the χ^2 function, generated by the lever arm of the difference in reference phase between the two subscans. The correct minimum was not the deepest minimum, for perfect, noise free data, even when the offset phase fit parameter was initially set very close to the correct value. In the presence of typically encountered sources of noise such as GLI detector noise, interferometer drift, vibration or spurious reflections, the χ^2 profile would be distorted. This would lead a sinefit to settle in an inappropriate, yet apparently deeper minimum, giving rise to a significant phase ratio error.

The causal relationships between sources of error in the measured length using the demonstrated linking analysis method presented in chapter 3, have been presented and investigated in this chapter.

Errors in the reference phase were shown to have an insignificant effect on reference phase linking which was instead dominated by etalon peak fitting errors.

The effects of etalon peak miscounting was explored in depth, with several possible strategies for detecting miscounts in the future presented; the most promising being the linked length of the short reference interferometer used as a cross check.

The GLI phase linking errors were also shown to be dominated, not by the errors in reference phase, but by the residual errors in the GLI phase anchor points. Only these GLI phase linking errors remain in the determined interferometer phase ratio. These GLI phase linking errors can be separated into extrapolation errors and GLI phase anchor point errors.

A significant contribution to the residual GLI phase anchor point errors was shown to be inaccuracies in the inter-subscan drift correction. This contribution has been reduced by applying a second correction in the analysis as demonstrated above. In future work, this error contribution can be reduced by tuning the non coarse tuning laser, over the same frequency interval in every fine tuning subscan. If this were done, the second inter-subscan drift correction in the analysis would be redundant.

The sinefitting of single laser data from each subscan was shown to make important error contributions both, to the extrapolation and to the local fitted phase of the GLI anchor points.

The definition of χ^2 introduced in chapter 5 for sinefitting data recorded in the presence of significant vibrations, is recommended for use in all future sinefitting analysis of FSI data, because it offers superior performance with degraded data.

Further work is needed to understand the ultimate limitations imposed on FSI measurement precision for interferometer signals degraded by vibrations, spurious reflections or both. These limits are likely to be the deciding factors in the success or failure of FSI as an alignment tool in ATLAS.

7. Conclusions

Frequency Scanning Interferometry (FSI) has been used to make remote simultaneous length measurements to sub-ppm precision by comparing the interferometers being measured with a reference interferometer. For example :

Repeated measurements of a 400 mm interferometer were made over a 6°C range, to characterise the thermal expansion of the steel table on which it supported. Other measurements of the same interferometer made over a period of two weeks were found to be consistent with the measured thermal expansion to within a micron. A 1195 mm interferometer was built on the same steel table. This was measured repeatedly over an hour with a repeatability of less than 250 nm, in two separate groups of ten measurements each.

These precise measurements were demonstrated using a system with reference interferometers that were neither evacuated nor thermally stabilised.

To achieve sub-ppm precision it was necessary to correct for the most significant systematic errors, which are primarily due to thermally driven interferometer drift. These drift errors were reduced using data analysis techniques which relied on quasi-simultaneous data from two lasers, tuned in opposite directions. In extreme cases the drift errors were reduced by up to three orders of magnitude.

In spite of the reductions in drift error, a significant fraction of the remaining errors appear to be indirectly caused by drift. Alternative methods for measurement and analysis have been proposed, which should reduce these remaining errors still further.

The effective fine-tuning range of one of the lasers was extended by connecting interferometer phase measurements made in separate subscans, using an etalon signal to guide the reconnection of the reference interferometer phase and using the linked reference phase to guide the reconnection of the phase of the interferometer being measured.

The error in the measured reference interferometer phase was estimated to be around 3 mrad per phase measurement. Direct and indirect contributions to the error in the linked subscan length measurement from errors in the reference phase were negligible.

The centres of etalon peaks used for linking the reference phase were fitted to a precision of around 310 mrad. This was much better than required, because the linking of the reference phase is only sensitive to peak centre errors in quantised steps of $\pm\pi$. Therefore etalon peak errors within $\pm\pi$ had no effect on the final result.

The effects of degrading the interferometer signal by reducing the power, vibrating elements within the interferometer and setting up spurious reflections, have been investigated.

The measurement precision was not significantly affected by decreasing the power fed to the interferometer. This was tested down to a SNR of around 1.4. This bodes well for the ATLAS SCT grid, (in which 800 interferometers will be simultaneously illuminated by a single laser), because, the smaller the power required in each interferometer, the cheaper the lasers which can satisfy the system power budget.

The errors induced by vibrations were more significant. For vibration frequencies slow compared to the data acquisition rate, there was a sharp rise in measurement error from ≈ 0.5 ppm to > 4 ppm as the peak to peak vibration amplitude reached 400 nm (around half an optical wavelength). When the vibration frequency matched the data acquisition rate, the errors rose steadily with increasing vibration amplitude, exceeding 4 ppm at a peak to peak amplitude of 300 nm. Further investigations have been suggested. These will be needed to understand the potential impact of vibrations on the measurement precision.

It should be possible to extend the use of remote fibre coupling to allow the lengths of many interferometers to be measured, provided the scheme for coupling light from the laser to the interferometers and from the interferometers to the detectors, is carefully designed

to provide a single optical path for the laser light, without introducing alternative optical paths; either directly or via significant spurious reflections.

Strong spurious reflections within the measured interferometer, (rather than in the fibres) were investigated and found to reduce measurement precision significantly. Further study of their effect is needed to quantify the risks posed by potential spurious reflections, within the ATLAS SCT and to investigate the best methods of analysing data containing spurious interference signals.

Spurious reflections and vibrations should therefore be studied in the near future, so that the FSI measurement and analysis technique can be made as robust as possible and its limitations quantified.

Bibliography

[Arc01] P. Arce, The CMS alignment system, *Nucl. Instr. and Meth. A*, Vol. 461, No. 1-3, p. 172-173, 2001.

[ATL94] The ATLAS collaboration, Technical Proposal for a General-Purpose pp Experiment at the Large Hadron Collider at CERN (CERN/LHCC/94-93 LHCC/P2), CERN, Geneva, 1994.

[ATL97a] The ATLAS collaboration, Inner Detector Technical Design Report (CERN/LHCC/97-16 ATLAS TDR 4), CERN, Geneva, 1997.

[ATL97b] The ATLAS collaboration, Muon Spectrometer Technical Design Report (CERN/LHCC/97-22 ATLAS TDR 10), CERN, Geneva, 1997.

(All ATLAS TDRs can be found at **http://atlasinfo.cern.ch/ATLAS/internal/tdr.html**).

[Bar98] G. P. Barwood, P. Gill, W. R. C. Rowley, High-accuracy length metrology using multiple-stage swept-frequency interferometry with laser diodes, *Meas. Sci. Technol.*, Vol. 9, p. 1036-1041, 1998.

[Bar00] G. P. Barwood (NPL UK), *Private communication*, October 2000.

[Bec98] K. Bechstein and W. Fuchs, Absolute interferometric distance measurements applying a variable synthetic wavelength, *J. Opt.*, Vol. 29, p. 179-182, 1998.

[Bir93] K. Birch & M. Downs, An updated Edlén equation for the refractive index of air, *Metrologia*, Vol. 30, p. 155-162, 1993.

[Ble65] B. I. Bleaney and B. Bleaney, Electricity and Magnetism, (2^{nd} Ed.), Oxford University Press, Oxford, 1965.

[Blu96] W. Blum, H. Kroha and P. Widmann, *Nucl. Instr. and Meth. A*, Vol. 377, No. 2-3, p. 404-408, 1996.

[Bob93] N. Bobroff, Recent advances in displacement measuring interferometry, *Meas. Sci. Technol.*, Vol. 4, p. 907-926, 1993.

[Bor65] M. Born and E. Wolf, Principles of Optics, (3^{rd} Ed.), Pergamon Press, Oxford, 1965.

[Bour79] G. L. Bourdet and A. G. Orszag, Absolute distance measurements by CO_2 laser multiwavelength interferometry, *Appl. Opt.*, Vol. 18, No. 2, p. 225-227, 1979.

[Bre89] A. Breakstone, W. Kucewicz, N. Redaelli and R. Turchetta, Design of a capacitive displacement-measuring system for vertex detectors at colliding beam machines, *Nucl. Instr. and Meth. A*, Vol. 281, p. 453-461, 1989.

[Bre91] A. Breakstone, Performance of the capacitive displacement measuring system of the Mark II detector at the SLC, *Nucl. Instr. and Meth. A*, Vol. 305, p. 39-47, 1991.

[Cac92] M. Caccia, W. Kucewicz, C. Meroni, N. Redaelli, C. Troncon, A. Stocchi and G. Vegni, 1990 data taking period results of the DELPHI CDM System, Vol. 315, p. 143-148, 1992.

[Car66] P. Carré, Installation et utilisation du comparateur photoélectrique et interférentiel du Bureau International des Poids et Mesures, *Metrologia*, Vol. 2, No. 1, p. 13-23, 1966.

[Cha96] V. Chabaud et al., The DELPHI silicon strip microvertex detector with double sided readout, *Nucl. Instr. and Meth. A*, Vol. 368, No. 2, p. 314-332, 1996.

[Che85] Y. Y. Cheng and J. C. Wyant, Phase shifter calibration in phase-shifting interferometry, *Appl. Opt.*, Vol. 24, No. 18, p. 3049-3052, 1985.

[Cid96] P. E. Ciddor, Refractive index of air: new equations for the visible and near infrared, *Appl. Opt.*, Vol. 35, No. 9, p. 1566-1573, 1996.

[Coo71] A. H. Cook, Interference of Electromagnetic Waves, Oxford University Press, Oxford, 1971.

[Cre88] K. Creath, Phase-Measurement Interferometry Techniques, (Ch. 5 p. 349-393) Progress in Optics Vol. 26 (Edited by E. Wolf), Elsevier Science Publishers B.V., Amsterdam, 1988.

[Cre93] K. Creath, Temporal Phase Measurement Methods, (Ch. 4 p. 94-140) *Interferogram Analysis* Digital Fringe Pattern Measurement Techniques (Edited by D. W. Robinson and G. T. Reid), IoP Publishing, Bristol, 1993.

[Dän88] R. Dändliker, R. Thalmann and D. Prongué, Two-wavelength laser interferometry using superheterodyne detection, *Opt. Lett.*, Vol. 13, No. 5, p. 339-341, 1988.

[Dän98] R. Dändliker, Y. Salvadé and E. Zimmermann, Distance measurement by multiple-wavelength interferometry, *J. Opt.*, Vol. 29, p. 105-114, 1998.

[Dav96] C. Davis, Lasers and electro-optics : Fundamentals and engineering, Cambridge University Press, Cambridge, 1996.

[Dij90] H. Dijkstra et al., Status of the DELPHI vertex detector : Alignment methods and geometrical resolution, *Nucl. Instr. and Meth. A*, Vol. 289, p. 400-405, 1990.

[Dit59] R. W. Ditchburn, Light, Blackie & Son, Ltd., Glasgow, (Reprinted) 1959.

[Dua95] F. J. Duarte, Tunable Laser Handbook, Academic Press, London, 1995.

[Fer85] A. F. Fercher, H. Z. Hu and U. Vry, Rough surface interferometry with a two-wavelength heterodyne speckle interferometer, *Appl. Opt.*, Vol. 24, No. 14, p. 2181-2188, 1985.

[Fle81] M. W. Fleming & A. Mooradian, Spectral Characteristics of External-Cavity Controlled Semiconductor Lasers, *IEEE J. Quantum Electron.*, Vol. QE-17, pp. 44-59, 1981.

[Foc97] E. Focardi, The ALEPH vertex detector, *Nucl. Instr. and Meth. A*, Vol. 386, No. 1, p. 18-22, 1997.

[Fox96a] A. F. Fox-Murphy, D. F. Howell, R. B Nickerson and A. R. Weidberg, Frequency scanned interferometry (FSI): the basis of a survey system for ATLAS using fast automated remote interferometry, *Nucl. Instr. and Meth. A*, Vol. 383, p. 229-237, 1996.

[Fox96b] A. F. Fox-Murphy, Development of a novel alignment system for the ATLAS Inner Detector and an investigation of the effect of alignment inaccuracies on tracker performance, *Doctoral Thesis*, University of Oxford, Oxford, 1996.

[Fuj98] I. Fujima, S. Iwasaki and K. Seta, High-resolution distance meter using optical intensity modulation at 28 GHz, *Meas. Sci. Technol.*, Vol. 9, p. 1049-1052, 1998.

[Gad01] S. Gadomski (for the ATLAS collaboration), ATLAS Inner Detector performance, *Nucl. Instr. and Meth. A*, Vol. 462, p. 285-290, 2001.

[Gre00] U. Griesmann (NIST USA), *Private communication*, October 2000.

[Gre99] A. S. Grewal, Detector Development for ATLAS and Supersymmetry Physics Studies, *Doctoral Thesis*, University of Oxford, Oxford, 1999.

[Ham97] Hamamatsu Photonics K.K Solid State Division, Hamamatsu Photodiode Catalogue (Cat. No. KPD 0001E05), Hamamatsu, Hamamatsu City, 1997.

[Har87] P. Hariharan, Interferometry with lasers, (Ch. 3 p. 103-164) Progress in Optics Vol. 24 (Edited by E. Wolf), Elsevier Science Publishers B.V., Amsterdam, 1987.

[Har91] K. Harvey & C. Myatt, External-cavity diode laser using a grazing-incidence diffraction grating, *Optics Letters*, Vol. 16, pp. 910-912, 1991.

[Hec87] E. Hecht, Optics (2nd Ed.), Addison-Wesley, Reading Mass., 1978.

[Hor89] P. Horowitz and W. Hill, The art of electronics (2nd Ed.), Cambridge University Press, Cambridge, 1989.

[How99] D. F. Howell, *Private Communication*, 1999.

[Ju00] L. Ju, D. G. Blair and C. Zhao, Detection of gravitational waves, *Rep. Prog. Phys.*, Vol. 63, p. 1317-1427, 2000.

[Kam81] I. P. Kaminow, Polarisation in Optical Fibers, *IEEE J. Quantum Electron.*, Vol. QE-17, No. 1, p. 15-22, 1981.

[Kay89] G. Kaye & T. Laby, Tables of Physical and Chemical Constants, Longman Scientific & Technical, Harlow England, 1986 (Reprinted 1989).

[Kik86] H. Kikuta, K. Iwata and R. Nagata, Distance measurement by the wavelength shift of laser diode light, *Appl. Opt.*, Vol. 25, No. 17, p. 2976-2980, 1986.

[Kle98] K. Kleinknecht, Detectors for particle radiation (2nd Ed.), Cambridge University Press, Cambridge, 1998.

[Kro97] H. Kroha, Laser-alignment system with transparent silicon strip sensors and its applications, *Nuc. Phys. B (Proc. Suppl.)*, Vol. 54B, p. 80-85, 1997.

[Ley99] *Private Communication with Leysop Ltd., manufacturers of the Isolator*, August 1999.

[Lou95] R. Loudon, The quantum theory of light (2nd Ed.), Oxford University Press, Oxford, (Reprinted) 1995.

[Lyo93] L. Lyons, Statistics for nuclear and particle physics, Cambridge University Press, Cambridge, (Reprinted) 1993.

[Mat01] T. Matsushita, S. Boogert, R. Devenish, R. Walczak, Optical alignment system for the ZEUS micro vertex detector, *Nucl. Instr. and Meth. A*, Vol. 466, No. 2, p. 383-389, 2001.

[Min98] U. Minoni, L. Rovati and F. Docchio, Absolute distance meter based on a frequency-modulated laser diode, *Rev. Sci. Instrum.*, Vol. 69, No. 11, p. 3992-3994, 1998.

[Mit01] A. Mitra, (To be published) *Doctoral thesis*, University of Oxford, Oxford, 2001/2.

[New00] *Private Communication with New Focus Inc. manufacturers of the Lasers*, 2000.

[Ogi95] E. Ogita, K. Ikezawa, K. Isozaki and K. Mikuriya, Progress in absolute distance measurement using a dye laser, *Nanotechnology*, Vol. 6, p. 148-151, 1995.

[Pfe93] T. Pfeifer and J. Thiel, Absolutinterferometrie mit durchstimmbaren Halbleiterlasern (Absolute interferometry with tunable semiconductor lasers), *Technisches Messen*, Vol. 60, p. 185-191, 1993.

[Pfl67] R. Pfleegor and L. Mandel, Interference of Independent Photon Beams, *Phys. Rev.*, Vol. 159, No. 3, p. 1084-1088, 1967.

[Pol73] C. Polhemus, Two-wavelength Interferometry, *Appl. Opt.*, Vol. 12, No. 9, p. 2071-2074, 1973.

[Rue96] J. M. Rüegger, Electronic Distance Measurement (4^{th} Ed.), Springer Verlag GmbH., Berlin and Heidelberg, 1996.

[Sal96] K. Salewski, K. Bechstein, A. Wolfram and W. Fuchs, Absolute Distanzinterferometrie mit variabler synthetischer Wellenlänge (Absolute distance interferometry with variable synthetic wavelength), *Technisches Messen*, Vol. 63, p. 5-13, 1996.

[Sau92] F. Sauli, Instrumentation in High Energy Physics, World Scientific, London, 1992.

[Sgu99] G. Sguazzoni et al., Monitoring the Stability of the ALEPH Vertex Detector, *Nuc. Phys. B (Proc. Suppl.)*, Vol. 78, p. 301-306, 1999.

[She99] J. Sheen, *Private Communication with John Sheen of SLS optics (formerly Technical Optics Ltd.)*, March 1999.

[Smi95] S. D. Smith, Optoelectronic Devices, Prentice Hall, London, 1995. (See p. 234-5 for a description of electro-optic intensity modulation.)

[Sta77] D. L. Staebler and C. R. Wronski, Reversible conductivity changes in discharge-produced amorphous Si, *Appl. Phys. Lett.*, Vol. 31, No. 4, p. 292-294, 1997.

[Sto99] J. A. Stone, A. Stejskal and L. Howard, Absolute interferometry with a 670-nm external cavity diode laser, *Appl. Opt.*, Vol. 38, No. 28, p. 5981-5994, 1999.

[Tec] The refractive index values for BK7 shown in Fig. 2.27b were taken from product information literature by Technical Optics Ltd, (Second Avenue, Onchan, Isle of Man, British Isles), c. 1990.

[Thi95] J. Thiel, T. Pfeifer and M. Hartmann, Interferometric measurement of absolute distances of up to 40 m, *Measurement*, Vol. 16, p. 1-6, 1995.

[Tur01] M. Turala (for the ATLAS SCT collaboration), The ATLAS semiconductor tracker, *Nucl. Instr. and Meth. A*, Vol. 466, No. 2, p. 243-254, 2001.

[Xia98] D. Xiaoli and S. Katuo, High-accuracy absolute distance measurement by means of wavelength scanning heterodyne interferometry, *Meas. Sci. Technol.*, Vol. 9, p. 1031-1035, 1998.

[Xu92] J. Xu and R. Stroud, Acousto-optic devices : Principles, Design and Applications, John Wiley and Sons Inc., New York, 1992.

[Yok99] S. Yokoyama, J. Ohnishi, S. Iwasaki, K. Seta, H. Matsumoto and N. Suzuki, Real-time and high-resolution absolute-distance measurement using a two-wavelength superheterodyne interferometer, *Meas. Sci. Technol.*, Vol. 10, p. 1233-1239, 1999.

[Zha99] Y. Zhao, T. Zhou and D. Li, Heterodyne absolute distance interferometer with a dual-mode HeNe laser, *Opt. Eng.*, Vol. 38, No. 2, p. 246-249, 1999.

A. Glossary

Abbreviations used in this thesis :

ADC	**A**nalogue to **D**igital **C**onvertor	APD	**A**valanche **P**hoto**d**iode
ATLAS	**A** **T**oroidal **L**HC **A**pparatu**s**	CIN	**C**ode **I**nterface **N**ode
CTE	**C**oefficient of **T**hermal **E**xpansion	DAC	**D**igital to **A**nalogue **C**onvertor
DAQ	**D**ata **Acq**uisition	FSI	**F**requency **S**canning **I**nteferometry
FWHM	**F**ull **W**idth **H**alf **M**aximum	GLI	**G**rid **L**ine **I**nterferometer
LHC	**L**arge **H**adron **C**ollider	OPD	**O**ptical **p**ath **d**ifference
OSA	**O**ptical **S**pectrum **A**nalyser	PMT	**P**hoto**m**ultipler **T**ube
PZT	**P**ie**z**oelectric **T**ransducer	ppb	**p**arts **p**er **b**illion
ppm	**p**arts **p**er **m**illion	ROI	**R**egion **o**f **I**nterest
RTD	**R**esistance **T**emperature **D**etector	SCT	**S**emi**c**onductor **T**racker
SNR	**S**ignal to **N**oise **R**atio	TDM	**T**ime **D**ivision **M**ultiplexing
VME	Not a standardised acronym, name of a DAQ system standard		

Terms used in this thesis :

Anchor point Interferometer phase value from within a subscan, used for linking.

Bridge Phase, time or frequency interval between two anchor points.

Drift Change in OPD of an interferometer during an FSI measurement. There are two forms of drift :
Inter-subscan drift Drift occuring during the bridge.
Intra-subscan dridt Drift occuring during the recording of a subscan.

Frequency Scanning Interferometry Interferometric length measurement technique used to compare length of a grid line interferometer with the Long Reference Interferometer, by illuminating both interferometers with a common frequency scanning laser and monitoring phase changes in both interferometers.

Grid Line Interferometer An interferometer whose length is estimated using Frequency Scanning Interferometry, especially an interferometer of the fibre-coupled, common-path, low mass design intended for use in the ATLAS Inner Detector.

Linking Procedure for combining phase information from different subscans, to increase the length measurement resolution available from FSI. Involves extrapolation of interferometer phase from one anchor point in one subscan, to a second anchor point in another subscan.

Long Reference Interferometer Michelson interferometer which forms the length standard against which Grid Line Interferometers are compared.

Subscan Block of raw data points recorded during a continuous period of fine tuning, or a block of processed data based on this raw data.

TDM table Two dimensional array in the DAQ software which controlled the readout timing of the ADC channels, allowing different channels to be multiplexed onto the same time slot. (See section 2.5.4).

B. List of Algebraic Symbols

The following list contains most of the mathematical symbols used throughout this thesis, excluding standard physical constants and those symbols used for self contained discussions in chapter 6.

The use of the prefix Δ denotes a change in the parameter, for example $\Delta\nu$ is the change in laser frequency ν. Many of the symbols are written with subscripts to denote different examples of the same basic parameter, for example v_1 is the frequency of laser 1.

Subscripts used in discussion of linking algorithm (section 3.6)

a Anchor point in subscan A when linking long reference interferometer phase
A Estimated GLI phase at anchor point in subscan A
b Anchor point in subscan B when linking long reference interferometer phase
B Estimated GLI phase at anchor point in subscan B, before correcting for inter-subscan drift.
$\tilde{B}$ Estimated GLI phase at anchor point in subscan B, after correcting for inter-subscan drift.
c Estimate of long reference interferometer phase at anchor point in subscan B, based on extrapolation from subscan A.
C Estimate of GLI phase at anchor point in subscan B, based on extrapolation from B.
g Gap between anchor point and extrapolation estimate in long reference interferometer phase.
G Gap between anchor point and extrapolation estimate in GLI phase.

Interferometer Optical path difference (OPD)

$\mathcal{L}$ Long Reference Interferometer OPD.
$\mathcal{D}$ Grid Line Interferometer OPD.
ε Differential Interferometer OPD drift (defined in equation 1.34c).

Estimated Interferometer length

L Long Reference Interferometer length estimated to be 859.09 mm (see section 3.1.1).
D Estimated Grid Line Interferometer length (defined by equation 3.1).

Interferometer signal components

γ Interference visibility.
C_{V} Power coupling coefficient of GLI R reflection mode (via retroreflector).
C_{V} Power coupling coefficient of GLI V reflection mode (via beam-splitter).
Γ Ratio between C_{V} and C_{R} (see equation 1.52).

Interferometer signal phase

Φ Phase of interference term in Long Reference Interferometer signal.
ϕ Φ modulo 2π.
Θ Phase of intererence term in Short Reference Interferometer signal.
θ Θ modulo 2π.
α_{S} Phase step angle (see equations 3.7a to 3.7d).
u Phase unwrapping index (see section 3.2.2).
ψ_{ab} Unwrapping index offset, (used in linking - see equation 3.34).

Sine fitting and intra-subscan drift correction

I_{DC}	Mean interferometer signal.
I_{AC}	Amplitude of cosinusoidal interference term.
q	Ratio of change of phase in measured interferometer with respect to change of reference phase (defined in equation 1.28).
q_k	Estimate of q based on sine fit of single subscan data from laser k.
q_0	Estimate of q based on combined laser result.
α	Arbitrary offset phase in fitted GLI signal.
X	Unwrapped long reference interferometer phase (defined in equation 3.21).
Y	GLI intensity data point for sinefitting (defined in equation 3.22).
χ^2	Quality of fit parameter used to guide a fit.

Timing parameters

τ	Photodetector integration time.
f_{TUN}	Clock rate used in laser fine tuning control electronics.
f_{DAQ}	Clock rate of DAQ system master clock.
t	Time.

Other symbols

ν	Laser frequency.
$\Delta\nu_{\mathrm{ET}}$	Free Spectral Range of (10 GHz) Etalon.
Ω	Reciprocal of the fractional change in frequency (defined in equation 1.34c).
ρ	Ratio of Ω values (defined in equation 1.41 and expanded in equation 3.29).
λ	Optical wavelength.
k	magnitude of optical wavevector.
n	Refractive index.
ϱ	Estimated refractivity of air.
ϑ	Scan average interferometer air temperature.
T	Effective GLI steel temperature.
α_{T}	Coefficient of thermal expansion (see equation 4.1).

C. Identification and fitting of etalon peaks

This appendix covers the software identification and fitting of etalon peaks for the 10 GHz etalon of the demonstration system.

C.1 Identification of etalon peaks

The etalon photodiode signal data points for each laser were checked using a two level threshold detection algorithm to locate etalon peaks.

If a cruder system, with just one threshold levels had been used instead any etalon photodiode signal data points above a threshold level, would have to be labelled as etalon peaks. Any fluctuations on top of the basic peak shape would lead to multiple crossings and one real peak would be mislabelled as several peaks.

The use of two widely separated threshold levels, ensured that small fluctuations could not disrupt the identification of a single etalon peak.

An example is shown in Fig. C.1, with the etalon signal from one laser, compared with two thresholds. A three state trigger indicates where the etalon signal lies with respect to the thresholds.

At first the trigger level is in state 0 and the background etalon signal is lower than the first threshold. Once the etalon signal crosses the first threshold, the trigger level switches to state 1, (indicated by the first arrow). Once in state 1, the trigger level is not allowed to return directly to state 0, but only to switch up into state 2, once the etalon signal has crossed a second, higher threshold, indicated by the second arrow. The trigger level remains in state 2, until the etalon signal drops below the lower threshold, (indicated by the third arrow), when it is allowed to return to state 0.

This separation of threshold levels, gives a distinct, continuous block of data, at which the threshold level is in state 2. The laser frequency axis values corresponding to the start

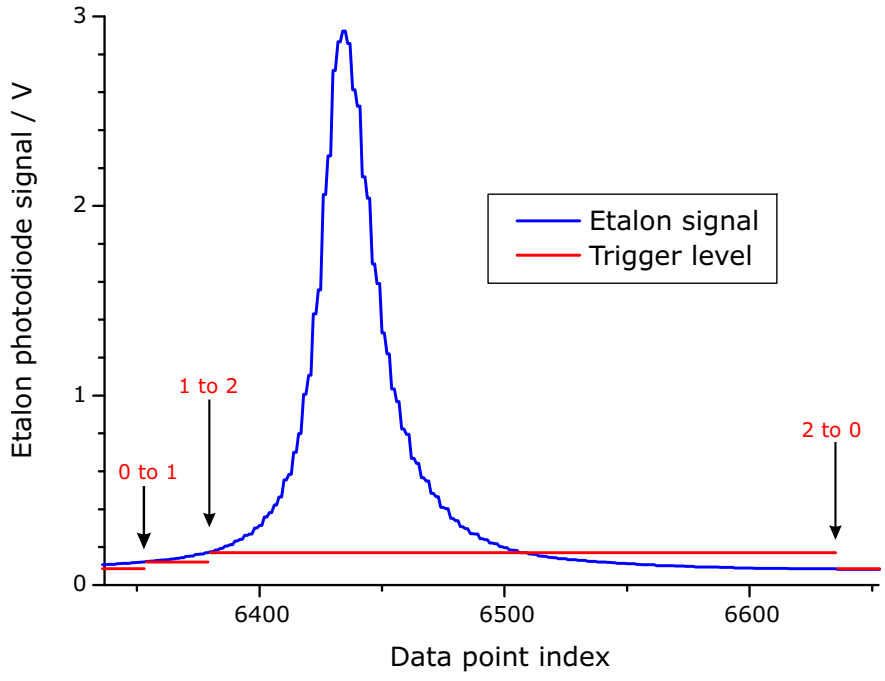

Figure C.1: *An example of the etalon peak detection using a three state trigger.*

and end of this block are used to provide a crude estimate of the peak midpoint, which is clearly biassed. The data used for fitting an etalon peak is taken from ±45 long reference radians either side of the estimated midpoint. The etalon peaks are ≈ 20 long reference radians wide at the level of the highest red line in Fig. C.1, so the fitting window is of ample width to encompass the etalon peak.

C.2 Etalon peak fitting

The etalon signal Y_i was fitted to a function of the frequency axis $I_i(X_i)$ given below in equation C.2a. The free parameters of the fit function were :

- q_{ET} The etalon Free Spectral Range in long reference radians.
- I_{B} The mean background signal.
- m_{B} The slope on the background due to slow changes in laser power.
- X_C The centre of the etalon peak.
- H The peak height normalisation.
- $\mathcal{F}$ This is proportional to the finesse of the etalon

according to

$$\text{Finesse} = \frac{\pi\mathcal{F}}{2} \tag{C.1}$$

The fit function is given by

$$I_i = I_{\mathrm{B}} + m_{\mathrm{B}}(X_i - X_C) + A(X_i) \tag{C.2a}$$

where

$$A(X_i) = \frac{H}{1 + \mathcal{F}^2 \sin^2\left[\frac{2\pi(X_i - X_C)}{q_{ET}}\right]} \tag{C.2b}$$

This is the scaled Airy function[1] of an etalon peak $A(X_i)$ added to a straight line background, which is used to account for the dark signal and any slow laser power changes across the etalon peak.

The function is fit using the χ^2 minimisation package MINUIT, where the χ^2 is defined by

$$\chi^2 = \sum_i (I_i - Y_i)^2 \tag{C.3}$$

with equal weight given to each data point.

The fit was initially minimised with the peak centre X_C frozen. Once the initial minimisation was complete, all six fit parameters were free for a final fit. An example of a typical fit result for each laser, is shown in chapter 2, in Fig. 2.25. The final best fit value of the reference phase at the peak centre was used in linking the reference interferometer phase as described in chapter 3.

[1] See for example [Hec87].

D. Binary File Format used for Acquired Data

The raw data acquired from the experiments described in this thesis, were saved in binary data files which were written according to the structure laid out in this chapter. This structure enabled sought after blocks of data to be read in easily for subsequent analysis. The results of the intermediate stages of analysis, were saved in similar data files based on the same protocol. It has been designed to be easily extendable, coherent framework for all data handling software. If it is followed correctly, it should be possible to read in data written by the very latest DAQ software, using old analysis software.

D.1 Protocol description

An FSI scan consists of N subscans[1]. The data file structure, a set of self-contained subscans, reflects this. The subscans need not be in numerical order as they are below.

File Prefix
subscan 1
subscan 2
.....
subscan N

The data file protocol is a top-down structure. At the top is a File Prefix which records how many self-contained subscan units are stored in the file. Search algorithms use the location of the File Prefix to identify it, rather than looking for a File Prefix label code. The first subscan is likewise identified by its location. This is fixed for two reasons; the fixed size of the File Prefix and because first subscan immediately follows the File Prefix. In contrast the size of this (or any other) subscan is not fixed by the protocol, so the start location of the next subscan is not fixed in advance. The location of the next subscan is one of the first things to be written at the top of the first subscan in a fixed size block called the Pointer (fig D.1). This pointing technique is used throughout the protocol to cope with variable sized data structures.

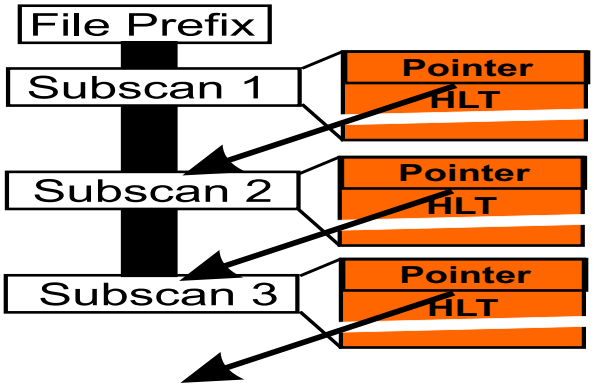

Figure D.1: Any subscan can be reached through a continuous set of links provided by the Pointers.

D.1.1 File Prefix

The order of the prefix data is given below.

- No of Subscans 1 byte (U8).
- FSI Version No. 1 byte (U8) and 1 byte (U8).

[1]In the description of the file structure which follows, the separated blocks of the file are called subscans : Some of these *subscans* correspond to the data for a single fine tuning subscan, as described in the thesis. The rest correspond to the data from a block of coarse tuning, between fine tuning subscans. Unfortunately the name *subscan* for these individual data blocks was an historical part of the software description, before the potential confusion came to light.

The first byte is the number of subscans stored in the file. Any search algorithm looking for subscan i, begins reading the number of stored susbcans N, from the File Prefix. Starting with the first subscan it will read the subscan label number from every subscan until it has either; found a subscan labelled i, or it has looked at N subscans. This prevents any search algorithm from crashing the software by reading past the end of the file. If this number N is not updated every time a new subscan is added to the data file, the new subscans will be effectively invisible to any search algorithm.

The FSI version number is *version.revision*. The first byte is the version number. The second byte is the revision number. All subscans within a scan should be generated by the same version of software to avoid creating havoc in linking subscans.

D.1.2 Basic outline of subscan structure

Each subscan has an internal structure as shown below. As a new subscan is being built up, (row by row of the diagram below), the Pointer is constantly updated with the location of the end of the subscan. This is one byte after the end of the most recent row.

Pointer
Header Location Table (HLT)
Header (only one section for processed data)
Data Prefix
Data Label
Data
Data Label
Data *etc.*

The pointer is of fixed size, which fixes the start location of the HLT with resepct to the the start of the subscan. This is vital for search algorithms. The Pointer has to say where the Data Prefix is located since this depends on the size of the header, which is not fixed.

D.1.3 The Pointer

- Subscan label (number within Scan) 1 byte (U8).
- Location of next Subscan 4 bytes (U32).
- Location of Data Prefix (of this subscan) 4 bytes (U32).

Each subscan *points* to the byte location immediately following the end of the subscan. When adding a new subscan to the file, the pointer of the previous subscan provides the correct start location for the new subscan. As the end subscan grows the location stored in its pointer must be updated so that it always points to one byte after the end of the subscan. Only the end subscan can be allowed to grow, since any additions to subscans higher up the file would overwrite the existing file structure and corrupt the file.

It is possible to get around this problem by copying the file up to the point where the new data is to be added, inserting the new data and then adding the rest of the old file. However since this involves writing the new file to disk, byte by byte via LabView this is a very slow process which is best avoided.

The possibility of generating more than one subscan has first arisen with the introduction of subscan linking in Version 2.3. Earlier versions of FSI software have not had to deal with

this problem. Software which writes to the data file must (from Version 2.3 onwards) be prevented from writing to all subscans except for the last.

The pointer facilitates rapid searching through the data file by pointing to the next subscan for a search algorithm trying to jump along to the appropriate subscan (fig. D.1). It also points to the data prefix of this subscan for any search algorithm which has found the subscan it is looking for and wants access to data contained therein. The subscans do not have to be stored in numerical order, since the search algorithms will read from the File Prefix how many subscans exist and search from one to the next until that number of subscans have been tried.

D.1.4 Header Location Table (HLT)

This table simply points to each section of the header to allow the appropriate section to be found rapidly.

Number of header sections 1 byte (U8).		
Id no. 1 byte (U8)	Location 4 bytes (U32)	Size 4 bytes (U32).
Id no. 1 byte (U8)	Location 4 bytes (U32)	Size 4 bytes (U32).
.....	.....	.....

When the HLT is being written, the locations of each header section are put in *by hand* in the DAQ program. Once these are decided by the DAQ program, each subsequent header section writer sub VI uses the HLT to find out where it should write each header section. Once any header section has been written, the header writer can use the HLT to find out how large the header section was supposed to be, by comparing the location of each section and the next section[2]. It can then determine if it is larger or smaller than expected and highlight an error caused by bad bookkeeping when developing new versions of the DAQ software. This approach also limits errors of this type because they can only come from the code of a new DAQ program, this makes them much easier to hunt down.

The identity number is used to represent the functional form of the header section. Including the identity numbers in the table allows the order of header sections to be altered as necessary without causing problems for software (such as data display programs or frequency axis fitting software) when searching for a particular header section. If instead, the header sections were intentified by their locations difficulties would arise whenever unused header sections were left out.

D.1.5 Header

The ID codes for header sections are given in subsection D.3.2 and at the start of each description below. These match the identity numbers used later for the (U8) short identity codes for data. Up to 255 different identity numbers may be assigned. Once designated they should be fixed by updating this protocol. Old identity codes should not be reassigned since this will corrupt the backward compatability of the protocol.

Comments block (Id. no. 0)

This consists of 1024 bytes and acts as a large string structure to hold user comments.

[2]The last section's location is compared with the location of the Data prefix to determine its expected size. This assumes that the header is followed immediately by the data as show above.

DAQ information (Id. no. 1)

- Timestamp 4 bytes (U32)[3].
- DAQ frequency 4 bytes (U32).
- Number of DAQ triggers in the subscan 4 bytes (U32).
- Number of consecutive points per laser 4 bytes (U32).

Environmental information (Id. no 2)

This section indicates how many environmental sensors are readout during a measurement. The first 4 bytes (U32) state how many sensors are expected. The overall section structure is given in the table below. The usage codes are defined just after the structure table.

No. of environmental sensors 1 byte (U8).	
Usage code 4 bytes (U32)	ON or OFF 1 byte (U8)
Usage code 4 bytes (U32)	ON or OFF 1 byte (U8)
Usage code 4 bytes (U32)	ON or OFF 1 byte (U8)
Usage code 4 bytes (U32)	ON or OFF 1 byte (U8)

The following (environmental sensor) usage codes are defined so far.

(U32) Usage code	Use
0	User read Room Temperature
i	Thermometry Channel i
32768	User read Relative Humidity

Reference Interferometer information (Id. no 3)

For each device in the reference interferometer section, this group of flags states whether or not the device was used for this subscan. To make things easier for search algorithms the first byte states how many reference interferometer devices are to be listed here.

No. of reference interferometer devices 1 byte (U8).	
Usage code 4 bytes (U32)	ON or OFF 1 byte (U8)
Usage code 4 bytes (U32)	ON or OFF 1 byte (U8)
Usage code 4 bytes (U32)	ON or OFF 1 byte (U8)
Usage code 4 bytes (U32)	ON or OFF 1 byte (U8)

The following (reference interferometer device) usage codes are defined so far.

(U32) Usage code	Use
0	Power monitor diode
1	Long reference photodiode
2	Short reference photodiode
3	10 GHz etalon diode
4	250 GHz etalon diode
5	Wavemeter

[3]This is the number of seconds since 12:00 AM Jan 1^{st} 1970 as in the ANSI C standard time

Laser source section (Id. no 4)

The first byte of this section records the numberof lasers used as 1 byte (U8). Each subsequent byte records whether or not a data channel was used to monitor each laser's tuning voltage.

Acousto-optic Phase stepping information (Id. no. 5)

The first part of this section covers general phase stepping information. The second part contains information for each phase step of the cycle.
(**Acousto-optic phase stepping in the GLI was never implemented**).

- Acousto-optic frequency monitoring physical[4] channel number 1 byte (U8) and 4 bytes (U32).
- Acousto-optic frequency control physical channel 1 byte (U8) and 4 bytes (U32).
- Acousto-optic modulation channel physical channel 1 byte (U8) and 4 bytes (U32).
- Number of DAQ triggers per phase step 4 bytes (U32).
- Phase step pattern combination code 4 bytes (U32).
- First step in cycle 1 byte (U8).
- Number of phase steps in cycle 1 byte (U8).

The phase step combinations can be written in a list in alphabetical order. When this is done each position is easily represented by a counter which starts at 0. An example is given below for 4 phase steps.

Combination code	PHASE STEP Combination
0	ABCD
1	ABDC
2	ACBD
3	ACDB
4	ADBC
5	ADCB

These six combination codes together with the phase step which comes first, uniquely define any of the 24 possible 4 step combinations. The same is true for any number of phase steps less than 14.

FSI channels (Id. no. 6)

This header section contains an initial two byte (U16) entry, saying how many FSI channels (apart from the short reference interferometer[5]).

Number of FSI channels 2 bytes (U16).	
Usage code 4 bytes (U32)	ON or OFF 1 byte (U8)
Usage code 4 bytes (U32)	ON or OFF 1 byte (U8)
Usage code 4 bytes (U32)	ON or OFF 1 byte (U8)
Usage code 4 bytes (U32)	ON or OFF 1 byte (U8)

[4]See section D.1.7 for a description of physical channel coding

[5]The short ref interferometer is FSI channel 0. It's presence/absence is already indicated by the reference interferometer header section so it is not included in this section nor in the count of FSI channels at the top.

D.1.6 Data Prefix

This is simply a 4 byte number recording the number of data channels stored in this subscan. The data writing sub VIs automatically update **every time** a new data channel is added to the subscan in the file.

D.1.7 Data Label

All labels take this standard form and are placed in front of each data channel.

- Usage code 1 byte (U8) and 4 bytes (U32).
- Start location of the next data channel's label 4 bytes (U32).
- Number of bits of recording instrument 1 byte (U8).
- Physical code of recording instrument 1 byte (U8)and 4 bytes (U32).
- Name of data channel 40 bytes (string).
- Code[6] representing data type (n bytes) stored 1 byte (U8).
- No of (*n byte*) blocks long 4 bytes (U32).

As with subscan pointers the pointer to the start location of the next data label points to the next free byte at the end of the file. When subscans are linked together and the subscan size is then frozen by the location of the next subscan this pointer should then be made to point to its own label. Thus preventing any search algorithms from going into the next subscan in the search for data channels (this should not happend anyway because they should stop after they have travelled through the stated numberof data channels even if they do not find the data channel they are looking for).

Usage Code

This usage or ID code uniquely labels the data. The ID codes consist of a category code 1 byte (U8) and a specific sub-code 4 bytes (U32). These ID codes are listed below in section D.3.

Start location of next data label

This gives a search algorithm the most direct route to the next data label as it searches for a specific data channel.

Number of bits recorded

The number of bits of the recording instrument is 32 for the present 32 bit scaler, 10 or 12 bits for the current ADC.

Physical Channel

If the channel is not a raw data channel then the code 0.0 is used. Otherwise the physical channel on the instrument which recorded the raw data is represented using ID codes given in section D.3.3.

[6]Uses convention set out in LabVIEW main manual page A-8

Data channel name

The data channel name is the label which would be used on displays and graphs to tell the user what this data is.

Start location

The start location allows search algorithms to find the data channel, once the correct channel has been located by checking each usage code. This is why the usage code is placed first.

D.1.8 Data

The data channels immediately follow the data label. The data label specifies the number of elements and the variable type.

D.2 Generating an FSI Data File

Any software generating Data files, follows the steps outlined below. In the LabVIEW implementation used in this work, each table corresponds to a custom written program (VI) which performs the task described by calling subprograms (sub VIs).

The following symbols are used in the representations of program steps tabulated below.

KEY

VI - Names of VIs in Bold
W - **Writer**
R - **Reader**
W @ - Writes at Location (Number of bytes from 0 at start of file)
R @ - Reads from Location (Number of bytes from 0 at start of file)
► - Calls

The main data file generating program therefore :

► **File Creator** Creates File and Writes File Prefix
Then for each Subscan of the File.
► **Header Writer** Writes File Pointer, HLT and Header
► **Data Prefix Writer** Writes the Data Prefix
► **Data Writer TYP**[7] Writes a Data Channel of TYP Data Type

File Creator	►	**Open File**	Creates New File
	►	**Prefix W**	W @ 0 : 0 Subscans
			W @ 1: Version no.
			W @ 2: Revision no.

[7]Where TYP is a Data Type, eg U32, DBL etc.

Header W ▶	**Pointer W** ▶	**Subscan Seeker** ▶ **Prefix R** R @ 0 : $N(=0)$ Subscans *Forces* $SL = 3$
		W @ SL : (This) Subscan is 1 W @ $SL+1$: Next Subscan Location is 0 W @ $SL+5$: Data Prefix Location is 0 Passes on : End of Pointer Location ($EoP = SL+9$) to **HLT W**
▶	**HLT W**	W @ EoP : No. of Header Sections W @ $EoP+1$: HLT Passes on End of Header Loc. (EoH) Now that new HLT exists, increment N in Prefix First read out Prefix
	▶	**Prefix R** R @ 0 : $N(=0)$ Subscans R @ 1 : Version no. R @ 2 : Revision no.
		Increment $N_{\text{NEW}} = N+1$ in Prefix
	▶	**Prefix W** W @ 0 : N_{NEW} Subscans W @ 1 : Version no. W @ 2 : Revision no.
▶	**Pointer W** ▶	**Subscan Seeker** ▶ **Prefix R** R @ 0 : $N(=1)$ Subscans 1^{st} Subscan Loc. $SL = 3$ Loops over N ⟼ R @ SL : (This) Subscan is 1 R @ $SL+1$: Next Subscan Loc. SL_{NEW} ∵ *this Subscan = target* *Matches* $SL = 3$ *leaves loop* End of Loop
		W @ SL : (This) Subscan is 1 W @ $SL+1$: Next Subscan Location is ($EoH+4$) W @ $SL+5$: Data Prefix Location is EoH
	Loops through calls to Header Section VIs ⟼	
	Example Iteration : ▶ **Comments Header Section**[8]	
	Searches HLT ID codes array for 0 (ID code for Comments)	
	If found :	Generate blank array same size as Comments HS
	▶	**Comment W** ▶ **HLT Scan**[9] Get Comments Loc. SeL
		W @ LC : Blank comment array Compares array size with Size from HLT[10]
	Else :	Continue
	End loop	

from **Header W**
Comments W ▶HLT scan

[8]Each Header Section calls its own sub VI.
[9]See **HLT Scan** Diagram on p.216 for full details.
[10]If the sizes do not match an error message is generated.
N.B. In general if this error occurs something will have been overwritten and the file corrupted.

HLT Scan ▶	**Pointer R** ▶	**Subscan Seeker** ▶	**Prefix R** R @ 0 : $N(=1)$ Subscans	
			1^{st} Subscan Loc. $SL = 3$	
			Loops over N $\longmapsto$	
			R @ SL : (This) Subscan is 1	
			R @ $SL + 1$: Next Subscan Loc. SL_{NEW}	
			$\because$ *this Subscan = target*	
			Matches $SL = 3$ *leaves loop*	
			End of Loop	
		R @ SL : (This) Subscan is 1		
		R @ $SL + 1$: Next Subscan Location is $EoH + 4$		
		R @ $SL + 5$: Data Prefix Loc. (ignored)		
		Passes on : HLT Location ($EoP = SL + 9$)		
▶	**HLT Top R**	R @ EoP : Number of HLT Entries (H)		
		Passes on Loc. $EoP + 1 = PoL$		
	Loops over H	Starts with PoL from **HLT Top Read**		
		▶	**HLT Line R**	R @ PoL. : ID Code
				R @ PoL+1 : Section Size
				R @ PoL+5 : Section Loc. SeL
				$PoL_{\text{NEW}} = PoL_{\text{OLD}} + 9$
	If last read ID code = 0 (Comments) : Break out of loop			
	Take last read Size and SeL			
	Else : Continue			

Data Prefix W uses **Pointer R** to find where the Data Prefix should go (by reading the End of Header).

Data Prefix W ▶	**Pointer R** ▶	**Subscan Seeker** ▶	**Prefix R** R @ 0 : 1	
			1^{st} Subscan Loc. $SL = 3$	
			Loops over N $\longmapsto$	
			R @ SL : (This) Subscan is 1	
			R @ $SL + 1$: Next Subscan Loc. SL_{NEW}	
			$\because$ *this Subscan = target*	
			Matches $SL = 3$ *leaves loop*	
			End of Loop	
		R @ SL : (ignored)		
		R @ $SL + 1$: (ignored)		
		R @ $SL + 5$: Data Prefix Loc. (EoH)		
	W @ EoH : 0 (The number of data channels so far)			

All Data Writer sub VIs follow the algorithm given below.

N.B. The word **Data** has been abbreviated by the letter **D** in the table below.

D W ▶	**D Label W**	▶	**D Freeslot Seeker**	▶	**Pointer R** returns Loc. NS[11]
	W @ NS : Data Label[12] (calculates Loc. NDL[13])				
	Passes on Loc. EoL (End of Label)				
▶	**Pointer R**	▶	**Subscan Seeker**	▶	**Prefix R** R @ 0 : $N(=1)$ Subscans
					1^{st} Subscan Loc. $SL = 3$
					Loops over N $\longmapsto$
					R @ SL : (This) Subscan is 1
					R @ $SL + 1$: Next Subscan Loc. SL_{NEW}
					$\because$ *this Subscan = target*
					Matches $SL = 3$ *leaves loop*
					End of Loop
	R @ SL : (ignored)				
	R @ $SL + 1$: (ignored)				
	R @ $SL + 5$: Data Prefix Loc. (EoH)[14]				
▶	**Pointer W**	▶	**Subscan Seeker**	▶	**Prefix R** R @ 0 : $N(=1)$ Subscans
					1^{st} Subscan Loc. $SL = 3$
					Loops over N $\longmapsto$
					R @ SL : (This) Subscan is 1
					R @ $SL + 1$: Next Subscan Loc. SL_{NEW}
					$\because$ *this Subscan = target*
					Matches $SL = 3$ *leaves loop*
					End of Loop
	W @ SL : (This) Subscan is 1				
	W @ $SL + 1$: (Updates) Next Subscan Location is NDL				
	W @ $SL + 5$: Data Prefix Location is EoH				
	W @ EoL : Data Array				
▶	**D Prefix Increment**	▶	**D Prefix R**		Get Ch (The no. of Data channels)
			Increment : $Ch_{\text{NEW}} = Ch + 1$		
		▶	**D Prefix W**		W @ EoH : Ch_{NEW}

D.3 Identification Codes

The following three subsections specify the identification codes defined so far. Further classifications will be added to the protocol as necessary (but only by taking up new identification codes and not replacing old codes, in order to maintain compatability).

There are some data channel categories which do not have corresponding header sections. The U8 number representing the data channel category should not be used for a different header category since it may be necessary in the future to associate header information with data in the original category. Therefore as soon as a U8 category number has been chosen, for either Data Type or a Header Section it applies to both and may not be reallocated for another purpose.

[11] Loc. NS is the Location of the next subscan

[12] See p.214 for the full description of the Data Label.

[13] Loc. NDL is the Location for the next Data Label

[14] Loc. EoH (End of Header) is the Location of the Data Prefix.

D.3.1 Data Channels

Environmental Monitoring

The data collected from environmental sensors which record temperature, humidity, pressure etc. is labelled under this category. So far codes for pressure monitors have not been defined and for relative humidity there is only the code for instrument readings taken by the software user.

U8 Usage Code : 2

Data type	U8.U32 ID code
Room Temperature (read by user)	2.0
Thermometry Channel i	2.i
Relative Humidity (read by user)	2.32768

Reference Interferometer Section Devices

The reference interferometer section devices data is first stored in the raw state. The raw data is further processed. First the data is separated out into data belonging to laser 1 and data belonging to laser 2. This data may then be normalised with respect to the power monitor[15].

U8 Usage Code : 3

Data type	U8.U32 ID code
Raw Data	
Power monitor	3.0
Long Reference	3.1
Short Reference	3.2
10 GHz etalon	3.3
250 GHz etalon	3.4
Wavemeter	3.5

Data type	U8.U32 ID code	Data type	U8.U32 ID code
Separated Data		**Normalised Data**	
Laser 1		**Laser 1**	
Power monitor	3.128	Power monitor	3.65536
Long Reference	3.129	Long Reference	3.65537
Short Reference	3.130	Short Reference	3.65538
10 GHz etalon	3.131	10 GHz etalon	3.65539
250 GHz etalon	3.132	250 GHz etalon	3.65540
Laser 2		**Laser 2**	
Power monitor	3.256	Power monitor	3.65792
Long Reference	3.257	Long Reference	3.65793
Short Reference	3.258	Short Reference	3.65794
10 GHz etalon	3.259	10 GHz etalon	3.65795
250 GHz etalon	3.260	250 GHz etalon	3.65796

[15]Assuming that a suitable spatial filter was present in the reference interferometer section

Laser operation

These data describe the operating conditions of the laser, as recorded by the laser control unit. Although the current laser 2 is not capable of coarse tuning, the wavelength of laser 2 may be variable in the future so this ID code has been defined.

U8 Usage Code : 4

Data type	U8.U32 ID code
Laser 1 λ /nm	4.1
Laser 2 λ /nm	4.2
Laser 1 Power /mW	4.129
Laser 2 Power /mW	4.130
Laser 1 Drive current /mA	4.385
Laser 2 Drive current /mA	4.386
Laser 1 Diode temp °C	4.513
Laser 2 Diode temp °C	4.514

Acousto-optic Phase stepping

U8 Usage Code : 5

Data type	U8.U32 ID code
Acousto-optic frequency monitor	5.0

FSI Channels

The codes are given for FSI channel i. This includes the short reference interferometer (channel 0) which is duplicated onto this data channel from the reference interferometer channel 3.2 since this is the most convenient way to include it in the FSI channels processing.

U8 Usage Code : 6

Data type	U8.U32 ID code
Raw Data Channel i	i
Laser 1 (separated)	$i + 16384$
Laser 2 (separated)	$i + 32768$

Frequency (x) axis

The frequency axis forms the x axis for the fringes which are fitted by MINUIT. Extraction of the frequency axis relies on intermediate stages of decoding the synchronisation signal, phase extraction and unwrapping.

There are 3 different index data types.

DAQ indices The first type are called DAQ indices. These represent, for a given subscan, the DAQ index value of those points which survived synchronisation assignment to one or other laser. From the original raw data array, each entry in the DAQ indices is the first point in a group of 4 which were assigned to one particular laser. For example, if the first value stored in data type 7.1025 was 5, this indicates that the data points 5,6,7 and 8 from the original raw data array have been saved as the first four data points in arrays of laser 1 data from all instruments.

Xy indices The second type are called xy indices. These represent for each laser, the selected points from the original DAQ indices array, which survived the process of phase extraction and unwrapping. The numerical values still represent the original location in the raw data array.

Matched indices The third type are called matched indices. These represent for each laser, those points from the xy indices of one laser, which have a surviving partner in the xy indices of the other laser. The points are paired off so that a corresponding pair came from the same synchronisation cycle, (ie the laser 1 point comes first). The numerical value of the match index is the position within the xy indices array and NOT the original raw data index, since it is used in conjunction with arrays of x and y points not with raw data.

U8 Usage Code : 7

Data type	U8.U32 ID code
Synchronisation signal (raw)	7.0
Laser 1 θ_{folded}	7.1
Laser 2 θ_{folded}	7.2
Laser 1 θ^2_{folded}	7.3
Laser 2 θ^2_{folded}	7.4
Laser 1 unwrapped θ	7.5
Laser 2 unwrapped θ	7.6
Laser 1 extracted phase step α	7.128
Laser 2 extracted phase step α	7.129
Laser 1 extraction errors	7.130
Laser 2 extraction errors	7.131
Laser 1 Frequency axis x_1	7.256
Laser 2 Frequency axis x_2	7.257
Laser 1 data DAQ indices	7.1025
Laser 2 data DAQ indices	7.1026
Laser 1 xy indices	7.1027
Laser 2 xy indices	7.1028
Laser 1 matched (time filter) indices	7.1029
Laser 2 matched (time filter) indices	7.1030

Measurement Arm Intensities (y) axis

For FSI channel i.

U8 Usage Code : 8

Data type	U8.U32 ID code
Laser 1 channel i y_1 values	$8.i$
Laser 2 channel i y_2 values	$8.(i + 65536)$

D.3.2 Header Sections

The U8 ID codes for header sections are given below. These match the categories used for Data Channel identification.

Header Section	Identity number
Comments block	0
DAQ information	1
Environmental information	2
Reference interferometer Section information	3
Laser information	4
Phase stepping	5
FSI channels	6
Processed Data	9

D.3.3 Instruments

These ID codes are only used with directly measured[16] data channels to indicate which instrument generated them.

Instrument type	Single byte code
Read by User	0.0[17]
GPIB Instrument on channel i	1.i
VME Scaler Lecroy Model 1151E	2.0
VME ADC Burr Brown Model 402	3.0

[16] As opposed to data derived through calculations on measured data. Separated data would count as directly measured data.

[17] This same ID code is used to represent processed data